INFORMATION TO USERS

This manuscript has been reproduced from the microfilm master. UMI films the text directly from the original or copy submitted. Thus, some thesis and dissertation copies are in typewriter face, while others may be from any type of computer printer.

The quality of this reproduction is dependent upon the quality of the copy submitted. Broken or indistinct print, colored or poor quality illustrations and photographs, print bleedthrough, substandard margins, and improper alignment can adversely affect reproduction.

In the unlikely event that the author did not send UMI a complete manuscript and there are missing pages, these will be noted. Also, if unauthorized copyright material had to be removed, a note will indicate the deletion.

Oversize materials (e.g., maps, drawings, charts) are reproduced by sectioning the original, beginning at the upper left-hand corner and continuing from left to right in equal sections with small overlaps.

Photographs included in the original manuscript have been reproduced xerographically in this copy. Higher quality 6" x 9" black and white photographic prints are available for any photographs or illustrations appearing in this copy for an additional charge. Contact UMI directly to order.

Bell & Howell Information and Learning
300 North Zeeb Road, Ann Arbor, MI 48106-1346 USA

UMI®
800-521-0600

OPTICAL PROPERTIES OF STRONGLY COUPLED D-WAVE SUPERCONDUCTORS WITH AN ANISOTROPIC MOMENTUM DEPENDENT INTERACTION

by

DWAYNE G. BRANCH

B.Sc. (Mount Allison) 1992
M.Sc. (McMaster) 1995

A Thesis
Submitted to the School of Graduate Studies
in Partial Fulfilment of the Requirements
for the Degree
Doctor of Philosophy

McMaster University

OPTICAL PROPERTIES OF STRONGLY COUPLED D-WAVE SUPERCONDUCTORS

DOCTOR OF PHILOSOPHY (1997)
(Physics)

McMaster University
Hamilton, Ontario

TITLE: Optical Properties of Strongly-Coupled d-wave Superconductors with an Anisotropic Momentum Dependent Interaction

AUTHOR: Dwayne G. Branch

SUPERVISOR: Dr. J. P. Carbotte

NUMBER OF PAGES: xii, 202

Abstract

We have studied within the Eliashberg framework properties of a two-dimensional d-wave superconductor where the electron-boson interaction leading to pairing in the superconducting state is a highly anisotropic function of momentum. Adding to the momentum anisotropy is an underlying single particle band structure based on a two-dimensional tight-binding model. The convolution of anisotropic interaction and anisotropic energy dispersion leads to a self energy which is strongly k-dependent in the Brillouin zone. Additionally, the boson spectral weight was assumed to extend over a large energy range with significant weight at both high and low frequencies.

The study begins with numerical calculations of the self-consistent electronic self energy. Renormalization effects are shown to play an important role in the quasiparticle properties. The effects of strong inelastic scattering on the electronic spectral density in both the normal and superconducting state are investigated.

Numerical calculations of the in-plane optical conductivity and electronic Raman scattering cross-sections are made for both the normal and superconducting states. Using a simple model to extract the effective quasiparticle scattering rates and mass renormalization factors, comparison of the optical results are made to the fundamental quasiparticle properties. The effects of momentum space anisotropy and strong electron-boson coupling on the optical scattering rates are discussed.

The low frequency behaviour of the various Raman scattering channels in the presence of strong inelastic scattering is investigated. It is shown that both inelastic and elastic scattering can lead to a crossover from ω^3 to ω dependence of the low frequency B_{1g} spectra in the superconducting state, while the B_{2g} response remains linear in frequency.

An effective boson spectral density, $g^2\chi''(\omega)$, is extracted form the calculated conductivity using a simple model. It is shown that the optical conductivity data may be used to extract the signature of the electron-boson coupling. The effective spectral density is then used in an isotropic model to determine whether or not such a function extracted from the conductivity would capture all the details of the momentum dependent interaction.

The effects of resonant impurity scattering on the low frequency conductivity and Raman spectra are also investigated. Numerical calculations confirm the existence of universal values for the zero frequency conductivity and zero frequency slope of the B_{2g} Raman response in the superconducting state. No such limit is observed in the Raman B_{1g} spectrum.

Acknowledgements

First of all, I would like to thank my supervisor, Jules Carbotte, for the patience and guidance he has shown over the past several years. Thanks should also go to the students, post docs, and visitors who have made up the condensed matter theory group. In particular, I would like to thank Bill Atkinson, Peter Arberg, Ewald Schachinger, Bozidar Mitrovic, Chris O'Donovan, and Jennifer Rendell for many helpful discussions. Wen-chin Wu deserves a special mention as he played a very important role in my education, and took the time to give the draft of this work a very thorough reading. Also, I wish to thank Elisabeth Nicol (U. Guelph) for allowing me time on her computer, without which, this work may never have been completed.

I would like to thank my parents, Lela and Percy, for all their support and encouragement over the years, and for at least feigning interest in my academic pursuit. Theirs is a debt I can never fully repay. I must also thank my sister, Tanya, and my brother, Trevis. Why, I do not quite know, but I am sure they will tell me at some point.

Most importantly, I wish to thank my wife, Sharon, for her patience and support throughout my graduate career.

Contents

List of Figures

List of Tables

Chapter 1

Introduction

1.1 High Temperature Superconductors

Prior to the discovery of superconductivity in a class of doped cuprate perovskites in 1986, the highest critical temperature was seen in Nb_3Ge with a T_c of 23 K. The first ceramic superconductor, $La_{2-x}Ca_xCuO_4$, beat this record having a critical temperature, T_c, of 30 K at optimal doping (Bednorz and Muller 1986). In the following year, a closely related material was discovered, $YBa_2Cu_3O_{7-\delta}$, with a $T_c \sim 93$ K for $\delta \sim 0.1$ (Wu et al. 1987). Since that time, intense effort has lead to the synthesis of other cuprate materials with larger T_c, the record currently held by a compound in the Hg family with $T_c \sim 150$ K (Chu et al. 1993).

The high-T_c cuprates can be viewed as a stack of closely spaced CuO_2 layers, separated by either normal or insulating layers which act primarily as charge reservoirs for the planes. The large anisotropy of the ab-plane to c-axis properties has lead to the belief that superconductivity in theses material is dominated by the physics of the CuO_2 planes and that the coupling or interlayer hopping is only a small perturbation.

The parent compounds are insulators which exhibit antiferromagnetic ordering of the copper spins in the CuO_2 planes. The magnetic ordering temperature (Neel temperature), T_N, is at a maximum in the undoped compounds. Increased doping results in a rapid reduction of T_N. Beyond a critical doping the copper spins no longer exhibit long range antiferromagnetic order as the antiferromagnetism is frustrated by

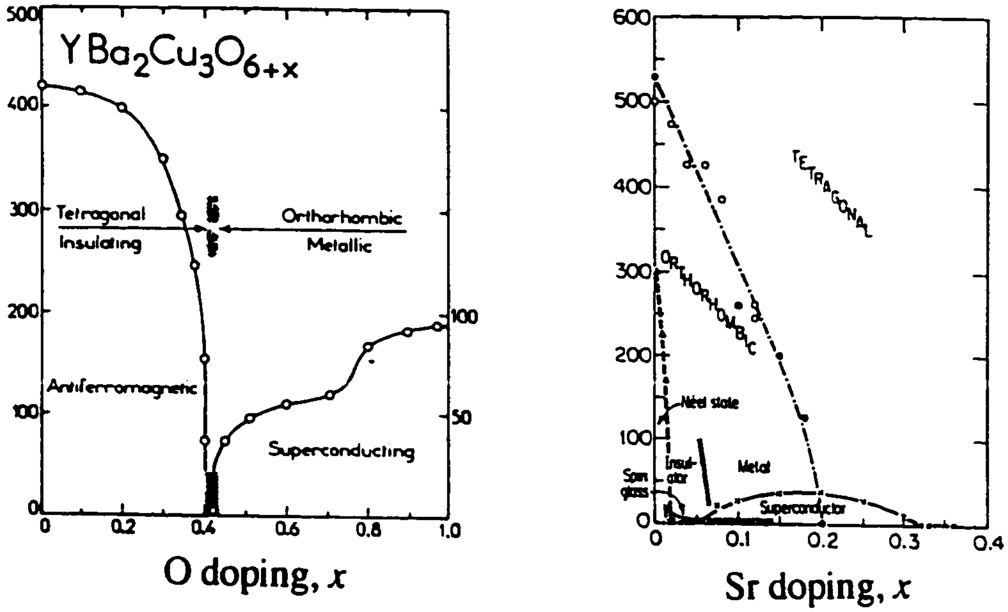

Figure 1.1: Phase diagram for a) $YBa_2Cu_3O_{7-\delta}$ (Rossat-Mignod et al. 1991) and b) LaSrCuO (Birgeneau et al. 1989)

the introduction of holes in the CuO_2 planes. With further doping, the material enters a region of superconductivity. In figure (1.1), the phase diagrams for $YBa_2Cu_3O_{7-\delta}$ (Rossat-Mignod et al. 1991a) and for LaSrCuO are shown (Birgeneau and Shirane 1989). Similar phase diagrams exist for other cuprate materials.

Along with the high critical temperatures came an array of unusual normal state properties. Nearly all the normal state properties are "anomalous" and differ from the standard Landau Fermi liquid behaviour of typical metals [for a review see (Iye 1992)]. This lead to the question of whether or not the Landau Fermi liquid is applicable to these new materials (Anderson 1987). Several non-Fermi liquid mechanisms were proposed which generally start form a doped insulator(for example see (Anderson 1987: Chakravarty and Anderson 1994; Lee and Nagaosa 1992)). Others kept Fermi liquid like approaches, introducing such theories as the marginal Fermi liquid (Varma et al. 1989) and the nearly antiferromagnetic Fermi liquid (Millis, Monien, and Pines 1990). Despite the intense research effort and the large number of publications on the high-T_c compounds, there is yet no consensus on the pairing mechanism.

Angle resolved photo-emission measurements on YBCO (Campuzano et al. 1990) and BSCCO (Olson et al. 1990; Ding et al. 1996) see evidence of a well defined

Fermi surface supporting the scenario of a Fermi liquid like state. In YBCO, the ARPES results are fairly independent of doping over a large region of phase space. Underdoped BSCCO, on the other hand, appears to lose sections of the Fermi surface along certain directions and develops hole pockets near $(\pi/2, \pi/2)$ and equivalent points in the Brillouin zone (Ding et al. 1997). This is often associated with the development of the normal state pseudogap seen in underdoped materials.

ARPES measurements and band structure calculations indicate that there is a large amount of momentum anisotropy in the quasiparticle dispersion relation and that the bands are better fit with a tight-binding band rather than the free electron dispersion. In quasi-2D systems, the tight-binding approach leads to van Hove singularities in the density of states and, therefore, a constant density of states at the Fermi energy may not be a good approximation. The effects of planar anisotropy in the single particle dispersion and a non-constant density of states near the Fermi energy are well understood (Zhou and Schulz 1992; Jiang 1992; Mitrović 1981; Mansor 1994).

It was recognized early on that the symmetry of the order parameter may not be the s-wave type of the conventional materials (Annett, Goldenfeld, and Renn 1992). A consensus is now emerging among members of the high-T_c community that the superconducting pairing symmetry is d-wave (more specifically, the cuprate superconductors are believed to exhibit $d_{x^2-y^2}$ symmetry). This will put a large constraint on the proposed mechanisms. A review review of the current experimental situation favouring the d-wave interpretation is given in Annet et al. (Annett, Goldenfeld, and Leggett 1996).

D-wave pairing of this sort can be explained by a repulsive interaction which strongly favours quasiparticle scattering with $\mathbf{q} = (\pi, \pi)$ momentum transfer. There are several theories which are consistent with this explanation, so clearly other constraints will be necessary in order to distinguish which theory, if any, is the correct one. One main feature in common between all pairing interactions leading to $d_{x^2-y^2}$ pairing symmetry is the strong momentum anisotropy of the interaction.

In this thesis we are not attempting to determine the correct pairing mechanism. Instead, we wish to study the effects of inelastic scattering and momentum-space anisotropy on the optical properties. Making quantitative fits to experiment and explaining details is not the purpose. With this in mind, we chose a particular mechanism for the features of large momentum anisotropy and the ability to stabilize d-wave superconductivity.

1.2 Tunneling vs. Optical Experiments

In many respects, the field of conventional superconductivity was "dominated" by tunneling experiments. In these experiments, a voltage difference is applied across either metal-insulator-superconductor or superconductor-insulator-superconductor junctions. The observed conductance is zero until the applied voltage is large enough to allow single particle tunneling to states above the gap. At $T = 0$ K, the voltage at which the conductance first becomes non-zero is related to the size of the superconducting gap.

These measurements give information not only on the symmetry and amplitude of the energy gap, but were also important in the establishment of the pairing mechanism (Schrieffer, Scalapino, and Wilkins 1963; McMillan and Rowell 1965; McMillan and Rowell 1969; Carbotte 1990). Structure in the conductance above the gap edge was identified with the electron-phonon interaction. Inversion of this data allowed for the electron-phonon spectral density, $\alpha^2F(\omega)$, to be extracted. This function is fundamental in that it contains all the information about the electron-phonon interaction. Once this function is known, it can be used to calculate other properties of the system. This formalism has proven to be a powerful technique which can quantitatively explain the material specific deviations away from the simple BCS predictions (Carbotte 1990).

An extensive industry has grown up around the use of tunneling junctions to extract the electron-phonon spectral functions from conventional superconductors. While calculation of $\alpha^2F(\omega)$ from first principles is possible, it is a difficult calculation to do. Since the prediction of observable properties such as the optical conductivity was the ultimate goal, the electron-boson spectral densities extracted from experiment contained all the material specific information needed to make accurate predictions.

Data extracted from tunneling experiments on the high-T_c compounds has not been as enlightening. Different experimental techniques have lead to different results. To make matters worse, data is not even consistent between different experimental groups performing the same experiment, however, improvements are being made (Hasegawa, Ikuta, and Kitazawa 1992). Conventional superconductors have coherence lengths on the order of 10^2 Åwhile those of the cuprate superconductors are on the order of 10 Å. The short coherence length of the high-T_c materials means tunneling is essentially a surface probe measuring only the first few layers. Surface quality is therefore an important aspect of good tunneling junctions.

Optical data, on the other hand, has been very important in obtaining information on the low energy excitations in the oxides. It has been known for a while that the optical conductivity can carry information of the spectral density of the underlying boson field. Joyce and Richards first observed such structure using infrared techniques (Joyce and Richards 1970). Soon after, Farnworth and Timusk managed to extract an $\alpha_{tr}^2F(\omega)$ from optical data resolving features seen in neutron data but not in tunneling data (Farnworth and Timusk 1974). Such experiments, while being difficult to perform with the required resolution in conventional superconductors, proved the potential of optical data to directly probe the mechanism of superconductivity. The resolution difficulty with these early materials was the reflectivity of near unity due to the fact they were fairly good metals. Because the cuprates are relatively poor metals, the reflectance data is not close to unity. Now that good crystals are available, reliable and reproducible measurements can be performed.

In-plane Raman scattering, or inelastic light scattering, experiments have also become important and revealing experiments in the high-T_c field. By varying the polarization of the incident photons and selecting the polarization of the scattered photons, different sections of the Fermi surface can effectively be probed. These experiments have confirmed the large anisotropy of the superconducting energy gap in the cuprate materials. Recently, attention has moved to measurements of the normal state properties of underdoped materials. Measurements such as these should be able to confirm the ARPES prediction of anisotropy in the pseudopgap.

1.3 Outline

In this thesis we adopted the point of view that the Fermi liquid approach is appropriate, and that, at least to a first approximation, the superconducting state may be described within Eliashberg formalism. We have studied a system in which the electron pairing is mediated by a highly momentum dependent repulsive interaction: spin-fluctuation exchange.

Chapter 2 contains an introduction to the Eliashberg equations and their origins in many electron theory. Specifics of the model, such as the form of the quasiparticle dispersion relation and pairing interaction, are introduced. In later sections, the results of numerical calculations are discussed comparing the normal and superconducting state results . The effects of inelastic scattering, impurity scattering and temperature variation on the electronic spectral density and the quasiparticle density of states is investigated.

Chapter 3 describes the results of optical conductivity calculations performed in the Eliashberg-Nambu formalism. After a brief introduction to the theoretical formalism, numerical results for the normal state frequency dependent conductivity are discussed. Emphasis is placed on the roles played by the energy dependent electronic density of states, the momentum anisotropy of the underlying system, and the frequency/momentum dependence of the electron-boson interaction. The theoretical conductivity spectrum is analyzed using an extended Drude model extracting the frequency dependent optical scattering rates and the optical mass renormalization function. Comparison of the optical results and the fundamental quasiparticle results described in chapter 2 are made. Using a simple model for the conductivity and scattering rates, an effective electron boson spectral density, $g^2\chi''(\omega)$, is extracted.

In a later section, the superconducting state results are introduced. Similarly to the normal state discussion, the extended Drude is used to extract scattering rates and mass renormalization results from the calculated spectra. Comparison is made with the normal state results and with the fundamental quasiparticle properties. In the last section, the effects of non-magnetic impurity scattering on the conductivity is investigated. Focus is placed on resonant scattering and the predictions of a universal saturation of the low frequency conductivity is confirmed.

In-plane electronic Raman scattering calculations are discussed in chapter 4 for both normal and superconducting states. Inclusion of inelastic scattering in our models allows for the calculation of the normal state response. The low frequency power laws for the superconducting state response are extracted. Effects of both inelastic scattering and elastic impurity scattering are investigated. A simple model is introduced which allows for the extraction of effective scattering rates from the various Raman scattering symmetries. Comparison of the results is made between the Raman spectra, conductivity, and quasiparticle properties.

Chapter 2

Theory

In this chapter, we will introduce the Eliashberg equations which constitute the strong-coupling formalism used throughout this thesis. These equations are a complicated set of coupled non-linear integral equations which usually require numerical calculation for any realistic pairing interaction. The Eliashberg formalism has proven to be a quantitative theory in conventional superconductivity with many of the deviations from simple BCS being explained within the more complicated theory (Carbotte 1990).

We introduce the Green's function approach to the many electron problem in section (2.1), first for the normal state and then generalize the theory to include pair correlations in the superconducting state. Particular models for the electron-boson interaction and impurity scattering contributions to the electronic self-energy are introduced. The Eliashberg equations are then derived using these models in order to highlight the assumptions behind the equations.

In section (2.3) we discuss the particular choice of models for the single quasiparticle dispersion relation and the pairing mechanism. Computational results for our model in both the normal and superconducting states are presented in section (2.4). The self-energy and renormalization effects are discussed in detail. We also present the results for the spectral density and the quasiparticle density of states.

The effects of non-magnetic impurity scattering is the topic of the last section.

2.1 Green's Functions

There are many good textbooks which describe the Green's function approach and their formal properties (Abrikosov, Gor'kov, and Dzyalosinski 1963; Doniach and Sondheimer 1974; Fetter and Walecka 1971; Mahan 1990; Rickayzen 1980) so we will not attempt to rederive everything here. Instead, we shall simply give enough details to understand the basic formalism used in the rest of this work.

The normal state electronic Green's function is defined as

$$G(\mathbf{k}, \tau) \equiv -\langle T_\tau c_{\mathbf{k}\sigma}(\tau) c^\dagger_{\mathbf{k}\sigma}(0)\rangle \tag{2.1}$$

where T_τ is Wick's time ordering operator which reorders the operators such that the imaginary time τ increases from right to left. This reordering operation respects the anticommutation relation introducing a minus sign every time two neighbouring operators are interchanged. The operators $c^\dagger(\tau)$ and $c(\tau)$ are operators in the Heisenberg representation

$$\begin{aligned} c_{\mathbf{k},\sigma}(\tau) &= e^{H\tau} c_{\mathbf{k},\sigma} e^{-H\tau} \\ c^\dagger_{\mathbf{k},\sigma}(\tau) &= e^{-H\tau} c^\dagger_{\mathbf{k},\sigma} e^{H\tau}. \end{aligned} \tag{2.2}$$

The angled brackets in equation (2.1) refer to the grand canonical average

$$\langle A\rangle = \frac{1}{tr[e^{-\beta H}]} tr[e^{-\beta H} A] \tag{2.3}$$

where A is an operator, $tr[A]$ is the trace and $\beta = 1/T$ is the inverse temperature (T is in units of energy). The Hamiltonian, H, is assumed to contain the term $-\mu N$ where N is the Number operator and μ is the chemical potential.

It can be shown that the thermal Green's function has the formal property that for $-\beta < \tau < \beta$,

$$G(\mathbf{k}, \tau + \beta) = -G(\mathbf{k}, \tau). \tag{2.4}$$

The Green's function can therefore be mapped into the range $\tau \in [-\beta, \beta]$. Since $G(\mathbf{k}, \tau)$ is a periodic function in τ, we can write it terms of a Fourier series

$$G(\mathbf{k}, \tau) = \frac{1}{\beta} \sum_{n=-\infty}^{+\infty} e^{-i\omega_n \tau} G(\mathbf{k}, i\omega_n) \tag{2.5}$$

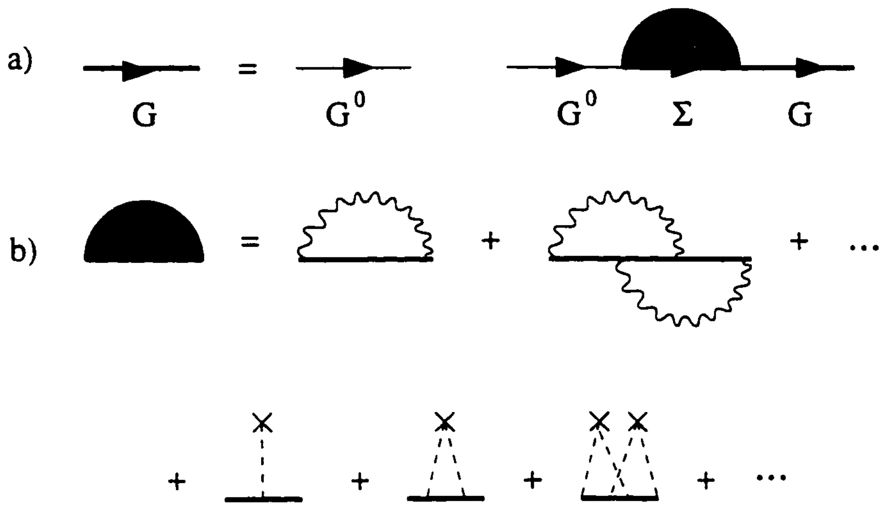

Figure 2.1: a) Diagrammatic representation of Dyson's equation for the electron Green's function. The self-energy b) is composed of electron-boson interactions and impurity scattering. The thick line represents the interacting Green's function, the wiggly line represents boson propagation, and the dashed line represents impurity scattering from the impurity centers (×). This problem requires a self-consistent solution.

where $\omega_n = (2n+1)\pi/\beta$ for $n = 0, \pm1, \pm2, ...$ are the fermionic Matsubara frequencies. The inverse Fourier transform is then given by

$$G(\mathbf{k}, i\omega_n) = \frac{1}{2}\int_{-\beta}^{\beta} d\tau e^{i\omega_n\tau} G(\mathbf{k}, \tau). \tag{2.6}$$

For a system of non-interacting electrons, the Hamiltonian is given by

$$H = \sum_{\mathbf{k}} \varepsilon_{\mathbf{k}} c_{\mathbf{k}}^{\dagger} c_{\mathbf{k}} \tag{2.7}$$

where $\varepsilon_{\mathbf{k}}$ is the non-interacting quasiparticle dispersion relation which implicitly contains the chemical potential, μ, and is therefore measured from the Fermi surface. The non-interacting Green's function is then easily shown to be

$$G_0(\mathbf{k}, i\omega_n) = \frac{1}{i\omega_n - \varepsilon_{\mathbf{k}}}. \tag{2.8}$$

Once the thermal Green's functions are known, we can calculate any property of the system, including thermodynamic and transport properties. The interacting

Green's function is given by Dyson's equation (see figure (2.1.a))

$$G(\mathbf{k}, i\omega_n) = G_0(\mathbf{k}, i\omega_n) + G_0(\mathbf{k}, i\omega_n)\Sigma(\mathbf{k}, i\omega_n)G(\mathbf{k}, i\omega_n). \tag{2.9}$$

The self-energy equation contains all terms which involve the electron-boson interaction and impurity scattering (figure (2.1.b)). After isolating the interaction Green's function we have

$$G^{-1}(\mathbf{k}, i\omega_n) = G_0^{-1}(\mathbf{k}, i\omega_n) - \Sigma(\mathbf{k}, i\omega_n) \tag{2.10}$$

or

$$G(\mathbf{k}, i\omega_n) = \frac{1}{i\omega_n - \varepsilon_{\mathbf{k}} - \Sigma(\mathbf{k}, i\omega_n)}. \tag{2.11}$$

The thermal (finite-temperature) Green's function formalism has been an extremely powerful method in describing many particle systems, however, the theory breaks down when the electron-electron interactions lead to pairing in the superconducting state. In order to describe the superconducting state within a Green's functions approach, one must build pair correlations directly into the formalism. The superconducting state is conceptually no more difficult than the normal state; the main difference being that in this case the Green's function and the self-energy function will be written in terms of matrices instead of scalar functions.

In order to describe superconductivity it is traditional to use Nambu's two-component formalism (Nambu 1960). Introducing Nambu's two component field operators

$$\begin{aligned}
\Psi_{\mathbf{k}} &= \begin{pmatrix} c_{\mathbf{k},\uparrow} \\ c^{\dagger}_{-\mathbf{k},\downarrow} \end{pmatrix} \\
\Psi^{\dagger}_{\mathbf{k}} &= \begin{pmatrix} c\dagger_{\mathbf{k},\uparrow} & c_{-\mathbf{k},\downarrow} \end{pmatrix}
\end{aligned} \tag{2.12}$$

the electronic Green's function becomes a 2×2 matrix,

$$\begin{aligned}
\hat{G}(\mathbf{k}, \tau) &= -\langle T_\tau \Psi_{\mathbf{k}}(\tau)\Psi^{\dagger}(0)\rangle \\
&= -\begin{pmatrix} \langle T_\tau c_{\mathbf{k},\uparrow}(\tau)c^{\dagger}_{\mathbf{k},\uparrow}(0)\rangle & \langle T_\tau c_{\mathbf{k},\uparrow}(\tau)c_{-\mathbf{k},\downarrow}(0)\rangle \\ \langle T_\tau c^{\dagger}_{-\mathbf{k},\downarrow}(\tau)c^{\dagger}_{\mathbf{k},\uparrow}(0)\rangle & \langle T_\tau c^{\dagger}_{-\mathbf{k},\downarrow}(\tau)\rangle c_{-\mathbf{k},\downarrow}(0) \end{pmatrix} \\
&= \begin{pmatrix} G_{1,1}(\mathbf{k}, \tau) & F(\mathbf{k}, \tau) \\ \bar{F}(\mathbf{k}\tau) & G_{2,2}(\mathbf{k}, \tau) \end{pmatrix}.
\end{aligned} \tag{2.13}$$

Transforming (2.13) to the imaginary frequency axis,

$$\hat{G}(\mathbf{k}, i\omega_n) = \frac{1}{2}\int_{-\beta}^{\beta} d\tau\, e^{i\omega_n\tau}\, \hat{G}(\mathbf{k}, \tau). \tag{2.14}$$

$G_{1,1}(\mathbf{k}, \tau)$, or the upper left-hand element of (2.13), is simply the "normal" Green's function introduced earlier in equation (2.1). The off-diagonal elements, $F(\mathbf{k}, \tau)$ and $\bar{F}(\mathbf{k}, \tau)$, describe particle-particle correlations. In the literature, these off-diagonal elements are commonly referred to as *Gorkov's anomalous propagators*. For non-interacting band electrons, the off-diagonal terms vanish and $G_{1,1}(\mathbf{k}, i\omega_n)$ has the same form as $G_0(\mathbf{k}, i\omega_n)$ [equation (2.8)].

Using the properties of the time ordering operator, T_τ, one can show that

$$G_{2,2}(\mathbf{k}, \tau) = -G_{1,1}(-\mathbf{k}, -\tau) \tag{2.15}$$

or, from equation (2.14),

$$G_{2,2}(\mathbf{k}, i\omega_n) = -G_{1,1}(-\mathbf{k}, -i\omega_n). \tag{2.16}$$

The non-interacting Green's function in Nambu formalism is therefore given by

$$\begin{aligned} \hat{G}_0(\mathbf{k}, i\omega_n) &= \begin{pmatrix} (i\omega_n - \varepsilon_{\mathbf{k}})^{-1} & 0 \\ 0 & (i\omega_n + \varepsilon_{\mathbf{k}})^{-1} \end{pmatrix} \\ &= \left[i\omega_n\hat{\tau}_0 - \varepsilon_{\mathbf{k}}\hat{\tau}_3\right]^{-1} \\ &= -\frac{i\omega_n\hat{\tau}_0 + \varepsilon_{\mathbf{k}}\hat{\tau}_3}{\omega_n^2 + \varepsilon_{\mathbf{k}}^2} \end{aligned} \tag{2.17}$$

where we have introduced the Pauli matrices,

$$\hat{\tau}_0 = \begin{pmatrix} 1 & 0 \\ 0 & 1 \end{pmatrix}, \quad \hat{\tau}_1 = \begin{pmatrix} 0 & 1 \\ 1 & 0 \end{pmatrix}, \quad \hat{\tau}_2 = \begin{pmatrix} 0 & -i \\ i & 0 \end{pmatrix}, \quad \hat{\tau}_3 = \begin{pmatrix} 1 & 0 \\ 0 & -1 \end{pmatrix}. \tag{2.18}$$

In similar fashion to the normal state, Dyson's equation in the superconducting state can be written

$$\hat{G}^{-1}(\mathbf{k}, i\omega_n) = \hat{G}_0^{-1}(\mathbf{k}, i\omega_n) - \hat{\Sigma}(\mathbf{k}, i\omega_n) \tag{2.19}$$

where $\hat{\Sigma}$ is the Nambu electronic self-energy which is now also a 2×2 matrix. The most general form of the self-energy is

$$\hat{\Sigma}(\mathbf{k}, i\omega_n) = i\omega_n(1 - Z(\mathbf{k}, i\omega_n))\hat{\tau}_0 + \xi(\mathbf{k}, i\omega_n)\hat{\tau}_3 + \phi(\mathbf{k}, i\omega_n)\hat{\tau}_1 + \bar{\phi}(\mathbf{k}, i\omega_n)\hat{\tau}_2 \tag{2.20}$$

where $Z(\mathbf{k}i\omega_n)$, $\xi(\mathbf{k}, i\omega_n)$, $\phi(\mathbf{k}, i\omega_n)$, and $\bar{\phi}(\mathbf{k}, i\omega_n)$ are four independent functions whose values will be determined later. Substituting (2.20) in Dyson's equation (2.19), the interacting thermal Green's function can be written

$$\hat{G}^{-1}(\mathbf{k}, i\omega_n) = \omega_n Z_{\mathbf{k}}(i\omega_n)\hat{\tau}_0 - \left[\varepsilon_{\mathbf{k}} + \xi_{\mathbf{k}}(i\omega_n)\right]\hat{\tau}_3 - \phi_{\mathbf{k}}(i\omega_n)\hat{\tau}_1 - \bar{\phi}_{\mathbf{k}}(i\omega_n)\hat{\tau}_2. \tag{2.21}$$

[Note: For ease of notation, we make the following definitions: $\tilde{\omega}_{\mathbf{k}}(i\omega_n) = \omega_n Z_{\mathbf{k}}(i\omega_n)$ and $\tilde{\varepsilon}_{\mathbf{k}}(i\omega_n) = \varepsilon_{\mathbf{k}} + \xi_{\mathbf{k}}(i\omega_n)$.] After inverting the matrix (2.21), the Green's function becomes

$$\hat{G}(\mathbf{k}, i\omega_n) = \frac{-1}{D_{\mathbf{k}}(i\omega_n)}\left(i\tilde{\omega}_{\mathbf{k}}(i\omega_n)\hat{\tau}_0 + \tilde{\varepsilon}_{\mathbf{k}}(i\omega_n)\hat{\tau}_3 + \phi_{\mathbf{k}}(i\omega_n)\hat{\tau}_1 + \bar{\phi}_{\mathbf{k}}(i\omega_n)\hat{\tau}_2\right) \tag{2.22}$$

where

$$D_{\mathbf{k}}(i\omega_n) = \left[\tilde{\omega}_{\mathbf{k}}(i\omega_n)\right]^2 + \left[\tilde{\varepsilon}_{\mathbf{k}}(i\omega_n)\right]^2 + \left[\phi_{\mathbf{k}}(i\omega_n)\right]^2 + \left[\bar{\phi}_{\mathbf{k}}(i\omega_n)\right]^2. \tag{2.23}$$

In the normal state, ϕ and $\bar{\phi}$ both vanish and $\hat{G}$ becomes diagonal. The functions Z and ξ can then be determined from the normal state Σ by noting that in equation (2.16), the $\hat{\tau}_0$ component of the Green's function is an odd function of $i\omega_n$ and the $\hat{\tau}_3$ component is even. Assuming that everything is even in $\mathbf{k}$, the definitions of Z and ξ are given by

$$\begin{aligned} i\omega_n(1 - Z_{\mathbf{k}}(i\omega_n)) &= \frac{1}{2}\left[\Sigma_{\mathbf{k}}(i\omega_n) - \Sigma_{\mathbf{k}}(-i\omega_n)\right] && (2.24) \\ \xi_{\mathbf{k}}(i\omega_n) &= \frac{1}{2}\left[\Sigma_{\mathbf{k}}(i\omega_n) + \Sigma_{\mathbf{k}}(-i\omega_n)\right]. && (2.25) \end{aligned}$$

In order to conserve this property in the superconducting state (with Σ replaced by $\Sigma_{1,1}$), we must also have that $\phi^2 + \bar{\phi}^2$ is an even function in $i\omega_n$.

As it turns out, ϕ and $\bar{\phi}$ are related to each other through a constant phase. By choosing this phase properly, $\bar{\phi}$ (or the $\hat{\tau}_2$ term) vanishes and we are left only with the $\hat{\tau}_1$ term in the off-diagonal elements of the Nambu Green's function (Allen and Mitrovic 1982).

2.2 Self-energy Contributions

So far we have only dealt with the self-energy as a general function. In this section we develop specific models for the self-energy due to the electron-boson interactions and normal (non-magnetic) impurity scattering.

2.2.1 Electron-Boson Interactions

First we will focus on the electron-boson contributions to the electronic self-energy. For a system which couples to both the charge and spin density channels, the effective interaction Hamiltonian, H_i, can be written (Millis, Sachdev, and Varma 1988)

$$H_i = H_d + H_s \tag{2.26}$$

where

$$H_d = -\frac{1}{2}\sum_{\mathbf{k},\omega_n} n(\mathbf{k},\omega_n)\alpha^2 D(\mathbf{k},\omega_n)n(-\mathbf{k},-\omega_n) \tag{2.27}$$

and

$$H_s = -\frac{1}{2}\sum_{\mathbf{k},\omega_n,i,j} S_i(\mathbf{k},\omega_n)I^2\chi_{ij}(\mathbf{k},\omega_n)S_j(-\mathbf{k},-\omega_n). \tag{2.28}$$

Here $D(\mathbf{k},\omega_n)$ is the propagator which couples to the charge density channel with coupling constant α (such as phonons); $\chi_{ij}(\mathbf{k},\omega_n)$ and I are the propagator and coupling strength respectively which couple to the spin density channel. The electron density, n, and the spin density, $\vec{S}$, are, in Nambu notation,

$$\begin{aligned} n(\mathbf{k},\omega_n) &= \sum_{\mathbf{q},m} \Psi^\dagger_{\mathbf{k+q}}(\omega_{n+m})\hat{\tau}_3\Psi_{\mathbf{q}}(\omega_m) && (2.29) \\ S_i(\mathbf{k},\omega_n) &= \sum_{\mathbf{q},m} \Psi^\dagger_{\mathbf{k+q}}(\omega_{n+m})\alpha^i\Psi_{\mathbf{q}}(\omega_m) && (2.30) \end{aligned}$$

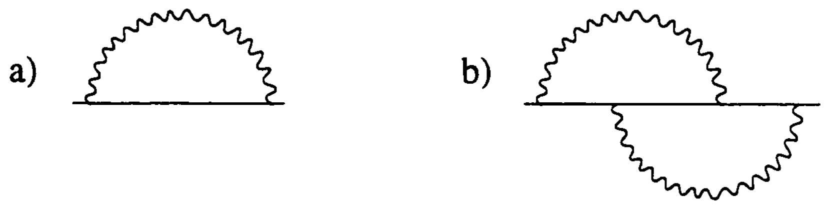

Figure 2.2: First a) and second b) order electron-boson contribution to the self-energy.

where the spin matrix α^i is given by (Millis, Sachdev, and Varma 1988; Maki 1969)

$$\alpha^i = \frac{1}{2}(1+\tau_3)\hat{\sigma}^i - \frac{1}{2}(1-\tau_3)(\hat{\sigma}^i)^T. \tag{2.31}$$

The $\hat{\tau}$ matrices act on the momentum space degrees of freedom while the $\hat{\sigma}$ matrices act on the spin degrees of freedom. [Note: it is somewhat unnatural to treat the spin fluctuation mechanism in two dimensional Nambu space. A more appropriate representation is the 4×4 Nambu representation which takes into account both spin and momentum degrees of freedom (Maki 1969). However, the final Eliashberg equations reduce to the same form (Millis, Sachdev, and Varma 1988), therefore, for notational simplicity, we will keep the 2×2 matrix form of the self energy.] It is typical to approximate $g^2\chi_{i,j}(\mathbf{k}, i\omega_n)$ with $g^2\chi(\mathbf{k}, i\omega_n)\delta(i,j)$, where $\delta(i,j)$ is the Kronecker delta and $\chi(\mathbf{k}, i\omega_n)$ the electronic susceptibility.

Later in this chapter we will assume the most important boson field (spin-fluctuations) couples to the spin-density channel and drop the charge density contribution (phonons). For now, in order to illustrate a fundamental difference between the two cases, we will keep both. The first two terms which contribute to the electronic self-energy are shown in figure (2.2). The first order contribution [figure (2.2.a)] is given by

$$\hat{\Sigma}(\mathbf{k}, i\omega_n) = -T\sum_{\mathbf{k}',m} \left\{ \begin{array}{c} \lambda_p(\mathbf{k}-\mathbf{k}', i\omega_n - i\omega_m) \\ \lambda_{sf}(\mathbf{k}-\mathbf{k}', i\omega_n - i\omega_m) \end{array} \right\} \left\{ \begin{array}{c} \hat{\tau}_3 \\ \hat{\tau}_0 \end{array} \right\} \hat{G}(\mathbf{k}', i\omega_m) \left\{ \begin{array}{c} \hat{\tau}_3 \\ \hat{\tau}_0 \end{array} \right\} \tag{2.32}$$

where $\lambda_p(\mathbf{q}, i\nu_n) = \alpha^2 D(\mathbf{q}, i\nu_n)$ represents the interaction kernel for the phonons and $\lambda_{sf}(\mathbf{q}, i\nu_n) = g^2\chi(\mathbf{q}, i\nu_n)$ for the spin-fluctuations (Millis, Sachdev, and Varma 1988; Kostur and Mitrović 1995). The vertex $\hat{\tau}_3$ or $\hat{\tau}_0$ is used depending on whether one couples to the charge density or spin density channels respectively.

The second order contribution, figure (2.2.b), is written

$$
\begin{aligned}
\hat{\Sigma}(\mathbf{k}, i\omega_n) = {} & T \sum_{\mathbf{k}',\mathbf{k}''} \sum_{l,m} \left\{ \begin{array}{c} \lambda_p(\mathbf{k}-\mathbf{k}', i\omega_n - i\omega_m)\lambda_p(\mathbf{k}'-\mathbf{k}'', i\omega_m - i\omega_l) \\ \lambda_{sf}(\mathbf{k}-\mathbf{k}', i\omega_n - i\omega_m)\lambda_{sf}(\mathbf{k}'-\mathbf{k}'', i\omega_m - i\omega_l) \end{array} \right\} \\
& \times \left\{ \begin{array}{c} \hat{\tau}_3 \\ \hat{\tau}_0 \end{array} \right\} \hat{G}(\mathbf{k}', i\omega_m) \left\{ \begin{array}{c} \hat{\tau}_3 \\ \hat{\tau}_0 \end{array} \right\} \hat{G}(\mathbf{k}'', i\omega_l) \left\{ \begin{array}{c} \hat{\tau}_3 \\ \hat{\tau}_0 \end{array} \right\} \qquad (2.33) \\
& \times \hat{G}(\mathbf{k}' + \mathbf{k}'' - \mathbf{k}, i\omega_m + i\omega_l - i\omega_n) \left\{ \begin{array}{c} \hat{\tau}_3 \\ \hat{\tau}_0 \end{array} \right\} .
\end{aligned}
$$

In the case of the electron-phonon interaction, the second order and higher terms may be neglected due to *Migdal's theorem* (Migdal 1958). No such theorem exists for electronic mechanisms, including spin-fluctuations, so higher order terms may be important in quantitative calculations (Wilkins 1980). Several estimates of the size of the second order correction term to the self-energy exist; most in agreement that the vertex corrections should be included in any quantitative calculations based on spin-fluctuation exchange (Sharifzadeh and Stamp 1996). In a recent paper Kostur and Mitrović have shown using a simple model that vertex corrections always lead to a decrease in T_c for a BCS-like model, but that for a strong-coupling model, such as the one used in this work, the vertex corrections may lead to either a decrease or an increase in T_c depending on the parameters chosen (Kostur and Mitrović 1995). In this work, we will ignore the second and higher order terms, using a spin-fluctuation model in very phenomenological way assuming that the effects of the vertex corrections are accounted for in the form of the interaction.

2.2.2 Impurity Scattering

Next, we move on to impurity scattering contributions to the self-energy. Assuming that the most significant contribution comes from single impurity scattering, we can approximate the self-energy, $\hat{\Sigma}_{imp}$, using the diagrams in figure (2.3.a). This approximation includes all terms which contain multiple scattering events from a single impurity center and ignores terms such as those shown in figure (2.3.b). This approximation is valid in the low impurity concentration limit.

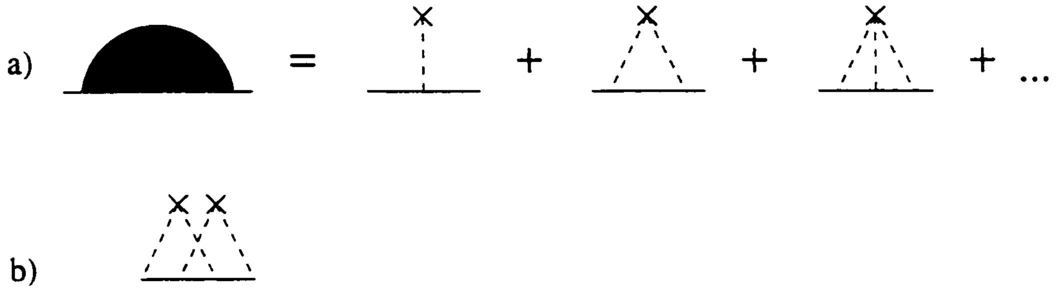

Figure 2.3: a)T-matrix approximation to impurity scattering which includes scattering from a single impurity center. Terms such as those in b) with scattering from two impurity centers are not included.

The diagrammatic sum shown in figure (2.3.a) can be performed using the T-matrix formalism where (Hirschfeld, Volhardt, and Wolfe 1986; Hirschfeld, Wolfe, and Einzel 1988)

$$\hat{\Sigma}_{imp}(\mathbf{k}, i\omega_n) = n_{imp}\hat{T}(\mathbf{k}, \mathbf{k}, i\omega_n). \tag{2.34}$$

Here, n_{imp} is the impurity concentration. The T-matrix function itself is given in the form

$$\hat{T}(\mathbf{k}, \mathbf{k}', i\omega_n) = V_{imp}(\mathbf{k}, \mathbf{k}') + \sum_{\mathbf{k}''} V_{imp}(\mathbf{k}, \mathbf{k}'')\hat{\tau}_3\hat{G}(\mathbf{k}'', i\omega_n)\hat{T}(\mathbf{k}'', \mathbf{k}', i\omega_n) \tag{2.35}$$

where

$$V_{imp}(\mathbf{k}, \mathbf{k}') = \langle \mathbf{k}' \mid V_{imp} \mid \mathbf{k} \rangle \tag{2.36}$$

is the impurity scattering matrix element. If we let the impurity potential be independent of momentum, $V_{imp}(\mathbf{k}, \mathbf{k}') = V_{imp}$, the T-matrix becomes a simple function of frequency only, $\hat{T}(\mathbf{k}, \mathbf{k}', i\omega_n) = \hat{T}(i\omega_n)$.

Equation (2.35) is therefore of the form

$$\hat{T}(i\omega_n) = V_{imp}\hat{\tau}_3 + V_{imp}\hat{\tau}_3\sum_{\mathbf{k}'}\hat{G}(\mathbf{k}', i\omega_n)\hat{T}(i\omega_n). \tag{2.37}$$

This can be rewritten as

$$\left[1 + V_{imp}\hat{\tau}_3\sum_{\mathbf{k}'}\hat{G}(\mathbf{k}', i\omega_n)\right]\hat{T}(i\omega_n) = V_{imp}\hat{\tau}_3 \tag{2.38}$$

where we have pulled $\hat{T}(i\omega_n)$ outside the momentum sum to the right hand side. Isolating $\hat{T}(i\omega_n)$ is now a matter of matrix inversion. Performing the proper operations results in the general equation for the self-energy with multiple impurity scattering

$$\hat{\Sigma}_{imp}(i\omega_n) = n_{imp}\frac{-i\Omega(n)\hat{\tau}_0 + \Phi(n)\hat{\tau}_1 + \left(V_{imp}^{-1} + \Xi(n)\right)\hat{\tau}_3}{V_{imp}^{-2} + \Omega(n)^2 + \Xi(n)^2 + \Phi(n)^2 + 2V_{imp}^{-1}\Xi(n)} \tag{2.39}$$

where

$$\begin{aligned} \Omega(n) &= \frac{1}{N^2}\sum_{\mathbf{k}}\frac{\tilde{\omega}_{\mathbf{k}}(n)}{D_{\mathbf{k}}(n)} \\ \Xi(n) &= \frac{1}{N^2}\sum_{\mathbf{k}}\frac{\varepsilon_{\mathbf{k}} + \xi_{\mathbf{k}}(n)}{D_{\mathbf{k}}(n)} \\ \Phi(n) &= \frac{1}{N^2}\sum_{\mathbf{k}}\frac{\phi_{\mathbf{k}}(n)}{D_{\mathbf{k}}(n)} \end{aligned} \tag{2.40}$$

and

$$D_{\mathbf{k}}(n) = \tilde{\omega}_{\mathbf{k}}(n)^2 + \left[\varepsilon_{\mathbf{k}} + \xi_{\mathbf{k}}(n)\right]^2 + \phi_{\mathbf{k}}(n)^2. \tag{2.41}$$

Two important limits exist for the T-matrix formulation. The first is the Born-scattering (weak scattering, or $V_{imp} \to 0$) approximation given by

$$\hat{\Sigma}_{imp}^{Born}(i\omega_n) = n_{imp}V_{imp}^2\left(-i\Omega(n)\hat{\tau}_0 + \Phi(n)\hat{\tau}_1 + \Xi(n)\tau_3\right). \tag{2.42}$$

The constant term in the $\hat{\tau}_3$ channel has been absorbed into the chemical potential. The Unitary limit, or resonant scattering limit ($V_{imp} \to \infty$) is given by

$$\hat{\Sigma}_{imp}^{Unitary}(i\omega_n) = n_{imp}\frac{-i\Omega(n)\hat{\tau}_0 + \Phi(n)\hat{\tau}_1 + \Xi(n)\hat{\tau}_3}{\Omega(n)^2 + \Xi(n)^2 + \Phi(n)^2}. \tag{2.43}$$

2.2.3 Eliashberg Equations

The electronic self-energy can be written as a sum of terms

$$\hat{\Sigma}(\mathbf{k}, i\omega_n) = \hat{\Sigma}_{boson}(\mathbf{k}, i\omega_n) + \hat{\Sigma}_{imp}(\mathbf{k}, i\omega_n) \tag{2.44}$$

where the electron-boson contribution is given by equation (2.32) and the impurity contribution is given by

$$\hat{\Sigma}_{imp}(i\omega_n) = n_{imp}\hat{\Gamma}(i\omega_n). \tag{2.45}$$

The 2 × 2 matrix function $\hat{\Gamma}(i\omega_n)$ is the appropriate impurity scattering matrix depending on the scattering strength (i.e. general, Born, or resonant).

The Eliashberg equations are found by equating (2.44) and the generalized form of $\hat{\Sigma}$, equation (2.20), and decomposing the self-energy into its irreducible representations (i.e. separating out the appropriate coefficients of the Pauli matrices). The resulting equations are a set of non-linear coupled integral equations which have the following form on the imaginary axis:

$$\begin{aligned}\tilde{\omega}(\mathbf{k}, i\omega_n) &= \omega_n + T\sum_m\sum_{\mathbf{k}'}\left\{\begin{array}{c}\lambda_{ph}(\mathbf{k}-\mathbf{k}', i\omega_n - i\omega_m)\\ \lambda_{sf}(\mathbf{k}-\mathbf{k}', i\omega_n - i\omega_m)\end{array}\right\}\frac{\tilde{\omega}(\mathbf{k}', i\omega_m)}{D(\mathbf{k}', i\omega_m)}\\ &\qquad + n_{imp}\Gamma^{\tilde{\omega}}(i\omega_n)\end{aligned} \tag{2.46}$$

$$\begin{aligned}\xi(\mathbf{k}, i\omega_n) &= -T\sum_m\sum_{\mathbf{k}'}\left\{\begin{array}{c}\lambda_{ph}(\mathbf{k}-\mathbf{k}', i\omega_n - i\omega_m)\\ \lambda_{sf}(\mathbf{k}-\mathbf{k}', i\omega_n - i\omega_m)\end{array}\right\}\frac{\varepsilon_{\mathbf{k}} + \xi(\mathbf{k}', i\omega_m)}{D(\mathbf{k}', i\omega_m)}\\ &\qquad - n_{imp}\Gamma^{\xi}(i\omega_n)\end{aligned} \tag{2.47}$$

$$\begin{aligned}\phi(\mathbf{k}, i\omega_n) &= T\sum_m\sum_{\mathbf{k}'}\left\{\begin{array}{c}\lambda_{ph}(\mathbf{k}-\mathbf{k}', i\omega_n - i\omega_m)\\ -\lambda_{sf}(\mathbf{k}-\mathbf{k}', i\omega_n - i\omega_m)\end{array}\right\}\frac{\phi(\mathbf{k}', i\omega_m)}{D(\mathbf{k}', i\omega_m)}\\ &\qquad + n_{imp}\Gamma^{\phi}(i\omega_n)\end{aligned} \tag{2.48}$$

where

$$D(\mathbf{k}, i\omega_n) = [\tilde{\omega}(\mathbf{k}, i\omega_n)]^2 + [\varepsilon_{\mathbf{k}} + \xi(\mathbf{k}, i\omega_n)]^2 + [\phi(\mathbf{k}, i\omega_n)]^2 \tag{2.49}$$

and $\Gamma^{\tilde{\omega}}$, Γ^{ξ}, and Γ^{ϕ} denote the $\hat{\tau}_0$, $\hat{\tau}_3$, and $\hat{\tau}_1$ components of the impurity scattering matrix $\hat{\Gamma}(i\omega_n)$. The fermionic (bosonic) Matsubara frequency, ω_n (ν_n) is given by $(2n+1)\pi k_B T$ ($2n\pi k_B T$). The function $\phi(\mathbf{k}, i\omega_n)$ is the frequency dependent superconducting order parameter and is therefore zero in the normal state.

Notice the difference in sign for the $\phi_{\mathbf{k}}(i\omega_n)$ channel in the phonon (charge density) and spin-fluctuation (spin density) cases. This is the main difference between interactions which couple to the charge density and those to the spin density. Later we will see how this extra minus sign can lead to a stable d-wave superconducting solution in a spin-fluctuation model.

A complete description of the high-T$_c$ compounds should probably include both phonon and spin-fluctuation contributions. These two interactions will then add in the $\tilde{\omega}$ and ξ channels and compete in the ϕ channel. Such competing effects have been studied previously (Millis, Sachdev, and Varma 1988; Williams 1990; Williams and Carbotte 1991). In our model we will ignore the electron-phonon contribution and limit the discussion to the language of spin-fluctuations.

2.2.4 Critical Temperature

Above the critical temperature, the pair correlation function, $\phi_{\mathbf{k}}$, is zero. Just below T_c, the value of $\phi_{\mathbf{k}}$ is finite, but small. The Eliashberg T$_c$ equations are given by linearizing equations(2.46)-(2.49) in terms of $\phi_{\mathbf{k}}$:

$$\begin{aligned}\tilde{\omega}(\mathbf{k}, i\omega_n) &= \omega_n + T\sum_m \sum_{\mathbf{k}'} \lambda_{sf}(\mathbf{k}-\mathbf{k}', i\omega_n - i\omega_m)\frac{\tilde{\omega}(\mathbf{k}', i\omega_m)}{D(\mathbf{k}', i\omega_m)} \\ &\quad + n_{imp}\Gamma^{\tilde{\omega}}(i\omega_n) \qquad (2.50)\end{aligned}$$

$$\begin{aligned}\xi(\mathbf{k}, i\omega_n) &= -T\sum_m \sum_{\mathbf{k}'} \lambda_{sf}(\mathbf{k}-\mathbf{k}', i\omega_n - i\omega_m)\frac{\varepsilon_{\mathbf{k}} + \xi(\mathbf{k}', i\omega_m)}{D(\mathbf{k}', i\omega_m)} \\ &\quad + n_{imp}\Gamma^{\xi}(i\omega_n) \qquad (2.51)\end{aligned}$$

$$\begin{aligned}\phi(\mathbf{k}, i\omega_n) &= -T\sum_m \sum_{\mathbf{k}'} \lambda_{sf}(\mathbf{k}-\mathbf{k}', i\omega_n - i\omega_m)\frac{\phi(\mathbf{k}', i\omega_m)}{D(\mathbf{k}', i\omega_m)} \\ &\quad + n_{imp}\Gamma^{\phi}(i\omega_n) \qquad (2.52)\end{aligned}$$

where

$$D(\mathbf{k}, i\omega_n) = [\tilde{\omega}(\mathbf{k}, i\omega_n)]^2 + [\varepsilon_{\mathbf{k}} + \xi(\mathbf{k}, i\omega_n)]^2. \qquad (2.53)$$

The $\tilde{\omega}_{\mathbf{k}}(i\omega_n)$ and $\xi_{\mathbf{k}}(i\omega_n)$ equations are then simply normal state functions since they in no way depend on ϕ. Equation (2.52) can then be written as an eigenvalue equation

$$\rho\phi(\mathbf{k}, i\omega_n) = \sum_{\mathbf{k}',m} M_{\mathbf{k}',\mathbf{k},m}\ \phi(\mathbf{k}', i\omega_m) \tag{2.54}$$

where

$$M_{\mathbf{k},\mathbf{k}',m} = -T\frac{\lambda_{sf}(\mathbf{k}-\mathbf{k}', i\omega_n - i\omega_m)}{D(\mathbf{k}', i\omega_m)} + \delta_{n,m}\delta_{\mathbf{k},\mathbf{k}'}\ n_{imp}\frac{\Gamma^{\phi}(i\omega_m)}{\phi(\mathbf{k}', i\omega_m)} \tag{2.55}$$

The critical temperature is now defined to be the temperature at which the largest eigenvalue, ρ, is unity (the algorithm used in the T_c calculation is presented in appendix A).

2.2.5 Real Frequency Equations

In order to study the thermodynamic properties only the imaginary axis formulation of the Eliashberg equations is necessary (Allen and Mitrovic 1982). However, we are interested in calculating the dynamic properties of the system. In order to do this we will require the 2 × 2 matrix thermodynamic Green's function and the corresponding $\hat{\Sigma}$ on the real frequency axis. There are two ways of doing this: the first is to perform the calculations on the real axis and the second is to use a numerical procedure to analytically continue the imaginary axis solutions to the real axis.

The real frequency Eliashberg equations can be found in a straight forward manner (Mahan 1990). To convert the sum over Matsubara frequencies to an integral over real frequencies we use the spectral representations,

$$\hat{G}(\mathbf{p}, i\omega_n) = -\int_{-\infty}^{\infty} d\omega \frac{Im\ \hat{G}(\mathbf{p}, \omega + i\delta)}{i\omega_n - \omega} \tag{2.56}$$

$$P(\mathbf{q}, i\nu_n) = \int_0^{\infty} d\Omega \frac{2\Omega\ \ Im\ P(\mathbf{q}, \Omega + i\delta)}{\Omega^2 + \nu_n^2} \tag{2.57}$$

where P is a generalized boson propagator (i.e. either χ for spin-fluctuations or D for phonons). It can be shown that after substituting (2.56) and (2.57) and performing the Matsubara sum in the prescribed manner (Mahan 1990), the self-energy on the real axis becomes

$$\begin{aligned}\hat{\Sigma}(\mathbf{p}, \omega + i\delta) &= \sum_{\mathbf{k}} \int_{-\infty}^{\infty} d\omega' \int_0^{\infty} d\Omega \; \hat{\tau}_i \; Im \; \hat{G}(\mathbf{k}, i\omega + i\delta) \; \hat{\tau}_i \\ &\times g^2 P(\mathbf{p} - \mathbf{k}, i\Omega) \left[\frac{f(-\omega') + n(\Omega)}{\omega' + \Omega - \omega} - \frac{f(\omega') + n(\Omega)}{\omega' - \Omega - \omega} \right] . \quad (2.58)\end{aligned}$$

where $\hat{\tau}_i$ takes on the appropriate Pauli matrix for the interaction. Equation (2.58) can be decomposed into its irreducible representations yielding the analytical continuation of the self energy functions described earlier:

$$i\omega_n(1 - Z_{\mathbf{k}}(i\omega_n)) \rightarrow \omega(1 - Z_{\mathbf{k}}(\omega + i\delta)) \quad (2.59)$$

$$\xi(i\omega_n) \rightarrow \xi(\omega + i\delta) \quad (2.60)$$

$$\phi(i\omega_n) \rightarrow \phi(\omega + i\delta). \quad (2.61)$$

It is conventional to make a further approximation in conventional electron-phonon theory for which the $\mathbf{k}$ dependence to the interaction is pinned to the Fermi surface and an angular average of the interaction is taken over the Fermi surface. This allows the momentum sum to be done directly as the only remaining dependence on $\mathbf{k}$ is in the Green's function. The self-energy becomes momentum independent and has the same ω dependence over the entire Fermi surface. The details of the interaction is then given by the electron-boson spectral density,

$$\alpha^2 F(\omega) = \frac{\int d\mathbf{k}' \delta(\varepsilon_{\mathbf{k}'}) \int d\mathbf{k} \delta(\varepsilon_{\mathbf{k}}) g^2 Im \; D(\mathbf{k}, \mathbf{k}', \omega)}{\int d\mathbf{k}'' \delta(\varepsilon_{\mathbf{k}''})}. \quad (2.62)$$

Once $\alpha^2 F(\omega)$ is known for a particular material, it is possible to calculate any properties of the system. The agreement between theory and experiment is excellent for conventional systems (Carbotte 1990).

We wish to keep the full momentum dependence of the interaction, therefore. we will solve the Eliashberg equations on the imaginary frequency axis and later analytically continue the results to the real frequency axis using the N-point Padé approximant method (Vidberg and Serene 1977). The details of this procedure are described in appendix A.

2.3 Model

2.3.1 Band-Structure

One feature common to all the cuprate superconductors is the presence of a layered structure having at least one CuO_2 layer per unit cell. The large anisotropy of the ab-plane to c-axis properties has lead many to assume that superconductivity in these materials is due to the physics of the CuO_2 plane and that coupling (or inter-layer hopping) is a small perturbation (Poole and Farach 1995).

Band structure calculations predict that the parent compounds should be metals. The undoped cuprates, however, are in fact insulators. This has lead to the belief that the cuprates should be treated as strongly-correlated electron materials. A tight-binding band structure is therefore more appropriate (Poole and Farach 1995).

The kinetic energy term of the Hubbard Hamiltonian is given (in second quantized notation) by (Hubbard 1963; Fradkin 1991)

$$H_0 = -\sum_{\mathbf{r},\mathbf{r}',\sigma=\uparrow,\downarrow} \left(c^\dagger_\sigma(\mathbf{r}) t(\mathbf{r}-\mathbf{r}') c_\sigma(\mathbf{r}') + c^\dagger_\sigma(\mathbf{r}') t(\mathbf{r}-\mathbf{r}') c_\sigma(\mathbf{r}) \right) \tag{2.63}$$

where $c^\dagger_\sigma(\mathbf{r})$ ($c_\sigma(\mathbf{r})$) is the creation (annihilation operator) for an electron at $\mathbf{r}$, and t($\mathbf{r}$-$\mathbf{r}$') is the hopping strength for an electron for electron at $\mathbf{r}$ to $\mathbf{r}'$.

It is convenient to go to Fourier (momentum) space so we introduce the operators

$$\begin{aligned} c^\dagger_\sigma(\mathbf{r}) &= \frac{1}{\Omega}\sum_{\mathbf{k}} c^\dagger_\sigma(\mathbf{k})\; e^{-i\mathbf{r}\cdot\mathbf{k}} \\ c_\sigma(\mathbf{r}) &= \frac{1}{\Omega}\sum_{\mathbf{k}} c_\sigma(\mathbf{k})\; e^{i\mathbf{r}\cdot\mathbf{k}}. \end{aligned} \tag{2.64}$$

We can then rewrite the Hamiltonian in the form

$$H = \sum_{\mathbf{k},\sigma} \varepsilon_{\mathbf{k}} c^\dagger_\sigma(\mathbf{k}) c_\sigma(\mathbf{k}) \tag{2.65}$$

where

$$\varepsilon_{\mathbf{k}} = -\sum_{\mathbf{r},\mathbf{r}'} t(\mathbf{r}-\mathbf{r}') e^{i\mathbf{k}\cdot\mathbf{r}} e^{-i\mathbf{k}'\cdot\mathbf{r}'}. \tag{2.66}$$

If we take the hopping integral to be

$$t(\mathbf{l}) = \begin{cases} t, & \text{nearest neighbours} \\ t' = tB, & \text{next-nearest neighbours} \\ 0, & \text{otherwise} \end{cases} \tag{2.67}$$

we get for the energy dispersion relation of the two-dimensional Hubbard Hamiltonian

$$\varepsilon_{\mathbf{k}} = -2\bar{t}\left\{\cos(k_x\, a) + \cos(k_y\, b) - 2B\cos(k_x\, a)\cos(k_y\, b)\right\} \tag{2.68}$$

where a and b are the in-plane lattice vectors. From now on we shall take $a, b = 1$. The values of k_x and k_y in the first Brillouin zone usually range from $-\pi$ to π. However, for computational reasons, we shall always choose the range 0 to 2π. One can show that in general one can expand the quasiparticle dispersion relations in the form

$$\varepsilon_{\mathbf{k}} = \sum_{\alpha=0}^{\infty}\sum_{\beta=0}^{\alpha} a_{\alpha,\beta}\left(\cos(\alpha\, k_x)\cos(\beta\, k_y) + \cos(\beta\, k_x)\cos(\alpha\, k_y)\right) \tag{2.69}$$

where α and β are integers, and $a_{\alpha,\beta}$ is the coefficient for the α, β harmonic.

Best fits using the above tight-binding dispersion relations have been performed using either experimental data or band structure calculations. In this work we are not worried about reproducing the experimental results, but are more interested in the effects of the anisotropy introduced using the tight-binding model. As such, we chose a set of parameters which have been extracted from fits to band structure calculations on LaSrCuO materials (Schneider and Sorensen 1991). Choosing numbers to fit exactly may be irrelevant since, as we will see later in the chapter, the introduction of quasiparticle interactions will renormalize the quasiparticle properties changing the quasiparticle dispersion relation dramatically.

2.3.2 Spin-Fluctuation Models

One of the unusual features of the cuprate superconductors is their proximity to an antiferromagnetic instability. Although long range antiferromagnetic order does not exist in the superconducting region, short range antiferromagnetic correlations do (Rossat-Mignod et al. 1988). This unique feature has lead several authors to propose the exchange of antiferromagnetic spin fluctuations as the mechanism leading to electron pairing in the high temperature compounds (Moriya, Takahashi, and Ueda 1990; Kampf and Schrieffer 1990; Millis, Monien, and Pines 1990).

The idea of superconductivity resulting from the exchange of spin fluctuations is not a new one. It has a rather long history in condensed matter physics which predates the discovery of superconductivity in the cuprate superconductors. A p-wave spin-triplet scenario within superfluid ^{3}He has been investigated with the pairing mediated by ferromagnetic spin fluctuations (Anderson and Brinkman 1978). More recently, the exchange of antiferromagnetic spin fluctuations has been argued to lead to singlet pairing in quasi-one dimensional metals (Emery 1983) and heavy fermion compounds (Hirsch 1985; Miyake, Schmitt-Rink, and Varma 1986; Scalapino, Loh, and Hirsch 1986; Norman 1988).

A large number of the spin-fluctuation models of the high-temperature superconductors involve simultaneously solving for the properties of the quasiparticles and the microscopic form of the pairing interaction. This approach remains a formidable task. However, two phenomenological models have been proposed where the form of the electronic susceptibilities have been fit to experimental data. This approach comes from a preference to address the issue of whether or not spin-fluctuation exchange can lead to the high critical temperatures observed in the cuprate materials. Millis, Monien and Pines (MMP) performed a fit to NMR data in order to extract the susceptibility (Millis, Monien, and Pines 1990). Their initial calculations, first in the BCS regime and later using Eliashberg theory provided "proof in concept" that spin-fluctuations could lead to the observed high T_c's. A second approach, known as the RUNL model, used neutron scattering data to extract the shape of the susceptibility and resistivity data to extract the electron-boson coupling constant which determines the strength of the interaction (Radtke et al. 1992). The two groups therefore took a somewhat different approach where MMP used the critical temperature to set the interaction strength and then calculated observable properties such as resistivity, while RUNL used resistivity data to set the coupling strength and then calculated T_c. Comparison of the MMP and RUNL models is made in a recent publication (Schüttler and Norman 1996). In this thesis, we take the MMP model as our pairing interaction, which we shall now describe.

As mentioned before, the MMP model is based on a phenomenological fit to NMR data. The imaginary part of the susceptibility takes the form

$$Im\chi_{mmp}(\mathbf{q},\omega) = \frac{\chi_Q \;\; \omega/\omega_{SF}}{\left(1+\xi^2(\mathbf{q}-\mathbf{Q})^2\right)^2 + \left(\omega/\omega_{SF}\right)^2} \tag{2.70}$$

where χ_Q is the static susceptibility at wavevector $\mathbf{Q}$, ξ is the antiferromagnetic correlation length, ω_{SF} is the characteristic spin fluctuation frequency, and $\mathbf{Q}$ is the commensurate wavevector (π,π).

The values of the parameters used in the MMP model extracted from experimental data are listed in a set of papers by Pines and coworkers (Monthoux, Balatsky, and Pines 1991; Monthoux, Balatsky, and Pines 1992). Our goal is not to present a series of fits to experiment so we chose typical values and considered the values fixed. As such, they are no longer to be viewed as free parameters. The values we have used are: $\omega_{SF} = 7.76$ meV and $\xi = 2.25$. The value of $g^2\chi_Q$, where g is the electron-boson coupling strength, was considered a single parameter and adjusted to give a desired critical temperature.

In order to carry out the Eliashberg calculations on the Matsubara imaginary frequency axis, we must first analytically continue the susceptibility from the real axis.

$$\chi_{MMP}(\mathbf{q},i\nu_n) = \int_0^\infty d\omega \frac{Im\chi_{MMP}(\mathbf{q},\omega)}{\nu_n^2+\omega^2}. \tag{2.71}$$

Using equation (2.70) one gets for the susceptibility on the imaginary frequency axis.

$$\chi_{MMP}(\mathbf{q},i\nu_n) = \frac{\chi_Q}{1+\xi^2(\mathbf{q}-\mathbf{Q})^2 + \frac{|\nu_n|}{\omega_{SF}}}. \tag{2.72}$$

In figure (2.4) we show $\chi(\mathbf{q},i\nu_o = 0)$ in the first Brillouin zone as a function of momentum. This function is strongly peaked at the (π,π) wavevector. As the magnetic correlation length, ξ, increases, the peak narrows approaching a delta function at the commensurate wavevector in the limit $\xi \to \infty$ indicating the onset of an antiferromagnetic instability.

The MMP model is non-separable, meaning that it cannot be separated into two functions: one with momentum dependence and the other with frequency dependence

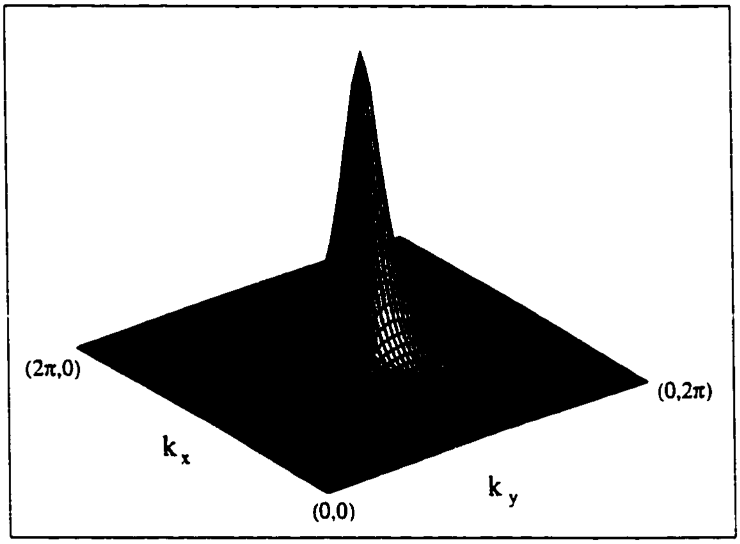

Figure 2.4: The MMP susceptibility, $\chi_{MMP}(i\nu_0)$, at the lowest Matsubara frequency is plotted as a function of momentum for the parameters given in the main text.

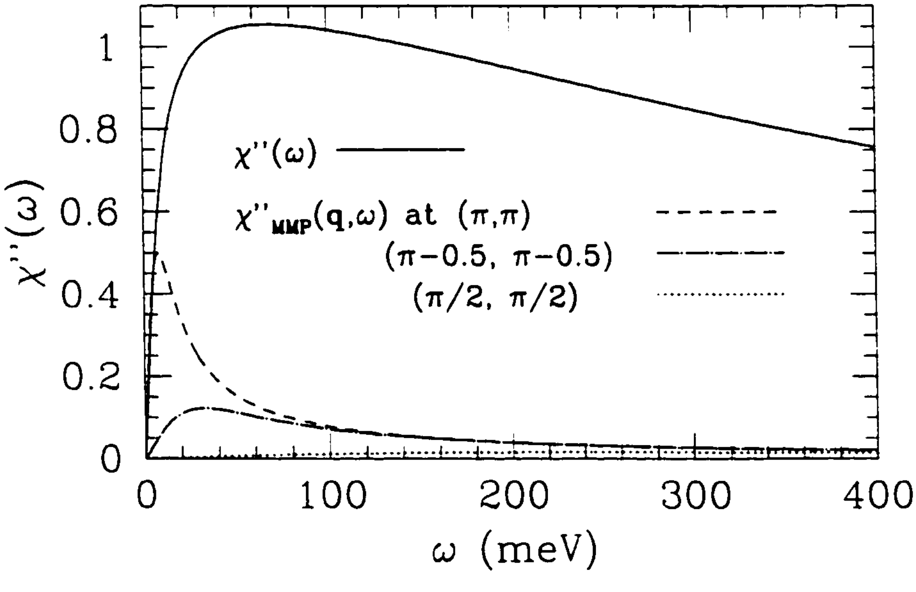

Figure 2.5: The momentum integrated $\chi''(\omega)$ (solid line) is shown for the MMP susceptibility. The frequency dependence of $Im\ \chi(\mathbf{k},\omega)$ is also shown for $\mathbf{k} = (\pi,\pi)$, $(\pi-0.5,\pi-0.5)$, $(\pi/2,\pi/2)$ for comparison.

only. The complicated interplay between the momentum and energy terms results in the frequency dependence of the susceptibility, $\chi(\mathbf{q},\omega)$, to be different on various parts of the Fermi surface. In figure (2.5) we show $Im\ \chi(\mathbf{q},\omega)$ as a function of ω for three different momenta in the first Brillouin zone: $\mathbf{q} = (\pi,\pi)$ [dashed line], $(\pi-0.5,\pi-0.5)$ [dash - dotted line], and $(\pi/2,\pi/2)$ [dotted line]. As the momentum $\mathbf{q}$ is moved off the commensurate wavevector, (π,π), the frequency at which $Im\ \chi(\mathbf{q},\omega)$ peaks increases while the overall amplitude of the peak decreases.

The local susceptibility, $\chi''(\omega) = \int Im\ \chi(\mathbf{q},\omega)d\mathbf{q}/\int d\mathbf{q}$, has been calculated for the MMP model analytically and is given by the function (Kostur and Mitrović 1995)

$$\chi''(\omega) = C^{-1}\left[\tan^{-1}\frac{\omega}{\omega_{SF}} - \tan^{-1}\frac{\omega}{\omega_{SF}}s(\omega)\right]\theta(\omega_{max}-\omega) \tag{2.73}$$

where C is a constant. The function $s(\omega)$ is limited to the range

$$\frac{1}{1+2\pi^2\xi^2} < s(\omega) < \frac{1}{1+\pi^2\xi^2}. \tag{2.74}$$

As χ_Q is an unknown parameter in our theory, we have chosen C such that the maximum of $\chi''(\omega)$ is 1. The function is plotted in figure (2.5) [solid line]. It is seen to rise quickly at small ω and then falls off rather slowly still having significant weight at 400 meV. By expanding the $\tan^{-1}$ functions, it can be seen that for small ω, $\chi''(\omega)$ has a linear frequency dependence and in the large frequency limit, $\chi''(\omega)$ falls off as $1/\omega$. Inelastic neutron scattering measurements of the local susceptibility in LSCO are consistent with this scenario (Hayden et al. 1996).

Quite often the function $g^2\chi''(\omega)$ is used to represent the spin fluctuation spectral density ($g^2\chi''(\omega)$ is therefore the spin fluctuation analogy to the electron-phonon $\alpha^2F(\omega)$). In this thesis, we will make no such approximation, but, instead, we will perform the full momentum space integrations keeping all momentum and frequency dependence of the MMP potential. It is easy to see why it is necessary to keep the full momentum and frequency dependence of the interaction. The pairing interaction is highly momentum dependent resulting in scattering to and from certain regions of the Brillouin zone being more important than others. Furthermore, the potential is not of separable form and the frequency dependence of the interaction is different for each $\mathbf{k}$ point. Also, because of the presence of the van Hove singularity in the non-interacting density of states, it is important to not artificially cut the energy dependence of the potential off since the large number of electronic states available at the van Hove energy plays an important role in the dynamics of the system. It has been shown that the conventional electron-phonon approach to spin-fluctuation mediated pairing leads to critical temperatures which are too low (Millis 1992). The spin fluctuation mechanism described above, in fact, predicts T_c's of reasonable size only if the full momentum and frequency dependence of the interaction is kept (Monthoux and Pines 1992; Monthoux and Pines 1993).

Self-consistent calculations of the electronic susceptibility have also been performed (Pao and Bickers 1994; Monthoux and Scalapino 1994; Lenck, Carbotte, and Dynes 1994). Such an approach leads to quantitative differences from the phenomenological model which will be important in a final theory of superconductivity. However, since our aim is not to promote a particular mechanism but to investigate the effects of momentum dependence on observable properties such as optical conductivity, the phenomenological approach is sufficient.

2.4 Computational Results

The Eliashberg equations, (2.46-2.49), and their linearized counter-parts, (2.50-2.53), were solved self-consistently on a 64 × 64 grid in momentum space. The number of Matsubara frequencies were chosen so that the maximum frequency, $\omega_{n_{cut}}$, was approximately three times the bandwidth,

$$n_{cut} = \text{ceil}\left[\frac{1}{2}\left(\frac{24\bar{t}}{\pi k_B T}\right)\right] \tag{2.75}$$

where the *ceil* function extracts the largest integer approximation to the argument. The bandwidth, W, for our model is $W = 8\,\bar{t}$.

Since the Eliashberg self-energy equations are in the form of convolution integrals, fast Fourier transform (FFT) routines were used to calculate the **k**-space integrations (Serene and Hess 1991). The frequency sums were done as discrete sums over the Matsubara frequencies. A complete description of the techniques and algorithms used to solve the equations are given in appendix A.

Numerical evaluation of the momentum-space integration by fast Fourier transform is what makes the calculation feasible. This limits the form of the equations we can solve to those which are convolution integrals. The constraint of requiring an efficient method of calculation is what limits the choice of model, and in particular is the main reason for ignoring the second order correction to the self-energy since it cannot be cast in the form of a convolution integral and, therefore, cannot be solved using FFT methods.

The chemical potential, μ, was adjusted self-consistently in order to maintain a constant (single spin) electron density of $\langle n\rangle = 0.4$. The electron density equation is (Abrikosov, Gor'kov, and Dzyalosinski 1963)

$$\begin{aligned}\langle n\rangle &= \frac{1}{2} + T\sum_{\mathbf{k}}\sum_{n\geq 0} Re\, G_{11}(\mathbf{k}, i\omega_n) \\ &= \frac{1}{2} - 2T\sum_{\mathbf{k}}\sum_{n\geq 0} \frac{\varepsilon_{\mathbf{k}} + \xi_{\mathbf{k}}(i\omega_n)}{\tilde{\omega}_{\mathbf{k}}(i\omega_n)^2 + \left[\varepsilon_{\mathbf{k}} + \xi_{\mathbf{k}}(i\omega_n)\right]^2 + \phi_{\mathbf{k}}(i\omega_n)^2}. \end{aligned} \tag{2.76}$$

Because the calculations were performed on a grid in momentum space, it was found that the results were more accurate if the filling equation (2.76) was changed slightly by adding and subtracting the noninteracting electron density (Mitrović and Castle 1996)

$$\begin{aligned}\langle n\rangle &= \frac{1}{2} - 2T\sum_{\mathbf{k}}\sum_{n\geq 0} \frac{\varepsilon_{\mathbf{k}}}{\omega_n^2 + \varepsilon_{\mathbf{k}}^2} \\ &\quad -2T\sum_{\mathbf{k}}\sum_{n\geq 0}\left[\frac{\varepsilon_{\mathbf{k}} + \xi_{\mathbf{k}}(i\omega_n)}{\tilde{\omega}_{\mathbf{k}}(i\omega_n)^2 + \left[\varepsilon_{\mathbf{k}} + \xi_{\mathbf{k}}(i\omega_n)\right]^2 + \phi_{\mathbf{k}}(i\omega_n)^2} - \frac{\varepsilon_{\mathbf{k}}}{\omega_n^2 + \varepsilon_{\mathbf{k}}^2}\right] \\ &= \int d\omega N_0(\omega) f(\omega) \\ &\quad -2T\sum_{\mathbf{k}}\sum_{n\geq 0}\left[\frac{\varepsilon_{\mathbf{k}} + \xi_{\mathbf{k}}(i\omega_n)}{\tilde{\omega}_{\mathbf{k}}(i\omega_n)^2 + \left[\varepsilon_{\mathbf{k}} + \xi_{\mathbf{k}}(i\omega_n)\right]^2 + \phi_{\mathbf{k}}(i\omega_n)^2} - \frac{\varepsilon_{\mathbf{k}}}{\omega_n^2 + \varepsilon_{\mathbf{k}}^2}\right] \end{aligned} \tag{2.77}$$

where the noninteracting density of states $N_0(\omega)$ is given by

$$N_0(\omega) = \int_{\delta S(\omega)} \frac{dS}{|\nabla_{\mathbf{k}}\varepsilon_{\mathbf{k}}|}. \tag{2.78}$$

Equation (2.78) was calculated numerically using the method of tetrahedrons (Lehmann and Taut 1972; Mitrović and Castle 1996). The algorithm is described in appendix A.

MMP model	ξ	2.25
	ω_{SF}	7.76 meV
dispersion	B	0.16
	$\bar{t}$	100 meV
other	T$_c$ (at $\langle n \rangle = 0.4$)	100 K ($g^2\chi_Q$ fixed)

Table 2.1: Fixed values for the parameters used in this work.

Throughout the rest of this work, we shall assume that the only tunable parameter is the electron density. The values of the parameters in the MMP model are fixed at the values given in the last section. The band structure is also assumed fixed with $\bar{t} = 100$ meV and $B = 0.16$. The chemical potential, μ, is then uniquely determined by the electron density, $\langle n \rangle$. Furthermore, it was assumed that for $\langle n \rangle = 0.4$ and with no impurities the system had a critical temperature of $T_c = 100$ K. This choice uniquely determines the value of our electron-boson coupling strength, $g^2\chi_Q$. In table (2.1) we list the values of the important parameters for easy reference. The $g^2\chi_Q$ used in the normal state calculations at temperatures smaller than T$_c$ was fixed in the same way as described above.

In the next two subsections we describe the results of numerical calculations using the parameters listed above. Critical temperature calculations for our model are first discussed, followed by the results of the full Eliashberg equations in both the normal and superconducting states.

2.4.1 Critical Temperature

The critical temperature, T$_c$, for our two-dimensional system with next-nearest neighbour hopping of $B = 0.16$ is shown in figure (2.6) as a function of electron density, $\langle n \rangle$. In this calculation, the critical temperature for $\langle n \rangle = 0.4$ was predetermined to be 100 K and the corresponding coupling constant was calculated. For the other values of $\langle n \rangle$, the coupling constant was kept fixed and the new values of T$_c$ were calculated. At $\langle n \rangle = 0.3$, the critical temperature is slightly below 89 K. As the filling is increased, T_c also increases reaching a maximum of just over 100 K at $\langle n\rangle \sim 0.425$. As the filling is increased further, T_c drops. At $\langle n\rangle = 0.5$ the critical temperature has a value of 98 K. The maximum T_c corresponds to the filling for which the Fermi energy corresponds to the energy of the van Hove singularity in the underlying single particle non-interacting density of states.

In figure (2.7) we show a second T_c calculation. This time the electron density has been fixed to $\langle n\rangle = 0.4$ and the next nearest neighbour hopping parameter , B, has been varied. Once again, the T_c at $B = 0.16$ has been set to 100 K. At $B = 0$, the critical temperature is 95.3 K. As B increases, T_c also increases until it reaches a maximum of 102.5 K at $B = 0.4$.

The calculations described above illustrate the importance of the shape of the Fermi surface. The size of T_c is influenced by two important factors, the first being the energy of the van Hove singularity, ε_{vH}, in the density of states. When ε_{vH} corresponds to the Fermi energy, ε_f, the number of electrons on the Fermi surface is at a maximum. As ε_f moves to either side of ε_{vH}, the density of states on the Fermi surface decreases. This has a negative effect on T_c. The second band structure effect is due to changing the shape of the Fermi surface so that certain regions are spanned by $\mathbf{Q}$, or *nested.* This nesting has the effect of increasing the size of the effective potential on the Fermi surface and therefore has a positive effect on the critical temperature.

2.4.2 Self-energy Results

The full Eliashberg equations were solved in both the normal and superconducting states for a range of temperatures both below and above the critical temperature (the normal state solutions are valid solutions of the above equations with $\phi_{\mathbf{k}}(i\omega_n) = 0.0$ everywhere, however, the superconducting solutions will have the lowest free energy). Representative normal state results are plotted in figure (2.8) for $\xi_{\mathbf{k}}(i\omega_0)$ and $\tilde{\omega}_{\mathbf{k}}(i\omega_0)$ respectively for a system with $B = 0.16$ and $\langle n\rangle = 0.4$ at $T = 20$ K. Both figures are represented two different ways. The first is a surface plot of the function in the first Brillouin zone and the second is a plot of the function along certain directions

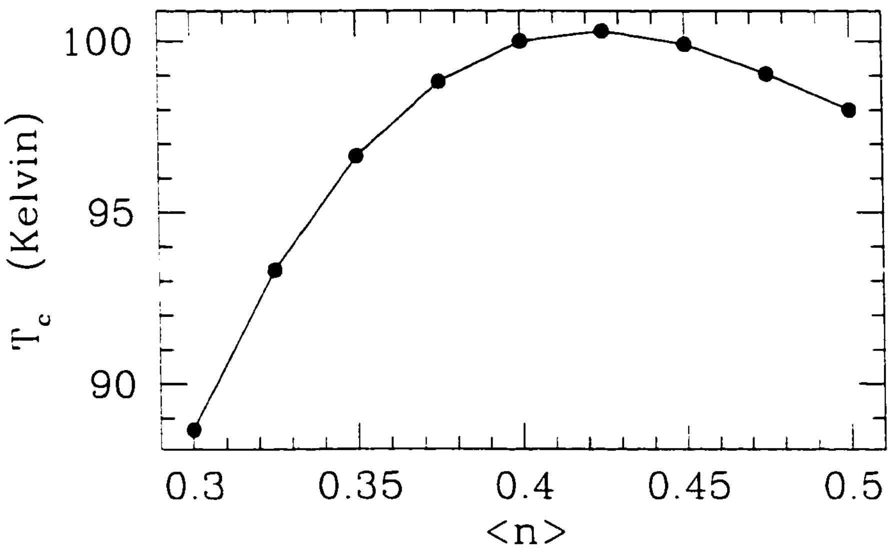

Figure 2.6: The critical temperature, T_c, vs filling, $\langle n \rangle$, for $B = 0.16$.

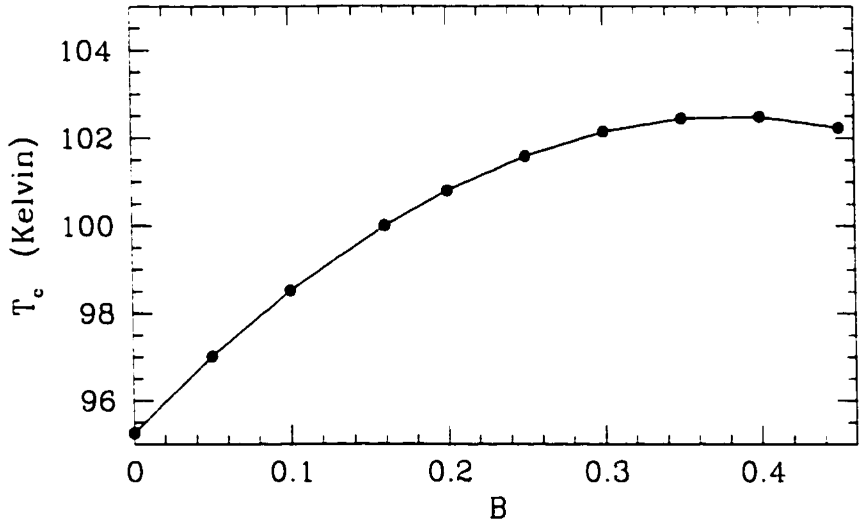

Figure 2.7: The critical temperature, T_c, vs B. The electron density is $\langle n \rangle = 0.4$ for all cases.

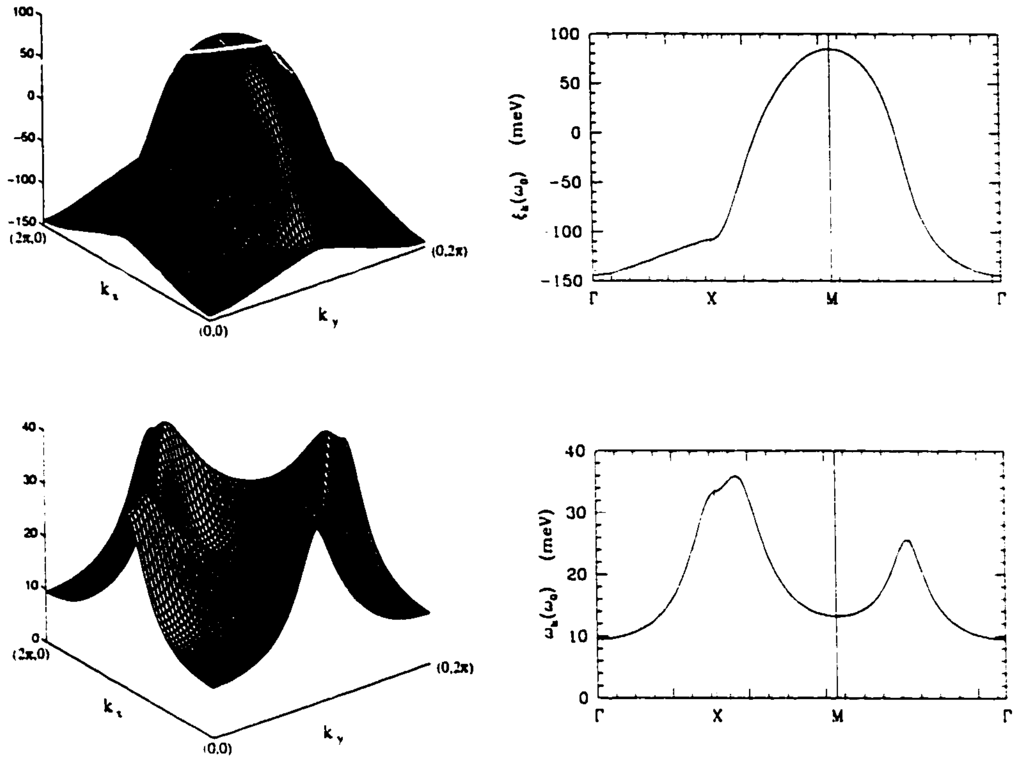

Figure 2.8: Solutions to the normal state Eliashberg equations at 20 K for the lowest Matsubara frequency, $i\omega_0 = i\pi T$, in the first Brillouin zone. $\xi(\mathbf{k}, i\omega_0)$ is plotted in panel a) and $\tilde{\omega}(\mathbf{k}, i\omega_0)$ in panel b). Units along vertical axis are in meV.

in k-space.

One can easily see that the electron-boson interactions introduce a large renormalization effect in this particular model. For free electrons, $\tilde{\omega}_{\mathbf{k}}(i\omega_0)$ would be a constant of value $\omega_0 = \pi T = 5.41$ meV throughout the entire Brillouin zone. For the interacting quasiparticle system, $\tilde{\omega}_{\mathbf{k}}(i\omega_0)$ is a function with a large amount of structure in momentum space having a minimum value of 9.6 meV and maximum value of 37 meV at different points in the Brillouin zone. As we will see later, the size of the renormalizations in the $\tilde{\omega}$ channel are related to the dynamical mass renormalization due to electron-boson interactions.

Similarly, the $\xi_{\mathbf{k}}$ function also contributes a large amount to the self-energy. We shall see that this function is related to shifts in the quasiparticle energies. The

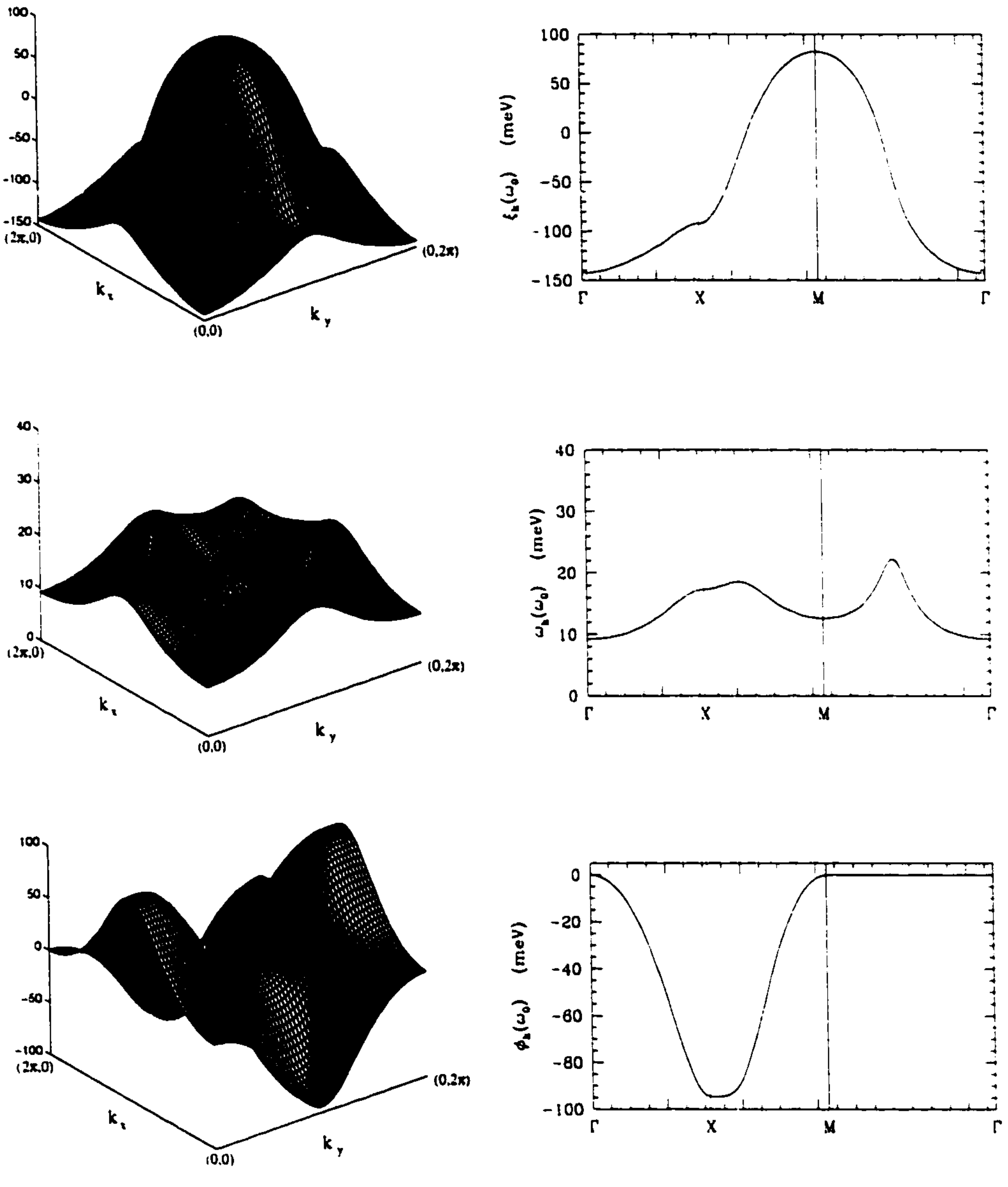

Figure 2.9: Solutions to the superconducting state Eliashberg equations for $T = 20$ K at the lowest Matsubara frequency, $i\omega_0 = i\pi T$, in the first Brillouin zone. $\xi(\mathbf{k}, i\omega_0)$ is plotted in panel a), $\tilde{\omega}(\mathbf{k}, i\omega_0)$ in panel b), and $\phi(\mathbf{k}, i\omega_0)$. Units along vertical axis are in meV.

function has a minimum of -143 meV and a maximum of 84 meV. In the past, this contribution to the self-energy has been ignored in a large number of studies. Calculations such as these suggest that retaining these terms is very important (Monthoux and Pines 1992).

For comparison purposes, the superconducting solutions are shown in figure (2.9). Panel a) shows the $\xi_{\mathbf{k}}$ solution in the superconducting state. The shape of the function remains unchanged. Values at the minimum and maximum in the Brillouin zone are not very different. The most significant difference between the normal and superconducting state is the value of function around the $(\pi, 0)$ and equivalent points. By comparing the values at the point Γ on the line graph of $\xi_{\mathbf{k}}$ versus k plot, one can see that the function is approximately 20 meV larger in the superconducting state.

A large deviation from the normal state result is seen in the $\tilde{\omega}_{\mathbf{k}}$ channel, however. The large peaks located near the $(\pi, 0)$ and equivalent points in the normal state results are strongly suppressed in the superconducting state. The peak which occurs along the diagonal is reduced slightly below the normal state value, but not as drastically as the previous along the Brillouin zone axis. We will discuss this in more detail in a later section after analytically continuing the results to the real frequency axis.

The results of the $\phi_{\mathbf{k}}$ channel are shown in figure (2.9.c). The solution has $d_{x^2-y^2}$ symmetry with lines of zeroes along the Brillouin zone diagonals. The maximum amplitude occurs near the $(\pi, 0)$ and equivalent points. Rotation of $\phi_{\mathbf{k}}$ by 90° is equivalent to multiplying the original function by -1. The average of $\phi_{\mathbf{k}}$ over the Brillouin zone is therefore zero.

The function we are most interested in at the moment is the gap energy, $\Delta_{\mathbf{k}}(i\omega_n)$, which is related to $\phi_{\mathbf{k}}(i\omega_n)$ through the relation

$$\Delta_{\mathbf{k}}(i\omega_n) = \frac{\phi_{\mathbf{k}}(i\omega_n)}{Z_{\mathbf{k}}(i\omega_n)}. \tag{2.79}$$

This function is only physically meaningful on the real frequency axis, so we analytically continued the function to real frequencies using the Padé approximant method described in appendix A.

The observed gap in the quasiparticle excitation spectrum is related to the gap

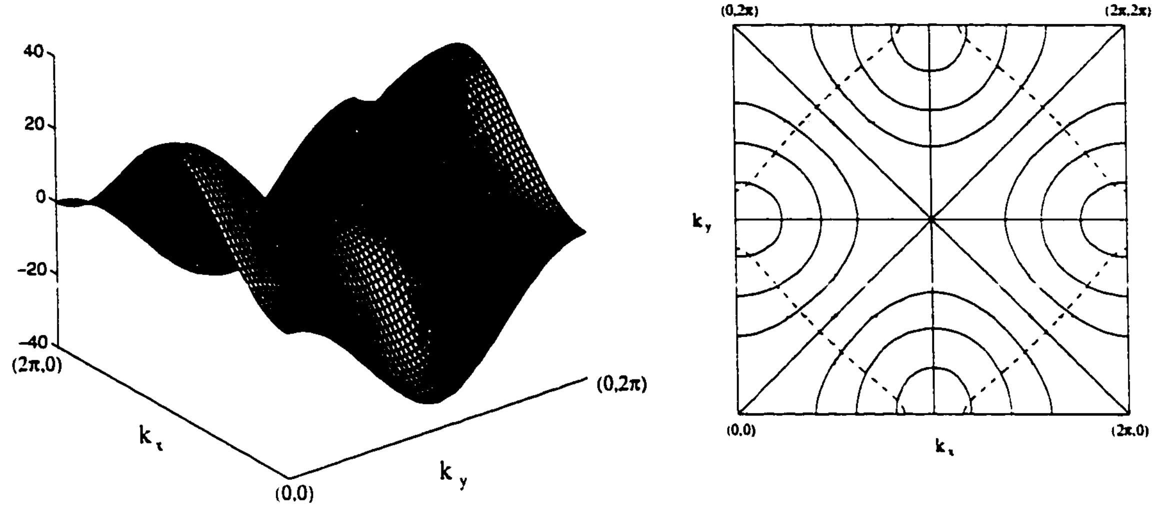

Figure 2.10: Gap edge, $\Delta_o(\mathbf{k})$, as a function of momentum in the first Brillouin zone. The Fermi surface is superimposed on the contour plot and is denoted by the dashed line.

edge, $\Delta_0(\mathbf{k})$, which is determined by the condition

$$\Delta_0(\mathbf{k}) = \Delta\left(\mathbf{k}, \Delta_0(\mathbf{k})\right). \tag{2.80}$$

The gap edge is plotted as a function of momentum in the first Brillouin zone in figure (2.10). It retains $d_{x^2-y^2}$ symmetry and has a maximum amplitude at X and equivalent points with a value of $\Delta^{BZ}_{max} = 33$ meV. As can be seen from the contour plot, the maximum of the gap edge on the Fermi surface, Δ^{FS}_{max}, does not correspond with Δ^{BZ}_{max}. Instead, Δ^{FS}_{max} has a value of 27 meV at $T = 20$ K. At this temperature, the size of Δ^{FS}_{max} is very similar to the $T = 0$ result. In this case, the value of $2\Delta^{FS}_{max}/k_B T_c = 6.27$.

In order to understand how a repulsive interaction with (π, π) scattering, such as the MMP interaction, leads to a superconducting pairing state with $d_{x^2-y^2}$ symmetry, we write the linearized order parameter equation valid near T_c

$$\begin{aligned}\phi(\mathbf{k}, i\omega_n) &= -g^2 T \sum_m \sum_{\mathbf{k}'} \chi_{mmp}(\mathbf{k}-\mathbf{k}', i\omega_n - i\omega_m) \frac{\phi(\mathbf{k}', i\omega_m)}{\tilde{\varepsilon}(\mathbf{k}', i\omega_m)^2 + \tilde{\omega}(\mathbf{k}', i\omega_m)^2} \\ &= -g^2 T \sum_m \sum_{\mathbf{k}'} M(\mathbf{k}-\mathbf{k}', i\omega_n - i\omega_m)\phi(\mathbf{k}', i\omega_m) \qquad (2.81)\end{aligned}$$

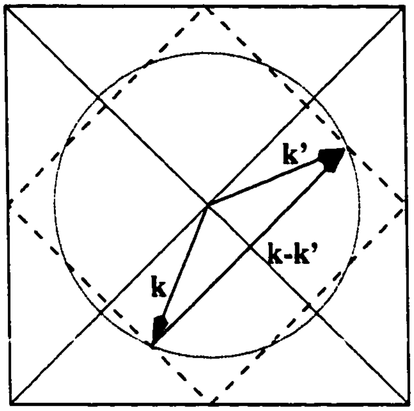

Figure 2.11: Illustration of why repulsive interactions with favoured momentum transfer $\mathbf{k}-\mathbf{k}'=(\pi,\pi)$ leads to superconductivity with $d_{x^2-y^2}$ symmetry.

with

$$M(\mathbf{k}-\mathbf{k}',i\omega_n-i\omega_m)=\frac{\chi(\mathbf{k}-\mathbf{k}',i\omega_n-i\omega_m)}{\bar{\varepsilon}(\mathbf{k}',i\omega_m)^2+\bar{\omega}(\mathbf{k}',i\omega_m)^2}. \tag{2.82}$$

Since $M(\mathbf{k}-\mathbf{k}',i\omega_n-i\omega_m)$ is positive-definite and the overall sign in equation (2.81) is negative, the most important values of $\phi(\mathbf{k}',i\omega_m)$ on the right-hand side of the equation must have the opposite sign as $\phi(\mathbf{k},i\omega_n)$ on the left-hand side in order to stabilize a non-zero value. A change in sign of $\phi(\mathbf{k},i\omega_n)$ necessarily indicates the existence of nodes in Brillouin zone. The susceptibility, and thus the pairing interaction, is strongly peaked at $(\pm\pi/a,\pm\pi/a)$, therefore the values of $\mathbf{k}$ and $\mathbf{k}'$ such that $(k_x-k_x'\pm\pi/a,k_y-k_y'\pm\pi/a)$ is a minimum make the most important contributions to the momentum sum in (2.81). These conditions are illustrated in figure (2.11).

2.5 Renormalization Effects

In order to discuss the renormalization effects of the self-energy, let us first consider the normal state, for which the interacting Green's function can be written

$$G(\mathbf{k},\omega+i\delta)=\frac{1}{\omega-\varepsilon-\Sigma(\mathbf{k},\omega+i\delta)}. \tag{2.83}$$

The pole is given by

$$\omega = \varepsilon + \Sigma(\mathbf{k}, \omega + i\delta). \tag{2.84}$$

If we write the real and imaginary part of ω as $E_{\mathbf{k}} + i\Gamma_{\mathbf{k}}$, we can separate (2.84) into its real and imaginary contributions,

$$\begin{aligned} E_{\mathbf{k}} &= \varepsilon_{\mathbf{k}} + Re\Sigma_{\mathbf{k}}(E_{\mathbf{k}}) & (2.85) \\ \Gamma_{\mathbf{k}} &= -Im\,\Sigma_{\mathbf{k}}(E_{\mathbf{k}} + i\delta) & (2.86) \end{aligned}$$

The first equation, (2.85), defines the new quasiparticle energy. The real part of the self-energy therefore describes a shift in quasiparticle energies due to the electron-boson interaction while the imaginary part is related to the damping rate or the quasiparticle lifetime. A similar interpretation of the self-energy can be make in the superconducting state replacing Σ in equations (2.85) and (2.86) by $\Sigma_{1,1}(\mathbf{k}, \omega)$.

The real and imaginary parts of the self-energy are plotted in figures (2.12) and (2.13). For a system with particle-hole symmetry, the $\hat{\tau}_3$ component of the self-energy is zero (Schrieffer 1964) making $Re\ \Sigma$ an antisymmetric function of ω and $Im\ \Sigma$ a symmetric function. Because of the narrow band and the large van Hove singularity in the density of states, our system does not have particle-hole symmetry and therefore the real and imaginary parts of Σ are neither symmetric nor antisymmetric with respect to ω. This remains true even for a finite sized band with particle hole symmetry. While $\xi_{\mathbf{k}}(\omega)$ is zero on the Fermi surface, it is finite in other parts of the Brillouin zone. As we saw in a previous section, the $\hat{\tau}_3$ component of the self-energy is not small and must be retained.

The frequency dependence of the normal state self-energy at $T = 20$ K is shown at five different points on the Fermi surface along the directions $\theta = 0°$ (solid line), 11.25° (short dashed line), 22.5° (long dashed line), 33.75° (short dashed - dotted line), and 45° (long dashed - dotted line) where the angle θ is measured from the $\overline{\Gamma M}$ line.

At all the graphed points, $Re\ \Sigma(\theta, \omega)$ is negative for the entire energy range shown. The value $Re\ \Sigma(\theta, 0)$ represents a constant shift to the chemical potential due

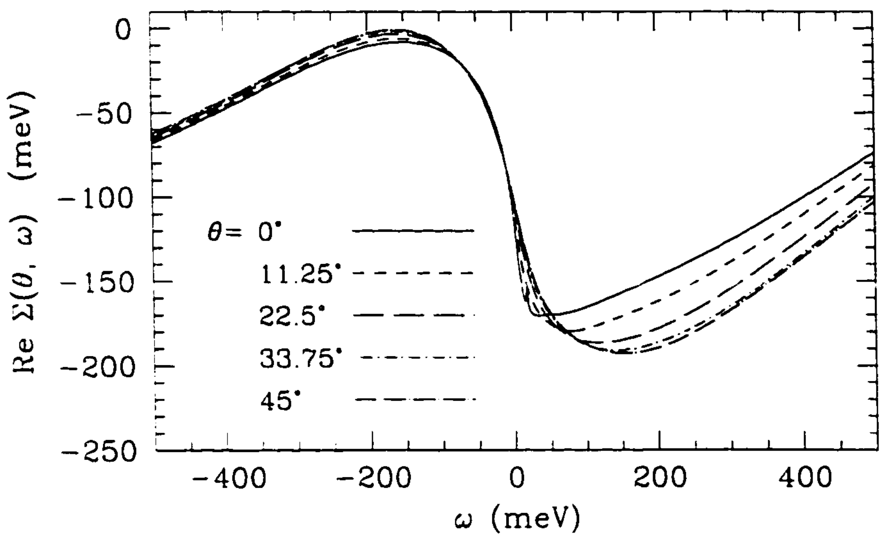

Figure 2.12: Frequency dependence of *Re* $\Sigma(\theta,\omega)$ in normal state for five points on the Fermi surface. The temperature is 20 K.

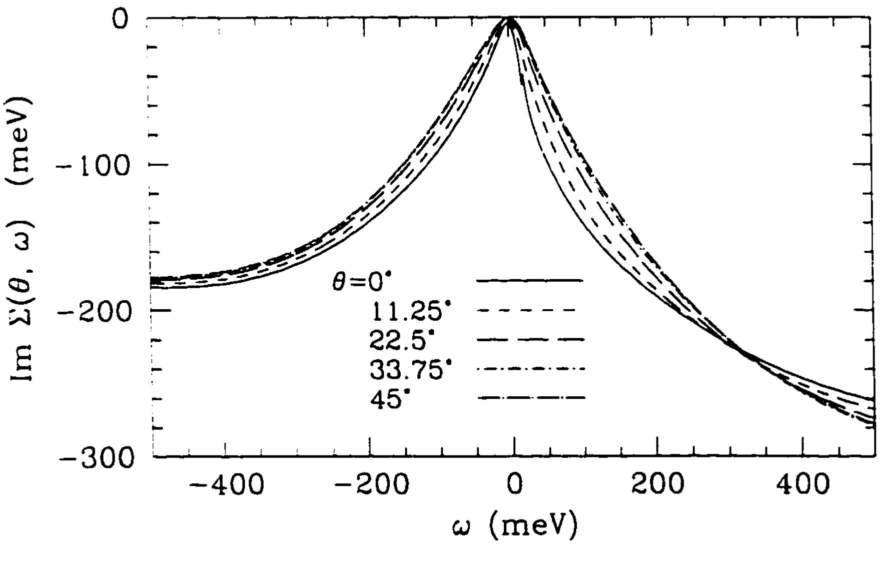

Figure 2.13: Frequency dependence of *Im* $\Sigma(\theta,\omega)$ in normal state for five points on the Fermi surface. The temperature is 20 K.

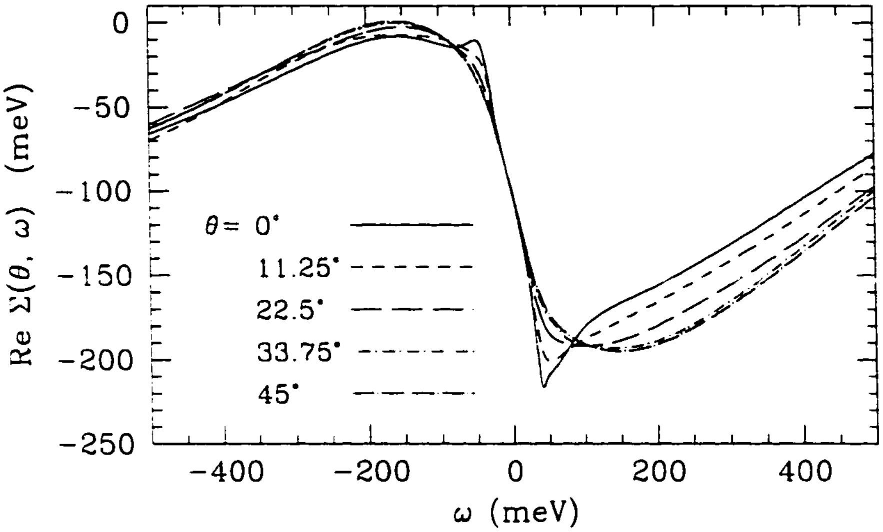

Figure 2.14: Frequency dependence of *Re* $\Sigma(\theta, \omega)$ in superconducting state for five points on the Fermi surface. The temperature is 20 K.

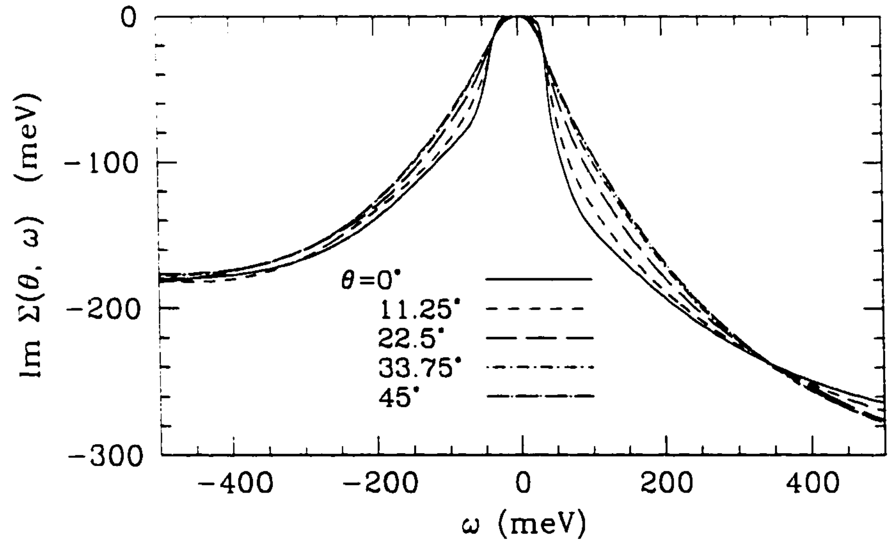

Figure 2.15: Frequency dependence of *Im* $\Sigma(\theta, \omega)$ in superconducting state for five points on the Fermi surface. The temperature is 20 K.

to interactions. In the case of particle-hole symmetry, this value would be identically zero. For our model, *Re* $\Sigma(\theta, 0) \sim 100$ meV for all points on the Fermi surface shown.

The imaginary part of the self-energy is shown in figure (2.13) for the same points on the Fermi surface as for the real part. The quasiparticle scattering rates are related to *Im* Σ through

$$\frac{1}{\tau_{\mathbf{k}}^{qp}(\omega)} = -2\ Im\ \Sigma_{\mathbf{k}}(\omega). \tag{2.87}$$

One can see from the figure that the scattering rates vary as a function of angle on the Fermi surface and that *Im* $\Sigma(\theta, \omega = 0)$ is largest at the point intersected by the line $\overline{\Gamma X}$ (or 0°) and smallest along $\overline{\Gamma M}$ (or 45°).

The superconducting state results for *Re* $\Sigma(\theta, \omega)$ on the Fermi surface are shown for the same five angles as in the normal state calculations in figure (2.14). The shape of the curve along $\theta = 45°$ has not changed. Along $\theta = 0°$, *Re* Σ develops a sharp structure at higher frequencies, which can be associated with the steep slope of *Im* Σ, shown in figure (2.15). At very low frequencies, *Im* Σ is suppressed from its normal state results with the most significant change at the point intersected by $\theta = 0°$. Since the quasiparticle excitation spectrum is gapped at this point, the quasiparticle scattering rate is reduced. Above the gap edge, *Im* Σ rises rather quickly to meet its normal state value. At energies above 100 meV, the normal and superconducting state results are identical. As the size of the gap edge varies on the Fermi surface, the scattering rate is suppressed more along $\theta = 0°$ than at the other points due to the angular dependence of $\Delta_o(\mathbf{k})$.

A surface plot of the non-interacting dispersion relation is shown in figure (2.16.a). The saddle points are clearly visible at the $(\pi, 0)$ and equivalent points. In figure (2.16.b) we show a similar plot, this time for the interacting quasiparticle picture. While the two dispersions are somewhat similar, it is clear from the second plot that the interactions have lead to an energy renormalization with the band of energies being flattened out in certain regions of the Brillouin zone. This flattened area is associated with the new quasiparticle Fermi surface. The quasi particle dispersion relation is plotted as a function of momentum along certain high symmetry lines in figure (2.16.c). The results of the interacting system (solid line) are to be compared

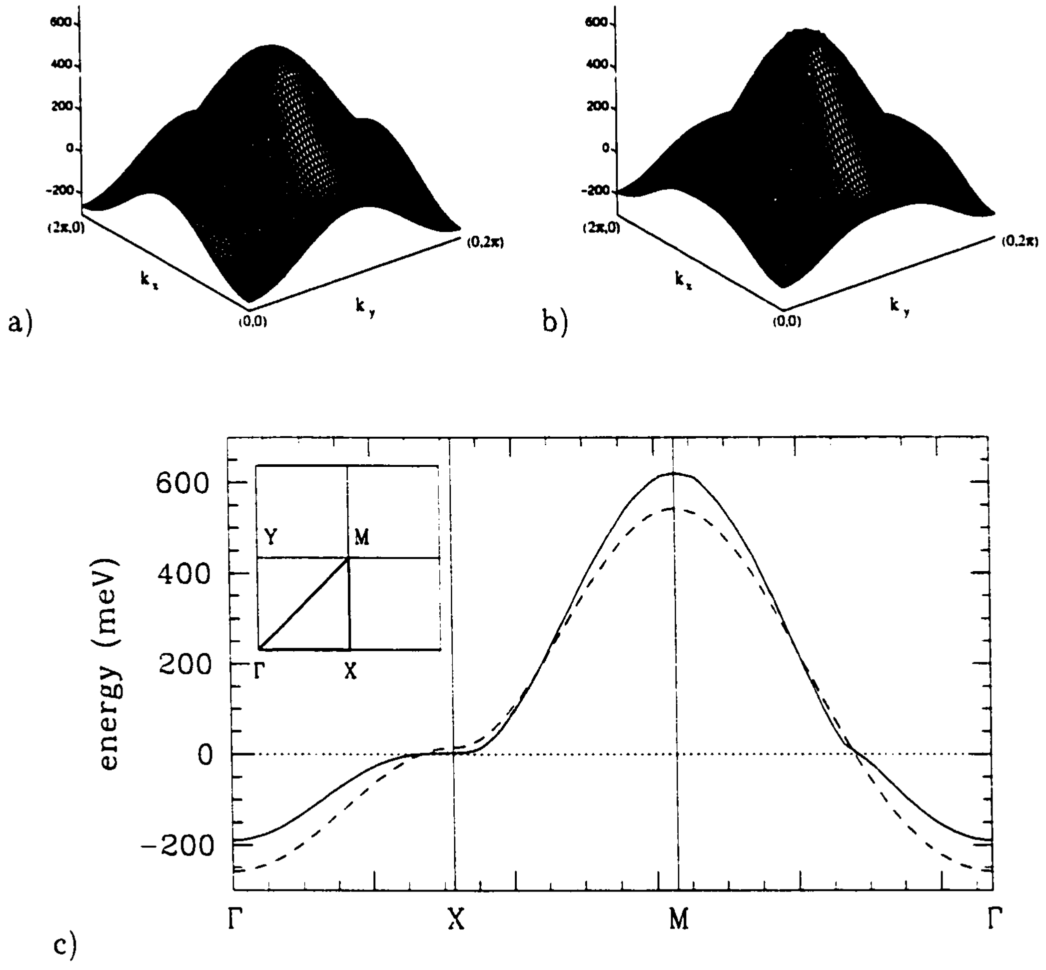

Figure 2.16: Surface plot of the a) non-interacting and b) interacting quasiparticle dispersion relations for an electron density of $\langle n \rangle = 0.4$ at 20 K. The quasiparticle dispersion relation along high symmetry lines is shown in c) for the interacting (solid line) and non-interacting (dashed line) systems.

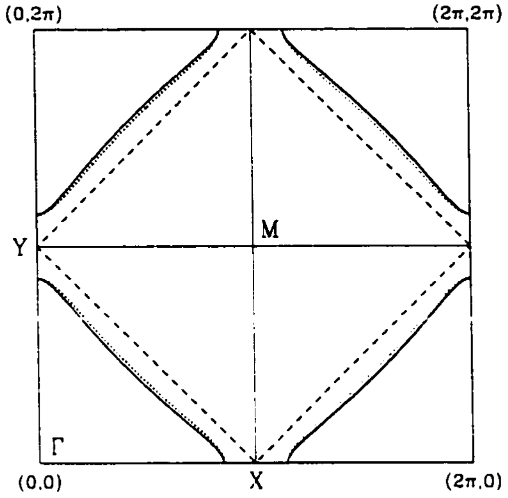

Figure 2.17: Fermi surface in the normal state for the non-interacting system (dotted lines) and for the fully interacting system (solid line) at 20 K. The magnetic Brillouin zone is indicated by the dashed line. The electron density is $\langle n \rangle = 0.4$.

to those of the non-interacting system (dashed line). Along $\overline{\Gamma X}$, the quasiparticle interactions have lead to an extended saddle point which is now centered about the Fermi energy. The slope of the dispersion crossing the Fermi surface along the $\overline{\Gamma M}$ line has also been reduced. however, the effect is not nearly as dramatic. Notice that although the occupied region of the quasiparticle band has been narrowed. the non-interacting and fully interacting dispersions cut the Fermi surface at nearly the same momentum points. This is emphasized in the contour plot, figure (2.17), which compares the Fermi surfaces of the non-interacting and quasiparticle pictures. The fully interacting Fermi surface is defined by the zero of equation (2.85)

$$\varepsilon_{\mathbf{k}} + Re\Sigma_{\mathbf{k}}(0) = 0.0. \tag{2.88}$$

The areas enclosed by the two Fermi surfaces are nearly identical. Luttinger's theory predicts that at zero temperature the areas enclosed by the Fermi surface of the interacting and non-interacting systems are identical (Luttinger 1960). The reason for the small difference in areas enclosed by the non-interacting and fully interacting systems is that we are at finite temperature.

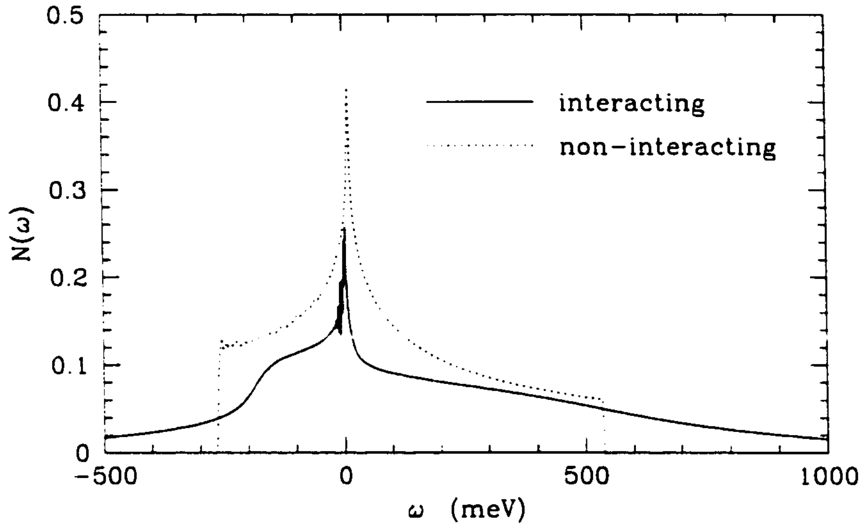

Figure 2.18: Single quasiparticle density of states, $N(\omega)$, in the normal state at $T = 20$ K. The non-interacting $N(\omega)$ [dotted line] is shown for comparison.

2.5.1 Density of States

The electronic density of states is given by

$$N(\omega) = -\frac{1}{\pi}\sum_{\mathbf{k}} Im \ G_{1,1}(\mathbf{k}, \omega + i\delta) \tag{2.89}$$

where $G_{1,1}$ is the (1,1) element of the 2×2 Nambu Green's function. In figure (2.18) we plot the normal state interacting density of states as a function of ω (solid line) at 20 K. Also plotted for comparison purposes is the non-interacting density of states (dotted line) which corresponds to the identical electron density of $\langle n \rangle = 0.4$.

The effects of strong interactions are clearly visible. While the band edges are clearly defined in the non-interacting system, the edges are smeared out into very broad shoulders when the interactions are turned on. As the total number of states remains unchanged, the density of states at small, but finite, ω is greatly reduced from the non-interacting case as the allowed electronic states are smeared out over a larger range of energies. Notice also the position of the peak in $N(\omega)$ is shifted down to the Fermi energy. This shift was also seen in the $E_{\mathbf{k}}$ vs k plot, figure (2.17.c), where the band was flattened out near the X point and the energy of the saddle point was

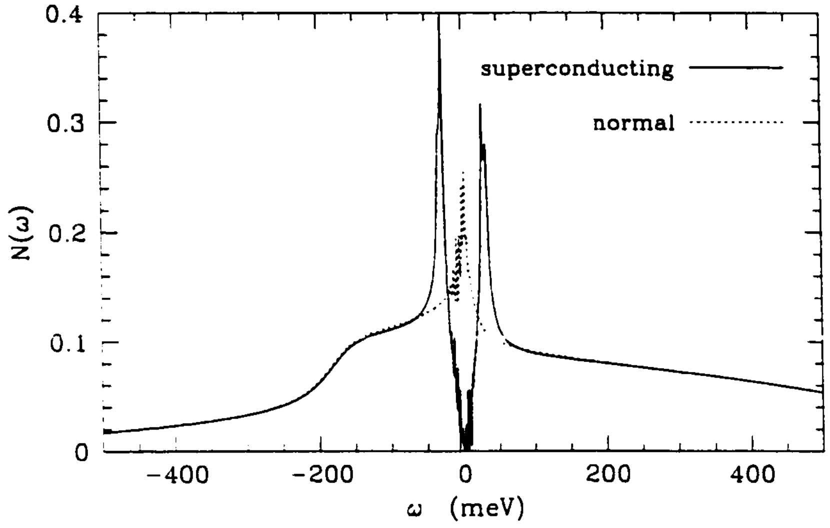

Figure 2.19: Single quasiparticle density of states, $N(\omega)$, in the superconducting state at $T = 20$ K. The normal state function [dotted line] is shown for comparison.

seen to sit at the Fermi level. The density of states at the Fermi energy is, however, the same in non-interacting and fully interacting systems (Mitrović 1981; Monthoux and Pines 1993).

As the system enters the superconducting state, a gap opens in the quasiparticle excitation spectrum and the density of states near the Fermi level is correspondingly reduced. In conventional s-wave theory, this gap is complete at low temperatures and no single particle excitations exist at energies between $-\Delta$ and Δ. In figure (2.19) we plot $N(\omega)$ for the superconducting state at $T = 20$ K (solid line). For comparison purposes, the equivalent normal state result is shown again (dotted line). The only significant difference between the two curves is at frequencies just off $\omega = 0$. Despite being at a low temperature, the gap is not complete, but instead rises continuously from $\omega = 0$ to $\omega = \Delta_{max}$, where Δ_{max} is the largest value of the gap edge on the Fermi surface. The gap is not complete since $\Delta_o(\mathbf{k})$ goes to zero on the Fermi surface along certain directions in the Brillouin zone and single quasiparticle excitations are easily promoted to states just off the Fermi surface in these directions. By noting the difference in energy between the two peaks in the superconducting $N(\omega)$, an estimate for the size of Δ_{max} can be given at 27 meV. This is consistent with the value found from the gap edge calculation earlier.

2.5.2 Mass Renormalization

As a starting point we take the single quasiparticle interacting Green's function for a wavevector near the Fermi wavevector, k_f, and small ω.

$$\begin{aligned} G_{\mathbf{k}}(\omega) &= (\omega + \varepsilon_{\mathbf{k}} - \Sigma_{\mathbf{k}}(\omega))^{-1} \\ &= (\omega + \varepsilon_{\mathbf{k}} - Re\ \Sigma_{\mathbf{k}}(\omega) - Im\ \Sigma_{\mathbf{k}}(\omega))^{-1} \end{aligned} \tag{2.90}$$

and expand the real part of the self-energy about $\omega = 0$ and $\varepsilon_{\mathbf{k}} = \varepsilon_{k_f}$,

$$Re\ \Sigma_{\mathbf{k}}(\omega) = Re\ \Sigma_{k_f}(0) + \omega \left.\frac{\partial Re\ \Sigma_{k_f}(\omega)}{\partial\omega}\right|_{\omega=0} + \varepsilon_{\mathbf{k}} \left.\frac{\partial Re\ \Sigma_{\mathbf{k}}(0)}{\partial\varepsilon_{\mathbf{k}}}\right|_{\mathbf{k}=k_f}. \tag{2.91}$$

The Green's function can be rewritten in the form

$$G_{\mathbf{k}}(\omega) = \left(\omega(1 - \left.\frac{\partial Re\ \Sigma_{k_f}(\omega)}{\partial\omega}\right|_{\omega=0}) + \varepsilon_{\mathbf{k}}(1 + \left.\frac{\partial Re\ \Sigma_{\mathbf{k}}(0)}{\partial\epsilon_{\mathbf{k}}}\right|_{\mathbf{k}=k_f}) - Im\ \Sigma_{\mathbf{k}}(\omega)\right)^{-1} \tag{2.92}$$

where the constant term from equation (2.91) has been absorbed into the chemical potential. We can then define the functions

$$\lambda = -\left.\frac{\partial Re\ \Sigma_{k_f}(\omega)}{\partial\omega}\right|_{\omega=0} \tag{2.93}$$

and

$$\lambda_c = \left.\frac{\partial Re\ \Sigma_{\mathbf{k}}(0)}{\partial\varepsilon_{\mathbf{k}}}\right|_{\mathbf{k}=k_f}. \tag{2.94}$$

Using equations (2.93) and (2.94), the Green's function becomes

$$\begin{aligned} G_{\mathbf{k}}(\omega) &= (\omega(1+\lambda) - \varepsilon_{\mathbf{k}}(1+\lambda_c) - Im\ \Sigma_{\mathbf{k}}(\omega))^{-1} \\ &= \frac{1}{1+\lambda}(\omega - \varepsilon^*_{\mathbf{k}} - \Gamma_{\mathbf{k}}(\omega))^{-1} \end{aligned} \tag{2.95}$$

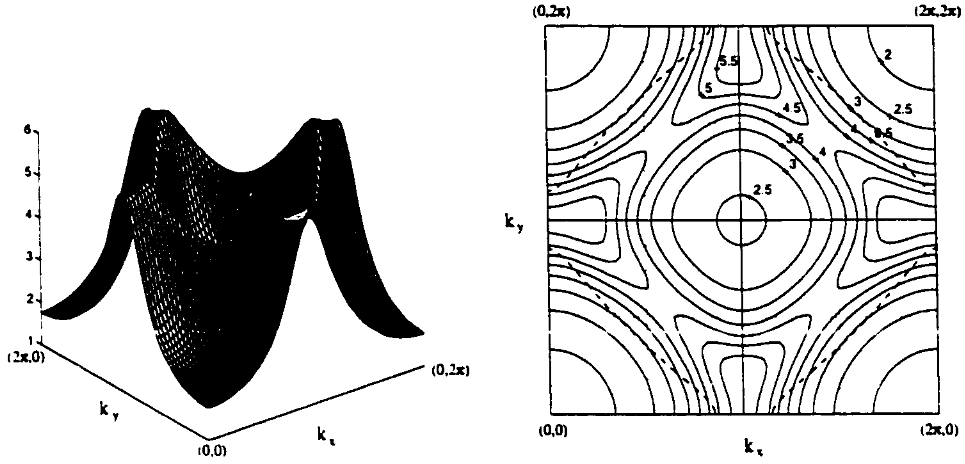

Figure 2.20: $Re\ Z(\mathbf{k}, \omega = 0)$ at $T = 20$ K in the normal state.

where

$$\varepsilon^*_{\mathbf{k}} = \varepsilon_{\mathbf{k}} \frac{1+\lambda_c}{1+\lambda} \tag{2.96}$$

is the renormalized energy and

$$\Gamma_{\mathbf{k}}(\omega) = \frac{Im\ \Sigma_{\mathbf{k}}(\omega)}{1+\lambda}. \tag{2.97}$$

The ratio $\frac{1+\lambda}{1+\lambda_c}$ can be interpreted as a dynamical mass renormalization, m^*/m_b, where m_b is the band mass (Scalapino 1969). By comparing the first line of (2.92) with the normal state value of $G_{1,1}(\mathbf{k}, \omega)$, we see that $Re\ Z_{\mathbf{k}}(\omega = 0) = 1 + \lambda_{\mathbf{k}}$. If λ_c is small, as it is in our case, the effective mass is related to the $\omega = 0$ value of the real part of the renormalization function, $Z_{\mathbf{k}}$.

It will be convenient to define a momentum and frequency dependent λ by

$$Z_{\mathbf{k},1}(\omega) = 1 + \lambda_{\mathbf{k}}(\omega) \tag{2.98}$$

where $Z_{\mathbf{k},1} = Re\ Z_{\mathbf{k}}$. The size of $Z_{\mathbf{k},1}(\omega)$ is indicative of the strength of the renormalizations due to the interactions. In fact, $Z_{\mathbf{k},1}(\omega)$ can be used to distinguish weak and strong coupling regimes (Scalapino 1969): $\lambda > 1$ for strong coupling and $\lambda \ll 1$ for weak coupling, where $\lambda = Z_{k_f,1}(0) - 1$. For a system of non-interacting electrons,

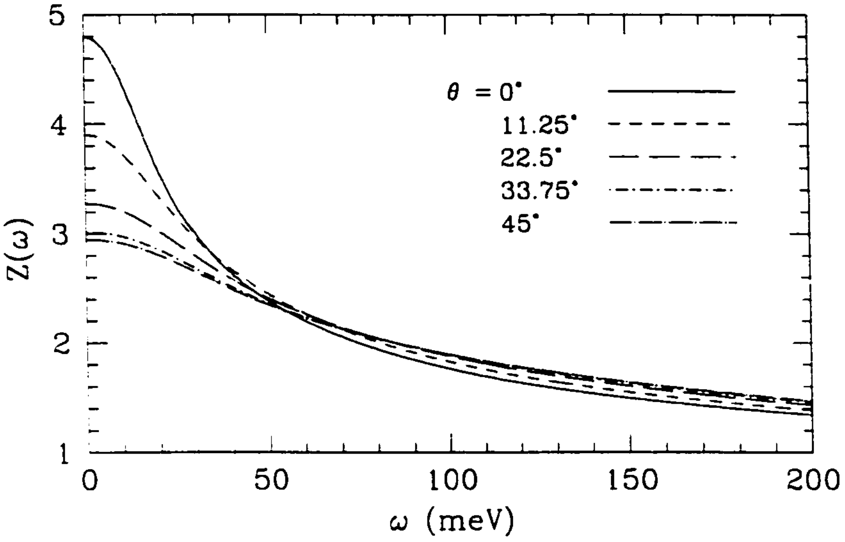

Figure 2.21: *Re* $Z(\theta, \omega)$ at $T = 20$ K in the normal state.

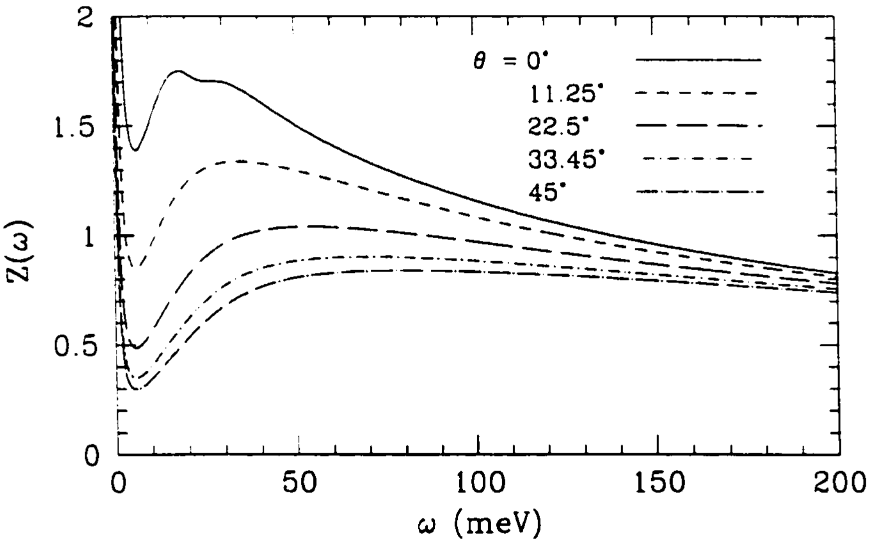

Figure 2.22: *Im* $Z(\theta, \omega)$ at $T = 20$ K in the normal state.

$Z_{\mathbf{k},1}(\omega) = 1$, or $\lambda = 0$. In figure (2.20) we plot *Re* $Z_{\mathbf{k}}(\omega = 0)$ in the first Brillouin zone at $T = 20$ K. Panel a) is a surface plot and b) is a contour plot with the renormalized Fermi surface superimposed (dashed line). As can be seen, the renormalizations are very strong everywhere in the Brillouin zone, even in regions well away from the Fermi surface. At the corners, $(0,0)$, $(2\pi,0)$, $(0,2\pi)$ and $(2\pi,2\pi)$, $Z_{\mathbf{k}}(0) \sim 1.8$ while for other $\mathbf{k}$-points along $(\pm\pi,0)$ and $(0,\pm\pi)$ direction close to the Brillouin zone faces, $Z_{\mathbf{k},1}(0)$ has a maximum of ~ 5.8. The Fermi surface, however, does not cut directly through the maximum points of $Z_{\mathbf{k},1}(0)$. The *Re* $Z_{\mathbf{k}}(\omega)$ as a function of ω is shown in figure(2.21) for five points on the Fermi surface denoted by θ, the angle measured form the line $\overline{\Gamma M}$. For $\theta = 0°$, *Re* $Z_\theta(\omega)$ is a maximum on the Fermi surface, with a value of ~ 4.8. As the angle is increased, *Re* $Z_\theta(\omega = 0)$ deceases rapidly until along the diagonal of the Brillouin zone, it has a value of ~ 2.9. At higher frequencies, *Re* $Z_\theta(\omega)$ also decreases, with all curves coalescing to a value of ~ 2.4 at $\omega = 50$ meV. At even higher energies, all the curves run approximately parallel to each other. For $\omega = 200$ meV *Re* $Z_{\mathbf{k}}(\omega) \sim 1.4 \pm 0.1$.

The imaginary part of $Z_{\mathbf{k}}(\omega)$ [figure (2.22)] is related to the damping. The peak in *Im* $Z(\omega)$ at small ω is due to finite temperature effects. As T is decreased from the present value, the width of the peak narrows so that at $T = 0$, $Z(\omega \to 0) = 0$. The broad shoulder in *Im* $Z(\omega)$ is reflective of the strength of the inelastic scattering. A larger value at $\theta = 0°$ reflects the larger scattering rates at this point. Also, the lower value of ω at which the shoulder is centered indicates that bosons at small frequencies are more important than in the other directions reflecting the fact that at this point, the Fermi surface in closer to the nesting condition.

The above results are to be compared to the superconducting state solutions. In figure (2.23), *Re* $Z_{\mathbf{k}}(\omega = 0)$ is shown for a similar system as discussed in the normal state, but in this case with the pair correlation channel, $\phi_{\mathbf{k}}$, turned on. The surface plot, figure (2.23.a), clearly shows that superconductivity has a large effect on $Z_{\mathbf{k},1}(\omega)$ in the Brillouin zone. Instead of the maximum peaks occurring near the center of the Brillouin zone faces as in the normal state, $Z_{\mathbf{k},1}(\omega)$ is peaked along the diagonals. By comparing the two surface plots, perhaps it is better to say that along $(\pm\pi,0)$, $(0,\pm\pi)$ directions the superconductivity has suppressed *Re* $Z_{\mathbf{k}}(\omega)$ much more than

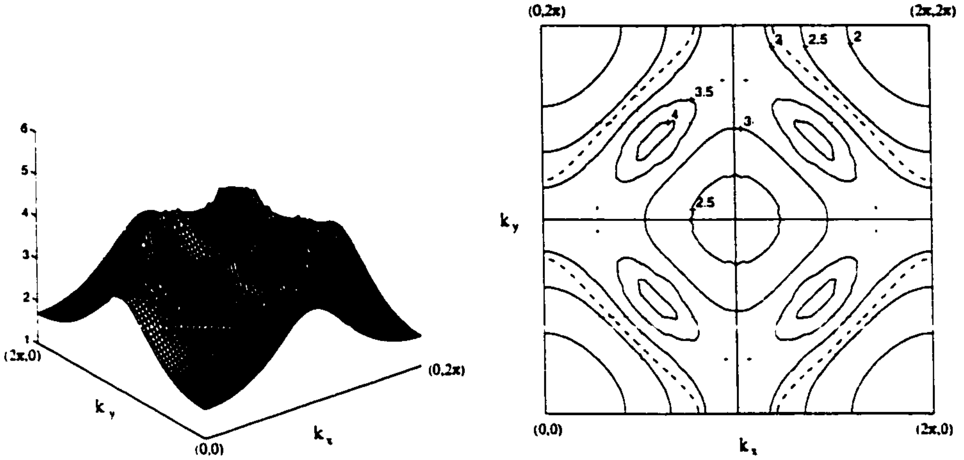

Figure 2.23: *Re* $Z(\mathbf{k}, \omega = 0)$ at $T = 20$ K in the superconducting state.

along the diagonals. The reason for this is that the electronic states along the former directions are gapped by the superconductivity. As we have seen earlier [figure (2.24)] the absolute value of the gap edge, $|\Delta_{\mathbf{k}}|$, is at a maximum along these lines. Nodes of the gap exist along the diagonals so, although the superconducting transition does have an effect on the quasiparticle states in this direction, they still appear normal state-like and therefore, are not drastically changed from the normal state results.

This interpretation is further supported by the real and imaginary parts of $Z_{\mathbf{k}}(\omega)$ plotted in figures(2.24) and (2.25) respectively for points on the Fermi surface at the same values of θ as in the normal state. The value of *Re* $Z_\theta(\omega = 0)$ for $\theta = 0°$ is greatly reduced from its normal state value. For points on the Fermi surface at other angles, the function is also reduced, including the $\theta = 45°$ point, but not quite as severely as the 0° curve. There is also not as large a difference in the 0° and 45° superconducting state values at $\omega = 0$ as there was in the normal state. By comparing the contour plots of the normal and superconducting states, this can be seen as the density of contours (i.e. gradient) along the Brillouin zone faces is not as large in the superconducting state. At higher energies, a peak develops in *Re* $Z_\theta(\omega)$ as electronic states at energies above the gap edge become available and the function rises to approach its normal state value. At $\omega = 200$ meV, the curves are identical to

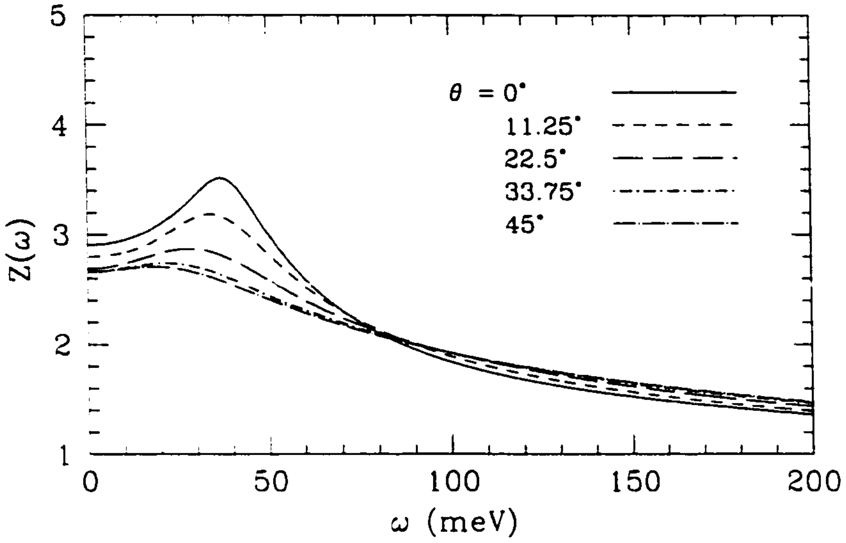

Figure 2.24: *Re* $Z(\theta,\omega)$ at $T = 20$ K in the superconducting state.

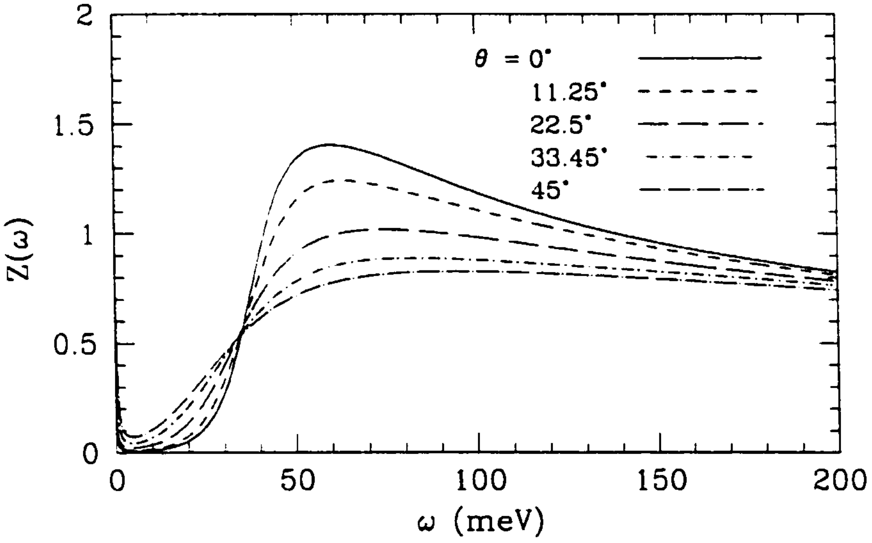

Figure 2.25: *Im* $Z(\theta,\omega)$ at $T = 20$ K in the superconducting state.

Material	λ	Method	Reference
$YBa_2Cu_3O_7$	0.2	resistivity	(Gurvich and Fiory 1987)
	0.3	resistivity	(Tanner and Timusk 1992)
	2.5	tunneling	(Kirtley et al. 1987)
$BiSrCuO_6$	0.2	resistivity	(Tanner and Timusk 1992)
$BiSrCuCu_2O_3$	0.3	resistivity	(Tanner and Timusk 1992)
$La_{1-x}Sr_xCuO_4$	0.1	resistivity	(Gurvich and Fiory 1987)
	2.0	H_{c1}	(Rammer 1987)
$Tl_2Ba_2CaCuO_8$	0.3	infrared	(Foster et al. 1990)

Table 2.2: Extracted values of λ reported in the literature.

the normal state results.

There is a correspondingly different low ω behaviour for $Im\ Z(\theta,\omega)$ in the superconducting state. At small ω, the function is suppressed for all angles, however, this suppression is largest for $\theta = 0°$. The function remains small until just above $\omega = \Delta_o(\mathbf{k})$ where the value of the function quickly rises. While at small ω the function $Im\ Z$ for $\theta = 0°$ is smallest, at intermediate frequencies, it is once again larger than the function at other angles. For $\omega = 200$ meV, $Im\ Z$ in the superconducting state is identical in size to the normal state results.

In table (2.2) values of λ extracted from experiments are listed for various materials. Only two values listed in the table are consistent with the values expected from the above theory: a tunneling experiment on $YBa_2Cu_3O_7$ yielded a value of 2.5 and critical field experiment on $LaSrCuO_4$ a value of 2.0. The majority of the extracted values are much smaller than the values expected by theory. In chapter 3 we will suggest why resistivity and infrared extractions may lead to misleading interpretations.

2.6 Spectral Density

The spectral density is a real valued positive-definite function given by

$$A_{\mathbf{k}}(\omega) = -\frac{1}{\pi} Im\ G_{(11)}(\mathbf{k}, \omega + i\delta^+) \tag{2.99}$$

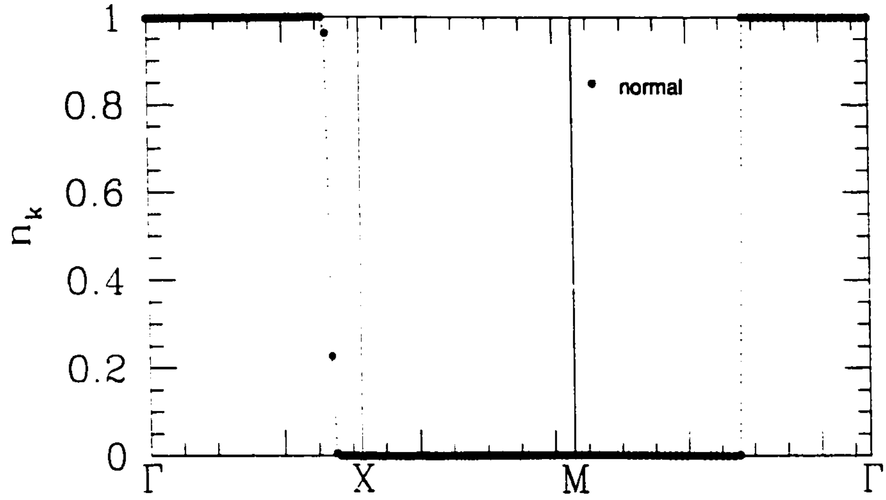

Figure 2.26: Occupation number along various high symmetry lines in the Brillouin zone for a non-interaction system

where δ^+ is an infinitesimal positive number. The function $A_{\mathbf{k}}(\omega)$ represents the probability of occupation of a state with energy ω for a particle of momentum **k**.

The occupation number of state **k** is given by

$$n_{\mathbf{k}} = \int d\omega A_{\mathbf{k}}(\omega) f(\omega) \tag{2.100}$$

where $f(\omega) = (e^{\beta\omega} + 1)^{-1}$ is the Fermi distribution function. Angle-resolved-photoemission (ARPES) probes directly the integrand in equation (2.100), the observed intensity of ARPES measurements being

$$I = R(\mathbf{k}, \omega) A_{\mathbf{k}}(\omega) f(\omega) \tag{2.101}$$

where $R(\mathbf{k}, \omega)$ is a resolution factor which leads to broadening of the observed lines in both frequency and momentum space. It is beyond the scope of this thesis to attempt direct fits to experimental data so we will deal only with calculations of $A_{\mathbf{k}}(\omega)$. Details of the influence of the resolution factor on the ARPES energy spectrum is nicely explained in other work (Fehrenbacher 1996).

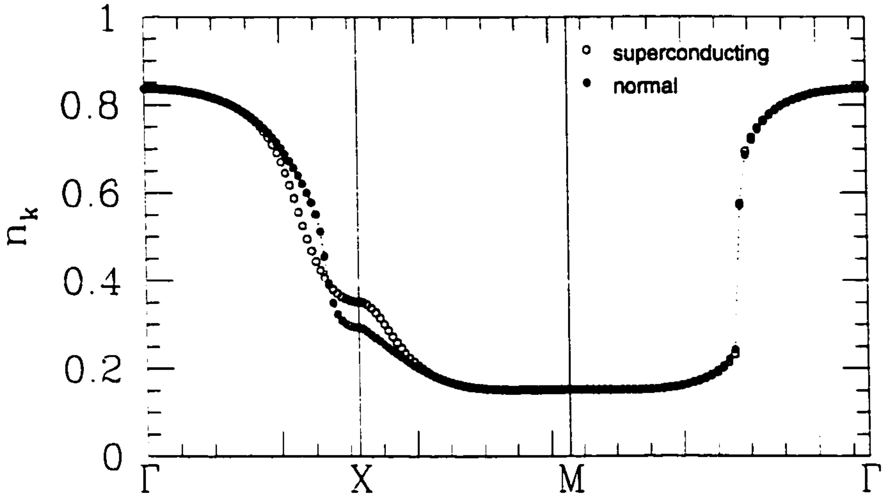

Figure 2.27: Occupation number along various high symmetry lines in the Brillouin zone for an interacting system

For a non-interacting system at T=0, the occupation factor, $n_{\mathbf{k}}$, exhibits a discontinuity as a function of **k**. The momentum state **k** is occupied with probability one for $|\mathbf{k}| < k_f$ and with probability zero for $|\mathbf{k}| > k_f$. When interactions between the particles is turned on, the occupation number is smeared some around k_f with there now being a finite probability of occupations of states above k_f and hole occupation below k_f. A discontinuity still exists at the Fermi level however, but now with height

$$z = Re\ Z_{k_f}(0)^{-1} \tag{2.102}$$

where $Re\ Z_{\mathbf{k}}(\omega)$ is the real part of the mass renormalization factor introduced earlier in the chapter. For finite temperature, the discontinuity is slightly smeared, however, by an amount $\sim k_B T$. At 10 K the thermal smearing is smaller than 1 meV and therefore negligible. In figure (2.26) the occupation number is plotted as a function of **k** along the high symmetry lines for a tetragonal system with a tight-binding dispersion relation and on interactions between electrons at $T = 10$ K. The function $n_{\mathbf{k}}$ exhibits sharp discontinuities as expected. When quasiparticle interactions are included via spin fluctuation exchange (i.e. the MMP model), the occupation number is smeared (see figure (2.27)). Along the line ΓM in the Brillouin zone (or along the diagonal), a finite discontinuity is still observed. However, along the line $\overline{\Gamma \mathrm{X}}$, which still intersects the Fermi surface according to earlier accounts, the discontinuity is not clearly visible. The smearing of the occupation factor is very strong in this direction. One can conclude that the quasiparticle picture holds much better along the diagonal than along the (0,0) to $(\pi, 0)$ direction. This is consistent with the calculations of the $Im\ \Sigma(\mathbf{k}, \omega)$ described earlier in the chapter where we saw that the quasiparticle scattering rate is much larger in the $\overline{\Gamma \mathrm{X}}$ direction than along the diagonal.

In the normal state, the spectral density, equation (2.99), reduces to

$$\begin{aligned} A_{\mathbf{k}}(\omega) &= -\frac{1}{\pi} \frac{Im\ \Sigma(\mathbf{k}, \omega)}{[\omega - \varepsilon_{\mathbf{k}} - Re\ \Sigma(\mathbf{k}, \omega)]^2 + [Im\ \Sigma(\mathbf{k}, \omega)]^2} \\ &= Z_{\mathbf{k},1}(\omega)^{-1} \frac{-Im\ \Gamma_{\mathbf{k}}(\omega)}{(\omega - \varepsilon^*_{\mathbf{k}}(\omega))^2 + Im\ \Gamma_{\mathbf{k}}(\omega)^2} \end{aligned} \tag{2.103}$$

The width of the spectral density is directly probed by ARPES measurements, as mentioned before. As such, these measurements probe $\Gamma_{\mathbf{k}} = -Im\ \Sigma_{\mathbf{k}}(\omega)/Z_{\mathbf{k}}(\omega)$, not the quasiparticle scattering rate itself.

In figure (2.28) we show plot of $A_{\mathbf{k}}(\omega)$ as a function of ω at a number of $\mathbf{k}$ points evenly spaced along the high symmetry directions. For panel 1, the direction probed in momentum space is along $\overline{\Gamma \mathrm{X}}$ (along (0,0) to $(\pi, 0)$). The lowest curve corresponds to the $\mathbf{k}$ point (0,0) or the Γ point. For clarity, the $A_{\mathbf{k}}(\omega)$ curves for different momenta are displaced along the vertical axis. For the smaller values of $\mathbf{k}$, the spectral density consists of a very broad curve of very small amplitude. As the momentum point nears the Fermi surface, the spectral density narrows significantly, until at k_f the peak height reaches a maximum. As one crosses the Fermi surface the peaks first narrow and then broaden again. In this picture, the spectral density is centered about $\omega = 0$ and reaches a maximum height for a momentum value on the Fermi surface. From the curves in the top panel, one can see that the Fermi surface lies at a k point some where between $k = 4/5\ \pi$ and $k = 9/10\ \pi$, corresponding to $\mathbf{k}$ points represented in the second and third highest curves shown.

The figure in the middle panel is for $\mathbf{k}$ points on the Brillouin zone face ranging from $(\pi, 0)$ to (π, π). Recall that at $(\pi, 0)$, one is at a momentum such that $|\mathbf{k}| > k_f$.

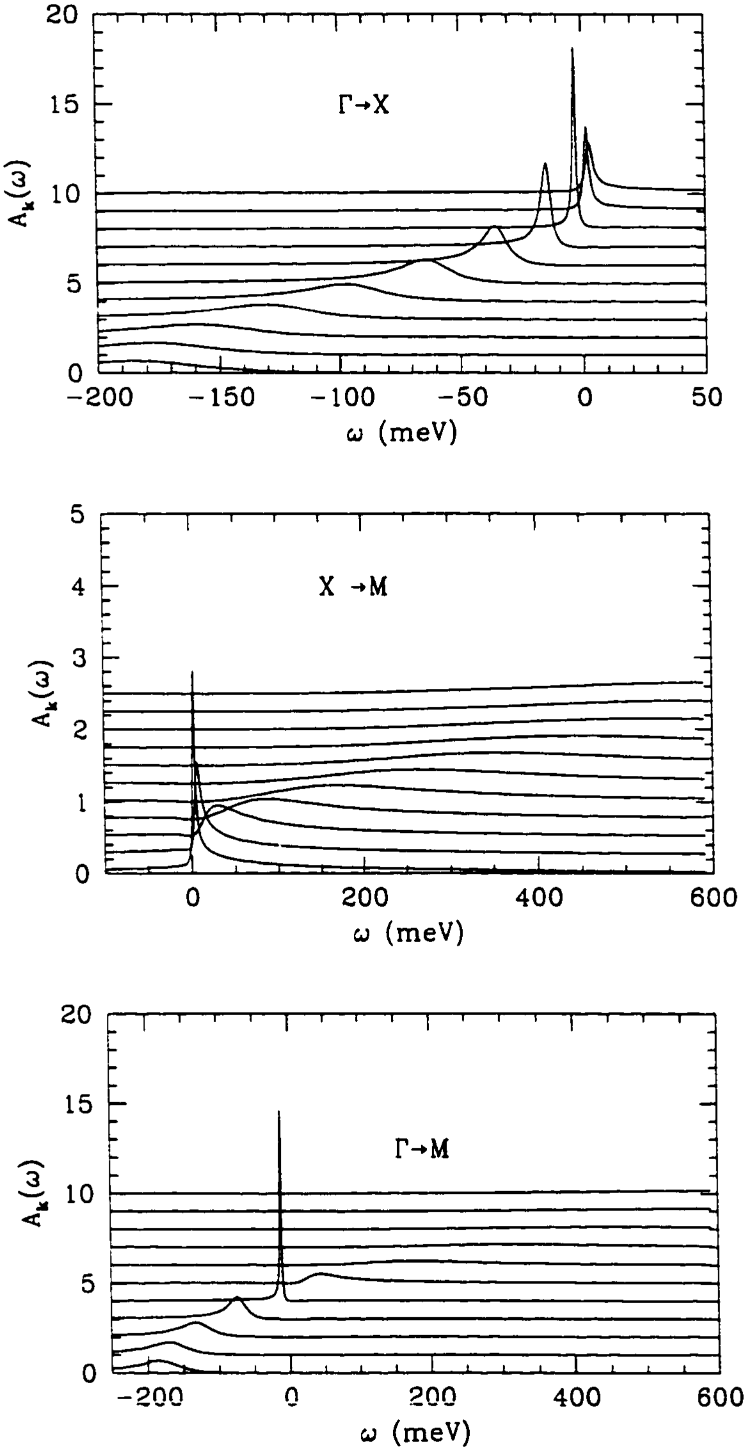

Figure 2.28: $A_{\mathbf{k}}(\omega)$ vs ω for various momenta in the Brillouin zone. Top panel is for equally spaced values of k along the line $\overline{\Gamma X}$, middle panel is for points along $\overline{XM}$, the bottom panel is for points along $\overline{\Gamma M}$. All curves are in the normal state at a temperature of 20 K.

The lowest curve in this panel corresponds identically to the highest curve in the top panel. (Note the difference in scales on both the vertical and horizontal axis in the three panels.) As one moves along in momentum space in the $\overline{XM}$ direction, $A_{\mathbf{k}}(\omega)$ quickly loses its quasiparticle nature becoming rather broad and low in amplitude.

The lowest panel corresponds to k-points along the diagonal of the Brillouin zone, in the direction $\overline{\Gamma M}$. The lowest curve corresponds to the Γ point. Similar to the results in the $\overline{\Gamma X}$ direction, the spectral function becomes more quasiparticle like with increasing $|\mathbf{k}|$, peaking just before the half-way point along the diagonal, and broadening again as the momentum value is moved through the Fermi surface. For $\mathbf{k}$ points above the Fermi wavevector, k_f, $A_{\mathbf{k}}(\omega)$ is quickly damped out. The line segment $\overline{\Gamma M}$ intersects the Fermi surface somewhere between $\frac{2\sqrt{2}\pi}{5} < |k_f| < \frac{\pi}{\sqrt{2}}$. In all cases described above, the spectral density at a particular k-point obeys the sum rule

$$\int_{-\infty}^{\infty} A_{\mathbf{k}}(\omega) d\omega = 1. \tag{2.104}$$

The spectral density in the superconducting state is more complicated than the normal state with the Nambu Green's function picking up off-diagonal contributions from the self-energy,

$$\begin{aligned} A_{\mathbf{k}}(\omega) &= \frac{-1}{\pi} Im\, G_{\mathbf{k}}^{(11)}(\omega + i\delta^+) \\ &= -\frac{1}{\pi} Im \frac{\tilde{\omega}(\omega) + \tilde{\varepsilon}_{\mathbf{k}}(\omega)}{\tilde{\omega}(\omega)^2 - \tilde{\varepsilon}_{\mathbf{k}}(\omega)^2 - \phi_{\mathbf{k}}(\omega)^2}. \end{aligned} \tag{2.105}$$

Equation (2.105) can be rewritten in the form

$$A_{\mathbf{k}}(\omega) = -\frac{1}{\pi} Im \left[\left(1 - \frac{\tilde{\varepsilon}_{\mathbf{k}}(\omega)}{\tilde{E}_{\mathbf{k}}}\right) \frac{1}{\tilde{\omega}(\omega) - \tilde{E}_{\mathbf{k}}} + \left(1 + \frac{\tilde{\varepsilon}_{\mathbf{k}}(\omega)}{\tilde{E}_{\mathbf{k}}}\right) \frac{1}{\tilde{\omega}(\omega) + \tilde{E}_{\mathbf{k}}} \right] \tag{2.106}$$

where we have defined

$$\tilde{E}_{\mathbf{k}} = \sqrt{\tilde{\varepsilon}_{\mathbf{k}}(\omega)^2 + \phi_{\mathbf{k}}(\omega)^2}. \tag{2.107}$$

In the BCS limit where there are no interactions between the normal state quasiparticles, the simplifications $\tilde{\omega} = \omega + i\delta$, $\tilde{\varepsilon}(\omega) = \varepsilon_{\mathbf{k}}$, and $\phi(\omega) = \Delta_{\mathbf{k}}$ are made. In this case equation (2.106) reduces to the familiar form (Schrieffer 1964)

$$A_{\mathbf{k}}(\omega) = -\frac{1}{\pi}\left[u_{\mathbf{k}}^2\delta(\omega - E_{\mathbf{k}}) + v_{\mathbf{k}}^2\delta(\omega + E_{\mathbf{k}})\right] \tag{2.108}$$

where $v_{\mathbf{k}}$ and $u_{\mathbf{k}}$ are the coherence factors

$$\begin{aligned} v_{\mathbf{k}}^2 &= \frac{1}{2}\left(1 - \frac{\varepsilon_{\mathbf{k}}}{E_{\mathbf{k}}}\right) \\ u_{\mathbf{k}}^2 &= \frac{1}{2}\left(1 + \frac{\varepsilon_{\mathbf{k}}}{E_{\mathbf{k}}}\right). \end{aligned} \tag{2.109}$$

In the strong-coupling regime the function $\tilde{\varepsilon}$, Z, ϕ, and $\tilde{\omega}$ are all complex functions and a simple reduction to a form similar to (2.108) is not possible.

In figure (2.29) we plot $A_{\mathbf{k}}(\omega)$ vs ω for various momenta along high symmetry lines for the superconducting state. For each direction in momentum space the selected **k** points and the scales on the axis are identical to the respective plots for the normal state spectral functions described earlier in figure (2.28) for easy comparison. We first consider the spectral densities for k-points along $\overline{\Gamma \mathrm{X}}$. The lowest curves once again is for $A_{\mathbf{k}}(\omega)$ at the point Γ and the top curve is for X. As the momentum is increased from its value at Γ, $A_{\mathbf{k}}(\omega)$ slowly narrows in frequency with the peak height simultaneously increasing. As $|\mathbf{k}|$ approaches k_f, a second peak begins to develop at higher frequencies. As $|\mathbf{k}|$ gets even closer to k_f, both peaks move closer together, narrowing significantly, and are centered about $\omega = 0$, the two peaks centered at $\pm\omega_o$ respectively. At $|\mathbf{k}| = k_f$, the amplitude of the two-peak structure is at a maximum. The separation between the two peaks is a measure of $2\Delta_o(\mathbf{k})$, where $\Delta_o(\mathbf{k})$ is the value of the gap edge at that particular **k**point. For $|\mathbf{k}|$ above k_f the two peaks, still centered about $\omega = 0$, begin to move apart while simultaneously broadening and decreasing in amplitude. At the X point, a two-peak structure still exists with both peaks still having significant amplitude.

We now shift our attention to the curves in the middle panel, corresponding to **k** points along the direction $\overline{\Gamma \mathrm{M}}$. The lowest curve is the same point at which we last left the discussion, $\mathbf{k} = (\pi, 0)$, or the X point. As the momentum is increased along the $\overline{\mathrm{XM}}$ direction, one can see that the peaks for a particular **k**value move further apart, both broadening quickly. The low frequency peak is suppressed more rapidly,

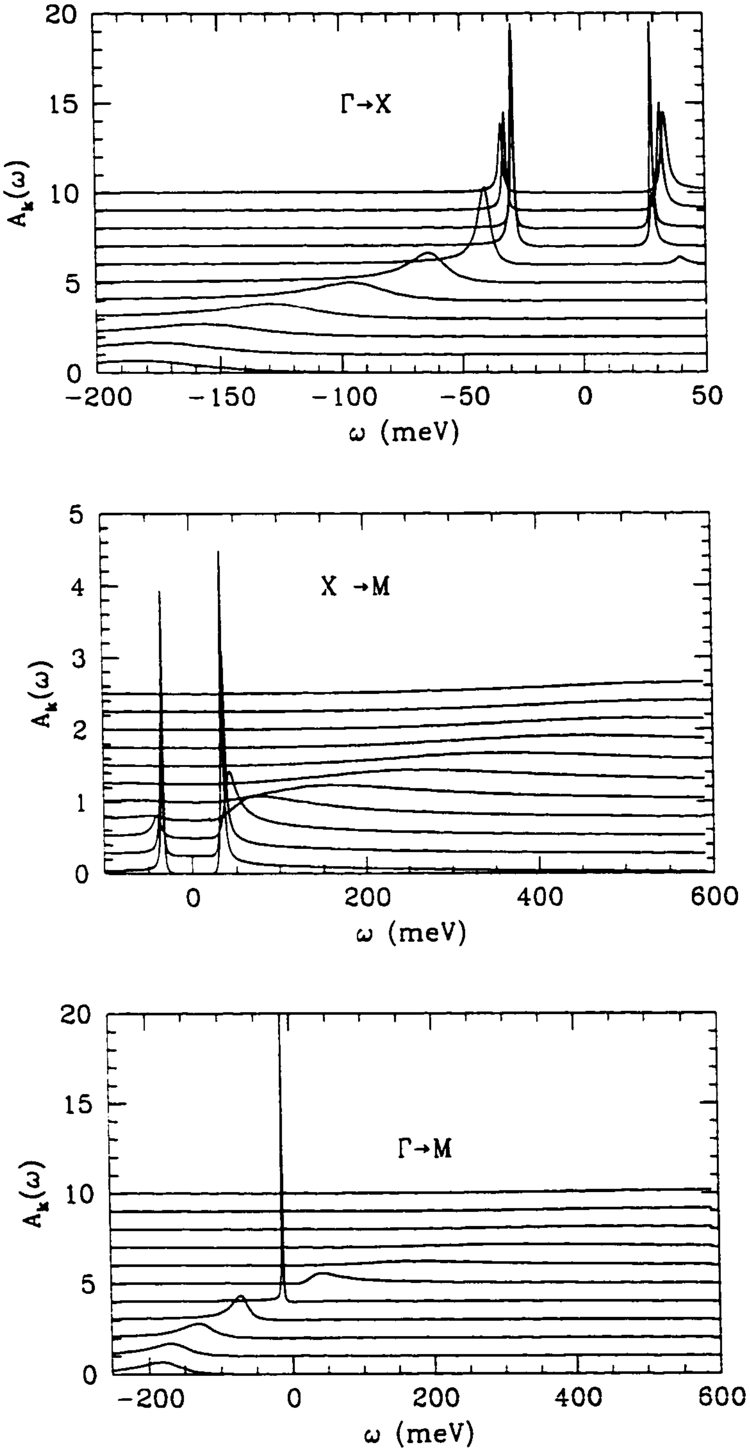

Figure 2.29: $A_{\mathbf{k}}(\omega)$ vs ω for various momenta in the Brillouin zone. Top panel is for equally spaced values of k along the line $\overline{\Gamma X}$, middle panel is for points along $\overline{XM}$, the bottom panel is for points along $\overline{\Gamma M}$. All curves are in the superconducting state at a temperature of 20 K.

having almost all trace disappear by $|\mathbf{k}| = 3/10\ \pi$ (fourth curve from the bottom). At higher values of .$\mathbf{k}$ $A_{\mathbf{k}}(\omega)$ once again becomes a single peaked function following the same trend as in the normal state being significantly damped before reaching the point M.

A cursory glance at the curves in the third panel, corresponding to equally spaced $\mathbf{k}$ points along the diagonal, shows a significant difference from the curves in the first two panels. Along this particular direction in k-space, $A_{\mathbf{k}}(\omega)$ remains a single peaked function. The normal state and superconducting state results are very similar along this direction. with $A_{\mathbf{k}}(\omega)$ moving through the Fermi surface in the same interval in k-space. The reason the spectral functions remains a single peak is that along the diagonal a pure d-wave energy gap is zero and the electronic states retain normal state-like behaviour.

One can see how ARPES experiments may be useful since these measurements directly probe $A_{\mathbf{k}}(\omega)$. By varying the momentum to move from a point away from k_f through the Fermi surface. these type of experiments can be used to map out the Fermi surface in the Brillouin zone by sweeping through $\mathbf{k}$ points in various directions. The tight-binding dispersion relation used in this thesis had its parameters chosen by a fit to a Fermi surface mapped out using this measurement technique. Another use is to extract the size of the energy gap on the Fermi surface as a function of angle. This particular technique is a $\mathbf{k}$-resolved probe, however. it is only sensitive to the magnitude of the gap. not its phase. Experiments to date are consistent with d-wave superconductivity (Shen et al. 1993).

The spectral density of the interacting system exhibits some interesting features as temperature is varied. In figure (2.30) we once again return to the normal state and show a plot of the spectral density as a function of frequency for evenly distributed points on the Fermi surface at 10 K. The lowest curve is for $\theta = 0^\circ$, θ being measured from the line $\overline{\Gamma X}$. Subsequent lines are for the points on the Fermi surface separated by 9°, the last (highest) curve being for $\theta = 45^\circ$. At all points on the Fermi surface, the peak in $A_{\mathbf{k}}(\omega)$ is very narrow and centered about $\omega = 0$ as expected. As the temperature is increased to 50 K, the inelastic scattering rate increases and the spectral function at the all points on the Fermi surface, figure (2.31), are broadened with

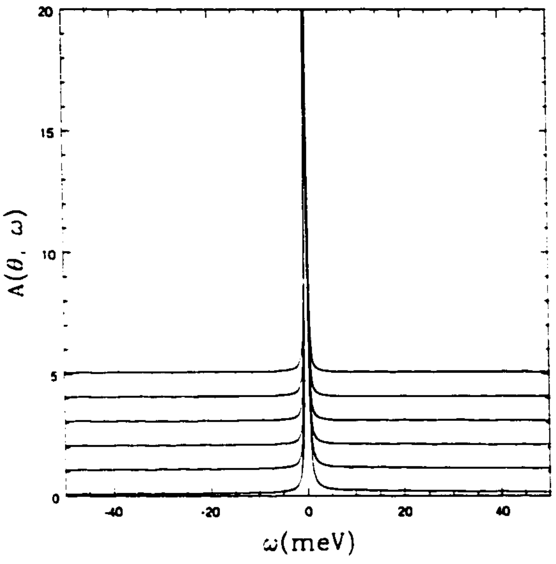

Figure 2.30: Frequency dependence of $A_{\mathbf{k}}(\omega)$ for various points on the Fermi surface in the normal state at $T = 10$ K.

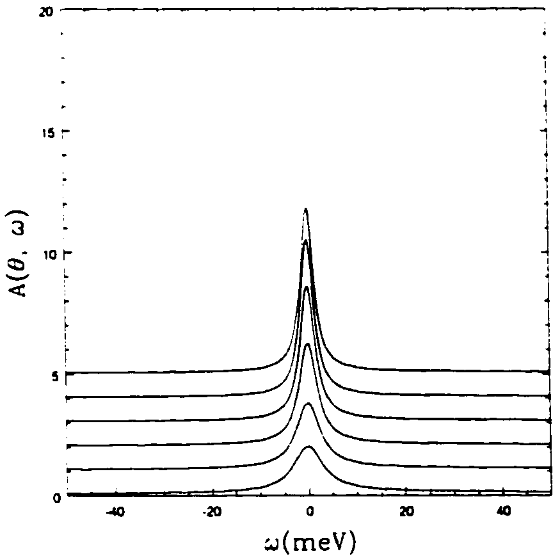

Figure 2.31: Frequency dependence of $A_{\mathbf{k}}(\omega)$ for various points on the Fermi surface in the normal state at $T = 50$ K.

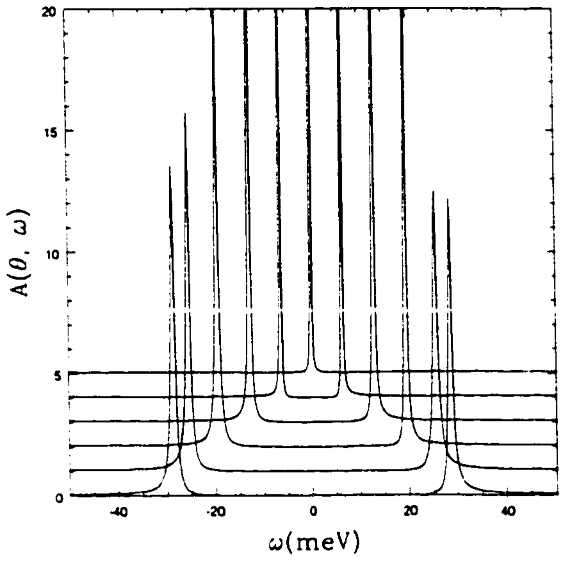

Figure 2.32: Frequency dependence of $A_{\mathbf{k}}(\omega)$ for various points on the Fermi surface in the superconducting state at $T = 10$ K.

the amplitude correspondingly decreased since $A_{\mathbf{k}}(\omega)$ obeys the sum rule in equation (2.104). The largest broadening occurs for $\theta = 0°$ where the quasiparticle scattering rates are largest.

The temperature dependence of the superconducting state spectral densities is even more interesting. In figure (2.32), $A_{\mathbf{k}}(\omega)$ is plotted for points on the Fermi surface corresponding to the same angles as the previous normal state calculations. The temperature is again set at $T = 10$ K. For $\theta = 45°$, $A_{\mathbf{k}}(\omega)$ is a single peaked function, as expected. As the angle is decreased, the spectral function bifurcates with a clear gap exhibited between the two peaks. The energy difference between the peaks is given by the value of $2\Delta_o$, or twice the gap edge, for that particular point on the Fermi surface. At $\theta = 0°$, the gap is a maximum with a value of $2\Delta_o = 54$ meV, a value consistent with the density of states shown earlier in figure (2.18).

In figure (2.33) we plot the same thing as in (2.32), but in this case for a temperature of 50 K. Several differences are clearly seen. The peaks in the spectral density curves are broadened by quite a bit and, as such, are significantly lower in amplitude. The value of $2\Delta_o$ on the Fermi surface for $\theta = 0°$ is reduced slightly with it being

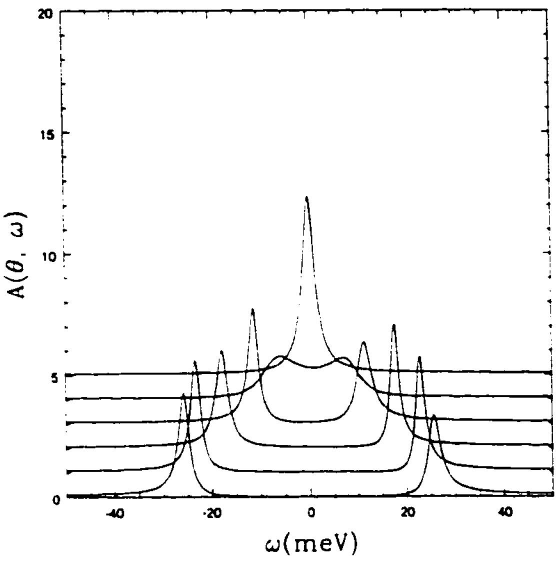

Figure 2.33: Frequency dependence of $A_{\mathbf{k}}(\omega)$ for various points on the Fermi surface in the superconducting state at $T = 50$ K.

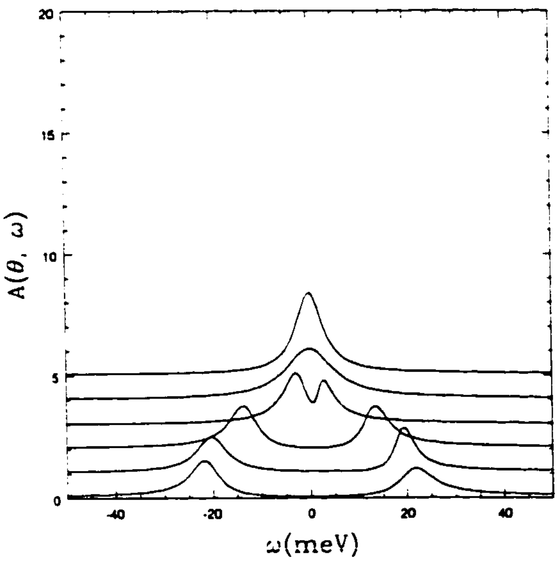

Figure 2.34: Frequency dependence of $A_{\mathbf{k}}(\omega)$ for various points on the Fermi surface in the superconducting state at $T = 80$ K.

approximately 52-53 meV. The most striking feature is the change to the curve at 36° (second from the top). The two side peaks have been drastically smeared and a finite spectral weight exists at zero frequency. Responsible for the gap being filled in is the normal carrier concentration developing at the nodes of the energy gap as the temperature increases due to inelastic scattering effects.

As the temperature is increased to even higher temperatures, in this case 80 K [figure (2.34)], the function at 36° is reduced to a single peak. Fehrenbacher has seen a similar effect in a simple BCS model for which the scattering is due to impurities and shows that it leads to *extended nodes* in the superconducting energy gap (Fehrenbacher 1996).

2.7 Impurities

So far we have only discussed the results of pure systems, however, we are also interested in the effects of impurities. In this section, we will describe the effects of non-magnetic impurities on the critical temperature, the spectral densities, and the density of states.

Anderson's theorem (Anderson 1959) states that normal impurities do not affect the critical temperature of conventional s-wave superconductors. This is no longer valid for d-wave superconductors. In section (2.2.4) we introduced the linearized Eliashberg equations used to calculate the critical temperature. For a pure d-wave superconductor, the impurity term in the ϕ channel vanishes since ϕ has an average of zero over the Brillouin zone. The impurities only affect the ϕ channel indirectly through $\tilde{\omega}$ and ξ.

The critical temperature is shown as a function of impurity concentration, n_{imp}, in figure (2.35). The solid line corresponds to the resonant scattering limit ($V_{imp} = \infty$). The other curves were calculated using the general impurity scattering function (2.39) with $V_{imp} = 5.0$ eV (short dashed line), 1.0 eV (short dashed - dotted line), 0.5 eV (long dashed-dotted line). The $V_{imp} = 5$ eV system is essentially in the resonant limit as indicated by the two curves being almost indistinguishable. To reduce the critical temperature by 25 % requires an impurity concentration of approximately 4.75 % at

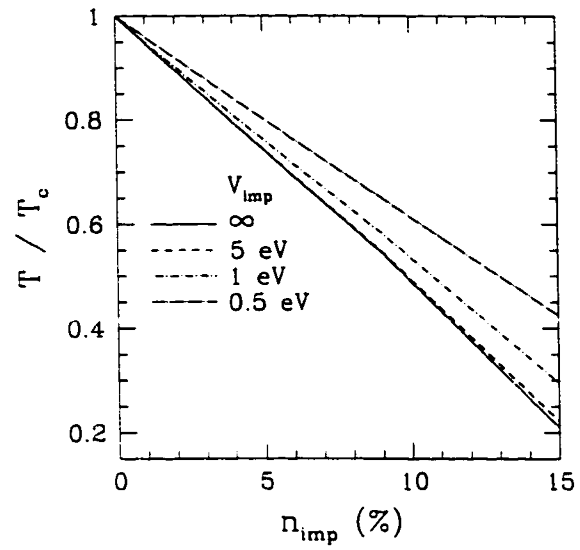

Figure 2.35: Critical temperature, T_c, vs impurity concentration, n_{imp}, for various scattering strengths. $V_{imp} = \infty$ is the resonant scattering limit.

the resonant limit (same for 5 eV), 5.25 % for $V_{imp} = 1$ eV and 6.5 % for $V_{imp} = 0.5$ eV.

Next we will look at the effects of non-magnetic impurities on the spectral density. All curves were calculated at $T = 10$ K , the lowest temperature we could easily calculate using our formalism. We also restrict ourselves to the unitary scattering limit. As impurity scattering increases the quasiparticle scattering rates, one might expect that the peaks in the spectral density would broaden. This is exactly what is seen. In figure (2.36) we show once again $A_{\mathbf{k}}(\omega)$ for various points on the Fermi surface. The bottom curve corresponds to an angle of $\theta = 0°$ and the top curve for 45°. Remaining points are at equally spaced angles. In this case the impurity concentration is 1.5 %. The 45° curve has been drastically broadened and the value of $2\Delta_o$ has decreased. As with the effects of inelastic scattering at higher temperatures, elastic scattering leads to low lying states inside the nodes to be filled in. For a d-wave superconductor, impurity scattering is pair breaking and leads to a residual normal carrier density of states at the nodes of the gap. As the impurity concentration is increased to 3.0 %, figure (2.37), the smearing of the 36° curve is even more dramatic.

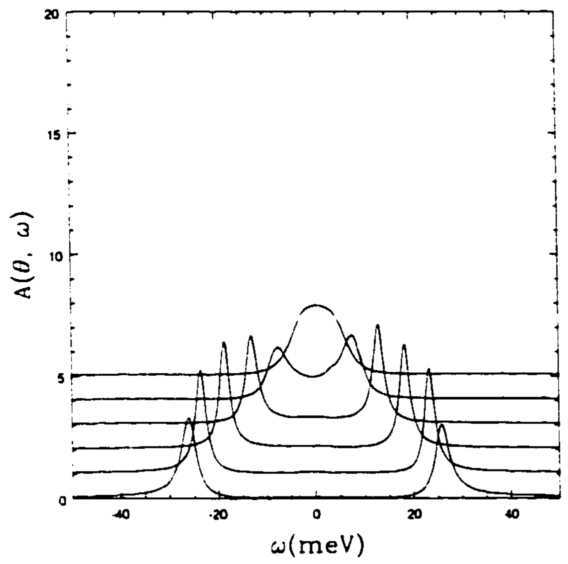

Figure 2.36: Frequency dependence of $A_{\mathbf{k}}(\omega)$ for various points on the Fermi surface in the superconducting state at $T = 10$ K. The impurity concenteration is $n_{imp} = 1.5$ %.

The existence of normal carrier concentration is even visible in the 25° curve (third from the top) at this impurity concentration. For an impurity concentration of 4.5 %, the two peak spectrum has been almost completely washed out for the 36° curve. The broadening of the peaks increases further and a finite value for $A_{\mathbf{k}}(\omega = 0)$ is seen for all points on the Fermi surface.

The density of states for the superconducting state is shown in figure (2.39) for various impurity concentrations at a temperature of 50 K. The impurity scattering is assumed to be in the resonant limit. The different curves correspond to $n_{imp} = 0.0$ %, or the pure case, (solid line) 1.5 % (short-dashed line), 3.0 % (long dashed line), and 4.5 % (dash-dotted line). Even for no impurities, $N(\omega)$ is finite at $\omega = 0$ in the superconducting state due to pair breaking effects of inelastic scattering. As the impurity concentration is increased, the scattering rate for particles inside the gap is increased, leading to a larger $N(\omega)$. Also notice that as the impurity concentration increases, the size of the gap, as measured by the separations of the two peaks, decreases.

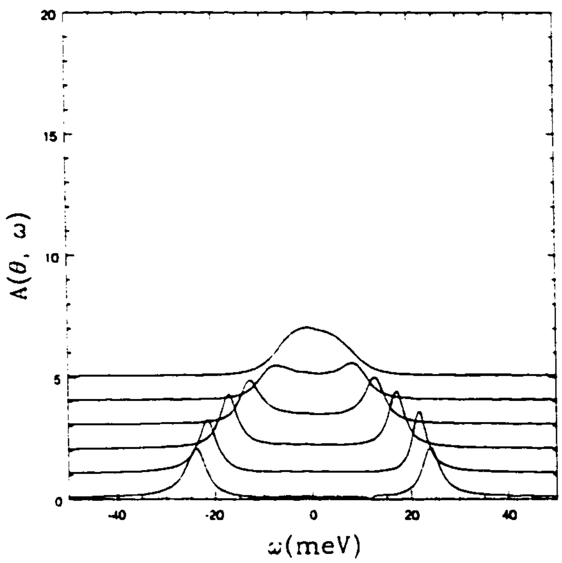

Figure 2.37: Frequency dependence of $A_{\mathbf{k}}(\omega)$ for various points on the Fermi surface in the superconducting state at $T = 10$ K. The impurity concenteration is $n_{imp} = 3.0$ %.

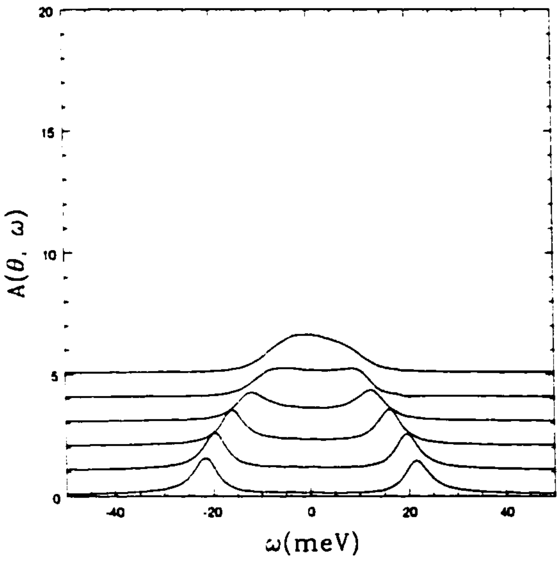

Figure 2.38: Frequency dependence of $A_{\mathbf{k}}(\omega)$ for various points on the Fermi surface in the superconducting state at $T = 10$ K. The impurity concentration is $n_{imp} = 4.5$ %.

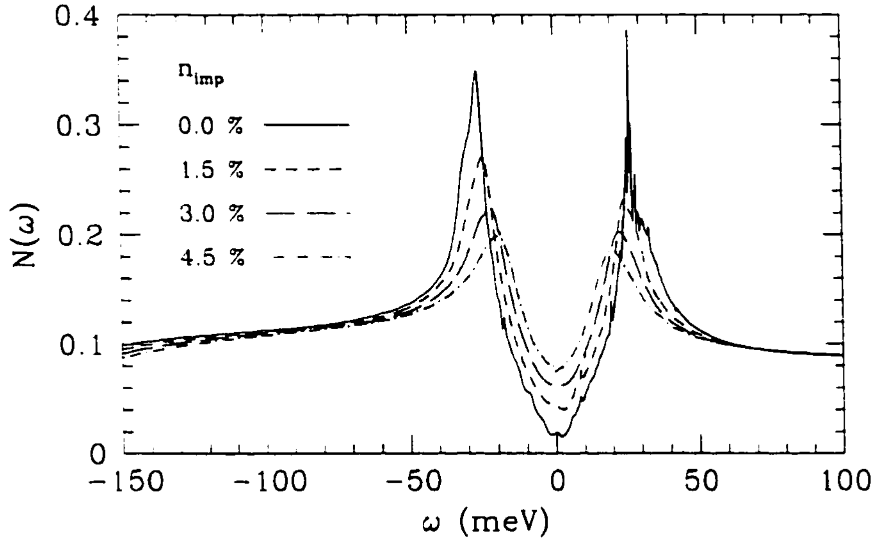

Figure 2.39: The density of states,$N(\omega)$, in the superconducting state state for various impurity concentrations at 50 K.

Chapter 3

Optical Conductivity

3.1 Introduction

An important feature of the BCS theory of superconductivity was the prediction of the existence of an energy gap in the quasiparticle excitation spectrum at zero temperature. In order to excite normal state particles across the gap, the electronic system would have to absorb at least 2Δ in energy, enough to break a Cooper pair and promote two quasiparticles to states above the gap. At low temperatures, therefore, one would expect to observe such a gap in optical experiments. Attempts were made to measure the energy gap using optical absorption methods in the far infrared. For example, Pb has a critical temperature $T_c = 7.2$ K, therefore $k_B T_c = 0.62$ meV. BCS theory then predicts an observable gap edge at $E_g = 2\Delta = 3.52\ k_B T_c = 2.2$ meV, or 17.7 cm^{-1}. The experimental value was determined to be approximately 22.5 cm^{-1} (Palmer and Tinkham 1968). The difference between the theoretical and experimental values can easily be explained using strong-coupling theory (Carbotte 1990; Mahan 1990).

The idea of using optical absorption techniques was therefore well established in the superconductivity field when the discovery of superconductivity in the cuprate materials was first made. Once again, using BCS formalism for isotropic conventional superconductivity, one predicts that the energy gap observed in such experiments should be $E_g = 3.52\ k_B T_c = 10.6$ meV $= 85.3$ cm^{-1} for a material with a $T_c = 35$ K.

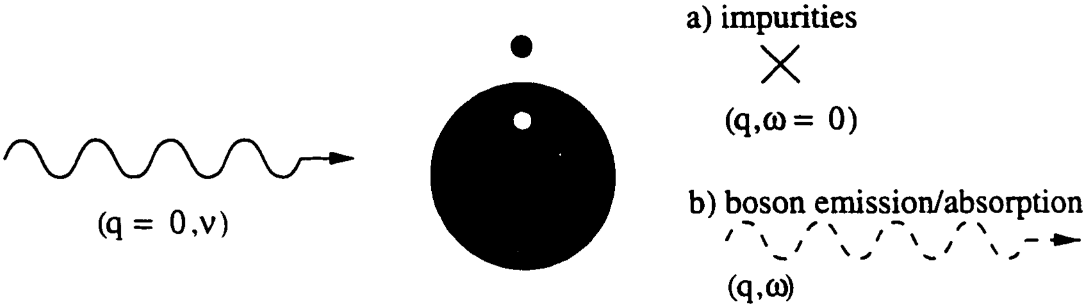

Figure 3.1: A schematic diagram of photon absorption by electrons. A photon of frequency ω incident on the electronic Fermi sea is absorbed by an electron and creates a particle-hold pair. Energy and momentum can be conserved by relaxing the system in two ways: a) by impurity scattering which can transfer momentum to/from the lattice and b) by the emission/absorption of bosons (phonons, spin fluctuations, etc.) which can transfer both energy and momentum to the system.

For $T_c = 100$ K, BCS theory gives 30.3 meV or 244.0 cm^{-1} as the absorption gap edge. Experiments, however, see no gap edge at any frequency in the cuprate materials, but instead observe finite absorption down to the lowest measured frequency even at low temperatures (Timusk and Tanner 1989; Tanner and Timusk 1992).

The frequency dependent in-plane optical conductivity is the topic of this chapter. Theoretical models of the conductivity are commonly divided into two main classes: one and two component models. For a one component model, the entire optical response is due to absorption of energy by charge carriers from only one source, the itinerant conduction electrons. A two component model is one in which there is a contribution to the frequency spectrum from the conduction electrons and the polarizable bound-state electrons which have their response centered around some higher frequency, usually in the mid-infrared for cuprate models.

For the one component model discussed in this chapter, optical absorption by normal state carriers can occur through two processes: boson-assisted absorption and impurity assisted absorption. These two processes are illustrated in figure (3.1). In both cases a photon of energy ν ($\hbar = 1$) and momentum $q = 0$ is incident on the electron sea in the metal and creates a particle-hole pair, which has both finite momentum and finite energy. This process alone does not conserve energy and mo-

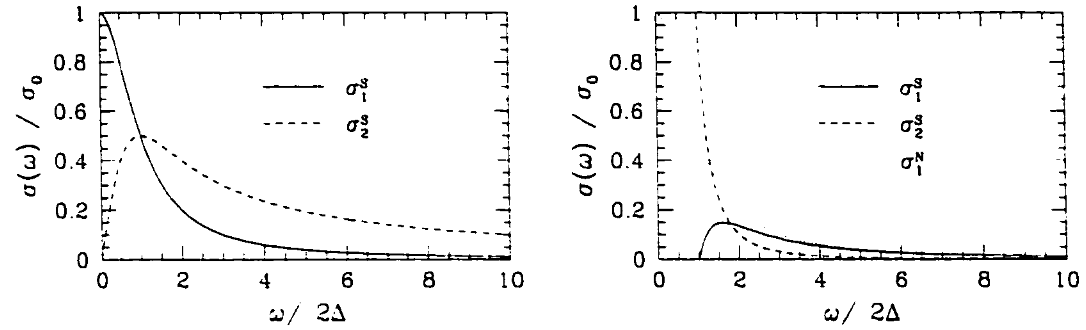

Figure 3.2: a) $\sigma_1(\omega)$ (solid line) and $\sigma_2(\omega)$ (dashed line) for the Drude model with $1/\tau = 1/2\Delta$ b) Superconducting values of $\sigma_1(\omega)$ and $\sigma_2(\omega)$. The dotted line indicates the normal state value for comparison.

mentum, therefore, another process is necessary in order to allow for the absorption of the photon.

Impurity scattering gives the electrons a finite lifetime allowing them to absorb photons and then decay transferring the extra momentum to the impurity scattering centers. There is no transfer of energy, however, since impurity scattering is an elastic scattering process. The scattering rate is therefore a constant at all frequencies. This process leads to the Drude conductivity discussed in many elementary solid state physics textbooks [see for example (Ashcroft and Mermin 1976; Ziman 1979)]. It is a simple picture which contains the element of viscous damping of the electrons in an applied electromagnetic field:

$$\begin{aligned} \sigma(\omega) &= \frac{ne^2}{m}\frac{1}{1/\tau - i\omega} \\ &= \frac{\omega_p^2}{4\pi}\frac{\tau + i\omega\tau}{1+\omega^2\tau^2} \end{aligned} \tag{3.1}$$

where n is the electron density, m is the electron mass, τ is the electron lifetime, and ω_p is the plasma frequency. The conductivity is seen to be a complex function, $\sigma(\omega) = \sigma_1(\omega) + i\sigma_2(\omega)$, where the real part, $\sigma_1(\omega)$, is related to the absorption of energy from the electromagnetic field and the imaginary component, $\sigma_2(\omega)$, is related to the electronic contribution of the dielectric function (Mahan 1990; Ashcroft and Mermin 1976). In figure (3.2.a) we plot $\sigma_1(\omega)$ and $\sigma_2(\omega)$ of the Drude conductivity. At $\omega = 0$, the dc conductivity is $\sigma(0) = \sigma_o = \frac{\omega_p^2\tau}{4\pi}$. The real part of the conductivity is a Lorentzian with a width at half-maximum of $1/\tau$, the optical scattering rate.

In the superconducting state, no absorption can occur until enough energy is absorbed to break a Cooper pair and excite two quasiparticles to states above the gap energy. For an isotropic s-wave, the threshold for absorption is therefore at $\omega = 2\Delta$. In figure (3.2.b), we plot $\sigma_1(\omega)$ and $\sigma_2(\omega)$ for the superconducting state of an isotropic s-wave superconductor. Below $\omega = 2\Delta$, $\sigma_1(\omega)$ is identically zero, while above the 2Δ threshold, the absorption turns on and $\sigma_1(\omega)$ quickly rises to reach the normal state value at higher frequencies (Mattis and Bardeen 1958).

There is an important sum rule which states that the area under the conductivity curve must be conserved (Tinkham 1975),

$$\int_0^\infty \sigma_1(\omega)d\omega = \frac{\omega_p^2}{8}. \tag{3.2}$$

Equation (3.2) must also be obeyed in the superconducting state (Ferrell and Glover 1958; Tinkham and Ferrell 1959), therefore,

$$\int_0^\infty (\sigma_1^s(\omega) - \sigma_1^n(\omega))\, d\omega = 0 \tag{3.3}$$

where the superscripts n and s denote the normal and superconducting states responses respectively. The difference in spectral weight between the $\sigma_1^n(\omega)$ and $\sigma_1^s(\omega)$ curves which appears to be lost in figure (3.2.b) has been shifted to the zero-frequency delta function at $\omega = 0$. The dc conductivity associated with the superconducting state is then

$$\sigma_1^s(\omega = 0) = \frac{\pi n_s e^2}{2m}\delta(0) \tag{3.4}$$

where n_s is the superconducting electron density of the phenomenological two fluid model (Rickayzen 1965).

The second process which aids the electronic absorption of photons is the boson-assisted, or Holstein, process. In such a system, the electrons are coupled to a boson field, such as phonons or spin fluctuations. The electrons can then absorb photons conserving both energy and momentum by decaying and emitting bosons. This transfers both energy and momentum from the electronic system requiring an overall energy conservation. Absorption can therefore only occur at specific energies associated with the fluctuations in the system.

In a series of seminal papers, Holstein (Holstein 1954; Holstein 1964) predicted that strong electron-phonon coupling should lead to a process where excited electrons would emit phonons and produce a spectrum in the frequency dependent conductivity which would be closely related to the $\alpha^2F(\omega)$ seen in tunneling spectroscopy. This predicted phonon structure was first observed by Joyce and Richards in lead, a strongly-coupled superconductor (Joyce and Richards 1970). They found an onset of absorption with photon energies large enough to emit, or excite, appreciable number of phonons. The observed structure correlated well with peaks in the $\alpha^2F(\omega)$. In the superconducting state, similar features were seen in the spectrum, but in this case, shifted by twice the gap, i.e. $\omega_{ph} \rightarrow 2\Delta + \omega_{ph}$. Farnworth and Timusk found similar results and went a step further (Farnworth and Timusk 1974). Using both the normal state and superconducting state absorptivity data, they managed to invert the spectra for $\alpha^2_{tr}F(\omega)$. The transport $\alpha^2_{tr}F(\omega)$ is related to the tunneling $\alpha^2F(\omega)$ but with additional weight given to large angle scattering as one expects in transport. The results correlated well with tunneling results, however, the optical data showed several extra features absent from tunneling, but present in neutron data. This suggested that far infrared spectroscopy could provide an alternative to tunneling for determination of $\alpha^2F(\omega)$.

In the next section we introduce the theory for the electromagnetic response in terms of Nambu Green's functions. An equation for the optical conductivity is derived in terms of the Eliashberg self-energy equations introduced in chapter 2.

Numerical calculations for the normal state frequency dependent optical conductivity are presented in section (3.3). Using a simple extension of the Drude model, frequency dependent scattering rates and optical mass renormalization function are extracted from the conductivity. The results are compared to the fundamental quasiparticle scattering rates and dynamical mass enhancement factor discussed in the last chapter. Using a simple model to invert the conductivity, an effective boson spectral density, $g^2\chi(\omega)$, is extracted. It is shown how the optical data may be used to determine the signature of the boson structure in the absorption spectra. The effects of k-space anisotropy on the normal state conductivity are also investigated. It is shown that in order to reproduce the conductivity spectrum for the system, the effects of anisotropy in the quasiparticle scattering rates on the Fermi surface must be taken into account.

Superconducting state results are presented in section (3.4). The extended Drude model is once again used to extract information on the optical scattering rates and mass renormalization. The effects of d-wave superconductivity on the observable optical properties is discussed.

Finally, in section (3.5) we treat the effects of non-magnetic impurity scattering on the optical conductivity. The predicted universal saturation limit to the low frequnecy conductivity in the resonant scattering limit is discussed.

3.2 Theory

In this section we derive a general expression for the optical conductivity in terms of Nambu Green's functions. Following Nam (Nam 1967a; Nam 1967b), the response of a conductor to the presence of an electromagnetic field is given by

$$J_\mu(\mathbf{q},\omega) = -\Pi_{\mu\nu}(\mathbf{q},\omega)A^\nu(\mathbf{q},\omega) \tag{3.5}$$

where $J_\mu(\mathbf{q},\omega)$ is the induced current, $\Pi_{\mu\nu}(\mathbf{q},\omega)$ is the electromagnetic (EM) response function, and $A^\nu(\mathbf{q},\omega)$ is the vector potential of the radiation field. The Cartesian coordinates are denoted by μ and ν. The EM response function is comprised of two components: a paramagnetic frequency dependent term, $\Pi^{(p)}_{\mu\nu}(\mathbf{q},\omega)$ and a frequency independent diamagnetic term, $\Pi^{(d)}_{\mu\nu}(\mathbf{q})$,

$$\Pi_{\mu\nu}(\mathbf{q},\omega) = \Pi^{(p)}_{\mu\nu}(\mathbf{q},\omega) + \Pi^{(d)}_{\mu\nu}. \tag{3.6}$$

The paramagnetic current operator is given by

$$J^{(p)}_\mu(\mathbf{q}) = -e\sum_{\mathbf{k}} \psi^\dagger_{\mathbf{k}}\hat{\gamma}(\mathbf{k}+\mathbf{q}/2)\psi_{\mathbf{k}+\mathbf{q}} \tag{3.7}$$

where the electromagnetic vertex function is

$$\hat{\gamma}_\mu(\mathbf{k}) = \hat{\tau}_0\frac{\partial\varepsilon_{\mathbf{k}}}{\partial k_\mu}. \tag{3.8}$$

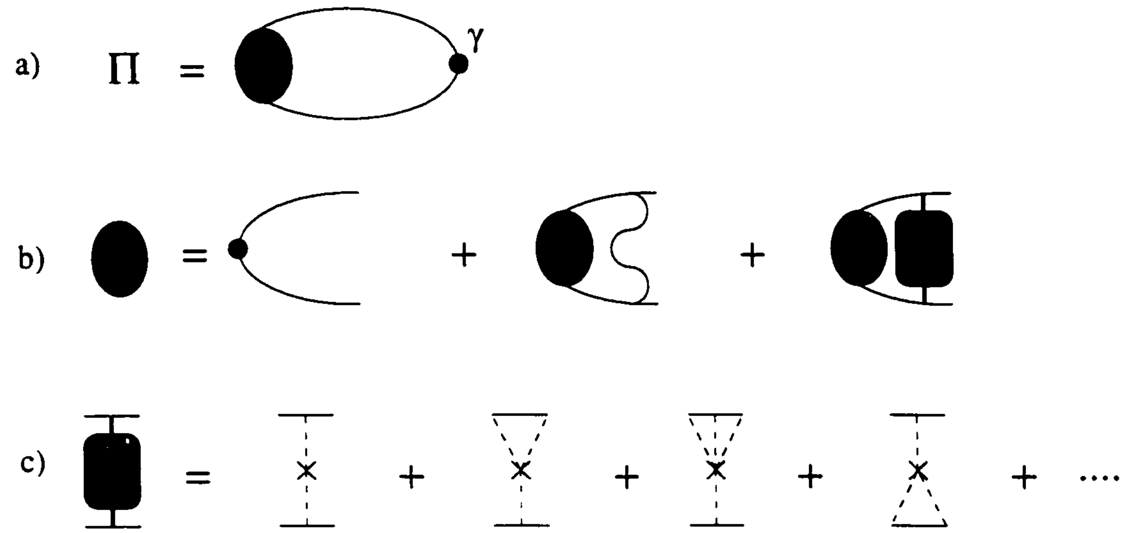

Figure 3.3: Feynman diagram for a) EM response function. The vertex corrections b) are given by boson exchange between the particle-hole pair and impurity scattering. The T-matrix approximation to impurity scattering vertex correction is shown in c).

Within the Kubo formalism (Mahan 1990), the EM response function can be written in terms of the paramagnetic current operators as

$$\Pi^{(p)}_{\mu\nu}(\mathbf{q},t) = \left\langle T_t J^{(p)}_{\mu}(\mathbf{q},\mathrm{t}) J^{(p)}_{\nu}(\mathbf{q},0)\right\rangle \tag{3.9}$$

where T_t is Wick's time ordering operator, t is the time, $J^{(p)}_{\mu}(\mathbf{q},t)$ is the paramagnetic current operator in the Heisenberg picture and $J^{(p)}_{\mu}(\mathbf{q},0)$ is in the Schroedinger picture. The Feynman diagram for the EM response function is shown in figure (3.3.a). In terms of the finite temperature Green's functions, equation (3.9) can be written

$$\Pi^{(p)}(i\nu_n) = -\frac{e^2 T}{N}\sum_{m,\mathbf{k}} Tr\left[\hat{\gamma}(\mathbf{k})\hat{G}(\mathbf{k}, i\omega_m + i\nu_n)\hat{\Gamma}(\mathbf{k}, i\omega_{m+n}, i\omega_m)\hat{G}(\mathbf{k}, i\omega_m)\right] \tag{3.10}$$

where Tr denotes a trace and $\hat{\Gamma}(\mathbf{k}, i\omega_{m-n}, i\omega_m)$ is the renormalized, or dressed, vertex correction function

$$\begin{aligned}\hat{\Gamma}(\mathbf{k}, i\omega_{m-n}, i\omega_m) &= \hat{\gamma}(\mathbf{k}) \\ &\quad + \frac{T}{N}\sum_{l,\mathbf{k}'} \lambda(\mathbf{k}-\mathbf{k}', i\omega_m - i\omega_l)\hat{\tau}_0 \hat{G}(\mathbf{k}-\mathbf{k}', i\omega_{l-n}) \\ &\qquad\qquad \times \hat{\Gamma}(\mathbf{k}', i\omega_{l-n}, i\omega_l)\hat{G}(\mathbf{k}', i\omega_l)\hat{\tau}_0 \\ &\quad + \frac{T}{N}\sum_{l,\mathbf{k}'} \hat{T}(\mathbf{k},\mathbf{k}', i\omega_l)\hat{\tau}_3 \hat{G}(\mathbf{k}', i\omega_m)\hat{\Gamma}(\mathbf{k}', i\omega_{l-n}, i\omega_l) \\ &\qquad\qquad \times \hat{G}(\mathbf{k}', i\omega_l). \end{aligned} \tag{3.11}$$

The Feynman diagram for the dressed vertex function is shown in figure (3.3.b), where the three diagrams on the right hand side correspond to the three terms in equation (3.11) respectively. The first term is simply the unrenormalized electromagnetic vertex given previously in equation (3.8). The second term is related to boson exchange between the particle-hole pair, while the third term is due to impurity scattering. These last two terms involve interactions between the particle-hole pair created by the initial photon absorption. The electron-boson vertex correction has the effect of renormalizing the electron-boson spectral density $\alpha^2 F$ to a transport function, $\alpha_{tr}^2 F$. The inclusion of the vertex corrections has only a quantitative, not qualitative, effect. Since we can only hope for a qualitative description anyway, the boson renormalization is ignored. Similarly, the impurity terms are expected to make only quantitative differences to the EM response function and are, therefore, also dropped. The $\hat{\Gamma}(\mathbf{k}, i\omega_n)$ vertex will therefore be approximated by the unrenormalized vertex, $\gamma_{\mathbf{k}}$, throughout this work. When impurities are present, the effects will simply be included in the single particle Green's functions.

The diamagnetic component of the EM response function is a frequency independent term which is similar in form to the paramagnetic term,

$$\Pi^{(d)} = -\frac{e^2 T}{N}\sum_{\mathbf{k},m} Tr\left(\hat{\gamma}'_{\mathbf{k}} \hat{G}(\mathbf{k}, i\omega_m)\hat{\gamma}'_{\mathbf{k}} \hat{G}(\mathbf{k}, i\omega_m)\right) \tag{3.12}$$

but with a slightly different vertex,

$$\hat{\gamma}'_{\mathbf{k}} = \hat{\tau}_3 \frac{\partial \varepsilon_{\mathbf{k}}}{\partial k}. \tag{3.13}$$

Substituting our expression for the interaction Green's function, equations (2.46 - 2.49), into our expressions for the diamagnetic and paramagnetic response functions, equations (3.10), using the unrenormalized vertices, one gets for the EM response function

$$\begin{aligned}
\Pi_{\alpha,\beta}(i\nu_n) &= \Pi^{(p)}(i\nu_n) - \Pi^{(d)} \\
&= 2e^2\frac{T}{N}\sum_{\mathbf{k},m}\frac{\partial\varepsilon_{\mathbf{k}}}{\partial\mathbf{k}_\alpha}\frac{\partial\varepsilon_{\mathbf{k}}}{\partial\mathbf{k}_\beta}\times \\
&\times\left\{\frac{\tilde{\varepsilon}_{\mathbf{k}}(i\omega_{m+n})\varepsilon_{\mathbf{k}}(i\omega_m)+\phi_{\mathbf{k}}(i\omega_{m+n})\phi_{\mathbf{k}}(i\omega_m)-\tilde{\omega}_{\mathbf{k}}(i\omega_{m+n})\tilde{\omega}_{\mathbf{k}}(i\omega_{m+n})}{[\tilde{\varepsilon}_{\mathbf{k}}(i\omega_{m+n})^2+\phi_{\mathbf{k}}(i\omega_{m+n})^2+\tilde{\omega}_{\mathbf{k}}(i\omega_{m+n})^2]\,[\tilde{\varepsilon}_{\mathbf{k}}(i\omega_m)^2+\phi_{\mathbf{k}}(i\omega_m)^2+\tilde{\omega}_{\mathbf{k}}(i\omega_m)^2]}\right. \\
&\qquad\left.-\frac{\tilde{\varepsilon}_{\mathbf{k}}(i\omega_m)^2-\phi_{\mathbf{k}}(i\omega_m)^2-\tilde{\omega}_{\mathbf{k}}(i\omega_m)^2}{[\tilde{\varepsilon}_{\mathbf{k}}(i\omega_m)^2+\phi_{\mathbf{k}}(i\omega_m)^2+\tilde{\omega}_{\mathbf{k}}(i\omega_m)^2]^2}\right\}. \qquad (3.14)
\end{aligned}$$

The frequency dependent conductivity is then related to the EM response through

$$\sigma(\omega) = i\frac{\Pi(i\nu_n \rightarrow \omega + i0^+)}{\omega} \qquad (3.15)$$

where $i\nu_n \rightarrow \omega + i0^+$ refers to the analytical continuation from the imaginary Matsubara frequencies to the real frequency axis (Mahan 1990).

The Drude conductivity, expressed in equation (3.1), can be derived from the EM response function in the normal state for a system with elastic scattering. In the absence of pair correlations (i.e. the normal state), $\phi = 0$ and equation (3.10) for the paramagnetic response function reduces to

$$\Pi_{\mu\nu}(i\omega_n) = \frac{2e^2}{\Omega}T\sum_{\mathbf{k},m}\gamma_\mu(\mathbf{k})\gamma_\nu(\mathbf{k})G(\mathbf{k}, i\omega_m + i\nu_n)G(\mathbf{k}, i\omega_m) \qquad (3.16)$$

where, once again, we have approximated the vertex $\Gamma(\mathbf{k})$ with the unrenormalized vertex, $\gamma_{\mathbf{k}}$. Using the spectral representation of the Green's function,

$$G(\mathbf{k}, i\omega_n) = \int dz\frac{A(\mathbf{k}, z)}{i\omega_m - z} \qquad (3.17)$$

we get

$$\Pi^{(p)}_{\mu\nu}(i\nu_n) = -\frac{2e^2}{\Omega}T\sum_{\mathbf{k},m}\gamma_\mu(\mathbf{k})\gamma_\nu(\mathbf{k})\int d\omega\int d\omega'\frac{A(\mathbf{k},\omega)}{i\omega_m + i\nu_n - \omega}\frac{A(\mathbf{k},\omega')}{i\omega_m - \omega'} \qquad (3.18)$$

We must first perform the Matsubara sum before we can analytically continue $i\nu_n \rightarrow \omega + i\delta$. Following the general prescription (Mahan 1990)

$$\begin{aligned}\Pi_{\mu\nu}(i\nu_n \rightarrow \nu + i\delta) &= -\frac{2e^2}{\Omega}T\sum_{\mathbf{k}}\gamma_\mu(\mathbf{k})\gamma_\nu(\mathbf{k})\int d\omega\int d\omega' A(\mathbf{k},\omega)A(\mathbf{k},\omega') \\ &\times\left\{\frac{f(\omega)}{\omega-\nu-\omega'-i\delta}+\frac{f(\omega')}{\omega'+\nu-\omega+i\delta}\right\} \qquad (3.19)\end{aligned}$$

where $f(\omega)$ is the Fermi distribution function. Recall that

$$\frac{1}{x-i\delta} = P\frac{1}{x}+i\pi\delta(x) \qquad (3.20)$$

where P stands for the principal part. The real part of the optical conductivity becomes

$$\begin{aligned}\sigma_1(\nu) &= -\frac{\Pi''(\omega)}{\nu} \\ &= \frac{2e^2}{\nu\Omega}\pi\sum_{\mathbf{k}}\gamma_\mu(\mathbf{k})\gamma_\nu(\mathbf{k})\int d\omega\int d\omega' A(\mathbf{k},\omega)A(\mathbf{k},\omega')\delta(\omega-\nu-\omega')\left[f(\omega)-f(\omega')\right] \\ &= \frac{2e^2}{\nu\Omega}\pi\sum_{\mathbf{k}}\gamma_\mu(\mathbf{k})\gamma_\nu(\mathbf{k})\int d\omega A(\mathbf{k},\omega)A(\mathbf{k},\omega+\nu)\left[f(\omega)-f(\omega+\nu)\right]. \qquad (3.21)\end{aligned}$$

[Note that the diamagnetic response, $\Pi^{(d)}$ is purely real and can therefore be ignored in the $\sigma_1(\omega)$ calculation.]

At this point we will make an approximation and assume we are dealing with an isotropic Fermi sphere and an infinite band model. The sum over momentum can be replaced by an integral over energy in the standard way,

$$\frac{1}{\Omega}\sum_{\mathbf{k}} \rightarrow \int N(\epsilon)d\epsilon. \qquad (3.22)$$

For the free electron model in the presence of impurities, the spectral densities can be written as

$$A(\mathbf{k},\omega) = A(\epsilon,\omega) = \frac{1}{\pi}\frac{\Gamma/2}{(\omega-\epsilon)^2+[\Gamma/2]^2} \qquad (3.23)$$

where Γ is a frequency independent.

The conductivity equation is of the form

$$\sigma_1(\omega) = \frac{ne^2}{m\pi}\int_{-\infty}^{\infty}d\epsilon\int_{-\infty}^{\infty}dx\frac{f(x)-f(x+\hbar\omega)}{\omega}\frac{\Gamma/2}{(x-\epsilon)^2+[\Gamma/2]^2}\frac{\Gamma/2}{(x+\hbar\omega-\epsilon)^2+[\Gamma/2]^2} \qquad (3.24)$$

The two integrals can be done analytically using

$$\int_{-\infty}^{\infty} d\epsilon \frac{\Gamma/2}{(x-\epsilon)^2+[\Gamma/2]^2} \frac{\Gamma/2}{(x+\hbar\omega-\epsilon)^2+[\Gamma/2]^2} = \pi \frac{\Gamma}{(\hbar\omega)^2+\Gamma^2} \tag{3.25}$$

and

$$\int_{-\infty}^{\infty} dx \frac{f(x)-f(x+\hbar\omega)}{\omega} = \hbar \tag{3.26}$$

This immediately gives us the final result

$$\sigma_1(\omega) = \frac{ne^2}{m} \frac{\Gamma}{(\hbar\omega)^2+\Gamma^2} \tag{3.27}$$

which is nothing more than the simple Drude formula once we make the substitution $1/\tau = \Gamma$.

When $Im\ \Sigma(\omega)$ is frequency dependent, the integrations in equations (3.25) and (3.26) may not be easy to perform. The scattering rates become frequency dependent and the simple Drude form (3.27) then is not general enough to model this extra complication.

3.3 Normal State Conductivity

3.3.1 Numerical Results

The optical conductivity was calculated numerically using the results of the Eliashberg self-energy calculations described in chapter 2. The EM response function was calculated at frequencies on the imaginary Matsubara axis and later analytically continued to the real axis using the N-point Padé approximant technique (see appendix A). Care was taken not to artificially introduce temperature variations in the sum over Matsubara frequencies in equation (3.14). The cutoff was chosen to be approximately the same at $\omega_{cut} \approx 3W$ where W is the band width. Analytical continuation to the real frequency axis was done using different numbers of Matsubara frequencies and the results were shown to be stable.

Results for the normal state calculation at various temperatures are shown in figure (3.4). In this case, $B = 0.16$ and $\langle n \rangle = 0.4$. The strength of the electron-boson

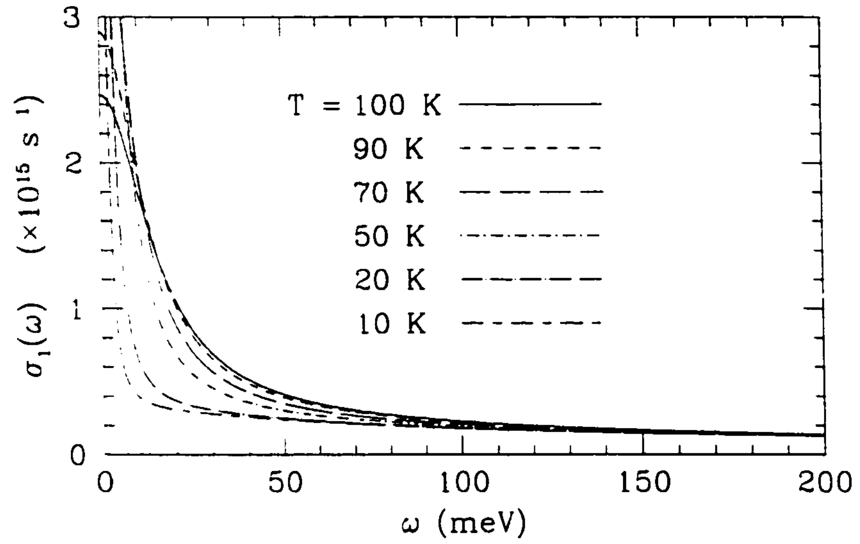

Figure 3.4: The real part of the optical conductivity, $\sigma_1(\omega)$, as a function of ω for various temperatures.

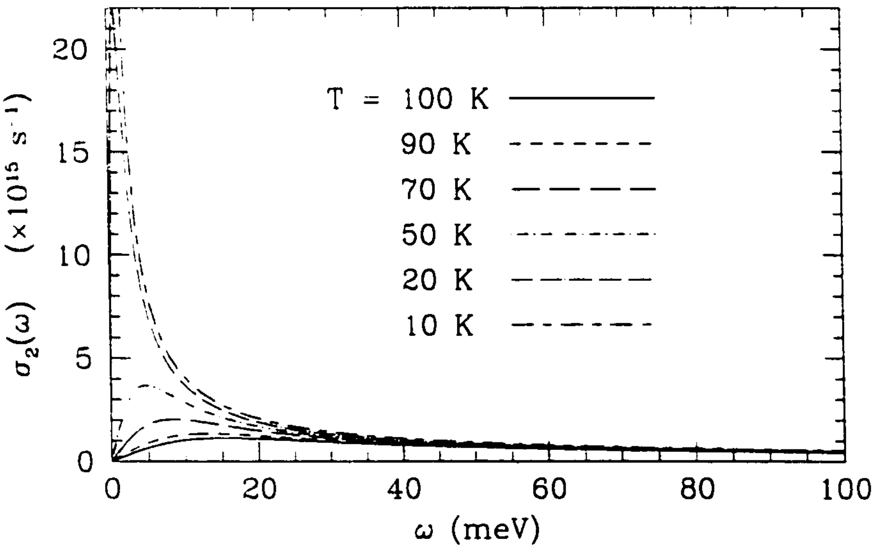

Figure 3.5: The imaginary part of the optical conductivity, $\sigma_2(\omega)$, as a function of ω for various temperatures.

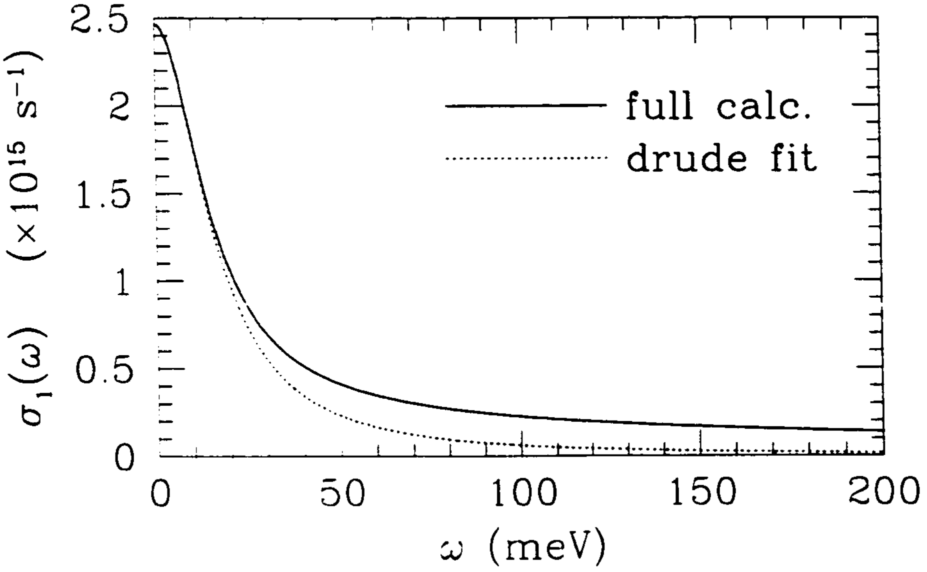

Figure 3.6: Conductivity at T = 100 K, and a Drude fit to low frequencies

coupling constant was set such that $T_c = 100$ K for the superconducting state. There is a low frequency Drude-like peak in the real part of the conductivity, $\sigma_1(\omega)$, which increases in height as the temperature is decreased. Accompanying the increased value of $\sigma_1(\omega = 0)$ is a decrease in the width of the peak.. This can be explained using the conductivity sum rule, equation (3.2). The plasma frequency, ω_p, is a temperature independent quantity, therefore the area under the $\sigma_1(\omega)$ curve must remain constant. If reducing the temperature causes the dc conductivity to increase, then spectral weight must be lost at higher frequencies.

Earlier we mentioned that the conductivity at $T = 0$ can be divided into two components: the impurity assisted component which leads to a Drude like conductivity and the Holstein absorption. At finite temperature the distinction between the two components is not at all clear. Temperature makes parts of the boson-assisted contribution appear Drude-like (Marsiglio and Carbotte 1995). Thermally excited bosons exist at finite temperature from which the electrons can scatter. This leads to a Drude-like component to appear in the optical frequency spectrum. At $T = 0$, the small ω peak narrows to the delta function at $\omega = 0$ that is expected for an electron system free of impurities.

The nearly constant background at high frequency is a result of the Holstein process discussed in the introduction. At low ω, this contribution exhibits a shoulder and goes to zero at $\omega = 0$. The spin fluctuation energy spectrum introduced in chapter 2 showed that even at small ω, there existed spectral weight for the spin fluctuations. Very low frequency excitations are therefore available and the Holstein process turns on at very small energy transfers. This is in marked difference to the phonon case which has a very small spectral weight at low ω. The threshold for Holstein absorption is therefore at a finite ω where the electron system has absorbed a large enough ω to create these phonons.

The imaginary part of the conductivity is shown in figure (3.5). As with the Drude conductivity discussed in the introduction, $\sigma_2(\omega)$, exhibits a peak at low frequencies. This peak occurs at frequencies where $\sigma_1(\omega)$ has fallen to half of the zero frequency value (i.e. where $\sigma_1(\omega) = \frac{1}{2}\sigma_1(\omega = 0)$). These frequencies can be associated with the size of the effective scattering rates which we will discuss in more detail later. The $\sigma_2(\omega)$ curves also saturate at higher frequency, going to a flat background of approximately the same size for all temperatures shown. This background is due to the inelastic scattering.

3.3.2 Extended Drude Analysis

It is clear that the Drude model will not suffice to explain the normal state conductivity curves. In figure (3.6) we show a Drude fit to the $T = 100$ K result for $\sigma_1(\omega)$ shown above. The real part of the Drude conductivity has only two free parameters, ω_p and τ, both of which are frequency independent. The fit was done using a nonlinear least squares algorithm so that the curves matched at low frequency. The Drude fit follows the full conductivity fairly closely at small ω to approximately the frequency at half height and then falls well below the full calculation. That the peak width is greater than the Drude width is consistent with experimental results on the cuprate materials (Arfi 1992). At higher frequencies, the Drude has fallen to almost zero, while a significant amount of weight is still seen for the interacting system. We know from the last chapter that the inelastic scattering from bosons leads to a frequency dependent scattering rate. As this scattering is reflected in the optical conductivity data, the Drude model with its ω independent τ should not be expected to give the right fit.

A model commonly used by experimentalists to extract information from the conductivity data is the *extended Drude model* (Timusk and Tanner 1989; Startseva et al. 1997) which is very similar in form to the Drude model,

$$\sigma(\omega) = \frac{\omega_p^2}{4\pi} \frac{1}{1/\tau(\omega) - i\omega\frac{m^*(\omega)}{m_b}} \tag{3.28}$$

where $m^*(\omega)/m_b$ is the effective dynamic electron mass and $1/\tau(\omega)$ is the effective relaxation rate. Both m^*/m and $1/\tau$ are, in general, frequency dependent. The extended Drude model is a specific application of the memory function method used in phenomenological models of correlation functions (Arfi 1992; Forster 1975).

The functions $1/\tau(\omega)$ and $m^*(\omega)/m$ can be extracted from the complex conductivity using

$$\frac{1}{\tau(\omega)} = \frac{\omega_p^2}{4\pi} Re\left(\frac{1}{\sigma(\omega)}\right) = \frac{\omega_p^2}{4\pi} \frac{\sigma_1(\omega)}{\sigma_1^2(\omega) + \sigma_2^2(\omega)} \tag{3.29}$$

and

$$\frac{m^*(\omega)}{m} = -\frac{\omega_p^2}{4\pi\omega} Im\left(\frac{1}{\sigma(\omega)}\right) = \frac{\omega_p^2}{4\pi\omega} \frac{\sigma_2(\omega)}{\sigma_1^2(\omega) + \sigma_2^2(\omega)}. \tag{3.30}$$

The renormalized relaxation rate $1/\tau^*(\omega)$ is another quantity often used, being related to the above quantities in the following way:

$$\frac{1}{\tau^*(\omega)} = \frac{1/\tau(\omega)}{m^*(\omega)/m}. \tag{3.31}$$

From equations (3.29) and (3.30), it can be seen that (3.31) reduces to

$$\frac{1}{\tau^*(\omega)} = \frac{\omega\sigma_1(\omega)}{\sigma_2(\omega)}. \tag{3.32}$$

This function has the advantage that it is a direct comparison of the real and imaginary components of the conductivity. For $m^*(\omega)/m = 1$ and frequency independent scattering rates, it can be shown that equation (3.29) and (3.32) are identical.

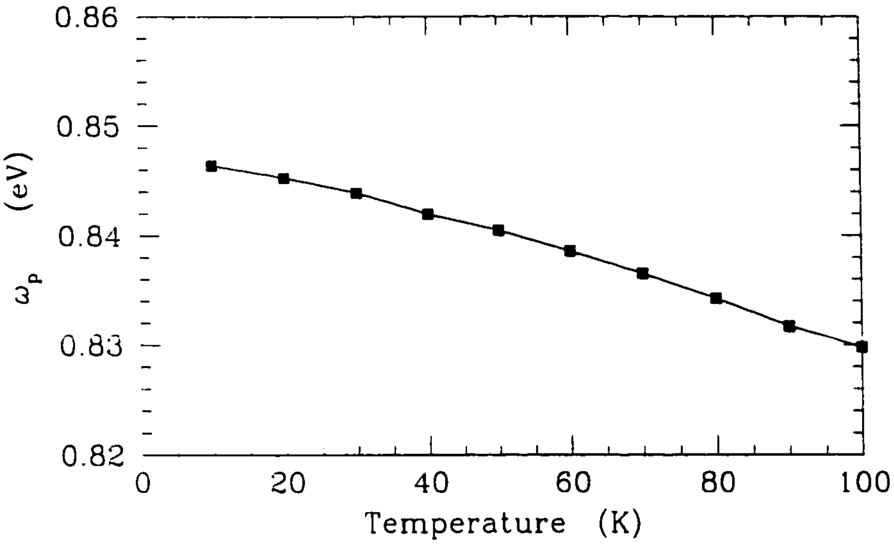

Figure 3.7: Plama frequency, ω_p, extracted using the partial sum rule, as a function of temperature, T, in the normal state.

Another constraint is needed to close the above set of equations, (3.29) and (3.30), since we have three unknowns, ω_p^2, $\tau(\omega)$, and $m^*(\omega)/m$, with only two knowns, $\sigma_1(\omega)$ and $\sigma_2(\omega)$. The conductivity sum rule, equation (3.2), can be used to determine ω_p independent of $\tau(\omega)$ and $m^*(\omega)/m$. Because the upper limit of integration is ∞, we will actually define ω_p through a partial sum rule (Puchkov et al. 1996),

$$\int_0^{\omega_{cut}} \sigma_1(\omega)\, d\omega = \frac{\omega_p^2}{8} \tag{3.33}$$

for numerical reasons. An upper cutoff of $\omega_{cut} = 1$ eV was used for all calculations in this chapter. In figure (3.7) we show ω_p as a function of temperature, where the plasma frequency has been extracted from $\sigma_1(T, \omega)$ using (3.33). The effective plasma frequency is not temperature independent decreasing in value as a function of increasing T. At $T = 10$ K, $\omega_p \sim 0.846$ eV while at $T = 100$ K, $\omega_p \sim 0.83$ eV. This represents a 1.9 % temperature variation from the $T = 10$ K value.

In figure (3.8) we show the effective relaxation rate, $1/\tau(\omega)$, as a function of frequency in the normal state for a set of temperatures, $T = 100$ K (solid line), 90 K (short dashed line), 70 K (long dashed line), 50 K (short dash-dotted), 20 K

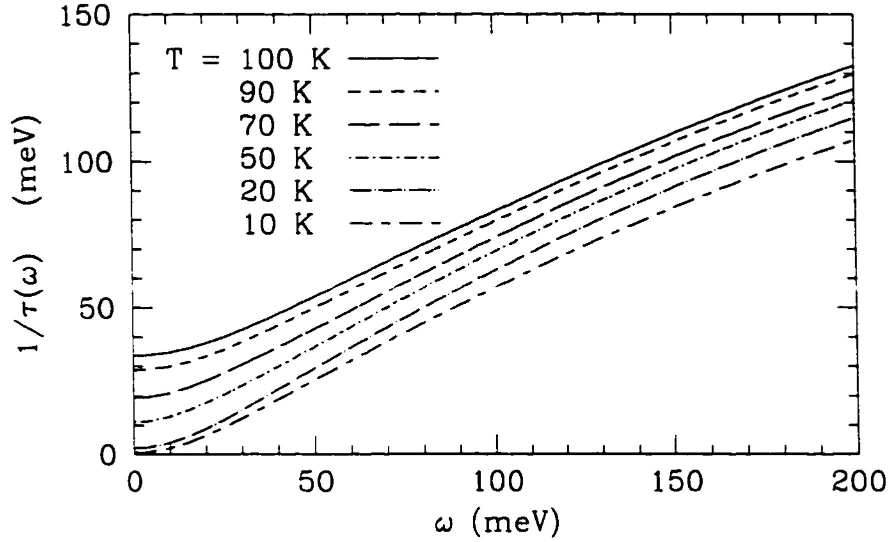

Figure 3.8: Optical scattering rate, $1/\tau(\omega)$, as a function of ω for various temperatures in the normal state.

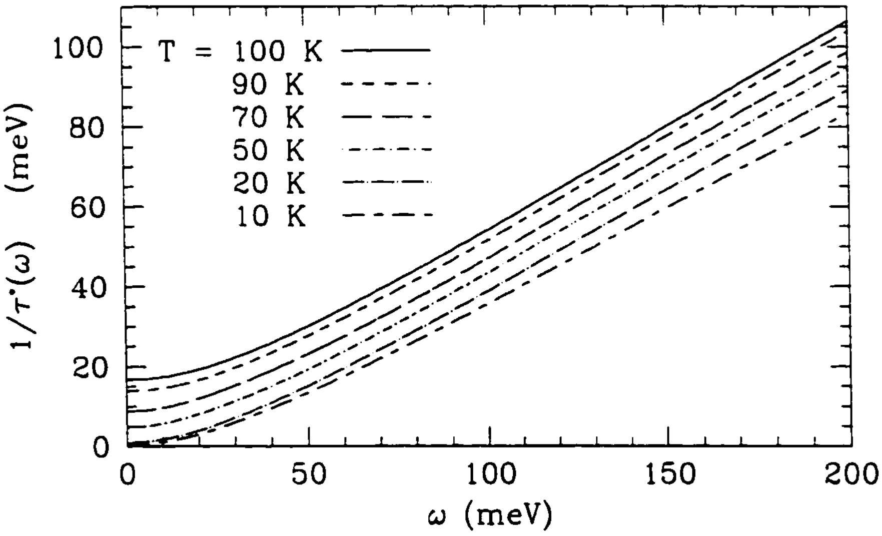

Figure 3.9: *Renormalizedopticalscatteringrate*, $1/\tau^*(\omega)$, as a function of ω for various temperatures in the normal state.

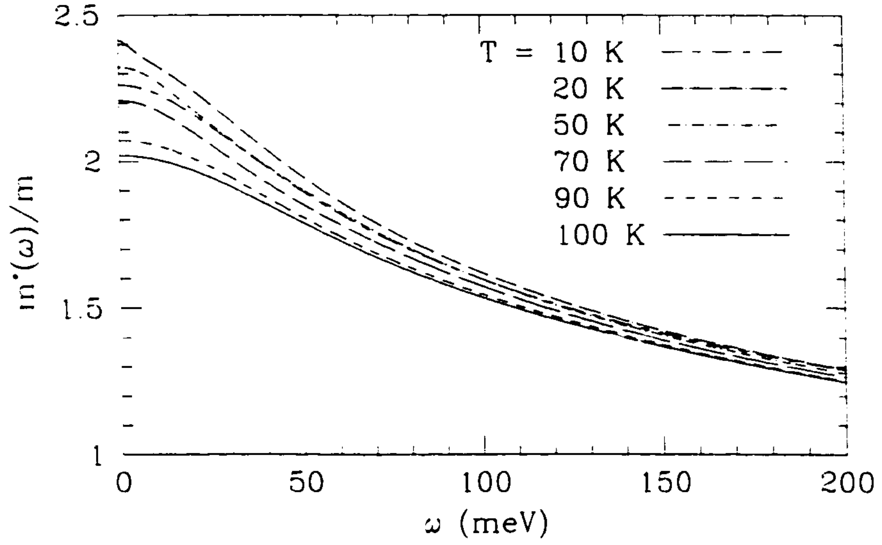

Figure 3.10: Optical mass renormalization, $m^*(\omega)/m$, as a function of ω for various temperatures in the normal state.

(long dash-dotted) and 10 K (long dash - short dash). At higher frequencies, the scattering rate is quasi-linear. As the frequency is decreased, $1/\tau(\omega)$ crosses over to a power law behaviour, ω^α, with $\alpha \sim 2$. For all temperatures shown, the curves exhibit very similar frequency behaviour, however, the scattering rates are larger at bigger T across the entire frequency spectrum. As T is decreased , the $\omega = 0$ scattering rate approaches zero. No thermally excited bosons exist at $T = 0$, so in the absence of impurities, the $\omega = 0$ lifetime is infinite.

The renormalized scattering rates, $1/\tau^*(\omega)$, are shown in figure (3.9). These curves are linear in ω at higher frequencies. Recall that $1/\tau^*(\omega)$ is a ratio of $\sigma_1(\omega)$ and $\sigma_2(\omega)$ multiplied by the frequency, ω. In figures (3.4) and (3.5) we saw that at high frequencies, both $\sigma_1(\omega)$ and $\sigma_2(\omega)$ had nearly constant backgrounds. The ratio is therefore constant at all frequencies. The frequency dependence of $1/\tau^*(\omega)$ then comes completely from the ω factor itself. At low ω, $1/\tau^*(\omega)$ exhibits similar saturation behaviour as $1/\tau(\omega)$.

Notice the size difference between $1/\tau(\omega)$ and $1/\tau^*(\omega)$. For all temperatures, the effective relaxation rate, $1/\tau$, is more than twice the renormalized value, $1/\tau^*$ at

$\omega = 0$. At $\omega = 200$ meV, while the ratio is no longer $2:1$, $1/\tau(\omega)$ is still significantly different from $1/\tau^*(\omega)$. The ratio of the scattering rates is related to the optical mass enhancement factor, $m^*(\omega)/m$. In figure (3.10) we plot the frequency dependence of $m^*(\omega)/m$ at the same set of temperatures as above. The $\omega = 0$ value of $m^*(\omega)/m$ at $T = 100$ K is indeed larger than 2. As ω increases, $m^*(\omega)/m$ decreases, however, it still has considerable size at $\omega = 200$ meV, being ~ 1.25 reflecting the importance of inelastic scattering at these higher frequencies. There is a larger difference between the high and low temperature values of the mass renormalization at low ω than at large ω.

We saw in section (3.2) that for a system with impurity scattering only (i.e. no inelastic scattering), $1/\tau$ was equal to the amplitude of the fundamental quasiparticle scattering rates, $\Gamma = -2\ Im\ \Sigma$. The optical scattering rate can therefore be regarded as a reflection of $Im\ \Sigma(\omega)$ in the optical data, even for frequency dependent scattering rates. Similarly, the optical renormalization is assumed to be related to the dynamical mass renormalization parameter, $1 + \lambda(\omega)$, introduced in the last chapter. The question now is to determine how similar the optical scattering rates are to the quasiparticle scattering rate, $\Gamma_{\mathbf{k}}(\omega) = -2\ Im\ \Sigma_{\mathbf{k}}(\omega)$. There are two important effects which come into $1/\tau(\omega)$. The first is due to **k**-space anisotropy. If the quasiparticle scattering rates vary from point to point on the Fermi surface, then the optical scattering rate, $1/\tau(\omega)$, is expected to be some weighted average of this anisotropy. We will discuss this in more detail in a later section.

The second important process is valid even for isotropic systems. It is known that for ω independent scattering rates, Γ and $1/\tau$ are identical. As inelastic scattering effects are introduced, $1/\tau(\omega)$ and $\Gamma(\omega)$ begin to differ. In the strong coupling regime, the two scattering rates may look very different indeed (Dolgov, Maksimov, and Shulga 1991; Shulga et al. 1991).

In figure (3.11) we plot $1/\tau(\omega)$ and $1/\tau^*(\omega)$ for $T = 100$ K. For comparison, we also plot $\Gamma_{\mathbf{k}}(\omega) = -2Im\ \Sigma_{\mathbf{k}}(\omega)$ at the same temperature as the optical scattering rates for three points on the Fermi surface which intersect the lines $\theta = 0°$ (dashed-dotted), 22.5° (short dashed-dotted) and 45° (long dashed). At $\omega = 0$, the $1/\tau(\omega)$ and $\Gamma(\theta = 45°, \omega = 0)$ curves are almost identical. The quasiparticle scattering rate is

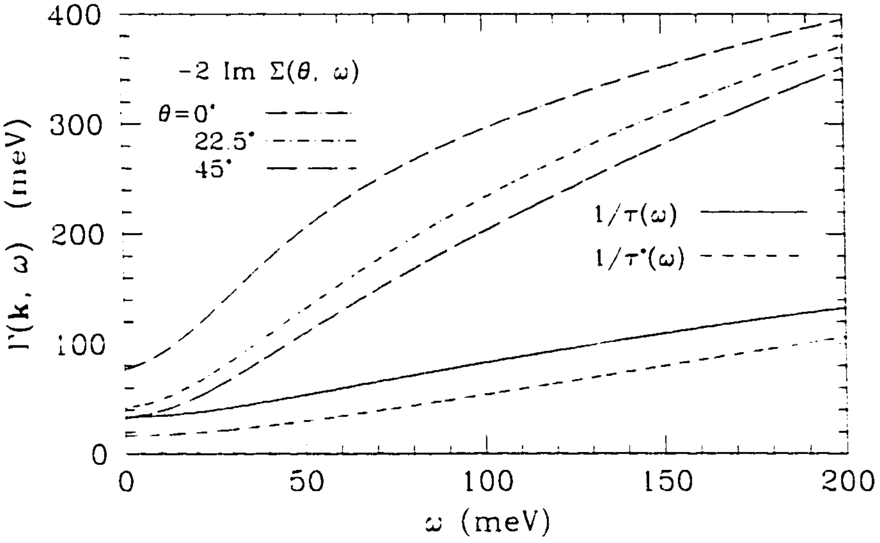

Figure 3.11: Comparison of optical and quasiparticle scattering rates.

a minimum on the Fermi surface at this point. For the other two angles, $1/\tau(\omega = 0)$ is smaller than $\Gamma(\theta, \omega)$. A factor of 2 exists between $\Gamma_{\mathbf{k}}(\omega = 0)$ and $1/\tau(\omega)$ in the case where $\theta = 0°$. At higher frequencies, the deviation is even more marked.

This result is not dependent of the form of the interaction or the **k**-space anisotropy. It is instead a general feature of strong coupling. Similar results have been found for an isotropic model using an $\alpha^2 F(\omega)$ approach in the electron-phonon model (Dolgov, Maksimov, and Shulga 1991; Shulga et al. 1991). One main difference with our work, however, is that at large ω there is significant difference between the optical scattering rates and $\Gamma(\omega)$. Dolgov and co-workers found that for electron-phonon coupling, $1/\tau(\omega)$ was approximately the same size as $\Gamma(\omega)$ at small ω and large ω. In their model, the $\alpha^2 F(\omega)$ is zero above 80 meV therefore $\Gamma(\omega)$ saturated and became constant for frequencies above this threshold frequency. There was, however, significant deviations between the optical and quasiparticle scattering rates in the energy range for which $\alpha^2 F(\omega)$ had significant weight. In our model, the boson spectral density has significant weight even at large ω and the scattering rate does not saturate (Grimvall 1980).

The amount of optical spectral weight, or oscillator strength, in the Drude peak

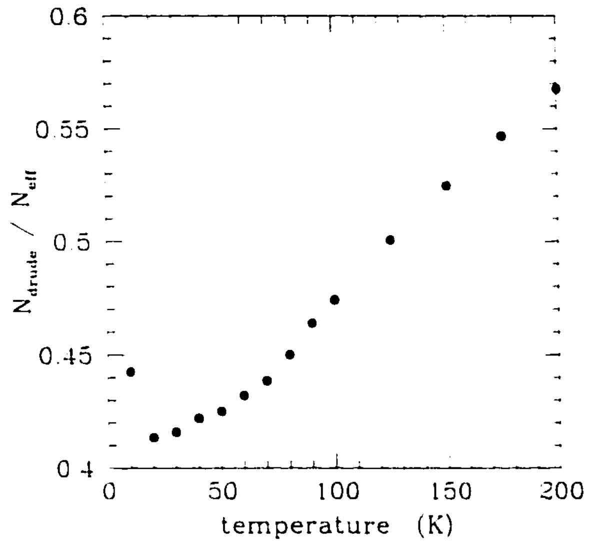

Figure 3.12: N_{Drude} / N_{eff} at a filling of $\langle n \rangle = 0.4$ at various temperatures in the normal state.

compared to the overall oscillator strength is given by the ratio N_{Drude}/N_{eff} where N_{Drude} is the effective carrier density contributing to the Drude peak in $\sigma_1(\omega)$. N_{eff} comes from defining an effective carrier density using the partial sum rule (Puchkov et al. 1996)

$$N_{eff} = \frac{2m}{\pi e^2} \int_0^{\omega_{cut}} \sigma_1(\omega)\, d\omega. \tag{3.34}$$

Drude fits to the low frequency $\sigma_1(\omega)$ were made and the effective carrier density ratios were calculated, shown in figure (3.12), as a function of temperature. Above $T = 100$ K, the ratio is quasi-linear in T. Below this temperature, the curve crosses over to a power low T^α, $\alpha > 1$. The ratio appears to be saturating at small temperature, but more accurate calculations at lower temperatures are necessary in order to see if there is a limiting value at $T = 0$ or not.

At $T = 100$ K, the fraction of oscillator strength in the Drude component is 0.47. Experiment indicates that our value underestimates the strength of the inelastic scattering at high temperatures by a factor of 2. This could be easily rectified by changing the boson spectral density, however, it must be remembered that in the

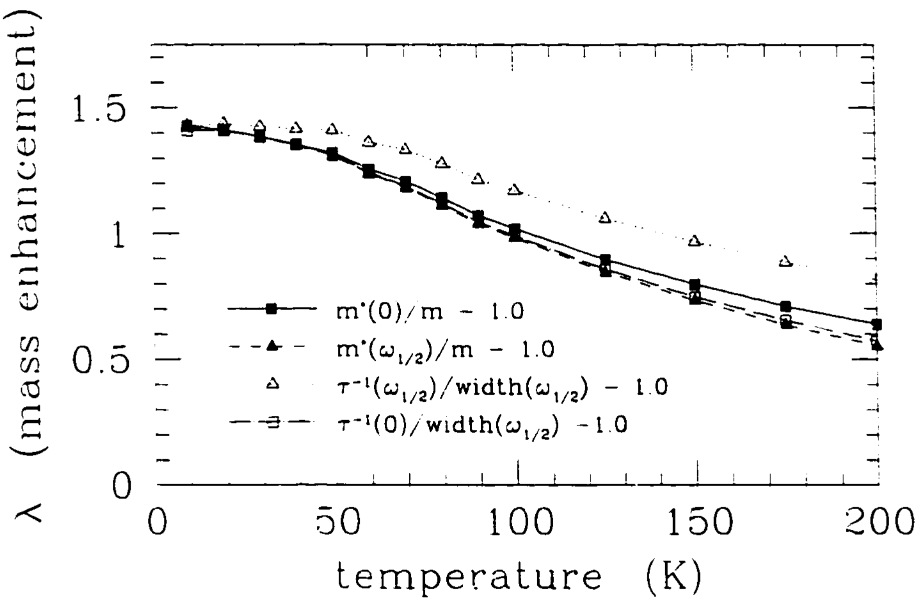

Figure 3.13: Mass enhancement factor, λ, extracted from the normal state optical conductivity as a function of temperature.

mid-infrared, part of the observed spectrum could come from interband transitions.

3.3.3 Effective Mass Renormalization Factor

The optical effective mass can easily be extracted from the complex conductivity using equation (3.30). A mass renormalization parameter, λ, is defined and related to the zero frequency value of the optical mass by

$$\frac{m^*(\omega = 0)}{m} = 1 + \lambda. \tag{3.35}$$

In figure (3.13), we plot as a function of temperature, the mass renormalization factor extracted from the normal state conductivity calculations four different ways. Values for λ extracted using equation (3.35) are denoted by the solid squares. Since this factor may not be directly measurable at $\omega = 0$, we extract an effective λ three other ways. If we use a simple extended Drude model where we set $\frac{m^*(\omega)}{m} = 1 + \lambda$ for any frequency, then the normal state conductivity at half-height is given by the relation $\omega_{1/2} = 1/\tau^*$ where $\omega_{1/2}$ is the width at half-height. Values of $\lambda = m^*(\omega_{1/2})/m - 1$

are denoted by the solid triangles. Using the relation in equation (3.31), we also plot $\tau^{-1}(\omega_{1/2})/\omega_{1/2} - 1$ [open triangles] and $\tau^{-1}(0)/\omega_{1/2} - 1$ [open squares].

At $T = 100$ K, the effective mass enhancement factor has a value of approximately 1. As the temperature is lowered, λ increases in value appearing to level off at low temperatures to a value of approximately 1.43. As the temperature is increase from $T = 100$ K, λ decreases falling to ~ 0.65 at $T = 200$ K. As can be seen from the figure, λ varies strongly with temperature. This calculation clearly shows that for a strongly-coupled system the extracted values of λ from the optical data should be not directly associated with *Re* $Z(0)$ or the results will be misleading.

A value for the optical mass enhancement factor can also be extracted from the temperature dependence of $1/\tau(0)$. For a simple isotropic model in which all the details are hidden in $\alpha^2F(\omega)$, the optical scattering rate is given by (Shulga et al. 1991)

$$\begin{aligned}\frac{1}{\tau(T,\omega)} &= \frac{2\pi}{\omega}\int d\omega'\alpha^2F(\omega')\left[\omega\coth\left(\frac{\beta\omega'}{2}\right) - (\omega+\omega')\coth\left(\frac{\beta(\omega+\omega')}{2}\right)\right. \\ &\qquad \left. +(\omega-\omega')\coth\left(\frac{\beta(\omega-\omega')}{2}\right)\right]. \qquad (3.36)\end{aligned}$$

In the high temperature limit where $T > \omega_D$ (ω_D being the characteristic frequency cutoff in $\alpha^2F(\omega)$) equation (3.36) reduces to a rather simple form at $\omega = 0$,

$$\frac{1}{\tau(T,\omega=0)} = 2\pi\lambda T, T > \omega_D \qquad (3.37)$$

where

$$\lambda = 2\int_0^\infty \frac{\alpha^2F(\omega)}{\omega}d\omega. \qquad (3.38)$$

Equation (3.37) is a well known result from transport theory (Grimvall 1980; Wilkins 1980) which predicts a linear T dependence to $1/\tau(0)$ and, therefore, to the resistivity, $\rho(T) = 1/\sigma_1(T,\omega=0) \propto 1/\tau(\omega)$, in the high temperature limit. By taking the derivative of both sides of (3.37) the mass enhancement factor is found to be

$$\lambda = \frac{1}{2\pi}\frac{\partial\frac{1}{\tau(\omega)}}{\partial T}. \qquad (3.39)$$

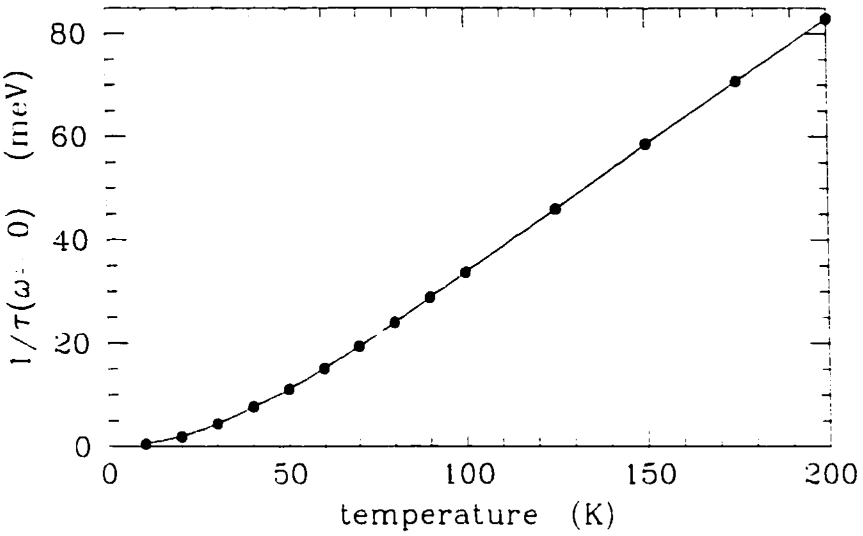

Figure 3.14: DC scattering rate, $1/\tau(\omega = 0)$, as a function of temperature, T.

The spin fluctuation model is known to lead to quasi-linear resistivity in the normal state at higher temperatures (Monthoux and Pines 1993). In figure (3.14) we plot $1/\tau(T, \omega = 0)$ as a function of T. Above $T = 100$ K, $1/\tau(0)$ is seen to be linear. Using equation (3.39), this gives a λ of ~ 0.92, which underestimates the actual size of the mass renormalizations in chapter 2.

The reason for the small effective value of λ observed in the resistivity is due to the large energy scale over which the boson spectral density extends. Only a small part the total effective $g^2\chi(\omega)$ is thermally activated, and therefore, the scattering is only described by a very small λ value. The nearly constant value for high ω contribution of the spectral density is what gives the quasi-linear T dependence to $\rho(T)$.

The linear temperature dependence of the resistivity in metals at higher temperatures is due to the thermal saturation of the $\alpha^2F(\omega)$. In systems such as ours where the cut off frequency is very large, $\omega_{cut} = 400$ meV, the temperature regime in which equation (3.37) is valid is ≥ 4600 K! While the definition can be made, the extracted λ will not be the actually mass enhancement factor of the quasiparticle system.

We have used a pairing interaction which is T independent. For a more realistic model, the parameters would be functions of T. Pines and co-workers have performed calculations using a T-dependent model and have found slopes more consistent with experiment. In this thesis, however, we are not interested in quantitatively fitting theoretical results to experiment. For our purposes, it has been enough to show that in a strongly-coupled interaction with boson spectral densities with large weight at high ω, the λ extracted from resistivity data using the general prescription (3.39) can lead to a value of λ which underestimates the actual strength of the electron-boson coupling.

3.3.4 Band Structure Effects

In chapter 2 we saw that the underlying density of states had a significant effect on the critical temperature. For the band structure with $B = 0.16$ the change in T_c is mostly attributable to the electronic density of states on the Fermi surface. The largest T_c occurred for a filling at which the Fermi energy, ε_f, and the van Hove energy, ε_{vH}, coincided. In this section we investigate the effect of the density of states and electron filling on the normal state conductivity.

In figure (3.15), the real part of the conductivity is shown for a series of electron densities, $\langle n \rangle = 0.3$ (solid line), 0.35 (short dashed line), 0.4 (long dashed line), 0.45 (short dashed-dotted), and 0.5 (long dashed-dotted). The calculations were done at a temperature of 20 K. The dc conductivity, $\sigma_1(0)$, is seen to decrease as the electron density is increased. There is a factor of 9 difference between the value of $\sigma_1(0)$ at $\langle n \rangle = 0.3$ and $\langle n \rangle = 0.5$. Accompanying the decreasing $\sigma_1(0)$ is an increase in the width of the $\sigma_1(\omega)$ peak indicating an increasing scattering rate.

It must be stressed that the only parameter being varied in this set of calculations is the electron density. The electron-boson coupling strength remains the same in all cases. That the conductivity is a decreasing function of filling throughout the range investigated is intriguing. The maximum critical temperature, as seen in chapter 2, occurs at $\langle n \rangle \sim 0.42$, the filling at which the Fermi energy corresponds the energy at which the van Hove singularity lies. At this value of filling the density of states on the Fermi surface, $N(0)$, is maximum. By looking at the simplified Drude conductivity, one might naively expect that the conductivity maximum would correspond directly

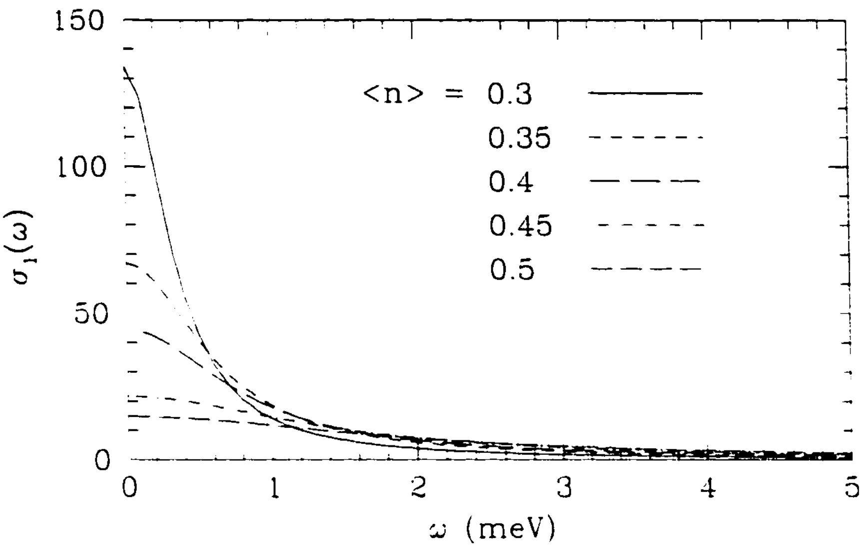

Figure 3.15: Real part of the conductivity, $\sigma_1(\omega)$, as a function of ω for various electron densities, $\langle n\rangle$, at $T = 20$ K.

to the $\langle n\rangle$ with the largest $N(0)$,

$$\sigma_{dc}(\omega) = \frac{\omega_p^2}{4\pi}\tau(0) = \frac{4\pi e^2 N(0) v_f^2}{3\Omega}\tau(0) \tag{3.40}$$

where v_f is the Fermi velocity.

The area under $\sigma_1(\omega)$ does not have to be conserved as a function of electron density. For a free electron gas, $\omega_p^2 = \frac{4\pi e^2\langle n\rangle}{m}$. In figure (3.16) we show ω_p^2 as a function of $\langle n\rangle$ calculated using the partial sum rule. Although ω_p^2 is monotonically increasing function of $\langle n\rangle$, it is clear that it is not varying linearly. Starting from $\langle n\rangle = 0.3$ the slope of the curve decreases with increasing density until near $\langle n\rangle \sim 0.4$, where the van Hove coincides with the Fermi energy. For $\langle n\rangle$ above this value, the slope begins increasing again until at least $\langle n\rangle = 0.5$.

Figure (3.16) initially appears to be in contradiction to the plot of $\sigma_1(\omega)$ [figure (3.15)]. The plasma frequency is smallest for $\langle n\rangle = 0.3$ while the conductivity the largest. Similarly, $\langle n\rangle = 0.5$ has the largest value of ω_p and the smallest dc conductivity. The problem is resolved by having scattering rates which vary enough with

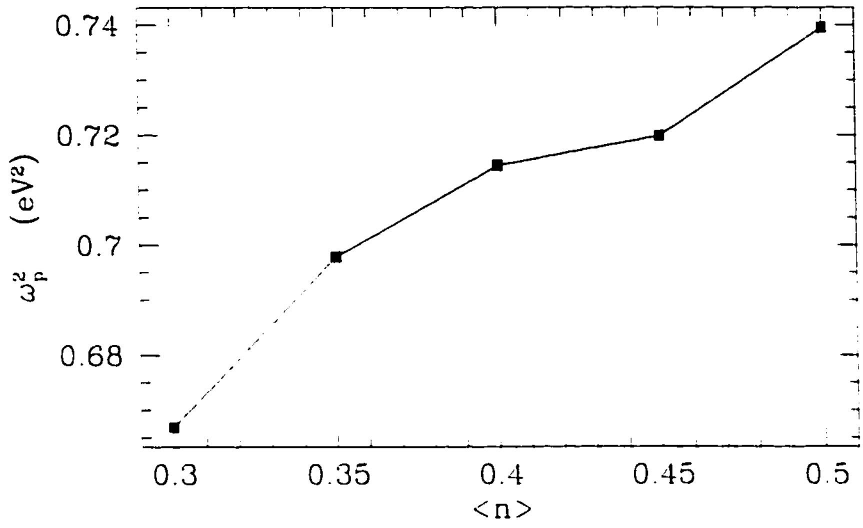

Figure 3.16: The plasma frequency, ω_p^2, as a function of electron density, $\langle n \rangle$.

$\langle n \rangle$ to overcome the increased ω_p^2. A plot of $1/\tau(\omega)$ as a function of ω for the set of electron densities is given in figure (3.17) showing that the scattering rate is smallest for $\langle n \rangle = 0.3$ and largest for $\langle n \rangle = 0.5$.

Due to the large **k** and ω anisotropy of the pairing interaction, the electrons near the Fermi surface which participate in the conductivity experience different internal scattering rates. As the filling increases, the shape of the Fermi surface allows for larger scattering rates in certain regions. In figure (3.18) we show the Fermi surface for the interacting system at $\langle n \rangle = 0.3$ (dashed dotted), 0.4 (dashed), and 0.5 (solid). The magnetic Brillouin zone, denoted by the dotted line is also shown. Points on the Fermi surface which intersect the magnetic Brillouin zone are spanned by the vector $(\pm\pi, \pm\pi)$ and experience nesting. The Fermi surface for $\langle n \rangle = 0.3$ is the furthest away from the nesting condition leading the smallest quasiparticle scattering rates on the Fermi surface. As the electron density is increased, two things happen. First, the electronic density of states on the Fermi surface, $N(0)$, increases which acts to increase the conductivity. However, the Fermi surface also moves closer to the magnetic Brillouin zone and the quasiparticle scattering on the Fermi surface is increased which acts to decrease the conductivity despite the larger number states on

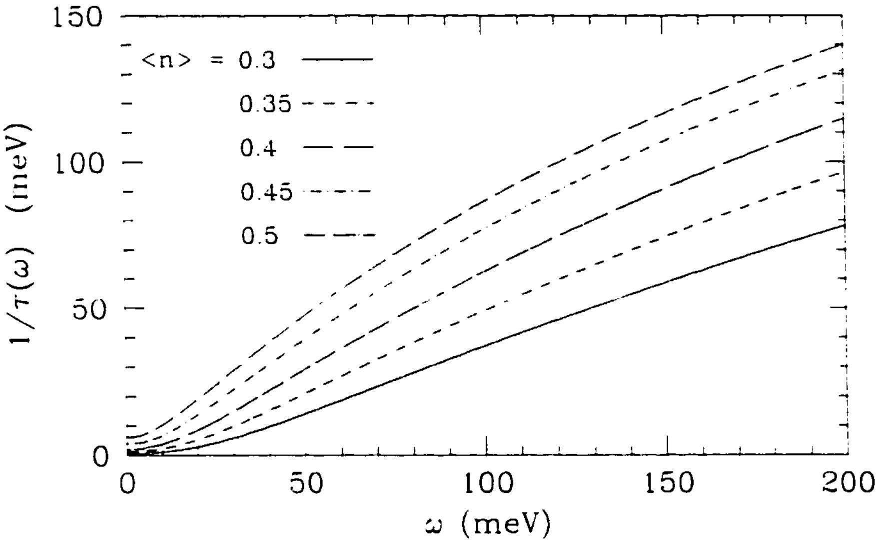

Figure 3.17: Optical scattering rate, $1/\tau(\omega)$, as a function of ω for various fillings, $\langle n\rangle$.

the Fermi surface. Since $\sigma_1(0)$ is reduced, the increased scattering rate must be the dominating factor.

Decreasing dc conductivities for fillings above $\langle n\rangle = 0.4$ are easy to understand since ε_f has moved above ε_{vH} and increased filling leads to a decrease in $N(0)$. Also, increased filling moves the Fermi surface closer to the nesting condition and the scattering rate is increased.

The increase in ω_p, on the other hand, is not as easy to see, however, the explanation once again lies in the Fermi surface contour plot in figure (3.18). As the Fermi surface approaches the magnetic Brillouin zone, the electrons experience more inelastic scattering. This leads to an enhancement of the effective boson spectral density, and thus, leads to strong Holstein absorption in the conductivity. This argument is supported by figure (3.15) where the high frequency value of $\sigma_1(\omega)$ is seen to increase slightly as a function of filling. The area under the conductivity curve, and thus ω_p^2, is increased by a significant amount as the small increase in $\sigma_1(\omega)$ is integrated over a large energy range. We will return to this point in the next section where we

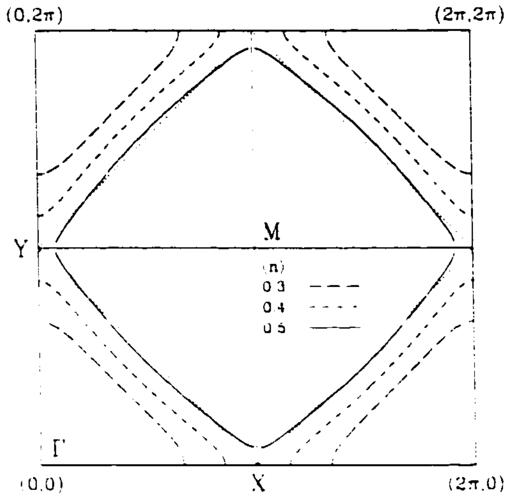

Figure 3.18: Quasiparticle Fermi surfaces as a function of electron density for $\langle n\rangle$ = 0.3 (dash-dotted line), 0.4 (dashed line), and 0.5 (solid line). The magnetic Brillouin zone is denoted by the dotted line .

introduce a simple model to extract the effective spectral densities, $g^2\chi(\omega)$ from the optical scattering rate.

In figure (3.19), we plot N_{Drude}/N_{eff} as a function of $\langle n\rangle$. The results indicate that inelastic scattering processes carry a larger amount of the spectral weight for $\langle n\rangle = 0.5$, where $N_{Drude}/N_{eff} \sim 0.32$. For $\langle n\rangle = 0.3$, which has the largest $\sigma_1(0)$, the ratio is 0.562. This result is consistent with the argument in the last paragraph.

3.3.5 Extraction of Boson Spectral Density

In this section we will use a simple theory to invert the calculated conductivity for an effective $\alpha^2F(\omega)$. The inversion process will be done using the optical scattering rate $1/\tau(\omega)$ extracted for the conductivity spectrum using the extended Drude model. The inversion process is based on an extension to the simple theory of Allen first introduced by Marsiglio and Carbotte (Allen 1971; Marsiglio and Carbotte 1997).

At zero temperature the frequency dependent scattering rate in an isotropic $\alpha^2F(\omega)$

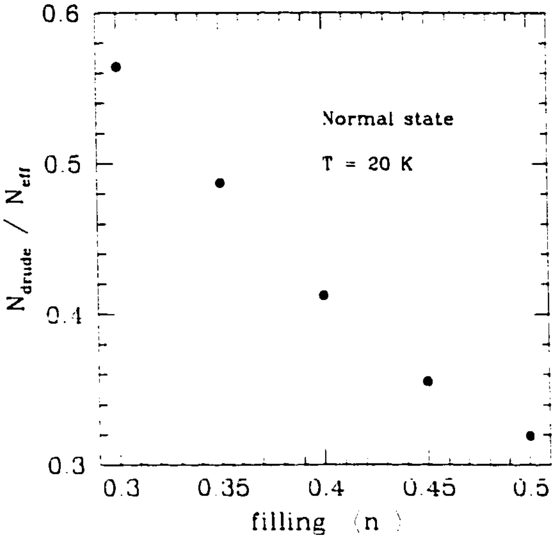

Figure 3.19: N_{drude} / N_{full} as a function of $\langle n\rangle$ at $T = 20$ K.

system described in equation (3.36) reduces to (Allen 1971)

$$\frac{1}{\tau(\omega)} = \frac{2\pi}{\omega}\int_0^{\omega} \alpha^2 F(z)(\omega - z)\, dz. \tag{3.41}$$

Inverting this for $\alpha^2F(\omega)$ gives

$$\alpha^2F(\omega) = \frac{1}{2\pi\omega}\frac{\partial}{\partial\omega}\left[\omega^2\frac{\partial}{\partial\omega}\frac{1}{\tau(\omega)}\right]. \tag{3.42}$$

Since $\alpha^2F(\omega)$ is usually used for the electron-phonon problem, we will introduce a generalized spectral density and change the left hand side of (3.42) to $g^2\chi_{eff}(\omega)$.

Equations (3.41) and (3.42) suggest that all information concerning the electron-boson interaction is included in the shape of the optical scattering rates. We first apply this model to the conductivity calculations presented in the last section and extract the effective spin fluctuation spectral densities as a function of $\langle n\rangle$. The results are plotted in figure (3.20).

All curves are consistent with $Im\ \chi(\omega)$ which we calculated in chapter 1, having an initial linear rise with low ω, followed by a $1/\omega$ high frequency tail. The main difference between the extracted $g^2\chi_{eff}(\omega)$ is the value at which the curves peak and

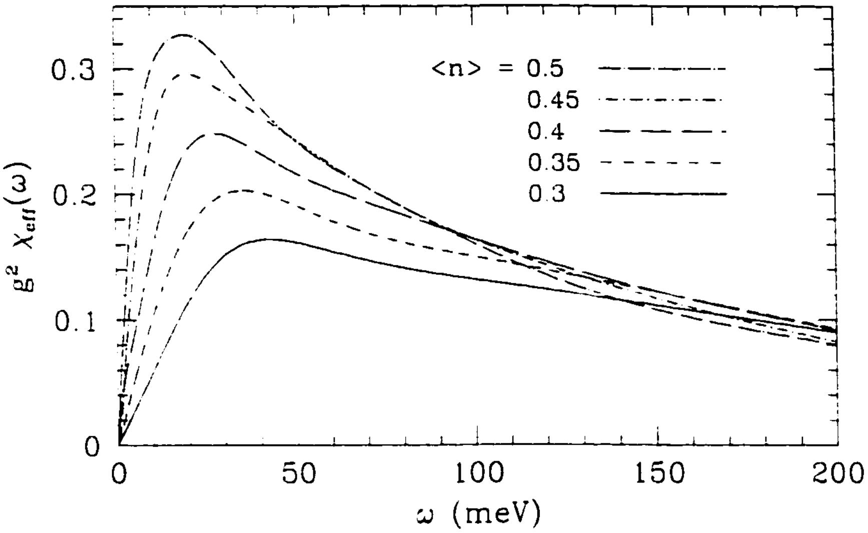

Figure 3.20: Effective spectral densities, $g^2\chi_{eff}(\omega)$, extracted from optical scattering rates for various fillings, $\langle n\rangle$, at $T = 20$ K.

the frequency at which the peaks are occur. In the case of $\langle n\rangle = 0.3$, the maximum height is half that for the $\langle n\rangle = 0.5$ curve. For larger electron densities, the electrons effectively feel a larger number of low frequency boson excitations. For smaller values of $\langle n\rangle$, the low frequency excitations are less important leading to smaller scattering rates and therefore, larger conductivities at small ω.

For conventional superconductors, all the details are hidden in $\alpha^2F(\omega)$. Once this function is known, in principle any thermodynamic or transport property can be calculated. A natural question to ask now is whether or not such an approximation could also be used in our strongly-coupled system. While the $g^2\chi_{eff}(\omega)$ might not be expected to be the actual electron-boson spectral density (if in fact there is one for the system), it might be hoped that all the essential features contained in the conductivity data would be hidden inside the extracted function. To investigate this point, we extracted the $g^2\chi_{eff}(\omega)$ from the 10 K conductivity calculation for $\langle n\rangle = 0.4$ using (3.42). The result of the inversion process for $g^2\chi_{eff}(\omega)$ is shown in figure (3.21).

The optical conductivity for an isotropic model is given by (Lee, Rainer, and

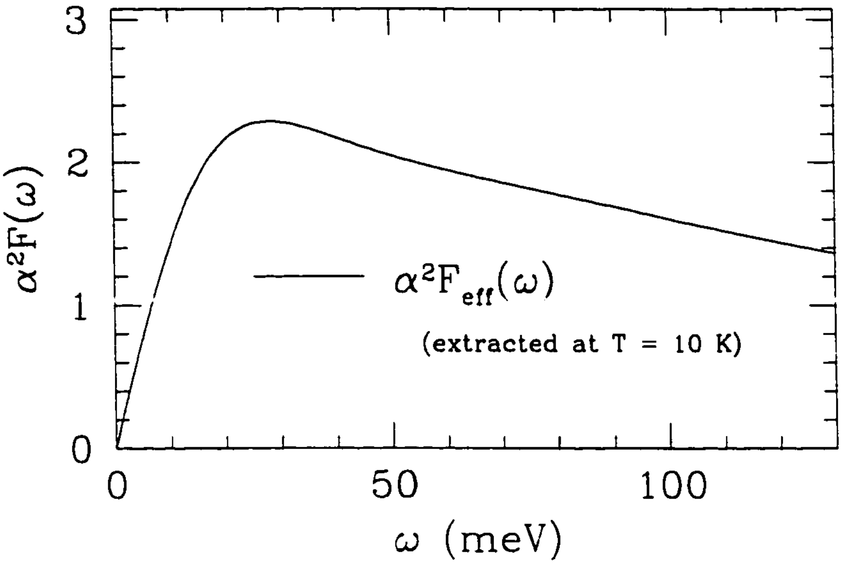

Figure 3.21: $\alpha^2F_{eff}(\omega)$ extracted from normal state optical conductivity at $10K$

Zimmermann 1989)

$$\begin{aligned}\sigma(\omega) &= \frac{\omega_p^2}{4\pi i\omega}\left\{\int_{-\infty}^{0} d\omega' \tanh\left(\frac{\omega+\omega'}{2T}\right) S^{-1}(\omega,\omega')\right. \\ &\left. + \int_{0}^{\infty} d\omega' \left[\tanh\left(\frac{\omega+\omega'}{2T}\right) - \tanh\left(\frac{\omega'}{2T}\right)\right] S^{-1}(\omega,\omega')\right\} \qquad (3.43)\end{aligned}$$

with

$$S(\omega,\omega') = \omega + \Sigma^*(\omega+\omega') - \Sigma(\omega') - i\gamma_{imp} \qquad (3.44)$$

where $\gamma_{imp} = \frac{1}{2\tau_{imp}}$. The self-energy can be written in terms of the spectral function

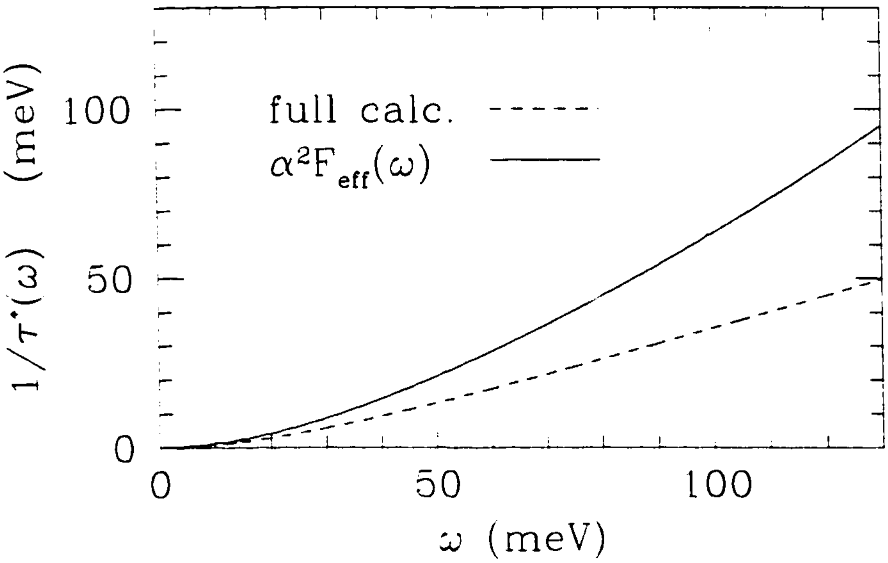

Figure 3.22: The renormalized scattering rate, $1/\tau^*(\omega)$, for the full and isotropic calculations

and temperature only.

$$
\begin{aligned}
Re\,\Sigma(T,\omega) &= -\int dz\,\alpha^2(a)F(z)\;Re\left[\psi\left(\frac{1}{2}+i\frac{\omega+z}{2\pi T}\right)\right.\\
&\qquad\left.-\psi\left(\frac{1}{2}+i\frac{\omega-z}{2\pi T}\right)\right] \qquad (3.45)
\end{aligned}
$$

$$
\begin{aligned}
Im\,\Sigma(T,\omega) &= -\frac{\pi}{2}\int dz\,\alpha^2(z)F(z)\left[2\coth\left(\frac{z}{2T}\right)\right.\\
&\qquad\left.-\tanh\left(\frac{\omega+z}{2T}\right)+\tanh\left(\frac{\omega-z}{2T}\right)\right] \qquad (3.46)
\end{aligned}
$$

where $\psi(z)$ is the logarithmic derivative of the gamma function (digamma function) (Abramowitz and Stegun 1972).

The effective boson spectral density extracted from the full conductivity calculation was used in equations (3.43) - (3.46) to calculate $\sigma(\omega)$ for the isotropic system. The $1/\tau(\omega)$ was extracted from this calculation using the extended Drude model. It was found that $1/\tau(\omega)$, and, therefore, $g^2\chi_{eff}(\omega)$, extracted from the isotropic calculation were identical to the original functions from the full calculation. A discrepancy between the isotropic calculation with the effective $g^2\chi(\omega)$ and the full calculation did arise, however. In figure (3.22) we show $1/\tau^*(\omega)$ for the two models. The solid line depicts the result of the isotropic calculation is larger than the full calculation. Since $1/\tau^*(\omega)$ is directly related to the ratio $\sigma_1(\omega)/\sigma_2(\omega)$, the result indicates a fundamental difference between the two models. The results are not related by a constant factor since the ratio of the isotropic model to the full calculation $\frac{1/\tau*_{iso}}{1/\tau^*_{full}}$ is ~ 1.75 at $\omega = 50$ meV and 1.9 at $\omega = 130$ meV. The discrepancy is due to a neglect of the k-space anisotropy and full dependence of the quasiparticle properties over the entire Brillouin zone.

3.3.6 k-space anisotropy

An important feature of the model presented in chapter 2 is the strong momentum anisotropy of the quasiparticle scattering rate, $\Gamma_{\mathbf{k}}(\omega) = -2Im\ \Sigma_{\mathbf{k}}(\omega)$, in the Brillouin zone. The effects of the momentum anisotropy must enter into the optical conductivity through some sort of weighted average since the in-plane frequency dependent conductivity in a tetragonal system is a scalar function of frequency. In this section we discuss the effect of **k**-space anisotropy of the underlying quasiparticle properties on the optical response. A similar investigation has recently been done using an analytical approach approximating the self-energy by second order Born scattering (Stojkovic and Pines 1997a; Stojkovic and Pines 1997b). The focus of the recent articles was on the difference between the *hot* and *cold* spots on the Fermi surface. Hot spots are defined as points on the Fermi surface which are intersected by the magnetic Brillouin zone satisfying the nesting condition. Cold spots are points on the Fermi surface way from these intersections. The model investigated in this section does not have any hot spots as the Fermi surface does not intersect the magnetic Brillouin zone. The full effects of a self-consistent self-energy are also included in the final results.

The EM response function, as defined by equation (3.14), has a momentum sum over the entire Brillouin zone. A partial conductivity, $\sigma(\mathbf{k}, \omega)$ can be defined for each

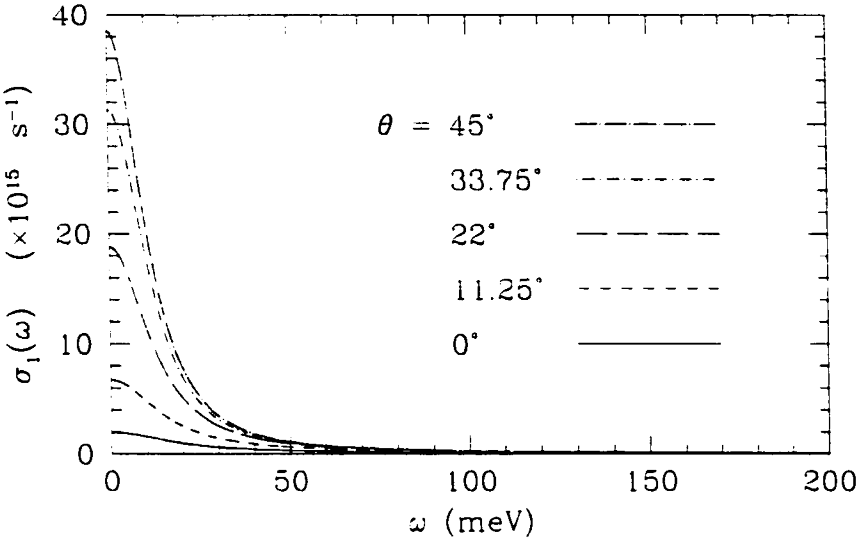

Figure 3.23: Real part of the **k**-dependent conductivity, $\sigma_{\mathbf{k},1}(\omega)$.

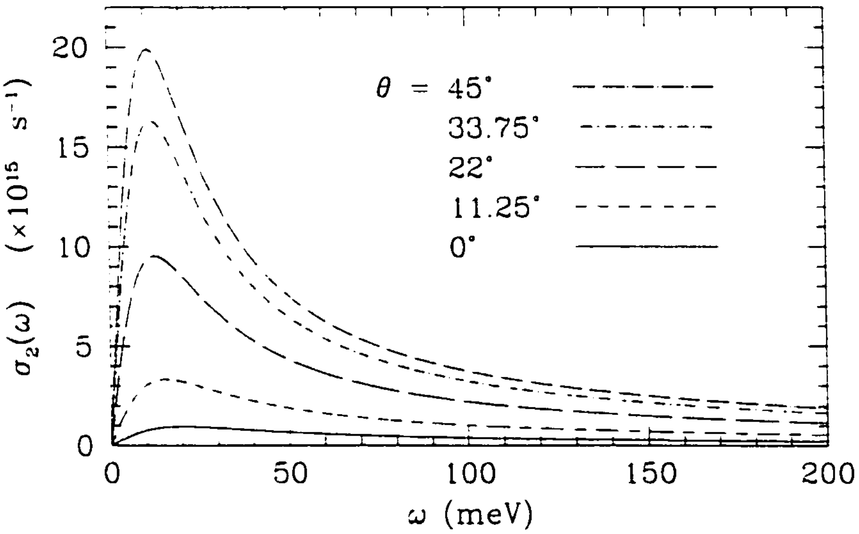

Figure 3.24: Imaginary part of the **k**-dependent conductivity, $\sigma_{\mathbf{k},2}(\omega)$.

point in the two-dimensional Brillouin zone such that

$$\sigma(\omega) = \frac{1}{\Omega}\sum_{\mathbf{k}} \sigma_{\mathbf{k}}(\omega) \tag{3.47}$$

where Ω is the number of **k**-points in the sum. The complex function $\sigma(\mathbf{k},\omega)$ is given by the analytical continuation of

$$\sigma(\mathbf{k},\omega) = i\frac{\Pi_{\mathbf{k}}(i\nu_n \rightarrow \omega + i\delta)}{\omega} \tag{3.48}$$

where $\Pi_{\mathbf{k}}(i\nu_n)$ is the local response function defined for each value of **k**. It is given by the same equation as (3.14), but without the sum over momentum (i.e. no $\Omega^{-1}\ \sum_{\mathbf{k}}$). Calculation of the normal state conductivity at $T = 100$ K was done solving $\Pi_{\mathbf{k}}(i\nu_n)$ at each **k** point, analytically continuing the results to the real frequency axis and then performing the momentum sum over values of $\sigma(\mathbf{k},\omega)$. No significant difference (i.e. ≤ 1 %) was found between the result of the conductivity calculation described above and the full calculation with all sums done before analytical continuation.

We plot the real and imaginary parts of the partial conductivity, $\sigma_1(\mathbf{k},\omega)$ and $\sigma_2(\mathbf{k},\omega)$, in figure (3.23) and (3.24) respectively for five points on the Fermi surface. Each point is labeled by an angle θ, where θ is measured from the $\overline{\Gamma X}$ line. The curve at $\theta = 45°$, therefore, is on the Fermi surface along the diagonal of the Brillouin zone while for $\theta = 0°$ the point is intersected by the line from $(0,0)$ to $(\pi,0)$. The conductivity is clearly much larger along the diagonal than along $\overline{\Gamma X}$ where there is an order of magnitude difference in $\sigma_1(\mathbf{k},\omega = 0)$ between the $\theta = 45°$ and 0° results. This is consistent with the idea that because the quasiparticle scattering rates are larger at the point along $\theta = 0°$, quasiparticles near this point contribute the least to the overall conductivity while those near $\theta = 45°$ on the Fermi surface where the scattering rates are smallest contribute the most.

In order to understand the results a little more, we apply the extended Drude analysis to the partial conductivity where the definition

$$\sigma_{\mathbf{k}}(T,\omega) \equiv \frac{\omega_p^2(\mathbf{k})}{4\pi}\frac{1}{\frac{1}{\tau_{\mathbf{k}}(\omega)} - i\omega\frac{m_{\mathbf{k}}^*(\omega)}{m_b}} \tag{3.49}$$

is used. The functions $1/\tau_{\mathbf{k}}(\omega)$ and $m_{\mathbf{k}}^*(\omega)/m$ are assumed to play the role of the local scattering rates and mass renormalization functions at each **k**-point. Similar to the extended Drude analysis of the full $\sigma(\omega)$, the functions $1/\tau_{\mathbf{k}}(\omega)$ and $m^*_{\mathbf{k}}(\omega)/m$ are given by

$$\frac{1}{\tau_{\mathbf{k}}(\omega)} = \frac{\omega_p^2(\mathbf{k})}{4\pi} \frac{\sigma_1(\mathbf{k},\omega)}{\sigma_1(\mathbf{k},\omega)^2 + \sigma_2(\mathbf{k},\omega)^2} \tag{3.50}$$

and

$$\frac{m^*_{\mathbf{k}}(\omega)}{m} = \frac{\omega_p^2(\mathbf{k})}{4\pi\omega} \frac{\sigma_2(\mathbf{k},\omega)}{\sigma_1(\mathbf{k},\omega)^2 + \sigma_2(\mathbf{k},\omega)^2}. \tag{3.51}$$

A local $\omega_p^2(\mathbf{k})$ was defined for each k-point through the function

$$\int_0^{\omega_{cut}} \sigma_1(\mathbf{k},\omega)\, d\omega = \frac{\omega_p^2(\mathbf{k})}{8} \tag{3.52}$$

motivated by the partial sum rule for the real plasma frequency. The relation between the full plasma frequency, ω_p, and the partial plasma frequency, $\omega_p(\mathbf{k})$, can be found using the partial sum rule

$$\frac{\omega_p^2}{8} = \int_0^{\omega_{cut}} \sigma_1(\omega)\, d\omega = \int_0^{\omega_{cut}} \frac{1}{\Omega} \sum_{\mathbf{k}} \sigma_1(\mathbf{k},\omega)\, d\omega. \tag{3.53}$$

After interchanging the order of interaction, we get

$$\frac{\omega_p^2}{8} = \frac{1}{\Omega} \sum_{\mathbf{k}} \int_0^{\omega_{cut}} \sigma_1(\mathbf{k},\omega)\, d\omega = \frac{1}{8\Omega} \sum_{\mathbf{k}} \omega_p^2(\mathbf{k}). \tag{3.54}$$

The square of the full plasma frequency, ω_p, is therefore given by the average value of $\omega_p^2(\mathbf{k})$ in the Brillouin zone.

Our numerical results for the $\mathbf{k}$ dependent scattering rates and the mass renormalization functions are shown in figure (3.25) and (3.26) for the same points on the Fermi surface as in figures (3.23) and (3.24). The results are consistent with the previous argument since $1/\tau_{\mathbf{k}}(\omega = 0)$ is largest for $\theta = 0°$ with a value of $\sim$ 22.2 meV and smallest for $\theta = 45°$ with a value of 10 meV. The largest zero frequency mass renormalization also occurs for $\theta = 0°$.

In figure (3.27) we plot $\omega_p(\mathbf{k})$ as a function of position on the Fermi surface. The value of the full plasma frequency is indicated by the dashed line. For $\theta = 0°$, $\omega_p(\mathbf{k}) \sim 0.6$ eV while for 45°, $\omega_p(\mathbf{k}) \sim 1.75$ eV. A large variation is clearly seen as

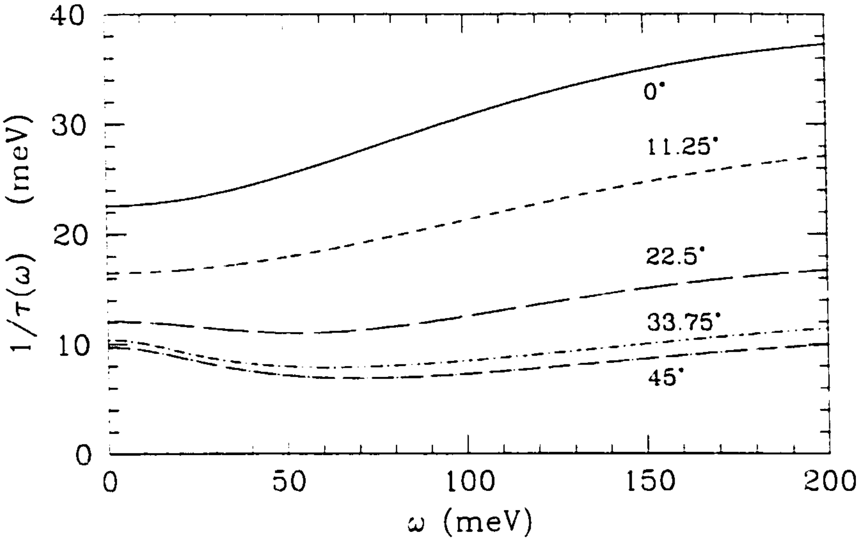

Figure 3.25: The **k**-dependent scattering rate, $1/\tau_{\mathbf{k}}(\omega)$, at various points on the Fermi surface.

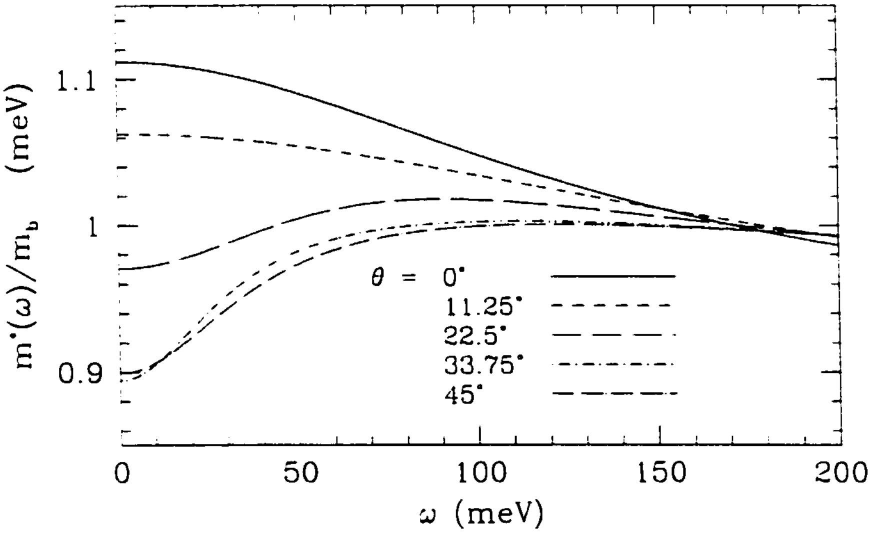

Figure 3.26: The **k**-dependent mass renormalization, $m^*_{\mathbf{k}}(\omega)/m_b$, at various points on the Fermi surface.

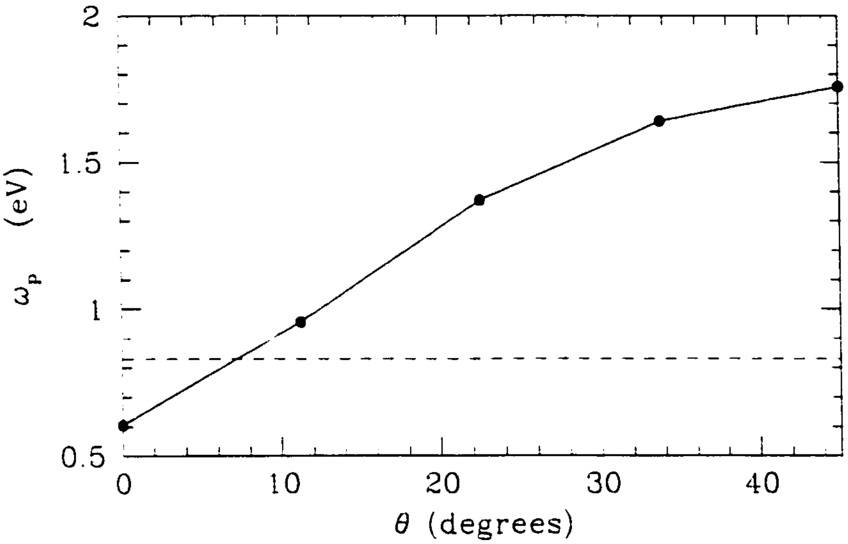

Figure 3.27: The **k**-dependent plasma frequency, $\omega_p(\mathbf{k},\omega)$, as a function of angle, θ, on the Fermi surface. The dotted line denotes the value of ω_p.

a function of position on the Fermi surface. The size of the local plasma frequency is indicative of the importance of the local quasiparticle contribution to the full conductivity at the respective **k**-points in the Brillouin zone. Figure (3.27) clearly shows that quasiparticles near the Fermi surface along the diagonal of the Brillouin zone contribute the most to the overall optical response.

The way the local values of the momentum dependent scattering rates and mass renormalizations come into the full conductivity is not trivial. To show this we write the total contribution to the full conductivity.

$$\sigma(\omega) = \frac{1}{N}\sum_{\mathbf{k}} \frac{\omega_{p\mathbf{k}}^2}{4\pi} \frac{\frac{1}{\tau_{\mathbf{k}}(\omega)} + i\omega\frac{m_{\mathbf{k}}^*(\omega)}{m_b}}{\left(\frac{1}{\tau_{\mathbf{k}}(\omega)}\right)^2 + \omega^2\left(\frac{m_{\mathbf{k}}^*(\omega)}{m_b}\right)^2}. \tag{3.55}$$

The real and imaginary part of the full conductivity can be separated out yielding

$$\sigma_1(\omega) = \frac{1}{N}\sum_{\mathbf{k}} \frac{\omega_{p\mathbf{k}}^2}{4\pi D_{\mathbf{k}}^2(\omega)} \frac{1}{\tau_{\mathbf{k}}(\omega)} \tag{3.56}$$

and

$$\sigma_2(\omega) = \frac{1}{N}\sum_{\mathbf{k}} \frac{\omega_{p\mathbf{k}}^2}{4\pi D_{\mathbf{k}}^2(\omega)} \omega \frac{m_{\mathbf{k}}^*(\omega)}{m_b} \tag{3.57}$$

respectively. The function $D^2_{\mathbf{k}}(\omega)$ is given by

$$D^2_{\mathbf{k}}(\omega) \equiv \left(\frac{1}{\tau_{\mathbf{k}}(\omega)}\right)^2 + \left(\frac{m^*_{\mathbf{k}}(\omega)}{m_b}\right)^2 . \tag{3.58}$$

If we define the weighted average of a general k-dependent function, $f_{\mathbf{k}}$, over the Brillouin zone by

$$\langle f_{\mathbf{k}}(\omega)\rangle \equiv \frac{1}{4\pi\Omega}\sum_{\mathbf{k}} \frac{\omega_p^2(\mathbf{k})}{D^2_{\mathbf{k}}(\omega)} f_{\mathbf{k}}(\omega), \tag{3.59}$$

then the real and imaginary parts of $\sigma(\omega)$ become

$$\sigma_1(\omega) = \left\langle \frac{1}{\tau_{\mathbf{k}}(\omega)} \right\rangle \tag{3.60}$$

and

$$\sigma_2(\omega) = \omega \left\langle \frac{m^*_{\mathbf{k}}(\omega)}{m} \right\rangle . \tag{3.61}$$

Using equations (3.60) and (3.61) to expand the extended Drude model for the full conductivity, we get

$$\begin{aligned} \frac{1}{\tau(\omega)} &= \frac{\omega_p^2}{4\pi} \frac{\sigma_1(\omega)}{\sigma_1^2(\omega) + \sigma_2^2(\omega)} \\ &= \frac{\omega_p^2}{4\pi} \frac{\left\langle \frac{1}{\tau_{\mathbf{k}}(\omega)} \right\rangle}{\left\langle \frac{1}{\tau_{\mathbf{k}}(\omega)} \right\rangle^2 + \omega^2 \left\langle \frac{m^*_{\mathbf{k}}(\omega)}{m} \right\rangle^2} \end{aligned} \tag{3.62}$$

and

$$\begin{aligned} \frac{m^*(\omega)}{m} &= \frac{\omega_p^2}{4\pi\omega} \frac{\sigma_2(\omega)}{\sigma_1^2(\omega) + \sigma_2^2(\omega)} \\ &= \frac{\omega_p^2}{4\pi} \frac{\left\langle \frac{m^*(\mathbf{k},\omega)}{m} \right\rangle}{\left\langle \frac{1}{\tau_{\mathbf{k}}(\omega)} \right\rangle^2 + \omega^2 \left\langle \frac{m^*_{\mathbf{k}}(\omega)}{m} \right\rangle^2} . \end{aligned} \tag{3.63}$$

Equations (3.63) and (3.62) indicate that the scattering rates and mass renormalization functions do not enter into the full conductivity as straight averages over the Brillouin zone or Fermi surface, but rather as a fairly complicated set of weighted averages. Even for $\omega = 0$, the functions are weighted averages with

$$\frac{1}{\tau(0)} = \frac{\omega_p^2}{4\pi} \frac{1}{\frac{1}{4\pi\Omega}\sum_{\mathbf{k}} \omega_p^2(\mathbf{k})\tau_{\mathbf{k}}(0)} \tag{3.64}$$

and

$$\frac{m^*(0)}{m} = \frac{\omega_p^2}{4\pi} \frac{\sum_{\mathbf{k}} \omega_p^2(\mathbf{k}) \frac{m_{\mathbf{k}}^*(0)}{m} \tau_{\mathbf{k}}^2(0)}{\sum_{\mathbf{k}} \omega_p^2(\mathbf{k}) \tau_{\mathbf{k}}(0)}. \tag{3.65}$$

3.4 Superconducting State

3.4.1 Numerical Results

In this section we present the results of conductivity calculations for the superconducting state. The model used had $\langle n \rangle = 0.4$ and $B = 0.16$, similar to the model in section (3.3.1) for the normal state calculations. In figure (3.28) we show the frequency dependence of $\sigma_1(\omega)$ as a function of ω for the temperatures $T = 100$ K (solid line), 90 K (short dashed), 70 K (long dashed), 50 K (short dashed-dotted), 20 K (long dashed-dotted), and 10 K(long dash-short dash). The $T = 100$ K curve is at T_c and is identical to the curve shown in figure (3.4) for the normal state results. As the temperature is reduced, the Drude-like peak begins to narrow as in the normal state, however, it narrows much more rapidly with decreasing temperature in the superconducting state. A dip, or suppression, in the low frequency part of the spectrum begins to appear at about 50 K continuing to deepen with decreasing temperature down to 10 K, the lowest temperature plotted. This low frequency suppression was not seen in the normal state where at $T = 10$ K, the inelastic background does not drop below 0.3×10^{15} s^{-1} at low ω. While the low ω spectrum for $\sigma_1(\omega)$ is suppressed in the superconducting state, there is no true absorption edge at finite frequency. Instead, there is a continuously decreasing spectrum down to $\omega = 0$. Because the d-wave order parameter has lines where the gap goes to zero which cross the Fermi surface, there are low lying states available for normal state excitations at small energies where single quasiparticles can be scattered leading to finite absorption below $2\Delta_{max}$. The shape of the conductivity spectrum in figure (3.28) in not unique to d-wave, however. Any gap symmetry which has nodes crossing the Fermi surface will yield similar results. The conductivity is only sensitive to the presence of nodes on the Fermi surface, not to the location of the nodes. Optical conductivity experiments

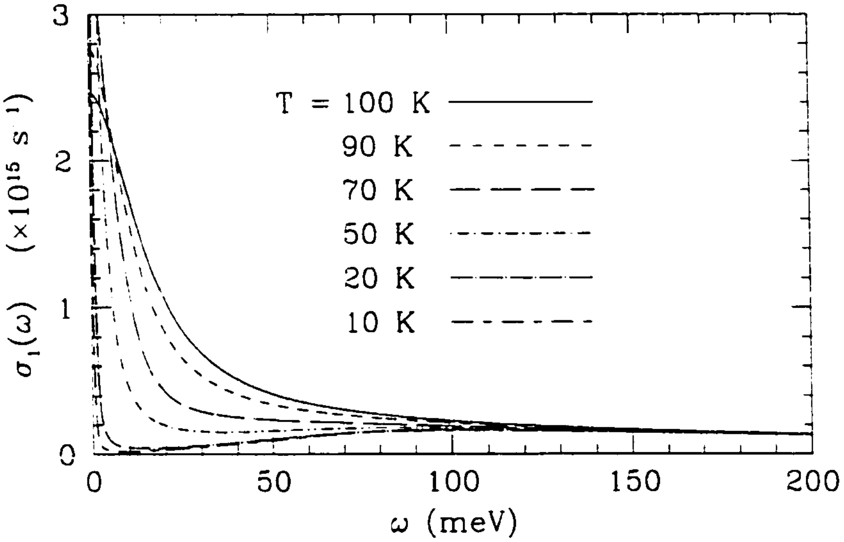

Figure 3.28: The real part of the optical conductivity, $\sigma_1(\omega)$, as a function of ω for various temperatures.

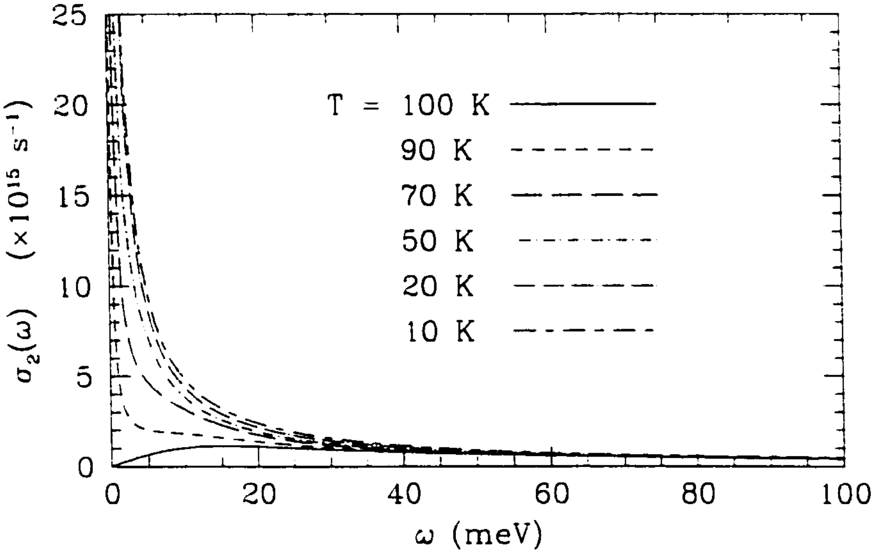

Figure 3.29: The imaginary part of the optical conductivity, $\sigma_2(\omega)$, as a function of ω for various temperatures.

alone, therefore, cannot uniquely identify the symmetry of the order parameter for non s-wave superconductors.

In figure (3.29) we plot the imaginary part of the conductivity, $\sigma_2(\omega)$. The normal state calculations discussed earlier showed that $\sigma_2(\omega)$ had a peak in the response at finite frequency for non-zero temperatures. In the superconducting state, $\sigma_2(\omega)$ goes to ∞ at $\omega = 0$. As the temperature is lowered below T_c, the width of this low frequency divergence increases. At higher frequencies, $\sigma_2(\omega)$ approaches the normal state result with a finite background to high frequencies due to inelastic scattering.

3.4.2 Scattering Rates

In figure (3.30) we show $1/\tau(\omega)$ extracted from the superconducting conductivity results using equation (3.29). At $T = T_c$, the scattering rate is finite for all frequencies. As T is decreased below T_c, the zero frequency limit of $1/\tau$ is zero. This can be seen in the $T = 90$ K curve where $1/\tau(\omega)$ is suppressed at low frequency going to zero at $\omega = 0$. At this temperature the superconducting gap is not fully formed and the effects of superconductivity are only clearly visible at the lowest frequencies. The scattering rate appears very similar to the normal state curves over most of the energy range, linear at high frequency crossing over to an ω^2 dependence at lower ω. However, at $\omega \sim 5$ meV the scattering rate drops sharply with decreasing frequency approaching the $\omega = 0$ limit of $1/\tau(0) = 0$ linearly. As the temperature is decreased even more, the suppression of the scattering rates increases. At $T = 10$ K, the lowest temperature calculated, there is an obvious suppression of the optical scattering rates below frequencies of 100 meV. There is no sharp threshold at finite frequency below which the scattering goes to zero. Instead, there is a continuous decrease in $1/\tau(\omega)$ down to $\omega = 0$ indicating the presence of low energy single particle excitations. The low temperature scattering rates in figure (3.30) should be compared to the results for $Im\ \Sigma_{\mathbf{k}}(\omega)$ at different points on the Fermi surface presented earlier in figure (2.15), since the imaginary part of the self-energy is related to the fundamental quasiparticle scattering rates, $\Gamma_{\mathbf{k}}(\omega) = 2\ Im\ \Sigma_{\mathbf{k}}(\omega)$. $\Gamma_{\mathbf{k}}(\omega)$ for a point on the Fermi surface along the diagonal of the Brillouin zone in the superconducting state was seen to be very

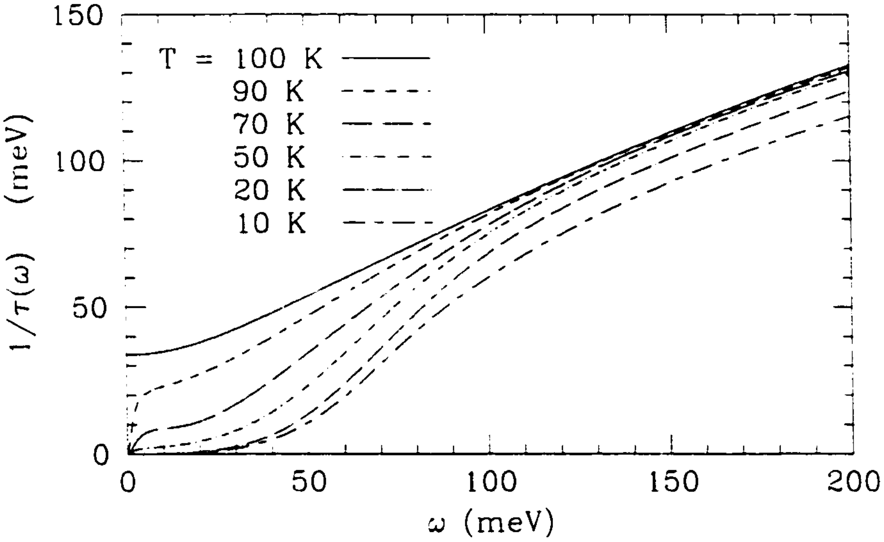

Figure 3.30: The optical scattering rate, $1/\tau(\omega)$, as a function of ω for various temperatures in the superconducting state.

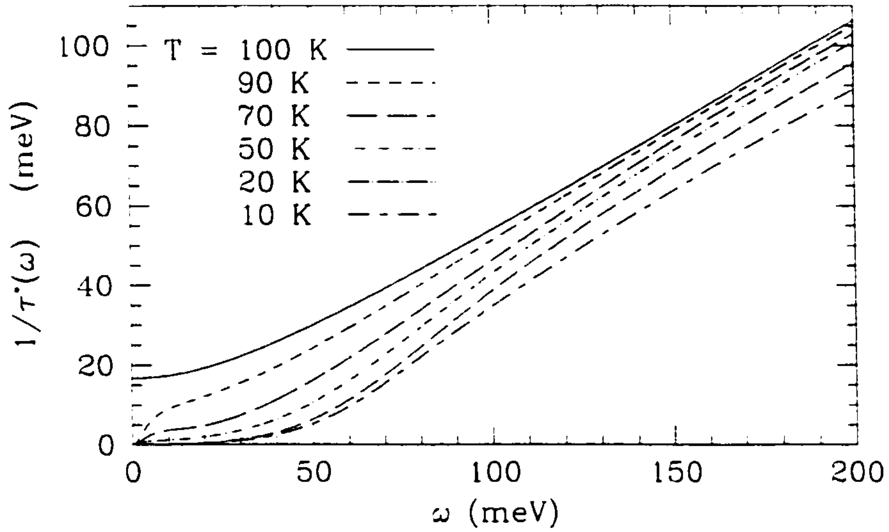

Figure 3.31: The renormalized optical scattering rate, $1/\tau^*(\omega)$, as a function of ω for various temperatures in the superconducting state.

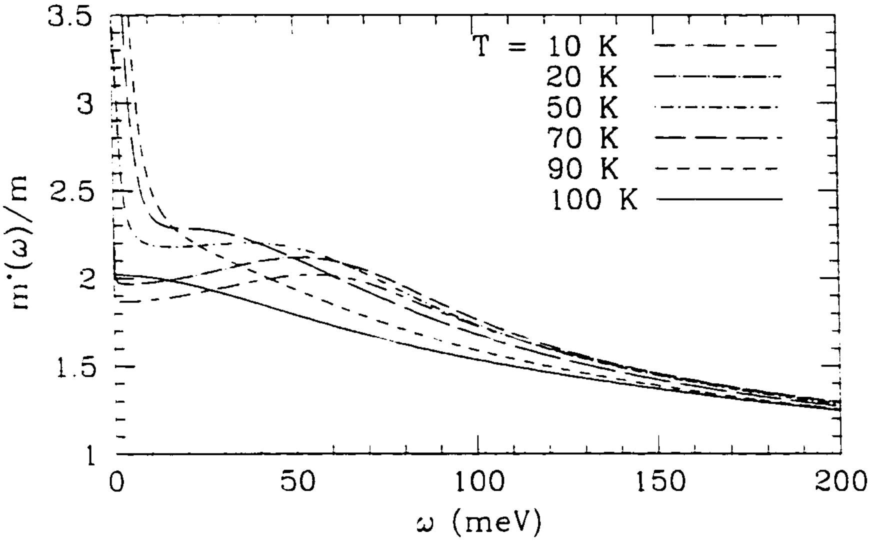

Figure 3.32: The optical mass renormalization, $m^*(\omega)/m$, as a function of ω for various temperatures in the superconducting state.

similar to the normal state result with a finite value at $\omega = 0$. Along the $\overline{\Gamma X}$ line, the superconducting quasiparticle scattering rate, $\Gamma_{\mathbf{k}}(\omega)$, was strongly suppressed at low ω being almost completely gapped to $\omega = 2\Delta_{max}$. For points on the Fermi surface between these two cases, the low ω dependence of $\Gamma_{\mathbf{k}}(\omega)$ changed smoothly from one limiting form to the other. As $1/\tau(\omega)$ is representative of some average of the k-dependent quasiparticle scattering rates, it is not surprising that the low frequency behaviour of $1/\tau(\omega)$ is an intermediate case between the two limiting forms of $\Gamma_{\mathbf{k}}(\omega)$.

The frequency dependence of $1/\tau^*(\omega)$ is shown in figure (3.31). As the behaviour of the renormalized scattering rate is similar to $1/\tau(\omega)$, we will not give a complete description of the curves. There is, however, one difference worth mentioning and that is the behaviour of $1/\tau^*(\omega)$ in the intermediate frequency range, $50 \leq \omega \leq 100$ meV. $1/\tau^*(\omega)$ undergoes a smooth transition between the suppression of the scattering rate at low ω to the quasi-linear regime at high ω. Missing is the region of steeper slope seen in the $1/\tau(\omega)$ curves where the scattering rates rise much quicker in order to match up the low and high frequency limits.

The optical mass renormalization function, $m^*(\omega)/m$, is shown in figure (3.32).

The $T = 100$ K curve is in the normal state and is identical to the curve shown for the normal state results previously in figure(3.10). As the temperature is lowered below the critical temperature, a large peak develops in the low frequency spectrum, as seen by the 90 K curve (short dashed line). At this temperature, however, the zero frequency limit of $m^*(0)/m$ is finite having a value of 15.76 [not shown on the plot]. As the temperature is lowered even more, the width of the low frequency peak is reduced and the value of $m^*(0)/m$ drops. By $T = 10$ K, the peak is no longer seen at $\omega = 0$ on the frequency scale shown.

A feature is seen to appear in m^*/m at finite frequency for temperatures below T_c. In the normal state, $m^*(\omega)/m$ is a maximum at $\omega = 0$ and decreases in size as frequency is increased. In the superconducting state, a shoulder begins to be develop, first seen in the $T = 70$ K curve (long dashed line). As T is lowered even farther, the frequency about which this shoulder is centered increases and the low frequency value of m^*/m is suppressed. For low T, $m^*(\omega)/m$ at small ω is less than its normal state value. As ω is increased, the mass renormalization function first rises reaching a maximum on the broad shoulder, and then decreases again approaching the normal state values at high frequency. By $\omega = 200$ meV, the curves are identical to the normal state results shown earlier. The height of $m^*(\omega)/m$ at the top of the shoulder is larger than the normal state results at the same frequency. At low T, the center frequency of the shoulder is just above $\omega = 2\Delta_{max} \sim 55$ meV, where Δ_{max} is the maximum of the gap edge on the Fermi surface.

As the calculated optical response has a large temperature dependence in both the normal and superconducting states, it may be difficult to differentiate the effects of temperature variation from the effects of superconductivity. To observe the true effects of d-wave superconductivity on the optical response, we plot in figure (3.33) the ratio $\sigma_1^S(T,\omega)/\sigma_1^N(T,\omega)$ as a function of frequency, since the effects of finite temperature are canceled out in this format. The curves shown are for different values of reduced temperature, $t = T/T_c$ [recall that $T_c = 100$ K]. As t is reduced from 1, a dip in the conductivity ratio is clearly seen. Decreasing the temperature causes the size of the depression to increase. At $t = 0.1$, the ratio of the two conductivities is

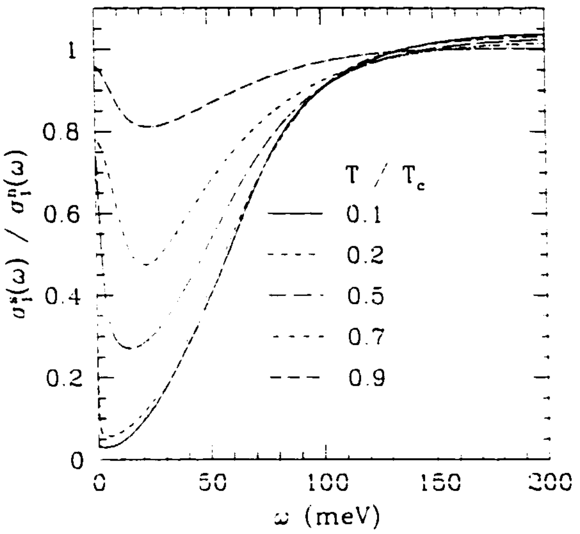

Figure 3.33: Ratio of $\frac{\sigma_1^s(\omega)}{\sigma_1^n(\omega)}$ as a function of frequency, ω, for various temperatures.

still finite due to finite temperature effects. However, the $\lim_{\omega\to 0}\frac{\sigma_1^S(T,\omega)}{\sigma_1^N(T,\omega)}$ at $T = 0$ is expected to be zero. It can be seen that the suppression of $\sigma_1^S(\omega)$ from the normal state value of $\sigma_1^N(\omega)$ begins at very large frequencies, slightly larger than $\omega = 4\Delta_{max}$ at $t = 0.1$. At $\omega = 2\Delta_{max}$, where Δ_{max} is the maximum of the gap edge, the ratio is ~ 0.5 for $T = 10$ K. This is the signature of d-wave superconductivity. While most of the low frequency spectral weight is transferred to the delta function at $\omega = 0$, some must also be moved to higher frequencies as at larger ω, figure (3.33) indicates that $\frac{\sigma_1^S(T,\omega)}{\sigma_1^N(T,\omega)}$ is > 1.0.

In figure (3.34) we plot similar ratio for the scattering rate, $\frac{1/\tau^S(\omega)}{1/\tau^N(\omega)}$. The effect of d-wave superconductivity is to suppressed the low frequency scattering rates. The reduced temperature of 0.9, $1/\tau(\omega)$ is suppress below a frequency of ~ 70 meV. The suppression is not large and at $\omega = 10$ meV, the scattering rate has only been reduced to 75 % of the normal state value. Below this frequency, however, $1/\tau(\omega)$ quickly vanishes as $\omega = 0$. Decreasing the temperature has the effect of further reducing the low frequency scattering rate. For intermediate temperatures, the ratio $\frac{1/\tau^S(\omega)}{1/\tau^N(\omega)}$ develops a shoulder, or flat region, with finite amplitude at low frequencies.

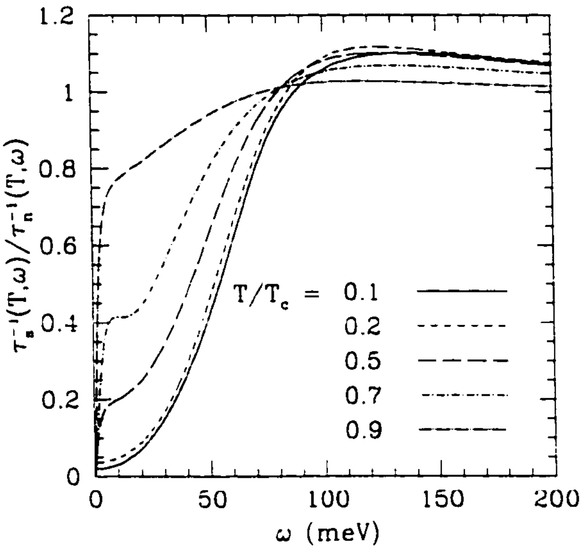

Figure 3.34: Ratio of $\frac{1/\tau^s(\omega)}{1/\tau^n(\omega)}$ as a function of frequency, ω, for various temperatures.

before turning around and falling rapidly to zero with decreasing frequency. At lower temperatures, the shoulder feature is suppressed and power law behaviour at low frequencies is seen. At the upper end of the frequency scale, the superconducting values are enhanced over the normal state values as indicated by the ratio being larger than 1.

3.4.3 Aside: Pseudogap

Just as an aside, we note that the normal and superconducting scattering rates shown in figures (3.8) and (3.30) respectively may, in fact, be relevant for a discussion of the pseudogap seen in the normal state of the underdoped materials. The normal state scattering rates, $1/\tau(\omega)$, of the overdoped compounds are linear with frequency at large ω. The height of $1/\tau(\omega)$, however, is temperature dependent (Startseva et al. 1997; Puchkov, Basov, and Timusk 1996). Similar temperature and frequency behaviours are seen for the results of the normal state calculations, figure (3.8). The underdoped compounds show a suppression of the low frequency scattering rates in the normal state. This suppression is what is referred to as the *pseudogap* since there appears to be a reduction in the quasiparticle scattering, however, the region is not completely gapped. At high frequencies, $1/\tau(\omega)$ is again linear in ω, however, the scattering rates are temperature independent. This insensitivity of $1/\tau$ to temperature at large ω has been used to argue that the underdoped materials, at least, are non-Fermi liquid (Puchkov, Basov, and Timusk 1996).

The temperature dependence of the high frequency scattering rates may not be enough to refute a Fermi liquid-like state in the underdoped materials, however. We will base our present argument on the normal and superconducting state results discussed in this chapter. The high frequency part of the superconducting $1/\tau(\omega)$ results in figure (3.30) are relatively T independent over a large temperature range, from $T = 100$ K to $T = 50$ K, while the normal state $1/\tau(\omega)$ showed a large temperature dependence. The reason for the difference in temperature sensitivity of the normal and superconducting state scattering rates is that as the superconducting gap opens up in the quasiparticle excitation spectrum, there is a corresponding shift of spectral weight from lower to higher frequency balancing the effect of reduced scattering rates for decreasing temperature.

In analogy, if a gap were to open in the normal state excitation spectrum above T_c, an upward shift of spectral weight would also be expected and the same process which leads to the nearly temperature independent behaviour of $1/\tau(\omega)$ in the superconducting state could lead to a T independent behaviour in the pseudogap regime.

3.4.4 Penetration Depth

The London penetration depth is given by the expression (Nam 1967b)

$$\lambda_{\mu\nu}(T) = \frac{2}{\pi}\int_0^\infty dq \frac{1}{q^2 + 4\pi\Pi_{\mu\nu}(0,0)}. \tag{3.66}$$

Evaluation of the above integral yields the simple result

$$\lambda_{\mu\nu}(T) = (4\pi\Pi_{\mu\nu}(0,0))^{-\frac{1}{2}}. \tag{3.67}$$

Writing the EM response function, $\Pi(0)$, in terms of the Eliashberg self-energy equations, as given in equation (3.14), a general expression for the penetration depth is given by

$$\Pi(0) = \frac{1}{4\pi}\frac{1}{\lambda^2(T)} = 4e^2\frac{T}{N}\sum_{\mathbf{k},m}\frac{\partial\varepsilon_{\mathbf{k}}}{\partial\mathbf{k}_\alpha}\frac{\partial\varepsilon_{\mathbf{k}}}{\partial\mathbf{k}_\beta}\frac{\phi_{\mathbf{k}}(i\omega_m)^2}{[\tilde{\varepsilon}_{\mathbf{k}}(i\omega_m)^2+\phi_{\mathbf{k}}(i\omega_m)^2+\tilde{\omega}_{\mathbf{k}}(i\omega_m)^2]^2}. \tag{3.68}$$

While the right hand side of equation (3.68) will remain nonzero in the superconducting state, it is identically zero in the normal state since $\phi_{\mathbf{k}}(i\omega_n)$, the pair correlation function, is guaranteed to vanish. Equation (3.68) can be calculated in the Matsubara imaginary frequency formalism directly and no analytical continuation to the real frequency axis is necessary since $\Pi(i\nu_n)$ is a function of the bosonic Matsubara frequencies, $2\pi nT$ and for $n = 0$, $i\nu_n = 0$.

At $\omega = 0$, the EM response function is purely real. We also know that for the conductivity, $\sigma(\omega) = i\frac{\Pi(\omega)}{\omega}$, which means that *Re* $\Pi(\omega) = \Pi_1(\omega) = \omega\sigma_2(\omega)$. This result indicates that the zero frequency limit of $\omega\sigma_2(\omega)$ is related to the inverse square of the penetration depth, $1/\lambda(T)^2$. Most of the work on optical properties have tended to focus on the real part of the conductivity. Since the real and imaginary components of $\sigma(\omega)$ are related through the Kramers-Kronig relations,

$$\sigma_1(\Omega) = \frac{2}{\pi}\int_0^\infty \frac{\omega\sigma_2(\omega)}{\omega^2-\Omega^2}d\omega + const. \tag{3.69}$$

$$\sigma_2(\Omega) = -\frac{2\Omega}{\pi}\int_0^\infty \frac{\sigma_1(\omega)}{\omega^2-\Omega^2}d\omega \tag{3.70}$$

the imaginary part of $\sigma(\omega)$ follows uniquely from a knowledge of the real component.

In figure (3.35) we plot $\omega\sigma_2(\omega)$ as a function of ω for various temperatures. At large ω, $\omega\sigma_2(\omega)$ is finite in both the normal and superconducting states. The 100 K curve is at T_c and is therefore in the normal state. As ω is lowered, $\omega\sigma_2(\omega)$ decreases in amplitude and at low ω approaches zero with ω^2 dependence. In the normal state

$$\lim_{\omega\to 0}\omega\sigma_2(\omega) = \Pi_1(0) = 0 \tag{3.71}$$

at all temperatures as seen from equation (3.14) since the diamagnetic and paramagnetic contributions to the response function cancel exactly at $\omega = 0$.

In the superconducting state, $\Pi^{(p)}(\omega = 0)$ and $\Pi^{(d)}$ do not cancel and $\lim_{\omega\to 0}\omega\sigma_2(\omega)$ is non-zero. As the temperature is lowered below $\mathrm{T_c}$, the results in figure (3.35) show

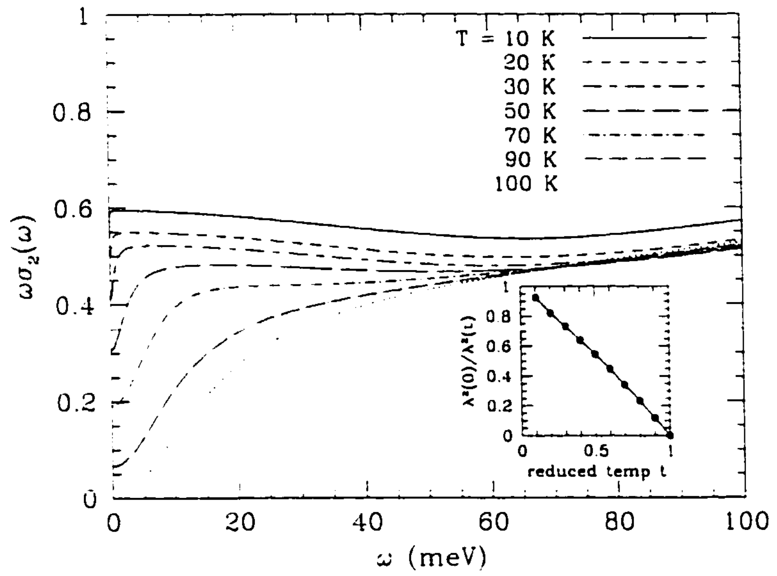

Figure 3.35: $\omega\sigma_2(\omega)$ vs ω for a set of temperatures.

that at high ω, the normal and superconducting states are of the same size. As the frequency is decreased, $\omega\sigma_2(\omega)$ decreases at low ω but remains finite in the limit $\omega \to 0$. The zero frequency value of the function increases with decreasing temperature. At some low frequency, $\omega\sigma_2(\omega)$ turns around from its background behaviour and decreases more rapidly as the frequency is lowered. The frequency at which the curves turn around gets smaller with decreasing temperature. At low T, $\omega\sigma_2(\omega)$ appears to saturate at small ω on the frequency scale shown here. However, a drop in amplitude of $\omega\sigma_2(\omega)$ still occurs even at low temperature, but for the $T = 10$ K curve, the turn around frequency is smaller than 0.1 meV. Clearly, extrapolating the low frequency spectrum to extract the zero frequency penetration depth requires care. The insert to figure (3.35) shows $\lim_{\omega\to 0}\omega\sigma_2(\omega) = \frac{1}{4\pi}\lambda^{-2}(T)$ as a function of reduced temperature, $t = T/T_c$, normalized to the $T = 0$ result. In this case, $T_c = 100$ K. The function $1/\lambda^2(T)$ is almost linear in T throughout the entire temperature range, consistent with previous results for d-wave superconductors (Arberg, Mansor, and Carbotte 1993; Arberg 1995).

There is more interesting information in $\omega\sigma_2(\omega)$ than just the zero frequency limit. Recent work has shown that the full frequency dependence of $\omega\sigma_2(\omega)$ can give information on gap symmetry (Jiang et al. 1996; Marsiglio et al. 1996). Marsiglio and co-workers found for conventional s-wave superconductors that a sharp downward cusp feature appears in the $\omega\sigma_2(\omega)$ spectrum at a frequency of 2Δ, where Δ is the size of the superconducting gap. Both elastic and inelastic scattering effects smear the feature and shift it up in frequency slightly, but do not damp out the depression to a point where it becomes too small to observe, even in the strong coupling limit. Such a feature has been identified in the superconducting $\omega\sigma_2(\omega)$ data for $Ba_{1-x}K_xBi_3$ adding to the evidence that the material exhibits s-wave superconductivity (Marsiglio et al. 1996).

The above features are not seen in the theoretical d-wave results for $\omega\sigma_2(\omega)$, as is easily seen in figure(3.35). At intermediate and high frequency, $\omega\sigma_2(\omega)$ is featureless. This result is consistent with previous work where an $\alpha^2F(\omega)$ approach was used to calculate the imaginary part of the conductivity for a d-wave system (Jiang et al. 1996). Recently a group of experimentalists (Basov et al. 1996) measured $\sigma_2(\omega)$ for $YBa_2C_3O_{7-\delta}$ and $YBa_2Cu_4O_8$. They found that the $\omega\sigma_2(\omega)$ spectrum for the cuprates was flat over the entire frequency range investigated, consistent with the curves in figure (3.35).

3.4.5 Sum Rule

To use the extended Drude model one must be able to determine the value of ω_p^2 by independent means. We have chosen to do this using the partial sum rule defined previously in equation (3.33). In the superconducting state, the opening of a gap in the quasiparticle excitation spectrum results in spectral weight being shifted from low frequencies to the delta function at $\omega = 0$. By integrating over the excitation spectra, $\sigma_1(\omega)$, shown earlier in figure (3.28), the delta function contribution is missed. A method is needed to extract this value so that the right value for ω_p^2 is determined.

The frequency dependent conductivity can be written in terms of two contributions (Bickers et al. 1990)

$$\sigma(\omega) = \sigma_{sc}(\omega) + \sigma_{exc}(\omega) \tag{3.72}$$

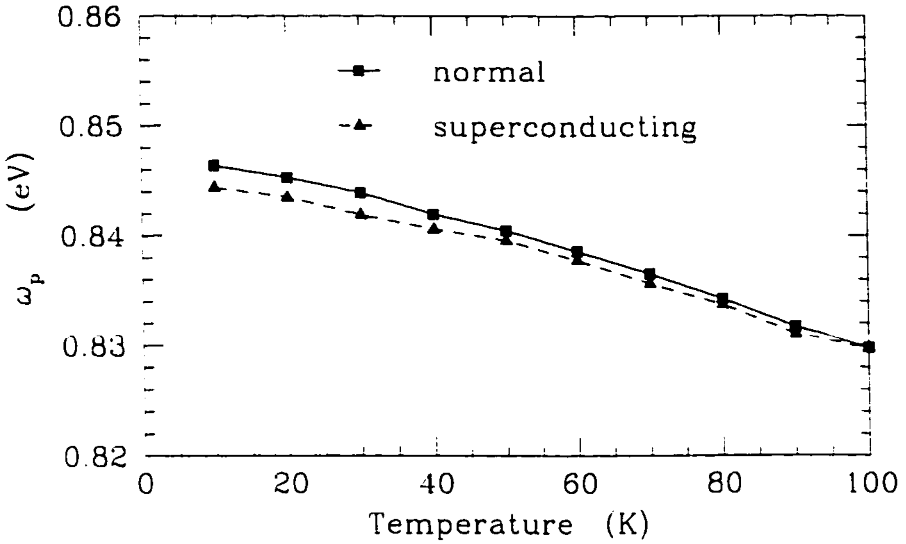

Figure 3.36: The plasma frequency, ω_p, as a function of temperature, T, for both the normal and superconduting state.

where the superconducting component is given by

$$\sigma_{sc}(i\nu_n) = i\frac{\Pi(0)}{i\nu_n} \tag{3.73}$$

and the single quasiparticle excitation component is

$$\sigma_{exc}(i\nu_n) = i\frac{\Pi(i\nu_n) - \Pi(0)}{i\nu_n}. \tag{3.74}$$

Analytically continuing equations (3.73) and (3.74) to the real axis yields

$$\sigma_{sc}(\omega) = \pi\Pi(0)\delta(\omega) + i\frac{\Pi(0)}{\omega} \tag{3.75}$$

and

$$\sigma_{exc}(\omega) = i\frac{\Pi(\omega) - \Pi(0)}{\omega}. \tag{3.76}$$

Recall that in the normal state, $\Pi(0) = 0$. The superconducting component in equation (3.75) is then zero and σ_{exc} reduces to the expected form, $i\frac{\Pi(\omega)}{\omega}$.

The conductivity sum rule states that

$$\int_0^\infty \sigma_1^S(\omega)d\omega = \int_0^\infty \sigma_1^N(\omega)d\omega = \frac{\omega_p^2}{8} \tag{3.77}$$

where the plasma frequency, ω_p, is the same in both the normal and superconducting states. The superscript N (S) denotes the normal (superconducting) state. Using equations (3.77) and (3.72) gives the result

$$\int_0^\infty \sigma_1^N(\omega)d\omega - \int_0^\infty \sigma_{1,sc}^S(\omega)d\omega = \frac{1}{2}\int_0^\infty \pi\Pi(0)\delta(\omega)d\omega \tag{3.78}$$

or

$$\int_0^\infty \left[\sigma_{1,exc}^N(\omega) - \sigma_{1,exc}^S(\omega)\right] d\omega = \frac{\pi}{2}\Pi(0). \tag{3.79}$$

We can therefore determine the plasma frequency for the superconducting state using the partial sum rule

$$\int_0^{\omega_{cut}} \sigma_1^S(\omega)d\,\omega + \frac{\pi}{2}\Pi(0) = \frac{\omega_p^2}{8}. \tag{3.80}$$

In figure (3.36) we plot the plasma frequency as a function of T determined using equation (3.80). The normal state values are included for comparison.

Recall from the last section that $\Pi(0)$ is related to λ_L^{-2}. Equation (3.79) therefore gives us an alternative way of determining the penetration depth using the real part of the conductivity. What is most useful about this relation, however, is that it can be used as a check on the numerical calculations. The diamagnetic response function, $\Pi^{(d)}$, is purely real and only affects the real part of the EM response. In the last section we determined that the penetration depth is given by the real part of $\Pi(\omega)$, and is therefore sensitive to the value of $\Pi^{(d)}$. On the other hand, the real part of the conductivity, $\sigma_1(\omega)$,is related to the imaginary part of $\Pi(\omega)$ and completely unaffected by $\Pi^{(d)}$. For calculations where only $\sigma_1(\omega)$ is required, the diamagnetic correction term can be safely ignored (Mahan 1990). Equation (3.79) can be used as numerical check since it relates the real part of the response to the imaginary part. Calculations of $1/\lambda^2(T)$ directly using the real part of $\Pi(0)$ were compared to calculations using the left hand side of the sum rule in (3.79). There was < 1 % difference between the two sets of results giving confidence in the numerical validity of the calculation, and more importantly, in the analytic continuation.

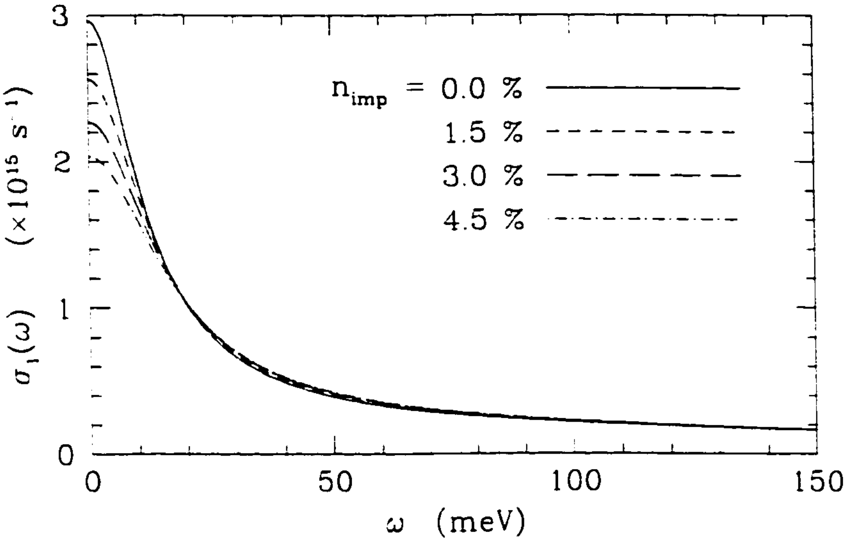

Figure 3.37: Real part of the normal state conductivity, $\sigma_1(\omega)$, as a function of ω for various impurity concentrations at $T = 90$ K.

3.5 Impurities

In this section the effects of impurity scattering on the dynamic conductivity are discussed. We will limit the discussion to the case of resonant impurity scattering only. For the sake of completeness, we start the discussion with normal state results. In figure (3.37), the real part of the optical conductivity is shown for various impurity concentrations, n_{imp}, at a temperature of 90 K. Impurities increase the quasiparticle scattering rate so that $\sigma_1(\omega)$ is broadened with increasing n_{imp}. As oscillator strength is added at higher frequencies, there must be an accompanying decrease in the low frequency value of $\sigma_1(\omega)$ in order for the sum rule to be satisfied. At very high frequencies, where the system is dominated by the effects of inelastic scattering, the pure and impure systems remain nearly identical.

In figure (3.38) we plot $\sigma_1(\omega)$ at a series of temperatures in the normal sate for a system with a an impurity concentration of $n_{imp} = 4.5$ %. This is a fairly large concentration since it reduces the critical temperature of the superconducting system to $T_c = 75.76$ K, or 75 % of the pure value. The effect of impurities is to decrease the temperature dependence of the low frequency conductivity. For the impure system,

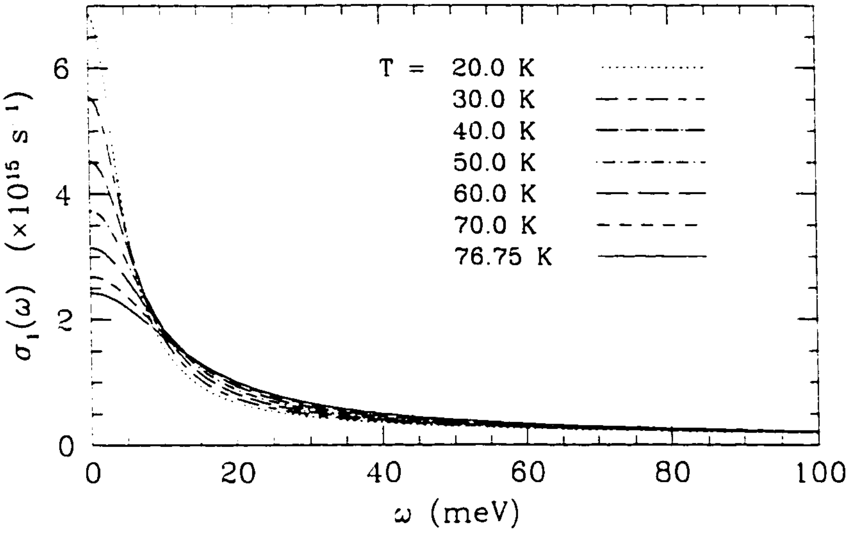

Figure 3.38: Real part of the normal state conductivity, $\sigma_1(\omega)$ at various temperatures for an impurity concenteration of 4.5 % in the unitary scattering limit

$\sigma_1(\omega)$ changes by a factor of ~ 2.5 between the temperatures $T = 20$ K and $T = 70$ K. For the pure case, the normal state values of $\sigma_1(\omega)$ in the same temperature range change by a factor of 10.

The superconducting state is far more interesting. In figure (3.39) we plot the real part of the optical conductivity with the same impurity concentration, namely $n_{imp} = 4.5$ %, for a series of temperatures ranging from the critical temperature of the impure system, $T_c = 76.75$ K down to 10 K. This figure should be compared to that of the pure system previously shown in figure (3.28) where a suppression of the low frequency conductivity was clearly observed with decreasing temperature. For the impure system, no such suppression is seen even at low temperatures. Unlike the pure case in which the low frequency conductivity peak narrowed and $\sigma_1(\omega \rightarrow 0)$ increased, the low frequency value of $\sigma_1(\omega)$ actually decreases. Although the peak does seem to narrow a little as the temperature is first dropped below the critical temperature, the width of the peak also seems to saturate with the peak in $\sigma_1(\omega)$ becoming flat and saturating at low value of $\sigma_1(\omega)$.

A saturation of $\sigma_1(\omega)$ at low frequencies is a general prediction for d-wave su-

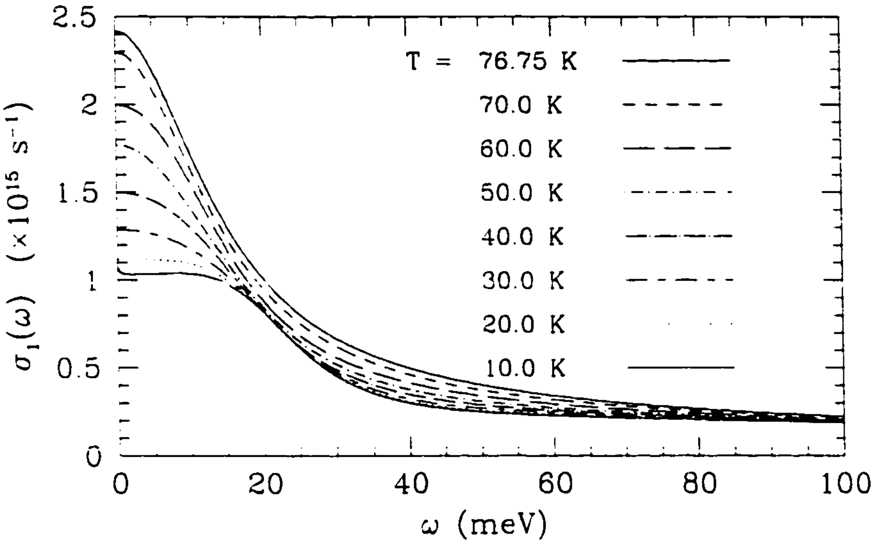

Figure 3.39: Real part of the superconducting state conductivity, $\sigma_1(\omega)$ at various temperatures for an impurity concenteration of 4.5 % in the unitary scattering limit.

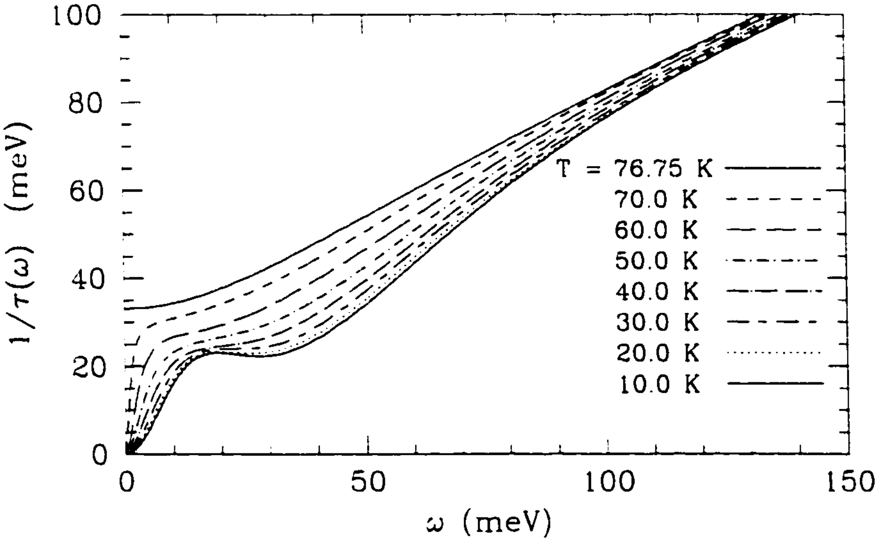

Figure 3.40: Optical scattering rate, $1/\tau(\omega)$, as a function of ω for various temperatures with an impurity concentration of 4.5 % in the unitary scattering limit.

perconductors in the resonant scattering limit (Lee 1993; Hirschfeld. Putikka. and Scalapino 1994). Lee used a simple isotropic model including only elastic impurity scattering. He predicted that in the low impurity concentration limit with resonant scattering at zero temperature,

$$\sigma_1(\omega \to 0) \simeq \frac{\omega_p^2}{4\pi}\frac{1}{\pi\Delta_0} \tag{3.81}$$

where Δ_0 is the size of the maximum gap edge on the Fermi surface. If we take the $T = 10$ K value of $\sigma_1(\omega \to 0) \sim 1.0 \times 15\ s^{-1}$ and the $T = 10$ K value of ω_p. we find that Δ_0 is predicted to be 27 meV. close to the actual value of 23 meV.

In figure (3.40) we plot $1/\tau(\omega)$ for the impure system at the same set of temperatures as in figure (3.39) for $\sigma_1(\omega)$. For $T = 70$ K. the scattering rate as a function of frequency is similar to what is expected for $1/\tau(\omega)$ at temperatures just below T_c. The curve goes to zero linearly as $\omega \to 0$ from above within a narrow frequency range. As the temperature is decreased further. the scattering rate never undergoes the suppression at low ω as was seen for the superconducting curves in the pure case at low T. Instead. $1/\tau(\omega)$ appears to approach a low temperature value of $\sim$ 23 meV at $\omega = 19$ meV. At frequencies below this. the scattering rate falls to zero at $\omega = 0$.

The predicted saturation value for $\sigma_1(\omega \to 0)$ is independent of impurity concentration. In figure (3.41). $\sigma_1(\omega)$ is plotted for the pure case (solid line). $n_{imp} = 1.5$ % (short dashed line). 3.0 % (long dashed line) and 4.5 % (dash-dotted line) at a temperature of $T = 10$ K. The reduced temperatures. T/T_c. for the different impurity concentrations ranges from 0.1 in the pure case and 0.13 at $n_{imp} = 4.5$ %. For the pure case. the small ω peak is very narrow and $\sigma_1(\omega \to 0)$ is two orders of magnitude larger than for the impure systems. The low frequency peaks in the impure systems are significantly wider. The low ω depression so clearly seen in the pure case is not observed in the impure case. While no extended flat region exists at low ω for $n_{imp} = 1.5$ %, the beginning of such a shoulder is seen for 3.0 % and is clearly fully developed for 4.5 %. The value of $\sigma_1(\omega \to 0)$ does appear to be approaching a saturation value with $\sigma_1(\omega)$ ranging from $1.0 \times 10^{15}\ s^{-1}$ and $1.1 \times 10^{15}\ s^{-1}$. The saturation of $\sigma_1(\omega)$ in the resonant scattering limit is made even more clear in figure (3.42) where $\sigma_1(\omega \to 0)$ is plotted as a function of reduced temperature. $t = T/T_c$. The pure case

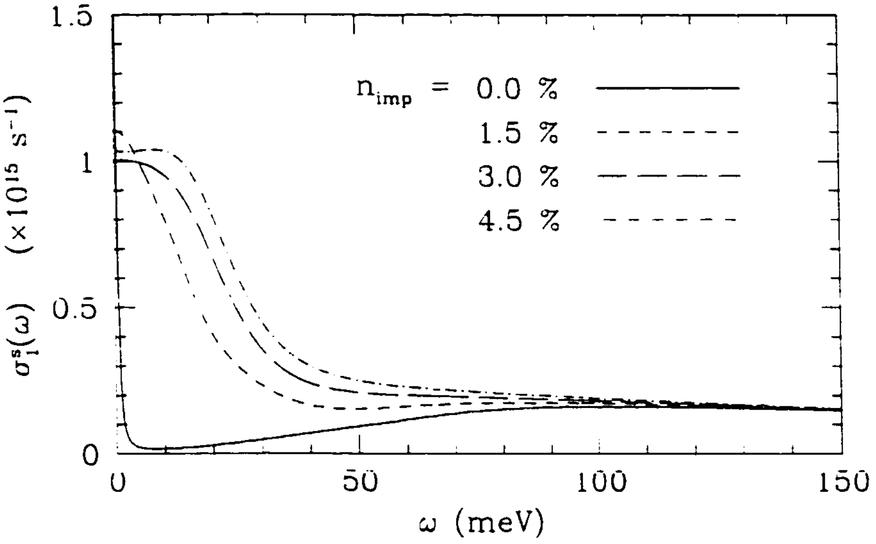

Figure 3.41: Real part of the conductivity, $\sigma_1(\omega)$, as a function of ω for various impurity concenterations in the unitary scattering limit at a fixed temperature of $T = 10$ K.

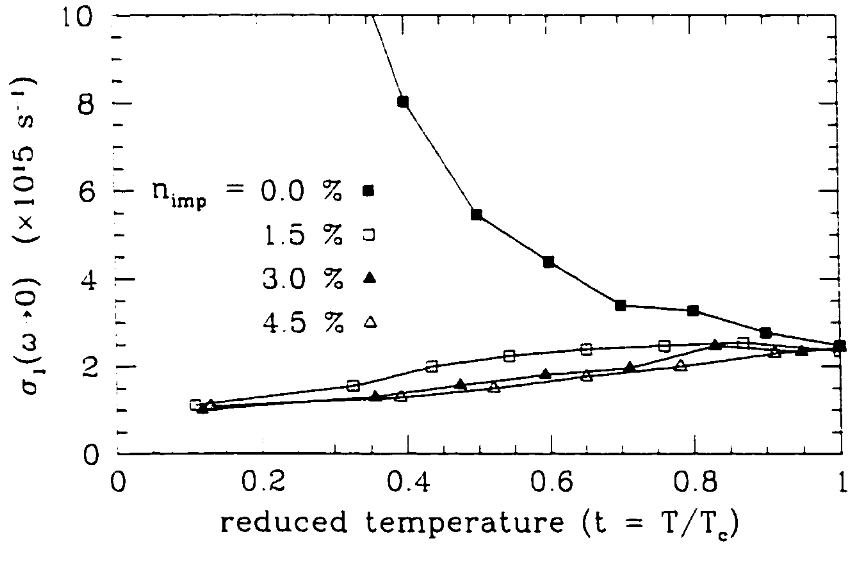

Figure 3.42: The zero frequency limit of the excitation component of the optical conductivity as a function of reduced temperature for various impurity concentrations in the unitary limit

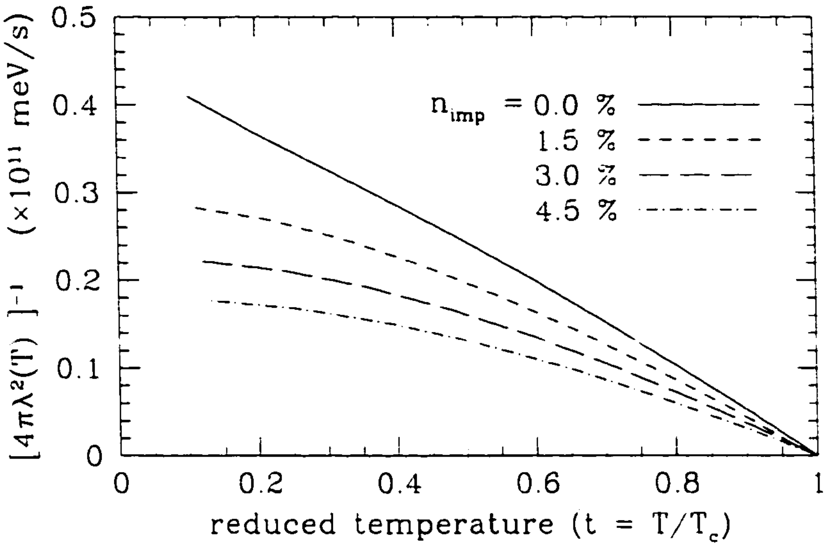

Figure 3.43: $[4\pi\lambda^2(T)]^{-1}$ as a function of reduced temperature. $t = T/T_c$. for various impurity concentrations. n_{imp}.

is seen to grow almost exponentially for decreasing t. For the impure systems. $\sigma_1(0)$ does not increase as a function of temperature. instead the value decreases slowly and the curves for all three impurity concentrations are seen to be approaching a limiting value at $T = 0$. The above calculations are therefore consistent with the predictions of Lee.

The effects of impurities on the penetration depth in d-wave superconductors is well understood. For the sake of completeness. we show $1/\lambda^2(T)$ for our model in figure (3.43). For a d-wave order parameter. the theory gives a nearly linear temperature dependence over the entire temperature range for a pure system (solid line). As impurities are added. $1/\lambda^2(T)$ crosses over from a T to a T^2 dependence in the resonant scattering limit (Arberg, Mansor. and Carbotte 1993).

Chapter 4

Electronic Raman Scattering

4.1 Introduction

Electronic Raman scattering is an inelastic light scattering process where a photon incident on an electronic system exchanges energy with the system and emerges from the scattering event with a different frequency. If the incident photon has frequency ω, the scattered photon emerges either with frequency $\omega + \nu$ after absorbing energy ν from the system or with frequency $\omega - \nu$ after transferring energy ν to the system. The former process, producing anti-Stokes lines, is due to energy gained by the photon after inducing the decay of electronic excitations. In the latter process, producing Stokes lines, the photon gives some of its energy to the system by producing electronic excitations. The Stokes and anti-Stokes intensity spectra are related to each other through a multiplicative thermal occupation factor. By taking the ratio of the two intensity spectra, an effective sample temperature can be determined.

The idea of using inelastic light scattering, or Raman scattering, as a means to probe the quasiparticle excitation spectrum of superconductors was first proposed in 1961 (Abrikosov and Fal'kovskii 1961). As with the optical conductivity discussed in the last chapter, the BCS prediction of a finite gap in the quasiparticle excitation spectrum suggested that in the superconducting state no absorption of energy from the incident photons should occur for energy shifts below that of 2Δ. Several unsuccessful attempts were made at verifying the prediction (Fraas, Williams, and

Porto 1970) ending in the first experimental observation of the superconducting gap in 2H-$NbSe_2$, a superconductor with a critical temperature of 7.2 K (Sooryakumar and Klein 1980). Soon after, clear evidence of a gap edge was seen using Raman techniques in the A15 compounds, namely V_3Si and Nb_3Sn (Dierker et al. 1983; Hackl, Kaiser, and Schicktanz 1983).

Improvements in the theory of electronic Raman scattering accompanied the improving experimental scene. A detailed theory for Raman scattering in s-wave superconductors now exists which includes the effects of Coulomb screening (Abrikosov and Genkin 1974), final state interactions (Klein and Dierker 1984; Monien and Zawadowski 1990), energy gap anisotropy (Klein and Dierker 1984; Fal'kovskii and Klama 1990) and impurity scattering (Devereaux 1992; Devereaux 1993; Devereaux 1995). Raman scattering for d-wave superconductors has only been addressed recently, the work motivated by the possibility of unconventional superconductivity in the high T_c superconductors (Annett, Goldenfeld, and Leggett 1996). Due to the success of experimental measurements, and the interpretation of these results as supporting a d-wave pairing scenario in the cuprates, a theory of electronic Raman scattering in d-wave superconductors has developed at a rather quick rate.

The advantage of electron Raman scattering experiments lies in the sensitivity of the energy spectrum to the selected polarizations of the incident and scattered photons making it a momentum sensitive probe. It measures a strongly weighted average over the Fermi surface, as opposed to other techniques such as thermodynamic and conductivity experiments, which are essentially Fermi surface averages with isotropic or weakly varying weighting factors. Additionally, the weighting of different parts of the Fermi surface can be adjusted by simply varying the polarization orientations of the incident and scattered photons. Further beneficial features of Raman experiments are that they are not very sensitive to surface effects, have sharp energy resolution, and are probes of the bulk material due to the long wavelength of the exciting laser. One major drawback, however, is that while Raman scattering is a momentum resolved probe, it is not sensitive to the phase of the superconducting order parameter, but only to the absolute value.

Raman experiments, when carried out using varying orientations of light polariza-

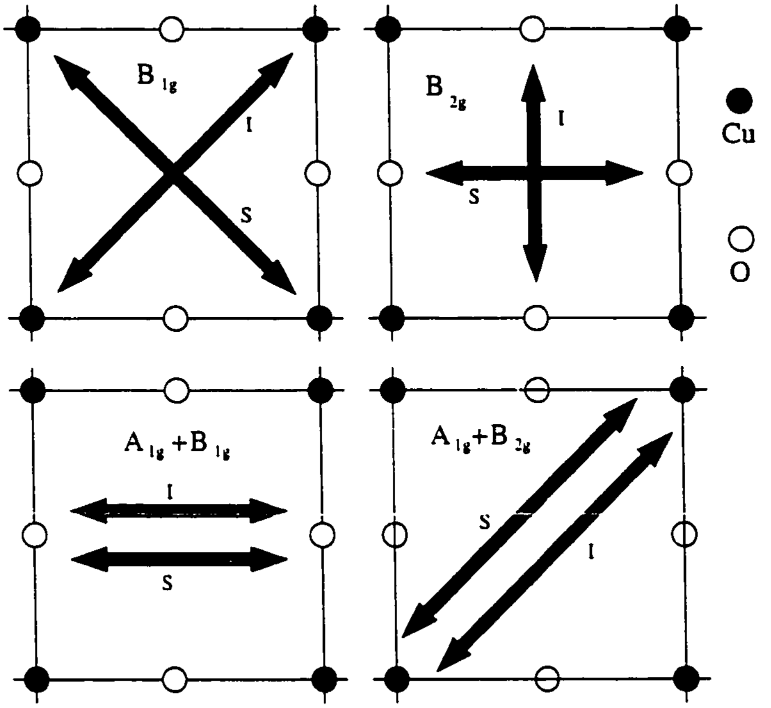

Figure 4.1: The relation between Raman symmetries and photon polarization. The polarization vector of the incident photon denoted by the black arrow while the polarization of the scattered photon is gray. Experimentally, the polarization $(x'y')$ measures the B_{1g}, (xy) the B_{2g}, (yy) a combination of A_{1g} + B_{1g} and $(x'x')$ a combination of A_{1g} + B_2. The x and y axes are aligned along the Cu-O bonds, while x' and y' are rotated by 45°.

tions, can probe different sections of the Brillouin zone and can, therefore, be used to map out the anisotropy of the quasiparticle excitation spectrum on the Fermi surface. In-plane Raman experiments are typically performed using the backscattering geometry, the incident and scattered photons propagating along the c-axis with the photon polarizations lying in a plane perpendicular to the direction of propagation and parallel to the ab-plane of the sample. In figure (4.1) we show how the different photon polarizations are related to the Raman spectra. Polarization of the incident photon is denoted graphically by a solid black arrow while that of the scattered photon is denoted by a gray arrow. The vectors $\hat{x}$ and $\hat{y}$ are oriented along the Cu-O bonds of the CuO_2 planes while $\hat{x}'$ and $\hat{y}'$ are rotated by 45° and lie along the diagonals. For incident and scattered photon polarizations $(\hat{x}', \hat{y}')$ the experiment measures scat-

Material	Reference
$YBa_2CuO_3O_{7-\delta}$	(Cooper et al. 1988a) (Hackl et al. 1988) (Cooper et al. 1988b)
$YBa_2CuO_4O_8$	(Donovan et al. 1995)
$Bi_2Sr_2CaCu_2O_8$	(Staufer et al. 1992) (Yamanaka et al. 1992)
$Tl_2Ba_2CuO_6$	(Nemetalek et al. 1993) (Gasparov et al. 1997)
$La_{2-x}Sr_xCuO_4$	(Chen et al. 1994) (Irwin et al. 1995)
$HgBa_2CaCu_2O_{6+\delta}$	(Sacuto et al. 1996)
$Nd_{2-x}Ce_xCuO_4$	(Stadlober et al. 1995)

Table 4.1: Representative references for electronic Raman scattering data on common high-T_c materials

tering in the B_{1g} spectrum. A crossed polarization $(\hat{x}, \hat{y})$ measures the B_{2g} channel. Incident and scattered polarization vectors oriented along $(\hat{x}, \hat{x})$ and $(\hat{x}', \hat{x}')$ measure a superposition of the A_{1g} + B_{1g} and A_{1g} + B_{2g} spectra respectively. No experimental setup can isolate the A_{1g} channel using a single experiment. As we will see later, the B_{1g} symmetry favourably selects states along the k_x and k_y axis of the Brillouin zone, while measuring the B_{2g} spectrum gives information about the excitation spectrum along the diagonals. The A_{1g} symmetry channel is an effective average over the entire Fermi surface and is very dependent on the geometry of the underlying band structure (Branch 1995; Branch and Carbotte 1996; Krantz and Cardona 1995).

Raman scattering has been used to probe the effects of the superconducting transition on the single particle excitation spectrum. While in theory the electronic Raman technique is a very powerful probe of anisotropy in the superconducting gap, measurement of conventional materials was extremely difficult because of the very low intensity of the electronically scattered spectrum. Raman scattering by single particle excitations in a simple metal is expected to be very weak and restricted to rather low frequency shifts (Virosztek and Ruvalds 1992). With the discovery of the high temperature superconductors, electronic Raman scattering was thrown into the limelight.

These materials have proven to be a rich source of data for Raman experimentalists. Data now exists for nearly all cuprate materials, both hole-doped and electron-doped. Several representative experiments are listed in table (4.1).

Experiments on hole-doped cuprate superconductors all show a number of common features independent of the number of CuO_2 planes in the unit cell (Chen et al. 1994). In the normal state, a very broad nearly flat background is observed in all symmetry channels extending to very high energies, in many cases beyond 1 eV. This large background has been associated with electronic scattering since, as the temperature of the materials is lowered below T_c, a low frequency redistribution of spectral weight is observed. This redistribution of low frequency scattering has been attributed to the opening of a superconducting gap in the excitation spectrum. The observed spectra, however, display a very strong symmetry dependence in the superconducting state with the characteristic features of the energy spectrum dependent on the orientation of the scattered and incident photon polarizations. Even at low temperatures, the low frequency redistribution is not complete in any of the scattering channels. The Raman intensity turns on continuously over a broad range of frequency. This is in sharp contrast to what is observed in conventional materials where experiments show that the intensity turns on sharply at an energy of 2Δ (Dierker et al. 1983).

A pronounced peak develops in the B_{1g} spectrum as the temperature is lowered below T_c, which is centered at a frequency approximately 30 % higher than that of the broad shoulder seen in the B_{2g} channel. The low frequency B_{1g} spectrum has an ω^3 dependence at low temperature for samples at optimal doping, while the small frequency behaviour of the B_{2g} spectrum is linear in ω.

The symmetry dependent redistribution of electronic states as seen at low frequency in Raman spectra below the superconducting critical temperature has been interpreted as due to the opening up of an anisotropic energy gap in the excitation spectrum. It has been shown (Devereaux and Einzel 1995) that the data of Staufer et al. (Staufer et al. 1992) in Bi-2212 can be well understood within a BCS framework in the region up to 700 cm^{-1} using a model superconducting gap with $d_{x^2-y^2}$ symmetry.

As one moves into the overdoped regime, only for a small region of doping (if any) does the low frequency behaviour of the B_{1g} symmetry channel remain cubic in frequency before crossing over to a linear low frequency behaviour. The other channels retain the linear frequency dependence at small frequencies. This linear behaviour cannot be explained by a pure d-wave model within a BCS formalism. Orthorhombic distortions, elastic impurity scattering, and as we shall see, inelastic scattering can lead to the observed linear behaviour. Devereaux and co-workers have approached this problem by arguing that increasing disorder leads to a process similar to impurity scattering. In this thesis we shall argue that similar behaviour is seen for inelastic scattering when the low frequency boson spectral density exhibits linear dependence on frequency without the addition of impurities. Inclusion of impurity scattering in the Eliashberg formalism will, however, enhance the low ω linear behaviour.

In the underdoped case, the intensity of the B_{1g} spectra drops and the entire spectrum freezes out becoming temperature independent below a certain temperature, while strong scattering is still seen in the other channels which retain the linear ω dependence (Devereaux and Kampf 1997). The overall loss of intensity of the B_{1g} scattering channel relative to the other channels is taken to be evidence for the existence of the pseudogap observed in other properties of underdoped materials. The pseudogap behaviour can be explained using ARPES measurements (Ding et al. 1997) which indicate the loss of the Fermi surface along $(\pm\pi, 0)$ and $(0, \pm\pi)$ directions, and the formation of hole pockets around $(\pi/2, \pi/2)$ and equivalent points.

All the materials listed in table (4.1) but $Nd_{2-x}Ce_xCuO_4$ are consistent with d-wave pairing. The odd compound out, also the only electron-doped cuprate superconductor in the table, $Nd_{2-x}Ce_xCuO_4$ exhibits a sharp turn on in intensity with no anisotropy observed in the different Raman channels. The data is consistent with an isotropic s-wave gap as in conventional superconductivity (Stadlober et al. 1995; Einzel and Hackl 1996).

A substantial amount of theoretical work has been done within the framework of BCS theory. While this type of formalism can capture the effects of the redistribution of electronic states due to superconductivity, normal state electrons do not participate in the Raman process unless some form of scattering is introduced allowing the electron to absorb energy from the photon field and conserve both momentum and energy. Inelastic scattering processes are naturally included in the Eliashberg formalism. The normal state quasiparticle acquire a finite life time even in the absence of impurities, and a non-zero Raman spectrum is obtained (Kostur and Eliashberg 1991; Kostur 1992).

In this chapter we present results for in-plane electronic Raman scattering calculations in a strong-coupling formalism. The solutions of the Eliashberg self-energy equations introduced in chapter 2 are used. Properties of both normal and superconducting state Raman spectra are investigated. In what follows, we will limit our discussion to a single band model with tetragonal crystal symmetry.

The theory of electronic Raman scattering in Nambu formalism is introduced in the next section. The origin of the polarization dependence is discussed. A connection is made between the irreducible symmetry channels and the experimentally probed spectra.

In section 4.3 we present the results of our numerical calculations for the normal and superconducting states. The effects of inelastic scattering on the Raman spectra are discussed and comparison is made to BCS calculations. A simple model is introduced which will allow us to extract frequency dependent scattering rates from our normal state spectra. Comparison of the scattering rates is made with the optical scattering rates and fundamental quasiparticle scattering rates.

In the last section, we investigate the effects of impurities on the Raman scattering channels.

4.2 Theory

The interaction Hamiltonian between electrons and photons is given by (Sakurai 1967)

$$H_{int} = \sum_i \left[-\frac{e}{2mc} (\mathbf{p}_i \cdot \mathbf{A}(\mathbf{x}_i, t) + \mathbf{A}(\mathbf{x}_i, t) \cdot \mathbf{p}_i) + \frac{e^2}{2mc^2} \mathbf{A}(\mathbf{x}_i, t) \cdot \mathbf{A}(\mathbf{x}_i, t) \right] \tag{4.1}$$

where $\mathbf{A}(\mathbf{x}_i, t)$ represents the quantized radiation field. The expression $\mathbf{A}(\mathbf{x}_i, t)$ is a field operator which acts on the photon state at $\mathbf{x}_i$, where $\mathbf{x}_i$ refers to the coordinate of the ith electron.

With Raman scattering, we are concerned with conserving the total number of photons before and after the interaction. If the number of incident photons is reduced by one, then the scattered photon number must increase by one. The interaction Hamiltonian is comprised of a linear $\mathbf{A}\cdot\mathbf{p}$ term and a quadratic $\mathbf{A}\cdot\mathbf{A}$ term. Since $\mathbf{A}$ is an operator which changes the photon number by one, $\mathbf{A}\cdot\mathbf{p}$ makes no contribution to the first order process. The $\mathbf{A}\cdot\mathbf{A}$ term, however, can contribute in the first order process provided it represents the creation of a photon in state $(\mathbf{k},\epsilon)$ and annihilation of a photon in the state $(\mathbf{k}',\epsilon')$.

The $\mathbf{A}\cdot\mathbf{p}$ term does, however, contribute to the scattering process in the second order of the perturbation. At least in terms of e, it is of the some order as the $\mathbf{A}\cdot\mathbf{A}$ term indicating that we must take the second order scattering term into consideration.

The two contributions can be put together in the *effective interaction Hamiltonian*

$$H_R = r_0 \left\langle A_S^\dagger A_I \right\rangle \tilde{\rho}_{\mathbf{q}} \tag{4.2}$$

where $A_S^\dagger$ contains the creation operator for the scattered photon, A_I contains the annihilation operator for the incident photon, and r_0 is the Thompson radius. The momentum transfer from the photon field to the electronic system is $\mathbf{q} = \mathbf{k}_I - \mathbf{k}_S$. In the case of light scattering, we take the long wavelength limit, $\mathbf{q} = 0$. The effective charge fluctuation around the Fermi surface, $\tilde{\rho}_{\mathbf{q}}$, is given by

$$\tilde{\rho} = \sum_{\mathbf{k},\sigma} \gamma(\mathbf{k},\mathbf{q}=0) c^\dagger_{\mathbf{k},\sigma} c_{\mathbf{k},\sigma} \tag{4.3}$$

with a scattering amplitude determined by the *Raman vertex*

$$\begin{aligned}\gamma(\mathbf{k},\mathbf{q}=0;\omega_I,\omega_S) &= \mathbf{e}^I\cdot\mathbf{e}^S + \frac{1}{m}\sum_{\nu}\left[\frac{\langle n,\mathbf{k}|\mathbf{e}^S\cdot\mathbf{p}|\nu,\mathbf{k}\rangle\langle \nu,\mathbf{k}|\mathbf{e}^I\cdot\mathbf{p}|n,\mathbf{k}\rangle}{\epsilon(\mathbf{k})-\epsilon_\nu(\mathbf{k})+\omega_I}\right. \\ &\qquad\left.+\frac{\langle n,\mathbf{k}|\mathbf{e}^I\cdot\mathbf{p}|\nu,\mathbf{k}\rangle\langle \nu,\mathbf{k}|\mathbf{e}^S\cdot\mathbf{p}|n,\mathbf{k}\rangle}{\epsilon(\mathbf{k})-\epsilon_\nu(\mathbf{k})-\omega_S}\right]\end{aligned} \tag{4.4}$$

where $\mathbf{e}^I$ ($\mathbf{e}^S$) is the polarization vector of the incident (scattered) photon, ω^I (ω^S) is the incident (scattered) photon energy, and $\varepsilon_{\mathbf{k}}$ and ε_ν are the Bloch conduction and intermediate state energies respectively.

According to Abrikosov and Genkin(Abrikosov and Genkin 1974) if the energy of the incident and scattered frequencies, ω_I and ω_S, are negligible compared to the relevant energy scale of the band gap, the vertex functions can be expressed in terms of the inverse mass tensor which is related to the curvature of the bands (ie: $\mathbf{k}\cdot\mathbf{p}$ theory) (Ashcroft and Mermin 1976) and the incident and scattered light polarization vectors as

$$\begin{aligned}\gamma(\mathbf{k}) &= \mathbf{e}^I\cdot\vec{\gamma}_{\mathbf{k}}\cdot\mathbf{e}^S\\ &= \sum_{\alpha,\beta} e^I_\alpha \frac{\partial^2\varepsilon_{\mathbf{k}}}{\partial k_\alpha \partial k_\beta} e^S_\beta. \end{aligned} \tag{4.5}$$

Here $\vec{\gamma}_{\mathbf{k}}$ is the Raman tensor and the symbols α and β take on the coordinates x and y.

This expression is valid so long as the incoming laser light cannot excite interband transitions, i.e. the system is non-resonant. The effective mass approximation, equation (4.5), has been used extensively to calculate the expected Raman spectra in unconventional superconductors (Branch and Carbotte 1995; Branch and Carbotte 1996; Strohm and Cardona 1997; Wenger and Käll 1997).

4.2.1 Many-body Theory

The transition rate from a state with $n_I \equiv n_{\mathbf{k}_I,\epsilon_I}$ incident photons and no scattered photons to a state with $n_{\mathbf{k}_I,\epsilon_I} - 1$ incident photons and $n_S \equiv n_{\mathbf{k}_S,\epsilon_S} = 1$ scattered photons at temperature T is given by

$$\Gamma(T;\mathbf{k}_I,\epsilon_I;\mathbf{k}_S,\epsilon_S) = \frac{2\pi}{\hbar} r_0^2 \mid \langle A_S^\dagger A_I\rangle \mid^2 \tilde{S}(T,\mathbf{q},\omega) \tag{4.6}$$

where

$$\tilde{S}(T,\mathbf{q},\omega) = \sum_{i,f} \frac{e^{-\beta E_i}}{\mathcal{Z}} \mid \langle f \mid \tilde{\rho}_{\mathbf{q}} \mid i\rangle \mid^2 \delta(E_f - E_i + \hbar\omega) \tag{4.7}$$

is the *generalized structure factor*, β is $1/k_BT$ and $\mathcal{Z}$ is the partition function. If we now sum over all final states in a certain region $d\Omega\ d\omega_S$ of k space around $\mathbf{k}_S$ and normalize to the incoming flux $\hbar c n_I$ one gets the differential Raman cross-section

$$\frac{\partial^2\sigma}{\partial\omega\partial\Omega} = \frac{\omega_S}{\omega_I} r_0^2 \tilde{S}_{\gamma\gamma}(\mathbf{q},\omega) \tag{4.8}$$

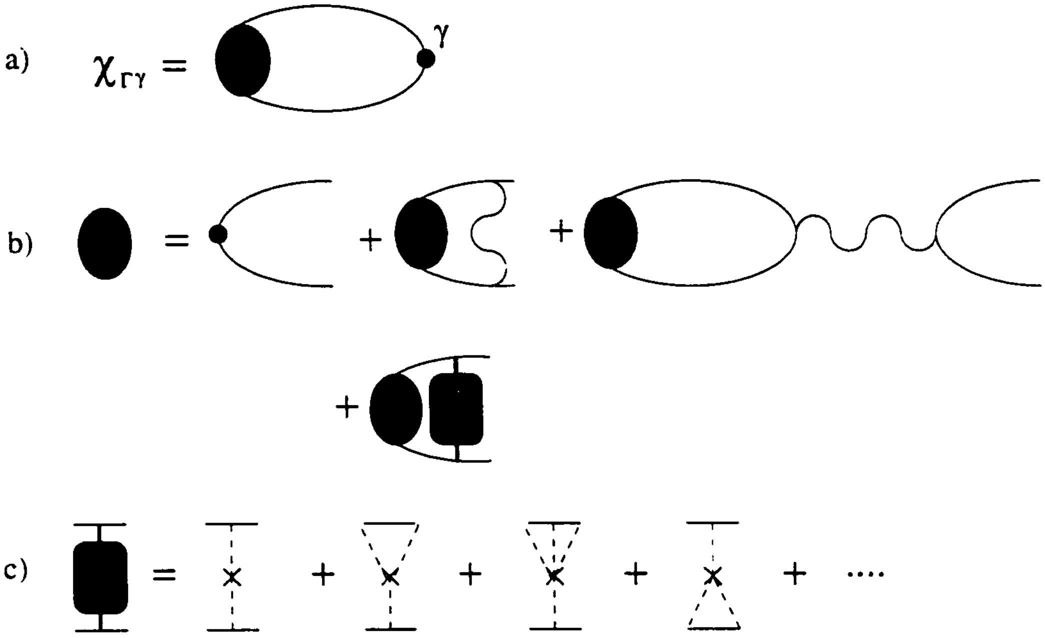

Figure 4.2: Feynman diagram for the Raman response function. a) Raman polarization bubble, b) Renormalized Raman vertex function, $\hat{\Gamma}$ and c) the impurity scattering T-matrix.

for a given momentum transfer $\mathbf{q}$ and energy shift $\hbar\omega$. $\tilde{S}_{\gamma\gamma}$ is the generalized structure function of the inelastic photon scattering process, which is related to the imaginary part of the Raman response function, $\chi_{\gamma\gamma}(\mathbf{q},\omega)$, through the fluctuation-dissipation theorem (Landau and Lifshitz 1960)

$$\tilde{S}_{\gamma\gamma}(\mathbf{q},\omega) = -\frac{1}{\pi}\left[1 + n(\beta\omega)\right] Im\chi_{\gamma\gamma}(\mathbf{q},\omega) \tag{4.9}$$

where $n(\beta\omega)$ is the Bose-Einstein distribution function

$$n(\beta\omega) = \frac{1}{e^{\beta\omega} - 1}. \tag{4.10}$$

The Raman response function, $\chi_{\gamma\gamma}$, is given by the effective density-effective density correlation function

$$\chi_{\gamma\gamma}(\mathbf{q},\omega) = \frac{i}{2\pi}\int_{-\infty}^{\infty} dt e^{-i\omega t} \langle[\tilde{\rho}_{\mathbf{q}}(0), \tilde{\rho}_{\mathbf{q}}(t)]\rangle \tag{4.11}$$

where $\langle\rangle$ denotes a thermal average. Equation (4.11) can be written on the imaginary axis in terms of thermal Green's functions as

$$\chi_{\gamma\gamma}(\mathbf{q}, i\nu_n) = -T \sum_{m,\mathbf{k}} Tr\left[\gamma_{\mathbf{k}+\mathbf{q}}\tau_3 \hat{G}(\mathbf{k}+\mathbf{q}, i\omega_m + i\nu_n)\hat{\Gamma}_{\mathbf{k}}\hat{G}(\mathbf{k}, i\omega_m)\right] \tag{4.12}$$

where $\hat{\Gamma}_{\mathbf{k}}$ is the renormalized vertex correction shown diagrammatically in figure (4.2.b) similar in form to the renormalized vertex in the EM response function.

The first two terms on the right hand side of the diagrammatic equation for $\hat{\Gamma}_{\mathbf{k}}$ are the unrenormalized vertex and the boson exchange terms similar to those described in the last chapter for the optical conductivity. The final set of terms is given by the T-matrix and corresponds to impurity scattering of the particle-particle pair. The third term, however, is a new term related to Coulomb screening effects. Mass fluctuations induced by inelastic light scattering can result in charge density fluctuations which would be screened out by the long range Coulomb interaction. We will make the approximation that the only important terms which introduce vertex corrections is the Coulomb screening term. In this case, the vertex function reduces to just two terms, the unrenormalized vertex and the Coulomb term,

$$\Gamma_{\mathbf{k}} = \gamma_{\mathbf{k}}\hat{\tau}_3 - V_{\mathbf{q}}\hat{\tau}_3 T \sum_{\mathbf{k}',m} Tr\left\{\hat{\tau}_3 \hat{G}(\mathbf{k}', i\omega_m)\hat{\Gamma}_{\mathbf{k}'}\hat{G}(\mathbf{k}, i\omega_l)\right\}. \tag{4.13}$$

In appendix B, we will show that with the inclusion of screening, the Raman susceptibility reduces to the form

$$\chi_{\Gamma\gamma}(\omega) = \chi_{\gamma\gamma}(\omega) - \frac{\chi_{\gamma 1}(\omega)\ \chi_{1\gamma}(\omega)}{\chi_{11}(\omega)} \tag{4.14}$$

where the generalize response function, $\chi_{\alpha\beta}(\omega)$, is given by

$$\chi_{\alpha\beta}(i\nu_n) = -T \sum_{\mathbf{k},m} Tr\left\{\alpha\hat{\tau}_3\ \hat{G}(\mathbf{k}, i\omega_{m+n})\ \beta\hat{\tau}_3\ \hat{G}(\mathbf{k}, i\omega_m)\right\}. \tag{4.15}$$

The labels α and β can assume the values $\gamma_{\mathbf{k}}$ and 1.

For the B_{1g} and B_{2g} Raman symmetries, the second term in equation (4.14) is always zero for a tetragonal system. The A_{1g} channel, however, may be strongly screened and is very dependent on the underlying quasiparticle energy dispersion (Branch and Carbotte 1996; Strohm and Cardona 1997). Because of the strong sensitivity of the A_{1g} spectrum. we will introduce only the unscreened response. In later sections when the Raman spectra are analyzed more carefully, we will ignore the A_{1g} scattering channel and concentrate on the information contained in the B_{1g} and B_{2g} spectra.

Before advancing any farther, it is important to ask whether or not our assumptions regarding the fluctuation-dissipation theorem and the inverse mass tensor approximation hold. The fluctuation-dissipation theorem is equivalent to the principle of detailed balance (Landau and Lifshitz 1960) which regards all transitions as instantaneous and invariant under time reversal. A simple relation between the Stokes and anti-Stokes spectra can be found using the law of detailed balance; the ratio of the two spectra is simply given by a thermal occupation factor. Experimental results have been analyzed and show support for this assumption (Einzel and Hackl 1996).

The effective density approximation is valid only if the conduction band is well separated from all other bands on an energy scale given by the frequency of the incident photons. By varying the frequency of the incident photons, the dependence of the intensity on the excitation wavelength has been studied. In the case of resonant scattering, one would expect very large changes in the intensity of the observed spectrum. Experimental data has given support for the above approximation (Einzel and Hackl 1996).

Furthermore, in support of the inverse mass approximations, a calculation of the absolute cross-section (i.e. absolute intensity) would require a complete knowledge of all bands involved in the case of resonant scattering, however, the spectral shape and the selection rules are much more robust and do not change significantly even if the scattering is resonantly enhanced (Einzel and Hackl 1996). It seems that, at least for qualitative predictions, that the inverse mass approximation to the Raman vertex is justified.

4.2.2 Tight-Binding Vertices

Through the polarization dependence of the Raman vertices, the various quasiparticle excitations can be probed. In this section, we will investigate the symmetry properties of the unrenormalized Raman vertex using a tight-binding dispersion relation. A connection is made between the irreducible representations of the Raman tensor and the spectra observed experimentally. In what follows, we will limit our discussion to a tetragonal system.

According to equation (4.5), the Raman tensor is directly related to the curvature of the underlying band dispersion relation.

$$\overleftrightarrow{\gamma}_{\mathbf{k}} = \begin{pmatrix} \gamma_{xx} & \gamma_{yx} \\ \gamma_{xy} & \gamma_{yy} \end{pmatrix} \tag{4.16}$$

where

$$\gamma_{\alpha\beta} = \frac{\partial^2 \varepsilon_{\mathbf{k}}}{\partial k_\alpha \partial k_\beta}. \tag{4.17}$$

We can expand the quasiparticle dispersion relation and the elements of the Raman tensor in terms of the Brillouin zone harmonics

$$\begin{aligned} \eta_0 &= \left[\cos(k_x) + \cos(k_y)\right]/2 \\ \eta_3 &= \left[\cos(k_x) - \cos(k_y)\right]/2 \\ \eta_0' &= \cos(k_x)\cos(k_y) \\ \eta_1 &= \sin(k_x)\sin(k_y) \end{aligned} \tag{4.18}$$

Using the above relations, the tight-binding dispersion relation can be written as

$$\varepsilon_{\mathbf{k}} = -4\bar{t}\,(\eta_0 - B\eta_0') - \mu \tag{4.19}$$

Similarly, the Raman vertex becomes

$$\overleftrightarrow{\gamma}_{\mathbf{k}} = \begin{pmatrix} 2\bar{t}(\eta_0 + \eta_3 - 2B\eta_0') & 4\bar{t}B\eta_1 \\ 4\bar{t}B\eta_2 & 2\bar{t}(\eta_0 - \eta_3 - 2B\eta_0') \end{pmatrix}. \tag{4.20}$$

The Raman tensor is then expanded in terms of quarternions

$$\overleftrightarrow{\gamma}_{\mathbf{k}} = \sum_s \gamma^s(\mathbf{k})\,\hat{\tau}^s \tag{4.21}$$

where $\hat{\tau}^s$, $s = 0, 1, 2, 3$, are the Pauli matrices. This expansion decomposes the Raman vertex into its irreducible representations, each of which can be represented by a scalar coefficient γ^s (for symmetry nomenclature, refer to Tinkham, 1960)

$$\gamma^s(\mathbf{k}) = \begin{cases} \bar{t}(\eta_0 - 2B\eta_0'), & s = 0\ (\mathrm{A}_{1g}) \\ 2\bar{t}B\eta_1, & s = 1\ (\mathrm{B}_{2g}) \\ 0, & s = 2\ (\mathrm{A}_{2g}) \\ \bar{t}\eta_3, & s = 3\ (\mathrm{B}_{1g}) \end{cases} \tag{4.22}$$

The light polarization vectors then select the elements of the Raman tensor according to the relation

$$\gamma(\mathbf{k}) = \mathbf{e}^I \cdot \overleftrightarrow{\gamma}_{\mathbf{k}} \cdot \mathbf{e}^S = \sum_s \left(\mathbf{e}^I \cdot \hat{\tau}^s \cdot \mathbf{e}^S \right) \gamma^s(\mathbf{k}). \tag{4.23}$$

We can now make the connection between the irreducible representations of the Raman vertices and the experimentally probed channels. Let us define the polarization vectors

$$\begin{aligned} \hat{x} &= (1, 0) \\ \hat{y} &= (0, 1) \\ \hat{x}' &= \frac{1}{\sqrt{2}}(\hat{x} + \hat{y}) = \frac{1}{\sqrt{2}}(1, 1) \\ \hat{y}' &= \frac{1}{\sqrt{2}}(\hat{x} - \hat{y}) = \frac{1}{\sqrt{2}}(1, -1). \end{aligned} \tag{4.24}$$

We get

$$\begin{aligned} \gamma^{xx} &= \gamma^0_{\mathbf{k}} + \gamma^3_{\mathbf{k}}, (A_{1g} + B_{1g}) \\ \gamma^{yy} &= \gamma^0_{\mathbf{k}} - \gamma^3_{\mathbf{k}}, (A_{1g} - B_{1g}) \\ \gamma^{x'x'} &= \gamma^0_{\mathbf{k}} + \gamma^1_{\mathbf{k}}, (A_{1g} + B_{2g}) \\ \gamma^{xy} &= \gamma^1_{\mathbf{k}}, (B_{2y}) \\ \gamma^{x'y'} &= \gamma^3_{\mathbf{k}}, (B_{1g}). \end{aligned} \tag{4.25}$$

We can see from the above discussion that, as mentioned in the chapter introduction, the A_{1g} symmetry channel cannot be isolated by a single Raman experiment, instead a subtraction procedure must be used. Also seen above is that an excitation which transforms as the A_{2g} symmetry is not coupled to the light. In appendix (B) we show how an orthorhombic distortion may effect the spectra seen by experiment and how the γ^{xx} polarization is comprised not just of the pure B_{1g} and A_{1g} Raman modes, but also introduces a mixing term.

In order to make things a little more concrete, we rewrite the terms of equation (4.23) in full functional form. The unrenormalized irreducible Raman vertices in the tight-binding system are given by

$$\begin{aligned}\gamma_{\mathbf{k}}^{A_{1g}} &= \gamma_{xx} + \gamma_{yy} \\ &= \frac{\partial^2 \varepsilon_{\mathbf{k}}}{\partial \mathbf{k}_x^2} + \frac{\partial^2 \varepsilon_{\mathbf{k}}}{\partial \mathbf{k}_y^2} \\ &= 2\bar{t}\left\{\cos(\mathbf{k}_x a) + \cos(\mathbf{k}_y b) - 4B\cos(\mathbf{k}_x)\cos(\mathbf{k}_y)\right\} \end{aligned} \tag{4.26}$$

$$\begin{aligned}\gamma_{\mathbf{k}}^{B_{1g}} &= \gamma_{x'y'} = \gamma_{xx} - \gamma_{yy} \\ &= \frac{\partial^2 \varepsilon_{\mathbf{k}}}{\partial \mathbf{k}_x^2} - \frac{\partial^2 \varepsilon_{\mathbf{k}}}{\partial \mathbf{k}_y^2} \\ &= 2\bar{t}\left\{\cos(\mathbf{k}_x a) - \cos(\mathbf{k}_y b)\right\} \end{aligned} \tag{4.27}$$

$$\begin{aligned}\gamma_{\mathbf{k}}^{B_{2g}} &= \gamma_{xy} \\ &= \frac{\partial^2 \varepsilon_{\mathbf{k}}}{\partial \mathbf{k}_x \partial \mathbf{k}_y} \\ &= 4B\bar{t}\sin(\mathbf{k}_x a)\sin(\mathbf{k}_y b). \end{aligned} \tag{4.28}$$

From equations (4.26), (4.27), and (4.28), one can see how the Raman vertices are affected by variations of band structure due to different next-nearest neighbour hopping strengths. Varying B can effect both the A_{1g} and B_{2g}, but has no effect on either the shape or the amplitude of $\gamma_{B_{1g}}$. The amplitude of $\gamma_{B_{2g}}$ is directly proportional to the strength of the next nearest neighbour hopping, but changes to B leave the shape unaltered. The $\gamma_{A_{1g}}$ is effected in a more subtle way, where B can actually change the shape of the vertex.

In figure (4.3) we plot the unrenormalized vertices, $\gamma_{\mathbf{k}}^{\alpha}$, for the three polarization symmetries, $\alpha = A_{1g}, B_{1g}, B_{2g}$ respectively. Panel (a) of each figure shows a surface

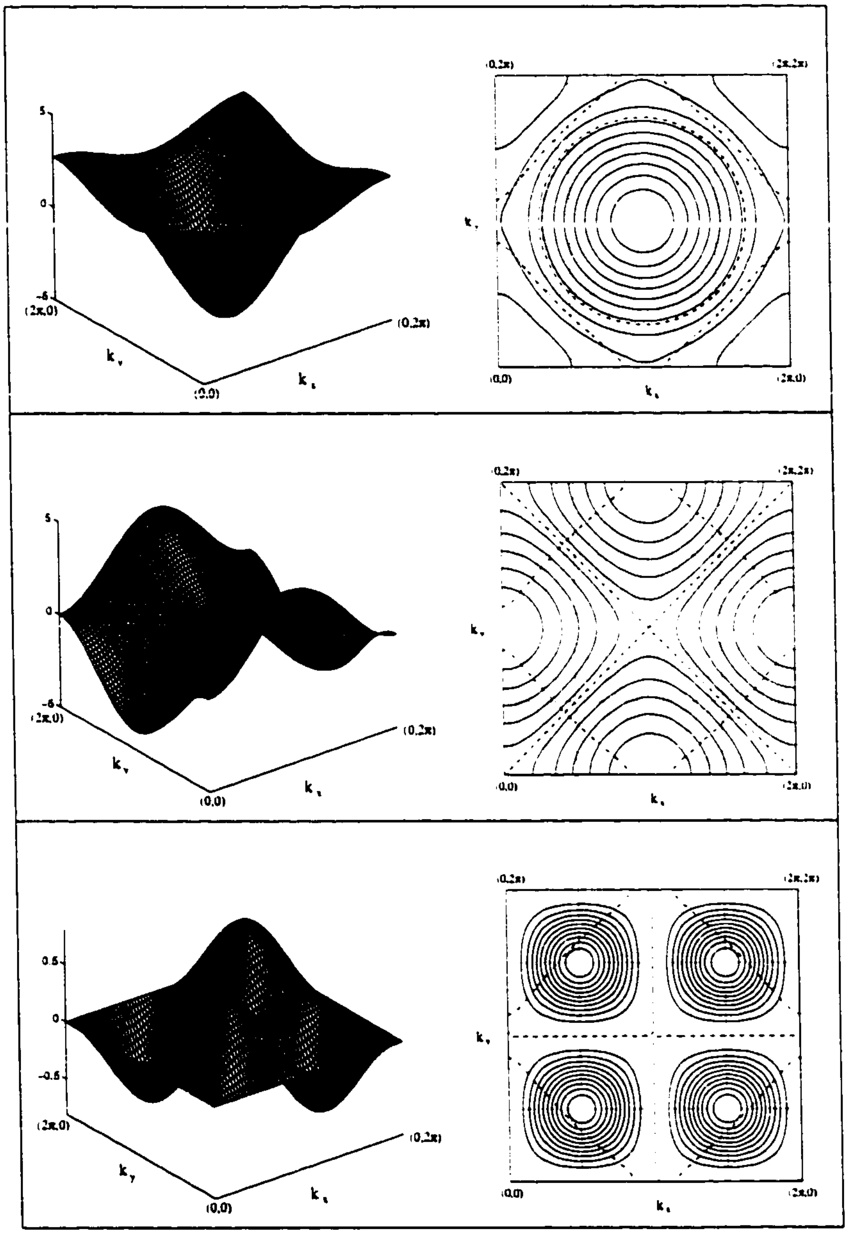

Figure 4.3: Unrenormalized Raman vertices for A_{1g}, B_{1g}, and B_{2g} polarization symmetries. The dashed line denotes the zeroes of the vertex, $\gamma_{\mathbf{k}}$, and the dashed-dotted line is the normal state interacting Fermi surface.

plot of the vertices in the first Brillouin zone. A contour plot is shown in panel (b), where the renormalized Fermi surface for a system at 20 K is superimposed and denoted by the dashed-dotted line. The zeros of the vertex functions are indicated by a dashed line.

The A_{1g} Raman vertex has the full symmetry of the underlying crystal symmetry. The zero contour is circular and encloses the (π, π) point. Depending on the electron density, or the size of the chemical potential, the Fermi surface may or may not be intersected by the zero contour of $\gamma_{A_{1g}}$. It is clear from the contour plot that A_{1g} is an average of the scattering from the whole Fermi surface.

The B_{1g} and B_{2g} Raman vertices, on the other hand, have zeroe lines which will always cross the Fermi surface in four places, along particular directions in **k** space. An average of the vertices on the Fermi surface always yields zero for tetragonal systems. The B_{1g} polarization symmetry can be seen to have its maximum along the Brillouin zone faces centered at $(\pi, 0)$ and equivalent points with nodes along the diagonals. The B_{2g} is exactly the opposite, having maximum weight centered around the $(\pi/2, \pi/2)$ and equivalent points. Zeros of the function fall on vertical and horizontal lines intersecting the points $(n\pi, 0)$ and $(0, n\pi)$, with $n = 0, 1, 2$. Anticipating an additional weighting to come from the Fermi surface, it can be seen that the B_{2g} scattering channel is most sensitive to those **k** points along the diagonals of the Brillouin zone, while the B_{1g} is zero (or very small) at these points. The B_{1g} has its largest weightings at points in the Brillouin zone where a superconducting gap with $d_{x^2-y^2}$ symmetry is expected to have maximum amplitude. One can now guess that the B_{1g} spectrum will be an effective probe of the gap amplitude in a d-wave superconductor, while the B_{2g}, preferentially selecting states along the diagonal, will directly probe the low lying quasiparticle excitations.

Coulomb screening can have a large effect on the A_{1g} channel in the tetragonal model while having no effect whatsoever on the B_{1g} and B_{2g} channels. This screening is very dependent on band structure (Krantz and Cardona 1994; Devereaux, Einzel, and Stadlober 1994) and so a very accurate description is required of not only the shape of the Fermi surface, but also the second derivative of the band structure. Effects such as this can make the A_{1g} very difficult to interpret so consensus is that

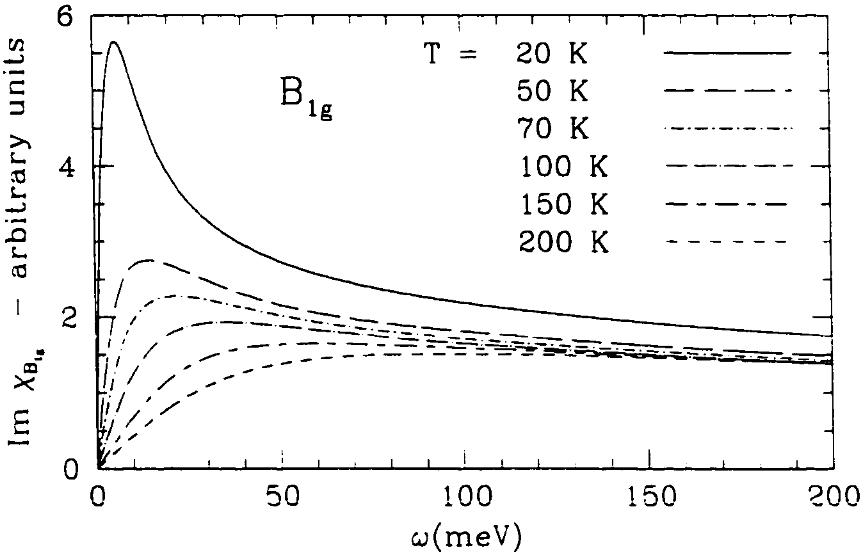

Figure 4.4: Normal state B_{1g} spectra as a function of ω at various temperatures.

only the B_{1g} and B_{2g} spectra should be focused on.

In an orthorhombic system, the B_{2g} channel remains unaffected by Coulomb screening effects while the B_{1g} channel is partially screened. This is explained in appendix (B). Recall that in experiment, the A_{1g} spectra could not be resolved by itself with any particular choice of polarization. While in a tetragonal system the A_{1g} channel can be isolated by performing two sets of experiments, the situation may be much more complicated in an orthorhombic system as mixing of the A_{1g} and B_{1g} vertices are naturally included. The mixing is enhanced when Coulomb screening is taken into account.

4.3 Raman spectra

4.3.1 Computational Results

The normal state Raman spectra for the B_{1g} scattering channel is shown in figure (4.4) for a set of temperatures ranging from 20 K to 200 K. The electronic background due to inelastic scattering is clearly visible in these plots. While the low frequency

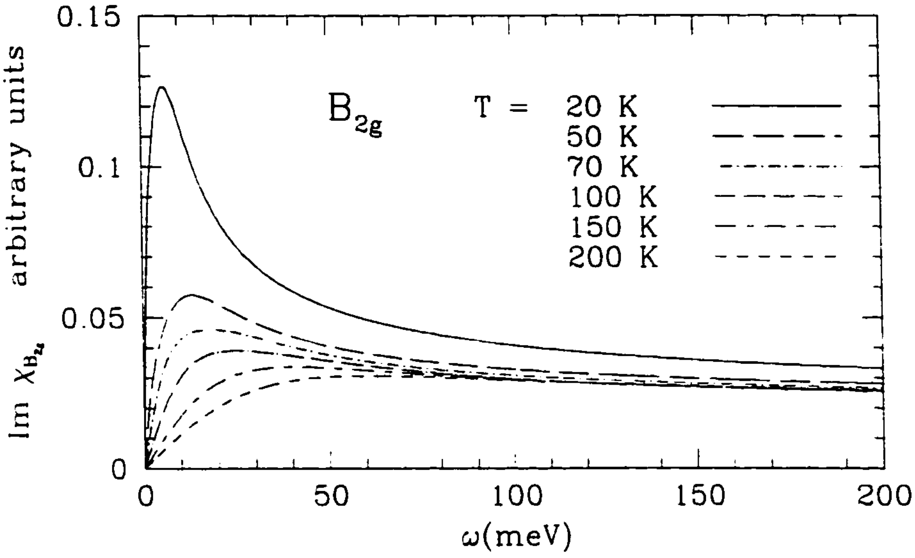

Figure 4.5: Normal state B_{2g} spectra as a function of ω at various temperatures.

behavior is linear. the high frequency spectra are relatively flat and weakly temperature dependent. The main temperature dependence is seen at lower frequencies at low temperatures. a peak begins to form and the zero frequency slope quickly increases. The growth and the change in the frequency of the peak, as we will discuss later, can be associated with the temperature dependent inelastic scattering rate. For completeness, we show the normal state B_{2g} spectra in figure (4.5). Except for the relative intensities, the two normal state spectra are virtually indistinguishable at this level.

Earlier calculations (Jiang and Carbotte 1996) based on the Eliashberg formalism used a modified $\alpha^2F(\omega)$ taken from tunneling experiments on conventional superconductivity. While these calculations resolved the large electronic background, the low frequency behavior of the normal state was markedly different. They found an ω^3 dependence at small T and small ω, not linear behaviour as we have. This is due to the difference in the low frequency $\alpha^2F(\omega)$. In the case of spin fluctuations, this behavior is linear, leading to the linear dependence in the response shown.

Upon entering the superconducting state however, large differences in the various scattering channels become apparent. In figures (4.6), (4.7), and (4.8) we plot the

Raman spectra for the B_{1g}, B_{2g}, and A_{1g} scattering channels respectively. The spectra for a range of temperatures are shown for all three symmetry channels. The 125 K curve (dotted line) is in the normal state, while the 100 K curve (long-dashed short-dashed line), also in the normal state, corresponds to the spectrum at T_c. Temperatures below 100 K are all in the superconducting state. As the temperature is lowered below the superconducting critical temperature, T_c, the low frequency excitation spectra is redistributed with the low frequency spectra being suppressed in the case of the A_{1g} and B_{1g} symmetries and a peak building at higher frequencies. At very high frequencies, the spectra remain relatively unchanged.

First we discuss the B_{1g} channel. As the temperature is decreased from 125 K to 100 K, the low frequency slope increases as the scattering rate decreases. As T is decreased below the critical temperature, T_c, the low frequency spectral weight is decreased while a very broad peak begins to form centered about $\omega = 40$ meV at 90 K. The low frequency behaviour becomes convex as opposed to the concave features of the normal state. As the temperature is lowered even farther, the slope of the low frequency turn on becomes smaller and smaller as the ω dependence begins to look more cubic. We will return to the low frequency behaviour of the B_{1g} scattering channel a little later.

The peak structure is also temperature dependent. As the temperature decreases, the high frequency peak becomes larger in amplitude and begins to narrow slightly. The process continues until approximately 20 K (short-dashed line) when the peak height, width, and central frequency saturate. The frequency at which the peak is centered is approximately 54 meV which corresponds to $2\Delta_{max}$, where Δ_{max} is the maximum value of the gap edge on the Fermi surface. As shown in earlier work using a BCS framework, the frequency at which the peak occurs in the superconducting state is related to $2\Delta_{max}(T)$ (Branch 1995; Branch and Carbotte 1995). In the normal state, the peak in the spectrum is related to the details of the inelastic scattering, namely $1/\tau_{eff}(\omega)$, the effective low frequency inelastic scattering rate.

The shape of the B_{2g} spectra are different. As the temperature is lowered from 125 to 100 K, the low frequency slope increases as was the case for the B_{1g} channel. However, as the temperature is lowered through T_c, the low frequency spectral weight

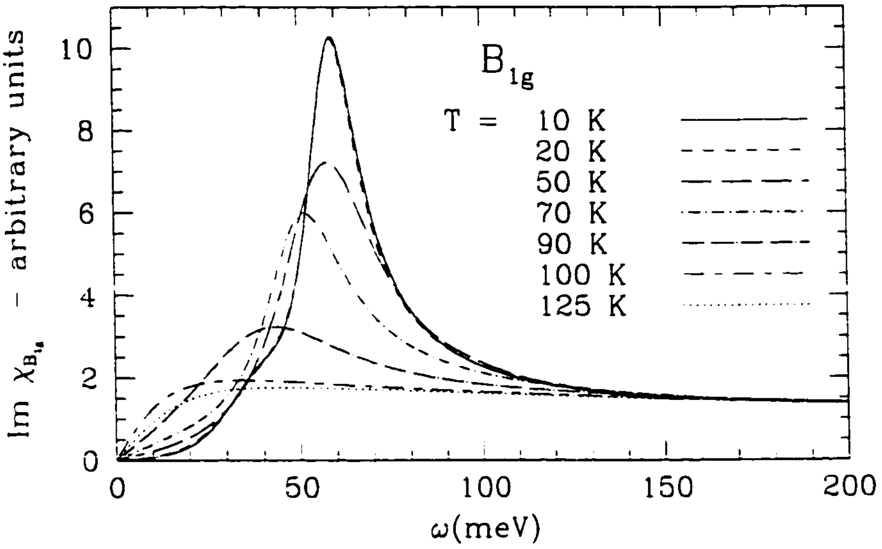

Figure 4.6: Superconducting B_{1g} Raman spectra as a function of ω for various temperatures.

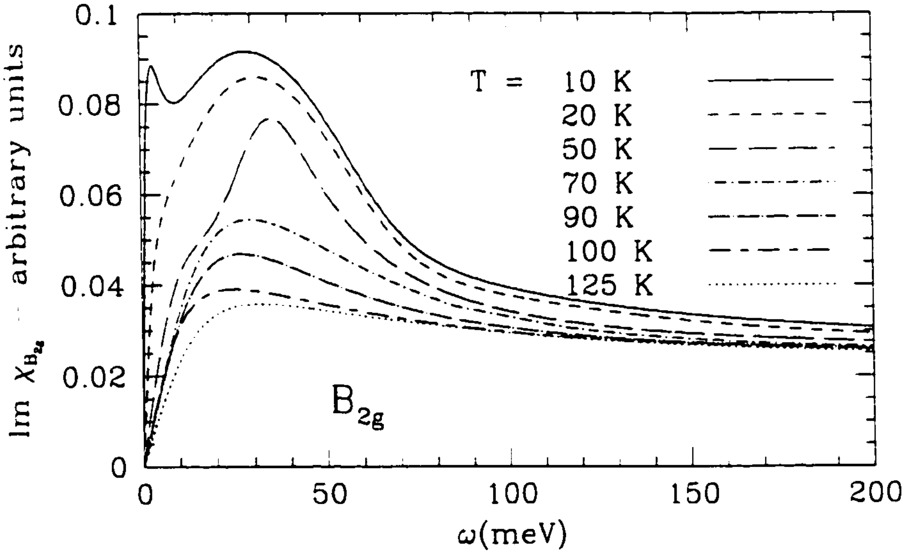

Figure 4.7: Superconducting B_{2g} Raman spectra as a function of ω for various temperatures.

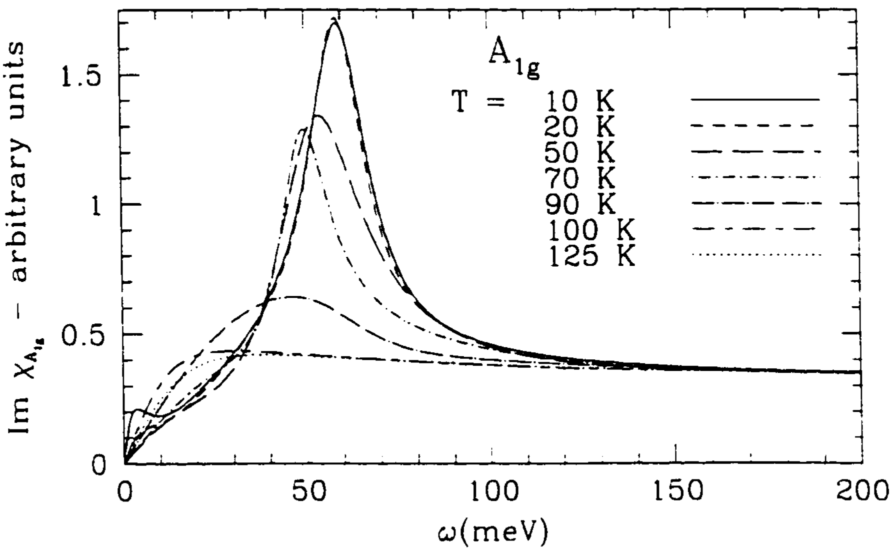

Figure 4.8: Unscreened superconducting A_{1g} Raman spectra as a function of ω for various temperatures

continues to increase. This is unlike the B_{1g} spectra where a suppression of low ω spectral weight was observed. At $T = 10$ K, a second peak develops at low frequencies, which is related to the scattering rate of the normal state excitations in the nodal region of the gap. This contribution is present at higher temperatures also but cannot be distinguished from the peak at higher frequencies due to superconductivity.

The unrenormalized A_{1g} response has an interesting low frequency behaviour. The normal state curves remain similar to those seen in both the B_{1g} and B_{2g} scattering channels. As the temperature is reduced below the superconducting critical temperature, a redistribution of the low frequency spectral weight is clearly visible with a fairly sharp peak developing at the same frequency as in the B_{1g} spectrum.

At very low frequencies the A_{1g} response is linear in ω for all temperatures. As the temperature is reduced from 125 K to 100 K the slope of the low frequency response increases. As the system is cooled below the critical temperature the slope initially decreases as the number of low lying states is gapped out.

Compare the above results with those from BCS calculations, figures (4.9) and

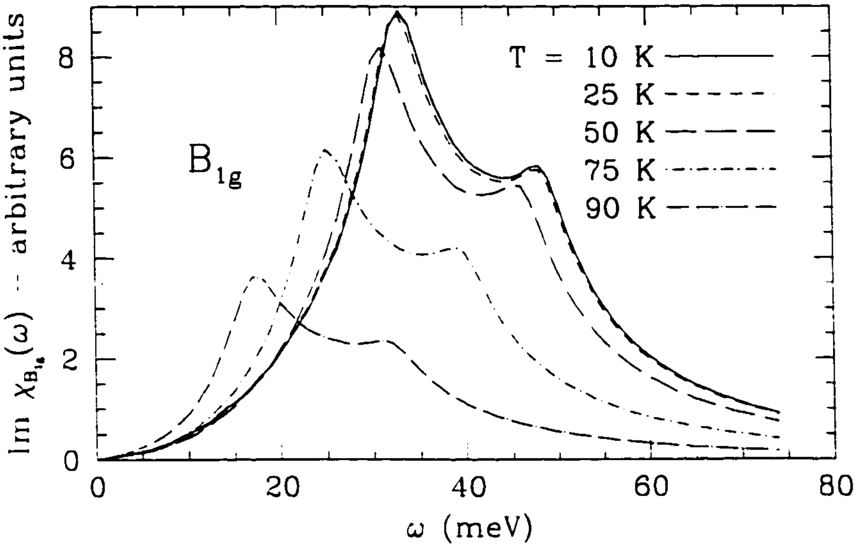

Figure 4.9: The B_{1g} Raman spectra for various temperatures in the BCS regime.

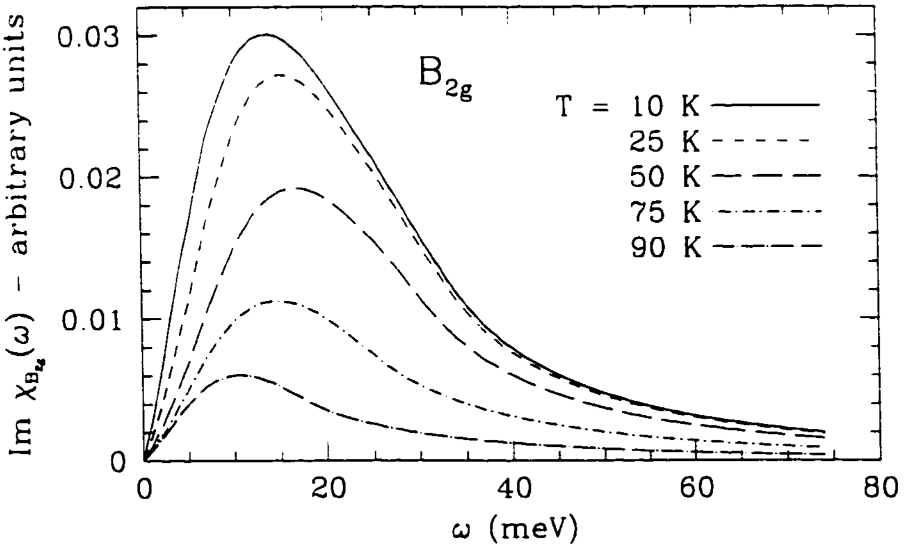

Figure 4.10: The B_{2g} Raman spectra for various temperatures in the BCS regime.

(4.10) which where obtained from self-consistent calculations in the weak-coupling regime using a frequency independent version of the MMP model (Branch 1995; Branch and Carbotte 1995; Branch and Carbotte 1996). The band structure parameters used were identical to those of the above strong-coupling calculations, namely, $B = 0.16$ and $\langle n \rangle = 0.4$. Just a quick cursory glance shows several obvious differences, however, between the BCS and Eliashberg Raman spectra.

The low frequency behaviour of the B_{1g} scattering channel clearly does not change with temperature (figure (4.9)). The entire response, however, vanishes above the critical temperature as the electrons cannot absorb energy from the photons and still conserve both momentum and energy.

In the superconducting state, the breaking of Cooper pairs results in two excitations which can conserve both momentum and energy. As the temperature approaches T_c from below, the number of pairs in the condensate is reduced leading to a decrease in the observed intensity which eventually disappears for $T > T_c$.

That a finite response due to inelastic light scattering from normal state quasiparticles in the $\mathbf{q} \to 0$ limit is seen at all may be surprising. To explain why, consider the density-density correlation function,

$$S(\mathbf{q}, \omega) = \langle [\rho_{\mathbf{q}}(t), \rho_{\mathbf{q}}(0)] \rangle \tag{4.29}$$

where

$$\rho_{\mathbf{q}} = \sum_{\mathbf{k}} c^{\dagger}_{\mathbf{k}+\mathbf{q}} c_{\mathbf{k}} \tag{4.30}$$

is the electron density. $S(\mathbf{q}, \omega)$ is the electronic structure function probed by inelastic neutron scattering. The f-sum rule (Pines and Nozieres 1966) states that

$$\int_{-\infty}^{\infty} d\omega \; \omega \; S(\mathbf{q}, \omega) \propto q^2. \tag{4.31}$$

In the limit $\mathbf{q} \to 0$, the integral in equation (4.31) goes to zero and therefore $S(\mathbf{q}, \omega)$ approaches zero in the long wavelength limit. One may then ask why the Raman spectra show a finite response in the normal state for the long wavelength limit. The difference between $S(\mathbf{q}, \omega)$ and $\tilde{S}(\mathbf{q}, \omega)$ is that the Raman structure factor is an effective density - effective density correlation function. It has been shown that in order to get a finite Raman response in the normal state as $\mathbf{q} \to 0$ at least one of the following conditions must be met (Kosztin and Zawadowski 1991): 1) contribution due to interlayer processes, and 2) presence of either inelastic or elastic scattering processes. In our model, there is no contribution from interband processes, however, there is a very strong inelastic contribution seen out to very high frequencies.

The above argument can also be used to explain why the observed intensity of the Raman spectra is so large in the high-T_c compounds relative to the conventional materials. Simple metals are usually well modeled by parabolic energy bands, a reasonable approximation for most conventional materials. The Raman vertex, given by the curvature of the band dispersion, will be a constant for parabolic bands, making the effective particle density, $\tilde{\rho}$ (equation (4.3)), approach ρ, the real particle density. For this case, $\tilde{S}(\mathbf{q},\omega)$ is identical to $S(\mathbf{q},\omega)$ which, in the long wavelength limit, is zero. At the momentum transfer of light, $S(\mathbf{q},\omega)$ is surely small.

Another major difference between the B_{1g} spectra in the BCS and Eliashberg formalisms is the double peak structure seen in the weak-coupling calculations. The second peak located at higher frequencies in the BCS B_{1g} spectra is a reflection of the van Hove singularity in the underlying density of states (see figure (2.18)) which is visible for a certain choice of parameters (Branch 1995; Branch and Carbotte 1995; Devereaux, Virosztek, and Zawadowski 1996; Strohm and Cardona 1997). For a saddle-point in the single particle dispersion located just off the Fermi surface at energy ε_{vH}, a large peak would occur at the energy $\sqrt{\varepsilon_{vH}^2 + \Delta^2}$. No such peak has been observed in the numerous experiments performed on almost every cuprate material. Clearly an explanation for its absence is needed since both the tight binding band model and LDA band structure calculations indicate that a van Hove singularity must be present in the density of states (Pickett 1989). The strongly coupled model gives a simple out to this problem. Recall the discussion on energy renormalization due to self-energy effects in section (2.5). The sharp peak in the interacting quasiparticle density of states is "pinned" to the Fermi surface and will not be seen as a secondary peak. The non-interacting van Hove is damped out and will no longer be resolved in the Raman spectra.

4.3.2 Effective Scattering Rates

Comparison of the Raman response function and the EM response function shows that the formalism of the two relations is very similar, the main difference being the vertex functions. The normal state response functions are identical except that the EM vertex involves the first derivative of the dispersion relation, $\varepsilon_{\mathbf{k}}$ and the second derivative for the Raman response. This similarity suggests that in making the definition

$$\sigma^R(\omega) = i\frac{\Pi^R(i\nu_n \to \omega + i\delta^+)}{\omega} \tag{4.32}$$

where

$$\Pi^R(i\nu_n) = \chi_{\gamma\gamma}(i\nu_n) - \chi_{\gamma\gamma}(0) \tag{4.33}$$

one might be able to perform the same type of analysis as for the optical conductivity and extract such information as an effective scattering rate. In equation (4.32) $\sigma^R(\omega)$ can be viewed as the Raman analogue of the optical conductivity. The close correspondence between the EM response and the Raman response has been noted before, however, no attempt to use this similarity to extract the full frequency dependence of the effective scattering rates has been done to our knowledge.

In analogy to the frequency dependent complex conductivity an effective scattering rate can be defined by

$$\begin{aligned} \frac{1}{\tau_R^*(\omega)} &= \omega\frac{\sigma_1^R(\omega)}{\sigma_2^R(\omega)} \\ &= -\omega\frac{\Pi_2^R(\omega)}{\Pi_1^R(\omega)} \end{aligned} \tag{4.34}$$

where the subscript 1 (2) refers to the real (imaginary) component of the complex function.

One can also make a definition similar to that of the extended Drude model,

$$\sigma^R(\omega) = \langle\gamma^2\rangle\frac{1}{\Gamma(\omega) - i\omega\frac{m^*(\omega)}{m}} \tag{4.35}$$

where $\Gamma(\omega)$ is an effective scattering rate, $m^*(\omega)/m$ is an effective mass renormalization factor, and $\langle\gamma^2\rangle$ plays the same role as the plasma frequency in the optical

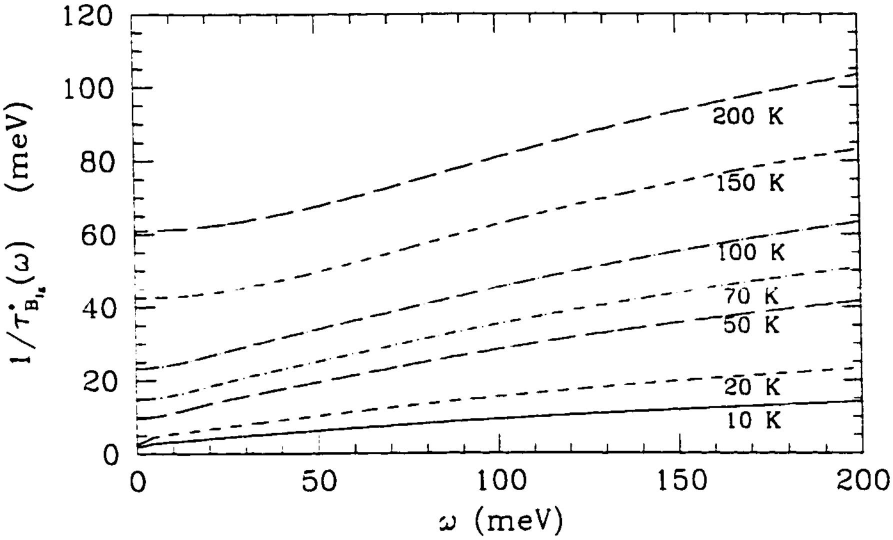

Figure 4.11: Effective scattering rate, $1/\tau^*(\omega)$, as a function of ω extracted from the B_{1g} normal state Raman spectra.

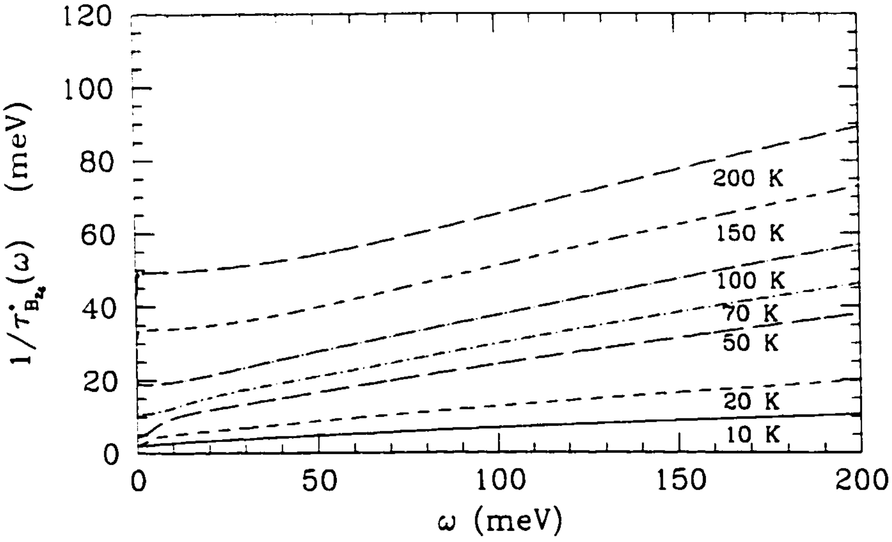

Figure 4.12: Effective scattering rate, $1/\tau^*(\omega)$, as a function of ω extracted from the B_{2g} normal state Raman spectra.

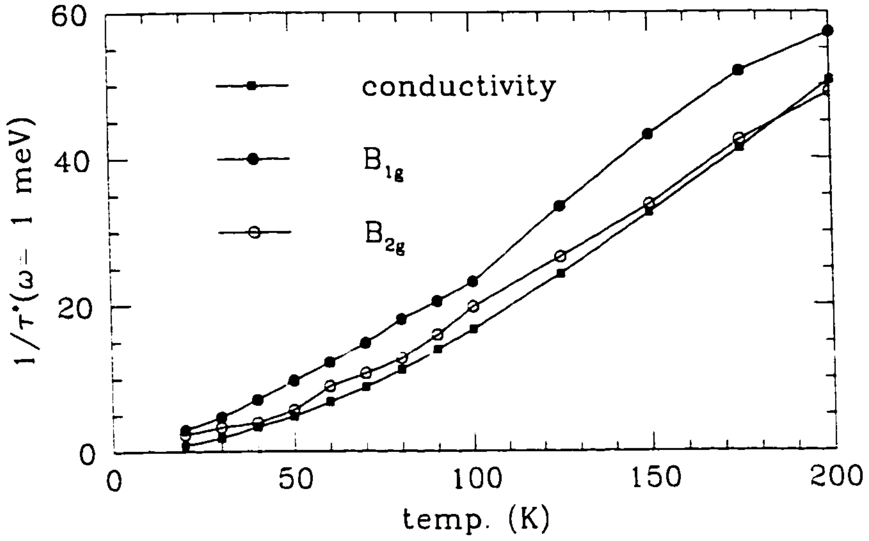

Figure 4.13: Comparison of $1/\tau^*(\omega = 1.0 \text{ meV})$ for normal state optical conductivity and Raman B_{1g} and B_{2g} spectra.

conductivity. While equation (4.35) is a natural extension, one does not know what to assume for the value of $\langle\gamma^2\rangle$ as the sum rule does not exist in our model. For this reason, we will only extract values for $1/\tau^*(\omega)$ in which all unknown constants in $\sigma^R(\omega)$ cancel out and only the ratio of the real and imaginary components of $\Pi^R(\omega)$ is important

In figures (4.11) and (4.12) we plot the function $1/\tau^*(\omega)$ in the B_{1g} and B_{2g} scattering channels respectively for a set of temperatures ranging from 10 K to 200 K. The first thing to notice is that the scattering rates extracted from the B_{1g} spectra are larger than the respective B_{2g} data over the entire frequency range. This is consistent with the quasiparticle scattering rates which come from the self-energy, where we saw that $\Gamma_{\mathbf{k}}(\omega) = -2\, Im\Sigma_{\mathbf{k}}(\omega)$ was greatest near the points $(\pm\pi, 0)$, $(0, \pm\pi)$ and smallest along the diagonals of the Brillouin zone.

Comparison of the Raman scattering rates with the optical $1/\tau^*(\omega)$ plotted earlier in figure (3.9), shows that the effective $1/\tau^*(\omega)$ for the Raman spectra have less variation as a function of frequency. The value of $1/\tau^*(\omega)$ at $\omega = 200$ meV is a little over five times larger than $1/\tau^*(\omega = 0)$ for the conductivity at a temperature

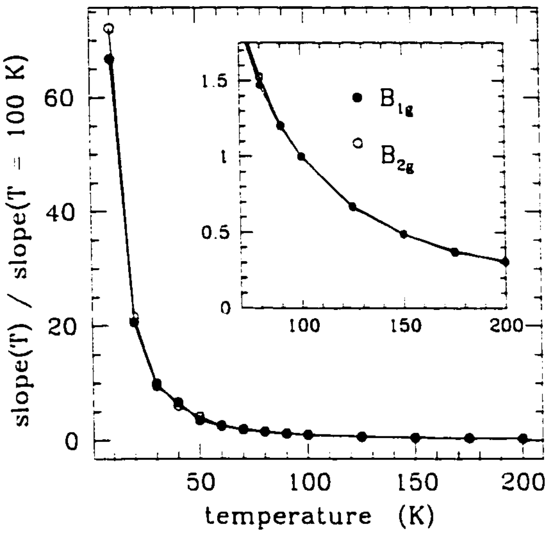

Figure 4.14: Normalized slopes of the zero frequency normal state B_{1g} and B_{2g} Raman responses.

of $T = 100K$, while in the Raman data, the scattering rates change by less than a factor of three over the same frequency range for the same value of T.

The values of $1/\tau^*(\omega = 1\text{meV})$ are plotted in figure(4.13) for the B_{1g}, B_{2g} and the conductivity for comparison purposes. Note that through all the temperature range, except the one point at $T = 200$ K, the Raman data are consistently larger than that of the conductivity, although for $1/\tau^*_{B_{2g}}$, not by very much.

4.3.3 Temperature Effects

Earlier in the chapter, we briefly discussed the effects of temperature on the Raman spectra over the whole frequency range. In this section, we will investigate more closely the effects of changing temperature on the frequency dependence of the Raman intensity at small ω in both the normal and superconducting states. Understanding the low frequency behaviour is very important as it is this ω dependence which is used to identify the order parameter symmetry (Devereaux and Einzel 1995).

We start this discussion by looking at changes to the low frequency behaviour of

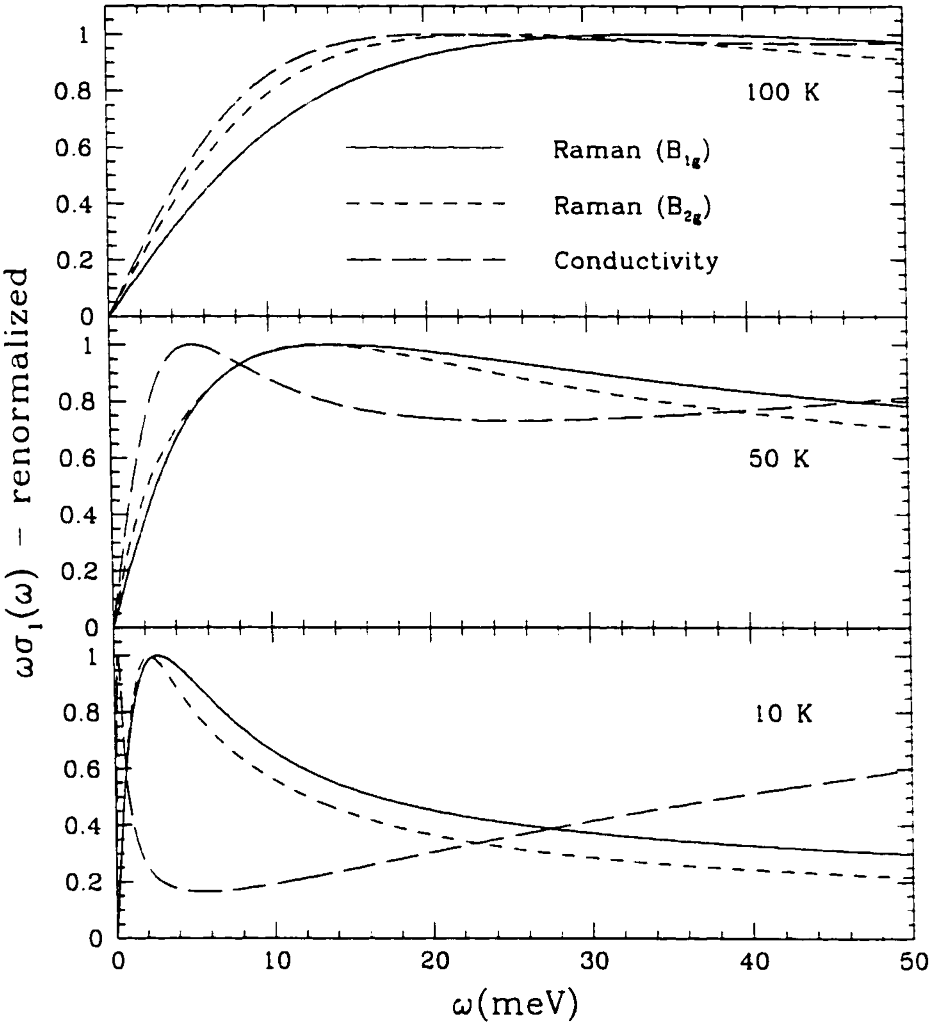

Figure 4.15: Comparison of $\omega\sigma_1(\omega)$ for the two Raman modes, B_{1g} and B_{2g}, and the optical conductivity at $T = 100$ K, 50 K, and 10 K.

the normal state Raman spectra as a function of temperature. The slope of $Im\ \chi_{\gamma\gamma}(\omega)$ at zero frequency is plotted as a function of temperature for the normal state B_{1g} and B_{2g} scattering channels in figure (4.14) normalized to unity at the $T = 100K$. An almost exponential rise is seen in the slopes for both scattering channels. In order to understand why the low frequency slope makes such a dramatic rise at low T, we will make comparisons with the optical conductivity results from the last chapter. Equation (4.32) indicates that as $\omega \to 0$, the value of the σ_1 is given by

$$\sigma_1^R(\omega \to 0) = -\frac{\partial \Pi_2^R(\omega)}{\partial \omega}|_{\omega=0} \tag{4.36}$$

so we can identify the zero frequency slope of the Raman spectra at as the $\omega \to 0$ limit of σ_1^R. The conductivity undergoes a similar sharp rise as the temperature approaches $T = 0$ since the effective low ω scattering rate is drastically reduced.

We saw in the last section that the effective inelastic scattering rates as seen by the conductivity and Raman probes are larger in the Raman case. In order to make this a little clearer, we plot the imaginary part of the response, $\Pi_2(\omega)$ (or $\omega\sigma_1(\omega)$, for the two Raman symmetries and the optical conductivity in figure (4.15) at three different temperatures: $T = 10$ K, 50 K, and 100 K. As the absolute amplitude of these curves are very different we have normalized them in such a way that the maximum value of the low ω peaks is one for comparison purposes. The frequency at which this peak is located is related to the effective scattering rates seen by the probes. At the lowest temperature, the B_{1g} peaks slightly higher than the B_{2g} indicating a slightly larger effective scattering rate. On the other hand, the peaks in both the B_{1g} and B_{2g} Raman responses occur at a value of ω several times larger than the optical response. As the temperature is increased, the scattering rates for all three channels increase and the B_{2g} and optical scattering rates begin to coalesce.

Next, we investigate the effects of inelastic scattering on the low frequency Raman behaviour in the superconducting state. We begin the discussion with the B_{1g} scattering channel. Shown in figure (4.16) is the same data as in figure (4.6), but in this case for a small frequency range, $0 \leq \omega \leq 50$ meV. The dotted line corresponds to the normal state response at the T_c (100 K). A corresponding curve is shown for nine other temperatures down to 10 K with T decreasing with step size 10 K. Clearly, the

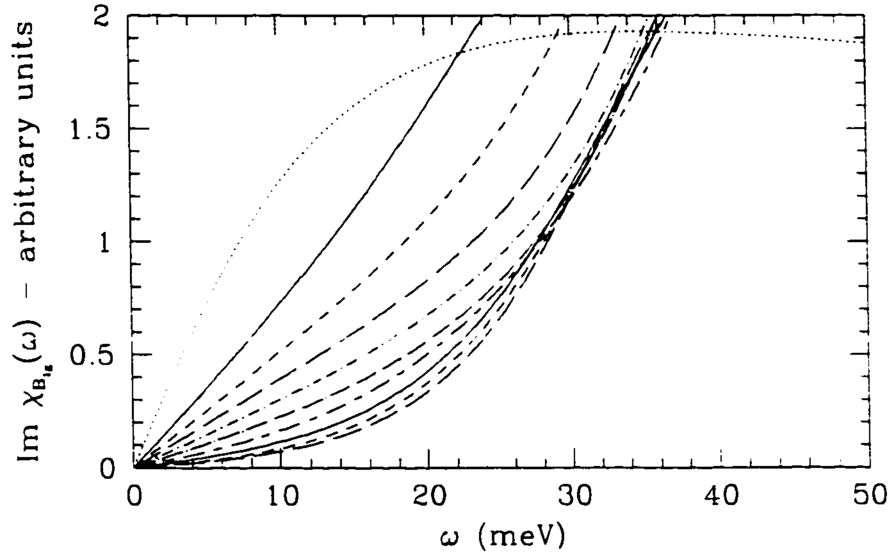

Figure 4.16: Superconducting state B_{1g} response at low frequencies.

low frequency behaviour of the response is linear in frequency. As the temperature is dropped below T_c, the low frequency spectral weight is reduced, but, unlike the BCS case in which even at temperatures just below T_c the B_{1g} spectrum has an ω^3 dependence, the low frequency behaviour of the response remains linear. These linear frequency dependences are observed to fairly low temperatures.

Figure (4.17) shows the superconducting data for $Im\ \chi_{B_{1g}}(\omega)$ at 50 K. The spectrum is shown with best fit ω and ω^3 curves denoted by dotted lines. The inset to the figure shows the same data, but on a log-log plot. The low frequency part of the frequency spectrum is dominated by a linear term until almost 10 meV. The ω^3 term only gains dominance above 25 meV.

As the temperature is lowered even further, the influence of the inelastic scattering on the low frequency behaviour is reduced, just as the scattering rates in the optical conductivity were reduced. Figure (4.18) shows a plot of the B_{1g} Raman spectrum, but in this case for a temperature of 20 K. Once again, a linear contribution to the low frequency part of the response channel is present, however, it only dominates the response below frequencies of 2 - 3 meV. The ω^3 dependence dominates at frequencies

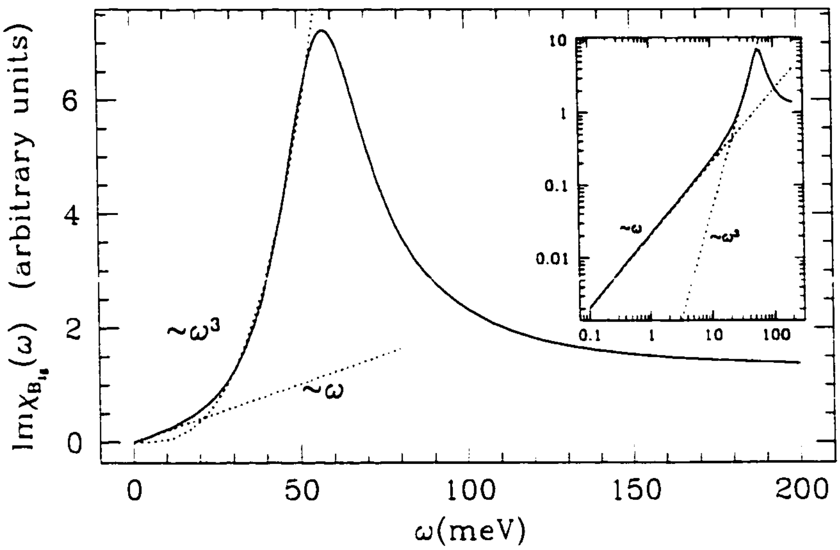

Figure 4.17: ω^3 and ω fits to the low frequency $Im\ \chi_{B_{1g}}(\omega)$ at T= 50 K.

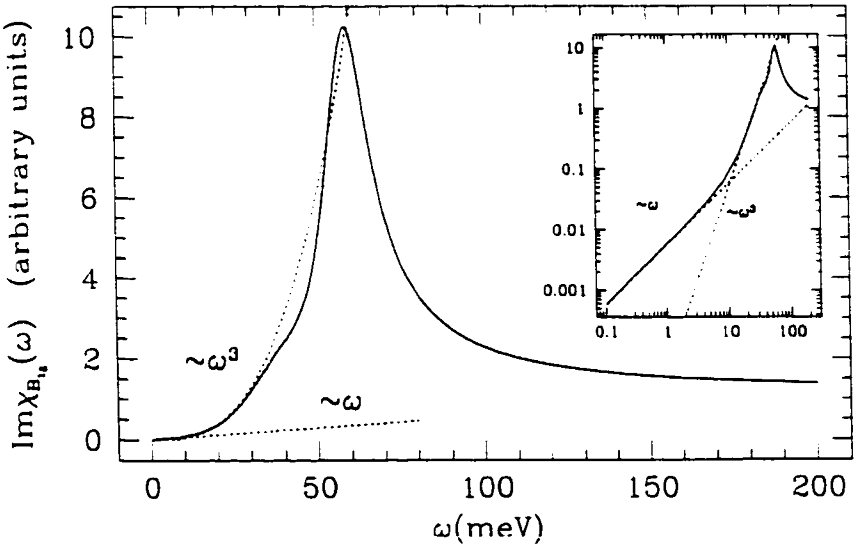

Figure 4.18: ω^3 and ω fits to the low frequency $Im\ \chi_{B_{1g}}(\omega)$ at T= 20 K.

above 10 meV. Plotted on the usual scale along with the best fit lines, the linear term is not noticeable on this scale and could easily be missed. The ω^3 term is seen to dominate the low frequency spectrum.

Linear behaviour at low frequencies is observed in the B_{1g} spectra of overdoped cuprate superconductors. Recently, it was proposed that increased disorder in the overdoped materials could act as static (impurity) scattering centers and that the resulting elastic scattering would lead to a linear term in the low frequency Raman response (Devereaux and Kampf 1997). In our model, the introduction of impurities is not needed, the inelastic scattering included in the strong-coupling calculations naturally providing such a linear term in pure samples.

At optimal doping, such linear terms are not seen in the B_{1g} spectra of certain superconductors. The difference between the optimally doped and overdoped experimental data may be due to the so called "collapse of the scattering rate" observed in the microwave surface resistance data (Bonn et al. 1992; Bonn et al. 1993; Nuss et al. 1991). Our model could be made consistent with these results by including a low frequency suppression of bosonic spectral density which would decrease the low frequency inelastic scattering. Such a low frequency cut off has been introduced to model the low frequency conductivity data (Schachinger and Carbotte 1997).

4.4 Impurity Effects

Impurity scattering was seen to introduce large effects in the observed frequency dependent conductivity. Impurities should also have an effect on the Raman spectra. Devereaux and Kampf have shown that impurity scattering can lead to a linear term appearing in the low frequency B_{1g} scattering channel using a weak coupling calculation. We have shown that a similar term may also appear due to inelastic scattering even in pure samples. Addition of impurities to this system would be expected to enhance the linear term in the low frequency spectrum.

Wu and Carbotte (Wu and Carbotte 1997) have shown using a model similar to that of Lee (Lee 1993) that impurity scattering should lead to a universal slope in the B_{2g} polarization spectrum. No universal slope should be seen in the B_{1g} spectra.

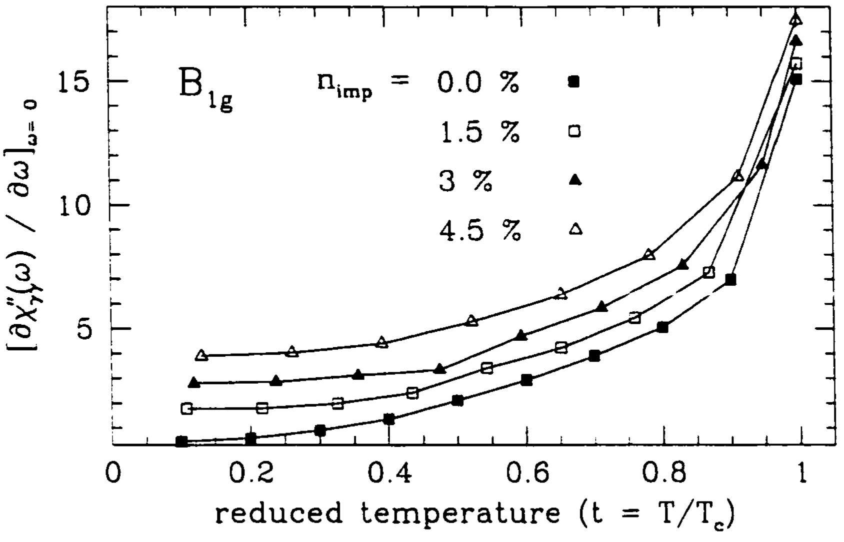

Figure 4.19: The zero frequency slope of the B_{1g} Raman response, $\left.\frac{\partial\chi''_{\gamma\gamma}(\omega)}{\partial\omega}\right|_{\omega=0}$, as a function of reduced temperature for various impurity concentrations in the unitary scattering limit.

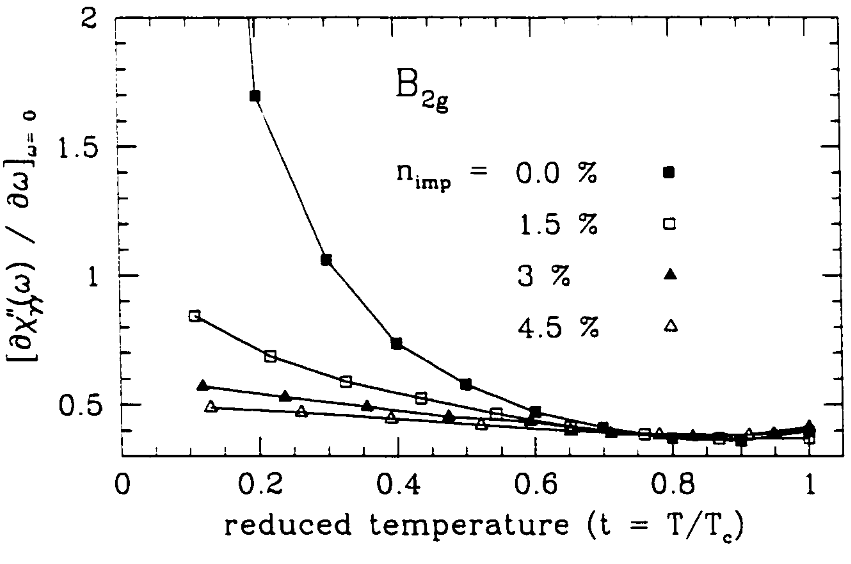

Figure 4.20: The zero frequency slope of the B_{2g} Raman response, $\left.\frac{\partial\chi''_{\gamma\gamma}(\omega)}{\partial\omega}\right|_{\omega=0}$, as a function of reduced temperature for various impurity concentrations in the unitary scattering limit.

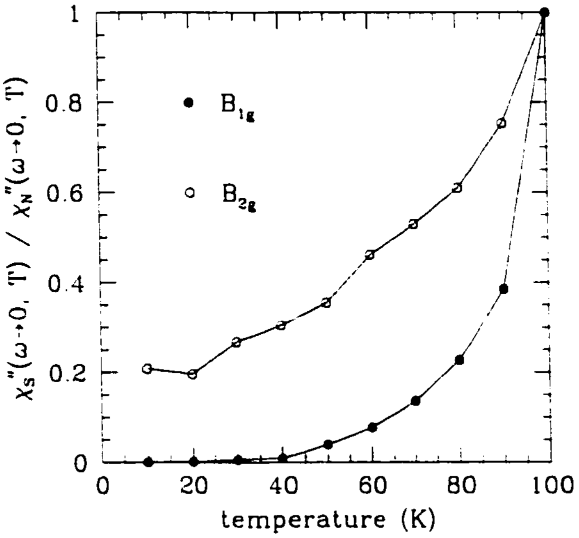

Figure 4.21: $\frac{\chi_S''(\omega\to0,T)}{\chi_N''(\omega\to0,T)}$ as a function of temperature for the pure case.

In figure (4.19), the slope of the imaginary part of the Raman susceptibility at zero frequency is plotted as a function of reduced temperature at four different impurity concentrations. In all cases the slopes were quickly reduced as the temperature was lowered below T_c. By $t = 0.9$, the slope of the pure channel has been reduced to half its value at T_c. Compare this to the normal state values of the zero frequency slope shown in figure (4.14). This curve indicates a near exponential increase in the slope as the temperature approaches zero. The decrease in the superconducting state values is due to the opening of the superconducting gap in the the quasiparticle excitation spectrum. As the B_{1g} Raman vertices favourably select those momentum states near the Fermi surface close the to maximum of the energy gap, the B_{1g} channel is sensitive to momentum states which have finite gaps and is zero along the nodes. At $T = 0$, the zero frequency slope vanishes for the pure case. As impurities are added to the system, the values of the slope increase, the spectrum being sensitive the residual normal state carrier density filling the low energy states inside the nodal regions of the Brillouin zone. As predicted, the low temperature slope of the B_{1g} polarization spectrum does not converge to a universal value independent of n_{imp}. Instead, the slope appears to increase monotonically with impurity concentration.

Now compare this to the results of the zero frequency slope of $Im\ \chi_{B_{2g}}(\omega)$. This channel is strongly weighted in regions of the Brillouin zone at the nodes of the gap near the Fermi surface. This channel should therefore be sensitive directly to the low frequency excitations along the gap nodes.

The slope of $Im\ \chi_{B_{2g}}(\omega)$ at zero frequency in the pure case shows almost exponential behaviour as the temperature is lowered below the critical temperature. This is similar behaviour observed in the normal state data, as seen in figure(4.14), however, with a much smaller amplitude as seen in figure(4.21) where we plot $\chi_s''(T)/\chi_n''(T)$ for comparison. Although the B$_{2g}$ is sensitive to a region along which very low energy normal state excitations are possible, the number of such states available for excitations is reduced.

As impurities are added, the slope of the zero frequency response is reduced. More impurities cause an even further decrease in the slope, however, even at impurity concentrations as large as 4.5 %, the zero frequency slope has not yet converged to a constant value at low temperatures. This is not the behaviour predicted earlier, however, the data does seem consistent with the idea that, eventually, with a high enough impurity concentration in the unitary scattering limit, the system will settle down with a constant zero frequency slope.

An explanation for the saturation of the conductivity data, but not the B$_{2g}$ Raman data at low frequency is needed. The hint as to the solution can be seen in an earlier figure (4.15). The effective scattering rates in the Raman response is much larger than that of the EM response, and hence, the $\omega \to 0$ limit of the conductivity. In the conductivity case, at low temperatures the optical scattering rate due to inelastic scattering effects is small enough that the impurity scattering contribution dominates. In the B$_{2g}$ Raman mode, the inelastic scattering dominates to a much lower temperature. A large impurity concentration is needed in order to have the effective scattering rates be dominated by impurity effects. Our calculations are not inconsistent with the above simple models, they simply include more physics with the scattering rates getting contributions from both elastic (impurity) and inelastic (spin-fluctuation) scattering.

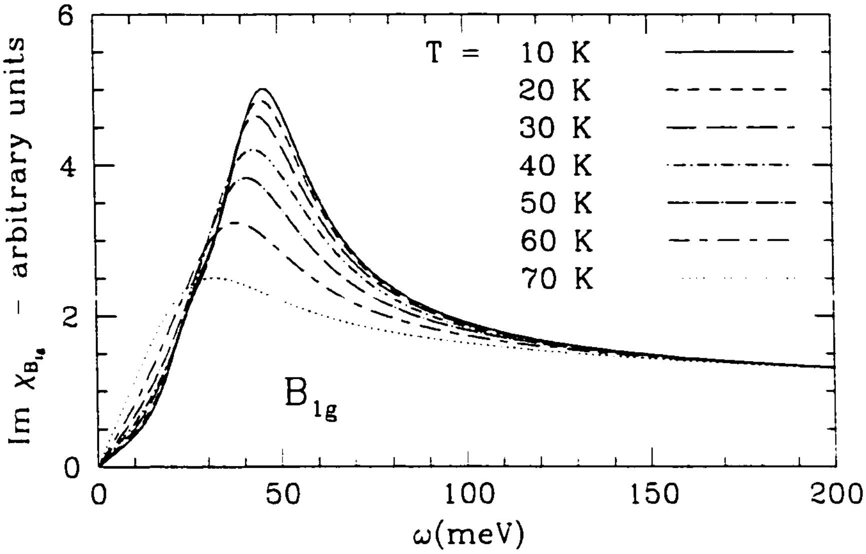

Figure 4.22: Superconducting state B_{1g} spectrum as function of ω for various temperatures $n_{imp} = 4.5$ % in the unitary scattering limit.

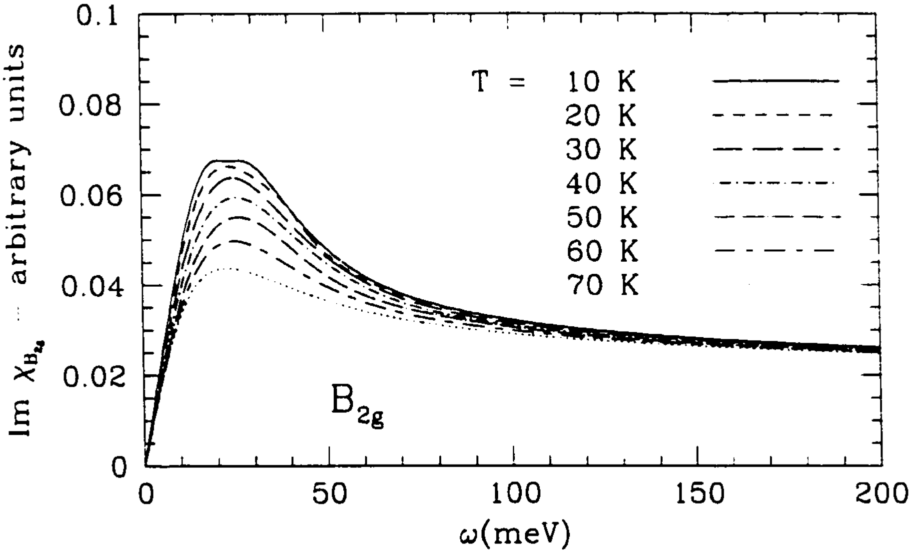

Figure 4.23: Superconducting state B_{2g} spectrum as function of ω for various temperatures $n_{imp} = 4.5$ % in the unitary scattering limit.

In figures (4.22) and (4.23) we plot the B_{1g} and B_{2g} superconducting state data for the case of resonant scattering with an impurity concentration of $n_{imp} = 4.5$ %. The low frequency B_{1g} spectra is now clearly linear in ω even down as low as 10 K. Furthermore, the B_{2g} spectra remains linear throughout the temperature range. The slope of the B_{2g} response is clearly changing, however, comparison with the pure case, figure (4.7), it can be seen that impurities have had a dramatic effect on the overall response.

The B_{1g} scattering channel is shown in figure (4.24) for the superconducting state response at $T = 10$ K, for a set if impurity concentrations $n_{imp} = 0.0$ %, 1.5 %, 3.0 %, and 4.5 %. The low frequency intensity increases with impurity concentration while the pronounced peak is reduced in height by a factor of 2. Accompanying the peak suppression is a peak broadening. The high frequency spectra is left unchanged.

In figure (4.25) we plot the B_{2g} spectra for the same set of impurity concentrations at 10 K. It is clear that as n_{imp} increases the low frequency slope decreases. The amplitude of the peak is also reduced, but not by as large an amount as in the B_{1g} spectra.

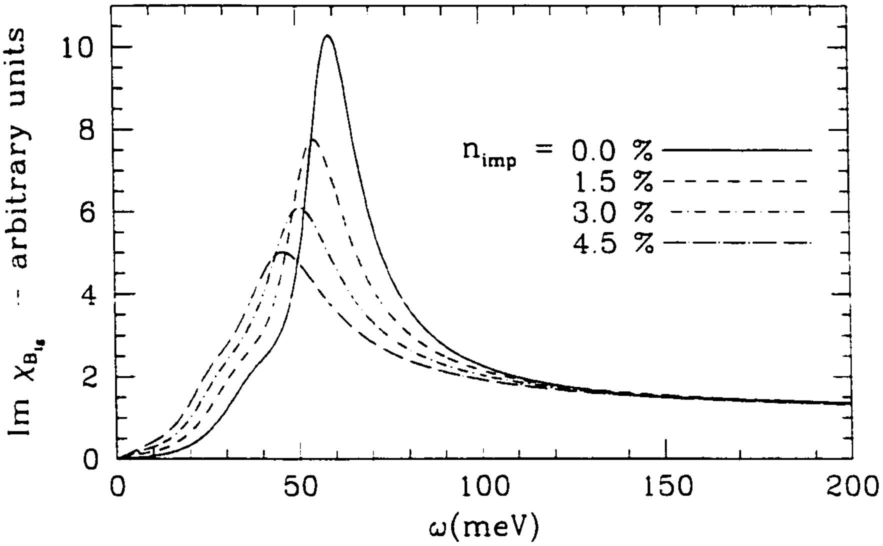

Figure 4.24: $Im\ \chi_{B_{1g}}(\omega)$ at 10 K for impurity concentrations n_{imp} of 0.0 % (solid line), 1.5 % (dashed line), 3.0 % (short dash-doted line), 4.5 % (long dash-dotted line).

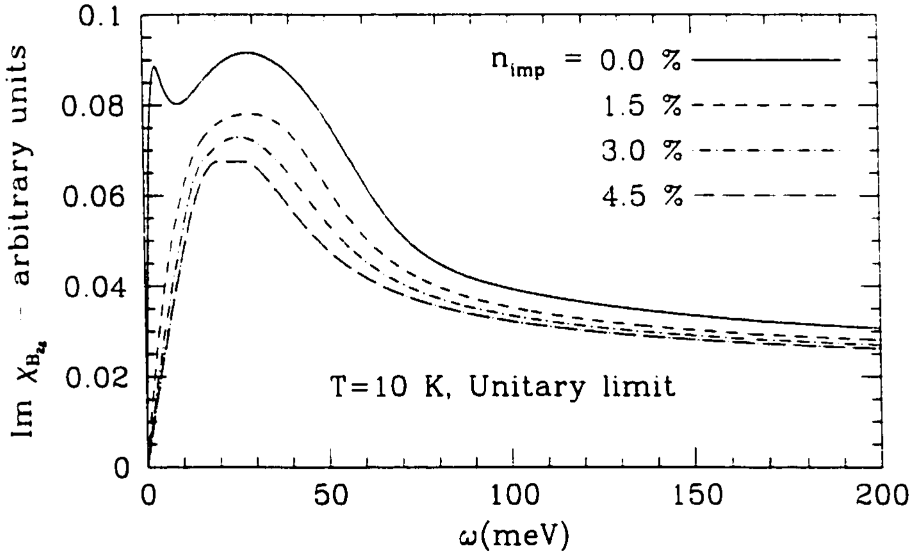

Figure 4.25: $Im\ \chi_{B_{2g}}(\omega)$ at 10 K for impurity concentrations n_{imp} of 0.0 % (solid line), 1.5 % (dashed line), 3.0 % (short dash-doted line), 4.5 % (long dash-dotted line).

Chapter 5

Conclusions

In this thesis we have investigated both the normal and superconducting properties of a quasi-two dimensional interacting system with a strongly anisotropic electron-boson interaction. As a specific model, we have used the phenomenological MMP model. While the language of this thesis was spin-fluctuation exchange mediated pairing, many results are far more general. The emphasis was on the effects strong momentum dependence and inelastic scattering on the optical properties. Any interaction which introduces a **k**-space dependence and which has significant spectral weight over a large frequency range will lead to similar conclusions.

The momentum anisotropy introduced into the system through both the pairing interaction and quasiparticle dispersion relation lead to a self-energy which varied significantly over the Brillouin zone. In chapter 2 we saw that such a model resulted in quasiparticle scattering rates which differed by more than a factor of 2 at certain points on the Fermi surface. The interaction also had a large effect on the single quasiparticle energies and lead to an extended van Hove singularity at the saddle points of the dispersion relation. Such renormalizations are important to keep since calculations based on tight-binding models in BCS formalism have concluded that a reflection of the van Hove singularity should be observable in many properties of the superconducting system (Zhou and Schulz 1992; Branch and Carbotte 1995; Nicol, Jiang, and Carbotte 1993). The renormalization picture naturally explains why observations of the van Hove singularity have not been made.

Inelastic scattering was shown to lead to important effects on the electronic spectral densities, $A_{\mathbf{k}}(\omega)$. In the superconducting state, inelastic scattering results in a normal carrier excitation concentration building up at states along the nodes of the gap at finite temperature. This normal state contribution fills in the density of states and for $\omega = 0$, at finite temperature the pure system has a non-zero density of states, $N(\omega)$. At high enough temperature, this normal charge carrier concentration leads to a local suppression of the gap around the nodes. Impurities were shown to enhance this renormalization.

We have concentrated on two main light scattering spectroscopies in this thesis: electronic Raman scattering and optical conductivity [It may be fair to add a third, ARPES. Although we did not discuss ARPES directly, it is a direct probe of the spectral function $A_{\mathbf{k}}(\omega)$ which we did discuss in great length in chapter 1.] Once the response functions where known, the frequency spectra were treated as experimental curves and analyzed using common techniques. Effective scattering rates were extracted using the extended Drude model. Analysis of the Raman and optical conductivity spectra showed that the extracted scattering rates had similar frequency dependence. The amplitudes of the renormalized scattering rates where also very similar. One important difference between the two experiments, however, is the possibility of extracting symmetry dependent scattering rates from the Raman experiments which effectively measure the scattering rates for quasiparticles in different regions of the Brillouin zone. The optical conductivity results in a single function which is some way represents the average scattering rate experienced by the quasiparticles.

The effects of both momentum dependence of the quasiparticle scattering rates and of the strong-coupling itself were shown to lead to optical scattering rates which differ significantly from the actual quasiparticle scattering rates determined by the imaginary part of the self-energy. While the optical data can give very important information on the underlying system, the extracted data should not be interpreted as reflecting directly the underlying quasiparticle excitation spectrum in a strongly-coupled anisotropic system or the results could be misleading. The mass enhancement factor extracted from the self-energy for a normal state system at $T = 20$ K was shown to vary from $\sim$ 3 to 5 on the Fermi surface. Extraction of a mass enhancement factor from the optical data at the same temperature yielded a value of $\sim$ 1.4.

A signature of the underlying electron-boson interaction was shown to be included in the optical conductivity data. Using a simple $T = 0$ theory, the conductivity was inverted to extract an effective spectral density, $g^2\chi_{eff}(\omega)$. The extracted function was shown to be qualitatively very similar to the momentum integrated susceptibility introduced in chapter 1. Calculations using $g^2\chi_{eff}(\omega)$ as an input parameter to the isotropic conductivity equations did not reproduce the conductivity spectrum of the full calculations. This indicates that the electron-boson spectral density extracted from such a simple theory may not contain all the information about the electron-boson interaction for a system where the interaction has large $\mathbf{k}$ dependence.

Electronic Raman scattering, as discussed in chapter 4, was shown to contain a large amount of information on the underlying electron system, perhaps even more than the optical conductivity since Raman spectra are somewhat momentum resolved and can therefore be used to obtain directionally dependent information in the normal state. Despite the wealth of information which could possibly be extracted from Raman experiments, studies of the high-T_c materials has tended to focus on the low frequency behaviour of the Raman cross-sections. This information has been used to identify the symmetry of the order parameter. As we saw earlier, Raman experiments should also be able to determine other properties of the electronic system such as effective quasiparticle scattering rates. In the Raman chapter we have described a method to extract such information. Experiments probe directly the imaginary part of the Raman response. Since the real and imaginary part are related uniquely through the Kramers-Kronig relations, the real part of the Raman response should be available. One limitation to this however, is that in order to allow for numerical inversion through the Kramers-Kronig, the frequency dependent spectrum is needed out to large frequencies. In the optical data, frequencies out to 50 eV are commonly used (Puchkov et al. 1996).

Throughout this work, we have taken the pairing interaction to be temperature independent. This may be a little naive. In a real system, if the interaction were electronic in origin, as the electronic wavefunctions were changed by superconductivity, a reflection of this would appear in the boson spectral density. As the low frequency electronic states become gapped, the low ω contribution to the boson spectral weight may also be reduced. In a sense, there would be a feed back effect between the electron-boson spectral density and the electronic wavefunctions. Such an effect may be the cause of the redistribution of spectral weight and the origin of the 41 meV peak seen in the imaginary part of the spin susceptibility of optimally doped YBCO using inelastic neutron scattering (Rossat-Mignod et al. 1991a; Rossat-Mignod et al. 1991b). A reduction in the low frequency spectral weight would have the effect of reducing the inelastic scattering. Earlier we mentioned that this would explain the collapse of the quasiparticle scattering rate as seen in microwave conductivity data. Calculations which include the suppression of low frequency spectral weight and its effects on the properties of the strongly interacting system are currently underway.

Appendix A

Computational Techniques

The Eliashberg equations (2.46 - 2.49) together with the electron density equation (2.76) compose a set of nonlinear integral equations which must be solved self-consistently. Analytical methods prove fruitless, so the calculations must be done numerically. In this appendix we describe the procedures used to perform the self-consistent calculations for the three irreducible components of the Nambu Green's function on the imaginary frequency axis. Procedures to find the superconducting critical temperature, T_c, are also described. This is the main focus of section A.1 of this appendix.

The Eliashberg self energy equations and the several response functions calculated in this thesis were computed on the imaginary axis. For thermodynamic properties, this approach is adequate. However, to calculate the dynamic properties of the system real frequency solutions are required (Allen and Mitrovic 1982). In section A.2 we describe a method of analytical continuation from the imaginary to the real frequency axis using Padé approximants.

In section (A.3), we describe the *method of tetrahedrons*, a numerical procedure for calculating surface integrals on a finite grid.

A.1 Self Consistent Eliashberg Calculation

The phenomenological pairing potential in the spin fluctuation model of superconductivity was introduced in chapter 2. It was of the form $V(\mathbf{k}', \mathbf{k}) = V(\mathbf{k}' - \mathbf{k})$ where only the difference between the two momenta $\mathbf{k}$ and $\mathbf{k}'$ is important. All three Eliashberg components can therefore be written in the form, ignoring any constant terms,

$$A(\mathbf{k}, i\omega_n) = T \sum_m \sum_{\mathbf{k}'} B(\mathbf{k}' - \mathbf{k}, i\omega_m - i\omega_n)\, C(\mathbf{k}', i\omega_m). \tag{A.1}$$

Equation (A.1) is in the form of a convolution integral. The convolution theorem (Press, Flannery, Teukolsky, and Vetterling 1993) states that the Fourier transform of the convolution integral is simply the product of the Fourier transforms of $B(\mathbf{q}, i\omega_{m-n})$ and $C(\mathbf{k}', i\omega_m)$,

$$\hat{A}(\mathbf{x}, i\omega_n) = T \sum_m \hat{B}(\mathbf{x}, i\omega_{m-n})\, \hat{C}(\mathbf{x}, i\omega_m) \tag{A.2}$$

where $\hat{A}(\mathbf{x}, i\omega_n) = \mathcal{F}_{\mathbf{k}}[A(\mathbf{k}, i\omega_n)]$ and $\mathcal{F}_{\mathbf{k}}$ denotes the momentum space Fourier transform

$$\begin{aligned} \hat{A}(\mathbf{x}) &= \mathcal{F}_{\mathbf{k}}[A(\mathbf{k})] = \sum_{\mathbf{k}} A(\mathbf{k})\, e^{-i\mathbf{k}\cdot\mathbf{x}} \\ A(\mathbf{k}) &= \mathcal{F}_{\mathbf{k}}^{-1}\left[\hat{A}(\mathbf{x})\right] = \frac{1}{\Omega} \sum_{\mathbf{k}} \hat{A}(\mathbf{x})\, e^{i\mathbf{k}\cdot\mathbf{x}}. \end{aligned} \tag{A.3}$$

In the following few sections we shall use the notation $G^{\alpha}(\mathbf{k}, i\omega_n)$ where $\alpha \in \{\tilde{\omega}, \xi, \phi\}$ to represent the functions

$$G^{\tilde{\omega}}(\mathbf{k}, i\omega_n) = \frac{\tilde{\omega}(\mathbf{k}, i\omega_n)}{D(\mathbf{k}, i\omega_n)} \tag{A.4}$$

$$G^{\xi}(\mathbf{k}, i\omega_n) = \frac{\varepsilon_{\mathbf{k}} + \xi(\mathbf{k}, i\omega_n)}{D(\mathbf{k}, i\omega_n)} \tag{A.5}$$

$$G^{\phi}(\mathbf{k}, i\omega_n) = \frac{\phi(\mathbf{k}, i\omega_n)}{D(\mathbf{k}, i\omega_n)} \tag{A.6}$$

where

$$D(\mathbf{k}, i\omega_n) = [\tilde{\omega}(\mathbf{k}, i\omega_n)]^2 + [\varepsilon_{\mathbf{k}} + \xi(\mathbf{k}, i\omega_n)]^2 + [\phi(\mathbf{k}, i\omega_n)]^2. \tag{A.7}$$

Using the above definitions, we can write the Eliashberg equations as

$$\begin{aligned}
\tilde{\omega}(\mathbf{k}, i\omega_n) &= \omega_n + T\sum_{\mathbf{k}',m}\lambda(\mathbf{k}-\mathbf{k}', i\nu_{n-m})G^{\tilde{\omega}}(\mathbf{k}', i\omega_m) + n_{imp}\Gamma^{\tilde{\omega}}(i\omega_n) && \text{(A.8)}\\
\xi(\mathbf{k}, i\omega_n) &= -T\sum_{\mathbf{k}',m}\lambda(\mathbf{k}-\mathbf{k}', i\nu_{n-m})G^{\xi}(\mathbf{k}', i\omega_m) - n_{imp}\Gamma^{\xi}(i\omega_n) && \text{(A.9)}\\
\phi(\mathbf{k}, i\omega_n) &= -T\sum_{\mathbf{k}',m}\lambda(\mathbf{k}-\mathbf{k}', i\nu_{n-m})G^{\phi}(\mathbf{k}', i\omega_m) + n_{imp}\Gamma^{\phi}(i\omega_n). && \text{(A.10)}
\end{aligned}$$

Impurity scattering has been included in the above equation by the function

$$\hat{\Gamma}(i\omega_n) = -i\Gamma^{\tilde{\omega}}(i\omega_n)\hat{\tau}_0 + \Gamma^{\xi}(i\omega_n)\hat{\tau}_3 + \Gamma^{\phi}(i\omega_n)\hat{\tau}_1 \qquad \text{(A.11)}$$

appropriate for the scattering regime (i.e. T-matrix, Unitary, or Born)[see section 2.2.2 for details].

One method of handling the Matsubara sums in the self-energy equations is to once again use the convolution theorem. The interaction kernel and the Eliashberg equations are not naturally periodic in frequency space, unlike, momentum space, so in order to make use of Fourier transform methods an artificial cutoff must be introduced in frequency space. In order to avoid errors introduced by the artificial periodicity, the functions must be zero-padded to frequencies twice the largest frequency needed. Since the frequency in the interaction kernel is significant out to values of $2n_c$, this function would have to be zero padded out the $4n_c$. Zero padding out to an equivalent frequency is necessary for the irreducible components of the Nambu Green's function requiring 3/4 of the elements to be zeros.

The convolution technique can lead to a large demand for memory when implemented. In this case, a trade off between memory demands and time can be made by performing the Matsubara sum explicitly. This is the method used for the work in this thesis. Using symmetries of the Eliashberg functions, we can reduce the Matsubara sum to sums over just the positive frequencies. It is known that the following symmetries hold:

$$\begin{aligned}
\lambda(\mathbf{q}, -i\nu_m) &= \lambda(\mathbf{q}, i\nu_m) && \text{(A.12)}\\
\tilde{\omega}(\mathbf{k}, -i\omega_m) &= -\tilde{\omega}(\mathbf{k}, i\omega_n) && \text{(A.13)}\\
\xi(\mathbf{k}, -i\omega_n) &= \xi(\mathbf{k}, i\omega_n) && \text{(A.14)}\\
\phi(\mathbf{k}, -i\omega_n) &= \phi(\mathbf{k}, i\omega_n). && \text{(A.15)}
\end{aligned}$$

The term containing the Matsubara sums in the above equations can then be rewritten

$$\begin{aligned}
&\sum_{m=-\infty}^{\infty} \lambda(\mathbf{q}, i\nu_{n-m}) G^{\alpha}(\mathbf{k}', i\omega_m) \\
&\qquad = \sum_{m=0}^{\infty} \lambda(\mathbf{q}, i\nu_{n-m}) G^{\alpha}(\mathbf{k}', i\omega_m) + \sum_{m=-1}^{-\infty} \lambda(\mathbf{q}, i\nu_{n-m}) G^{\alpha}(\mathbf{k}', i\omega_m) \\
&\qquad = \sum_{m=0}^{\infty} \lambda(\mathbf{q}, i\nu_{n-m}) G^{\alpha}(\mathbf{k}', i\omega_m) + \sum_{m=1}^{\infty} \lambda(\mathbf{q}, i\nu_{n+m}) G^{\alpha}(\mathbf{k}', i\omega_{-m}) \\
&\qquad = \sum_{m=0}^{\infty} \lambda(\mathbf{q}, i\nu_{n-m}) G^{\alpha}(\mathbf{k}', i\omega_m) + \sum_{m=0}^{\infty} \lambda(\mathbf{q}, i\nu_{n+m+1}) G^{\alpha}(\mathbf{k}', i\omega_{-m-1}) \\
&\qquad = \sum_{m=0}^{\infty} \left[\lambda(\mathbf{q}, i\nu_{n-m}) \pm \lambda(\mathbf{q}, i\nu_{n+m+1})\right] G^{\alpha}(\mathbf{k}', i\omega_m) \qquad \text{(A.16)}
\end{aligned}$$

where the minus sign in the last line is for $\alpha = \tilde{\omega}$ and the plus sign is for $\alpha = \xi$ or φ. We have also made use of the relation $\omega_{-m} = -\omega_{m-1}$. Also, given that $\nu_{-m} = -\nu_m$ and using the fact that the interaction kernel is even in frequency space, we only have to deal solutions to the Eliashberg equations at nonnegative Matsubara frequencies. The symmetries therefore reduce the demands of memory by a factor of two on implementation.

A.1.1 Eliashberg Functions

We describe below the algorithm used to solve the Eliashberg equations self-consistently on an $N \times N \times M$ grid in momentum/frequency space where N is the length of the grid in momentum space and M the length in Matsubara frequency space. Use of the phenomenological MMP pairing potential makes this calculation less time consuming since the potential does not have to be recalculated at each iteration as would a self-consistent pairing potential [see, for example, (Lenck, Carbotte, and Dynes 1994)].

Algorithm for Self Energy Calculation

1. Given the appropriate input parameters, calculate $\lambda(\mathbf{q}, i\nu_m)$ for all values of q and $m \in [0, 2n_c + 1]$ where ω_{n_c} is the Matsubara frequency cutoff.

2. Fourier transform the interaction kernel, $\hat{\lambda}(\mathbf{x}, i\nu_m) = \mathcal{F}\left[\lambda(\mathbf{k}, i\nu_m)\right]$ for each value of m.

3. Initial the irreducible components of the Green's function for all $\mathbf{k}$ and $n \in [0, n_c]$.
    (a) Initialize $\tilde{\omega}(\mathbf{k}, i\omega_n)$ with ω_n. This is equivalent to setting $Z(\mathbf{k}, i\omega_n) = 1.0$.
    (b) Initialize $\xi(\mathbf{k}, i\omega_n)$ with zero.
    (c) Initialize $\phi(\mathbf{k}, i\omega_n)$ with some appropriate starting configuration $\phi_0(i\omega_n)\eta(\mathbf{k})$ where $\phi_0(\omega_n)$ is a function which decays with increasing ω_n. The function $\eta(\mathbf{k})$ is chosen from a set of eigenfunctions of the irreducible representations of the system. Since we are interested in pairing states with $d_{x^2-y^2}$ symmetry, $\eta(\mathbf{k})$ is typically chosen to be of the form $\cos(k_x) - \cos(k_y)$.

    [Note: The values for negative n are set according to the symmetries given in equations (A.12) - (A.15).]

4. While $\tilde{\omega}(\mathbf{k}, i\omega_n)$, $\xi(\mathbf{k}, i\omega_n)$, and $\phi(\mathbf{k}, i\omega_n)$ have not converged do:
    (a) Calculate $G^{(\alpha)}(\mathbf{k}, i\omega_n)$ for $\alpha = \tilde{\omega}, \xi, \phi$ for all values of $\mathbf{k}$ and $n \in [0, n_c]$
    (b) Perform Fourier transform $\hat{G}^{(\alpha)}(\mathbf{x}, i\omega_n)$ for each n.
    (c) Calculate $\hat{\alpha}(\mathbf{x}, i\omega_n) = \sum_m \hat{\lambda}(\mathbf{x}, i\nu_{m-n})\, \hat{G}^{(\alpha)}(\mathbf{x}, i\omega_n)$, where $\alpha = \tilde{\omega}, \xi, \phi$, for each value of $\mathbf{x}$ and n.
    (d) Save $\tilde{\omega}_{ave}(i\omega_n) = \hat{\tilde{\omega}}(\mathbf{x} = 0, i\omega_n)$, $\xi_{ave}(i\omega_n) = \hat{\xi}(\mathbf{x} = 0, i\omega_n)$, and $\phi_{ave}(i\omega_n) = \hat{\phi}(\mathbf{x} = 0, i\omega_n)$ for each n.
    (e) Calculate the inverse Fourier transform of the result for every $n \in [0, n_c]$ and add the impurity terms

$$\tilde{\omega}(\mathbf{k}, i\omega_n) = \omega_n + \mathcal{F}^{-1}\left[\hat{\tilde{\omega}}(\mathbf{x}, i\omega_n)\right] + n_{imp}\Gamma^{\tilde{\omega}}(i\omega_n) \tag{A.17}$$

$$\xi(\mathbf{k}, i\omega_n) = -\mathcal{F}^{-1}\left[\hat{\xi}(\mathbf{x}, i\omega_n)\right] - n_{imp}\Gamma^{\xi}(i\omega_n) \tag{A.18}$$

$$\phi(\mathbf{k}, i\omega_n) = -\mathcal{F}^{-1}\left[\hat{\phi}(\mathbf{x}, i\omega_n)\right] + n_{imp}\Gamma^{\phi}(i\omega_n) \tag{A.19}$$

    where $\Gamma^{\alpha}(i\omega)$, $\alpha = \tilde{\omega}, \xi, \phi$, is an appropriate function for impurity scattering.

A.1.2 Critical Temperature

The critical temperature calculation involves solving an eigenvalue equation in the $\phi(\mathbf{k}, i\omega_n)$ channel, which is dependent on the self consistent values of the normal state functions $\xi(\mathbf{k}, i\omega_n)$ and $\tilde{\omega}(\mathbf{k}, i\omega_n)$ [see section (2.2.4)].

The linearized version of equation (A.10) can be written in the form

$$\rho\phi(\mathbf{k}, i\omega_n) = \sum_m \sum_{\mathbf{k}'} M(\mathbf{k}, i\omega_n, \mathbf{k}', i\omega_m)\phi(\mathbf{k}', i\omega_m) \tag{A.20}$$

where the "matrix" $M(\mathbf{k}, i\omega_n; \mathbf{k}', i\omega_m)$ is defined as

$$M(\mathbf{k}, i\omega_n, \mathbf{k}', i\omega_m) = -\frac{T\lambda(\mathbf{k}-\mathbf{k}', i\omega_n - i\omega_m)}{\tilde{\omega}(\mathbf{k}', i\omega_m)^2 + [\varepsilon_{\mathbf{k}'} + \xi(\mathbf{k}', i\omega_m)]^2}. \tag{A.21}$$

The critical temperature, T$_c$, is now defined as the largest temperature for which an eigenvalue of $\rho = 1$ exists. Equation (A.20) is solved using the *Power method* (Golub and van Loan 1989) which involves making an initial guess for the eigenfunctions, $\phi(\mathbf{k}, i\omega_n)$, and iterating the equation until convergence is reached. At each new temperature, the normal state solutions of $\xi(\mathbf{k}, i\omega_n)$ and $\tilde{\omega}(\mathbf{k}, i\omega_n)$ are calculated self consistently using the algorithm described in the last section.

The above method is only guaranteed to find the eigenvalue with the largest absolute value. A problem arises should there exist an eigenvalue λ such that $\lambda < 0$ but $|\lambda|$ is larger than the largest positive eigenvalue. In this case, the eigenvalues can be shifted without altering the eigenvectors by replacing $M_{\mathbf{k},\mathbf{k}'}$ with

$$M'_{\mathbf{k},\mathbf{k}'} = M_{\mathbf{k},\mathbf{k}'} + \sigma\delta_{\mathbf{k},\mathbf{k}'} \tag{A.22}$$

The eigenvalue equation then becomes

$$\begin{aligned} \rho'\phi(\mathbf{k}, i\omega_n) &= T\sum_m \sum_{\mathbf{k}'} M'_{\mathbf{k},\mathbf{k}'}\phi(\mathbf{k}', i\omega_m) \\ &= T\sum_m \left\{ \sum_{\mathbf{k}'} M_{\mathbf{k},\mathbf{k}'}\phi(\mathbf{k}', i\omega_m) + \sigma\phi(\mathbf{k}, i\omega_m) \right\} \end{aligned} \tag{A.23}$$

Shifting the eigenvalue spectrum, therefore, does not inhibit use of the FFT method. By subtracting $\sum_m \sigma\phi(\mathbf{k}, i\omega_m)$ for the the new eigenvalue ρ', the original eigenvalue ρ is recovered.

The algorithm for determining T$_c$ without the eigenvalue shift is described below.

Algorithm for $\mathbf{T}_c$

1. Choose starting configuration for $\phi(\mathbf{k}, i\omega_n)$ where $\phi_0(\mathbf{k}, i\omega_n)$ is normalized such that its maximum value in the Brillouin zone, $\phi_0(\mathbf{k}, i\omega_0)$, is one.
2. Choose a temperature interval $[T_lo. T_hi]$ such that the actual value of the critical temperature T_c is bracketed.
3. For each of the bounding temperatures:
    (a) Initialize $\phi(\mathbf{k}, i\omega_n)$ to the starting configuration $\phi_0(\mathbf{k}, i\omega_n)$ for each $\mathbf{k}$ and $n \in [0, n_c]$.
    (b) Calculate the eigenvalue ρ for the current vector $\phi(\mathbf{k}, i\omega_n)$. See below for the algorithm.
4. Reset $\phi(\mathbf{k}, i\omega_n) = \phi_0(\mathbf{k}, i\omega_n)$.
5. Use root finding routine to calculate the temperature T such that $\rho = 1$.

The routine which calculates ρ uses the following algorithm:

1. Calculate the function $G^\Phi(\mathbf{k}, i\omega_n)$:

$$G^\Phi(\mathbf{k}, i\omega_n) = \frac{\phi(\mathbf{k}, i\omega_n)}{[\tilde{\omega}(\mathbf{k}, i\omega_n)]^2 + [\varepsilon_\mathbf{k} + \xi(\mathbf{k}, i\omega_n)]^2} \tag{A.24}$$

   where $\phi(\mathbf{k}, i\omega_n)$ is the starting configuration or the solution to the last iteration.

2. Calculate the Fourier transform $\hat{G}(\mathbf{x}, i\omega_n) = \mathcal{F}[G(\mathbf{k}, i\omega_n)]$ for each $n \in [0, n_c]$
3. Calculate the new $\hat{\phi}(\mathbf{x}, i\omega_n)$ by performing the direct Matsubara sum

$$\hat{\phi}(\mathbf{x}, i\omega_n) = \sum_m \hat{\lambda}(\mathbf{x}, i\omega_n - i\omega_m)\hat{G}(\mathbf{x}, i\omega_m) \tag{A.25}$$

4. Perform the inverse Fourier transform $\phi(\mathbf{k}, i\omega_n) = \mathcal{F}^{-1}\left[\hat{\phi}(\mathbf{k}, i\omega_n)\right]$ for each n.
5. Add the impurity term $\phi(\mathbf{k}, i\omega_n) = \phi(\mathbf{k}, i\omega_n) + n_{imp}\Gamma^\Phi(i\omega_n)$.

6. The new value of ρ is easily determined by $\rho = \phi(\mathbf{k_0}, i\omega_0)$ where $\phi(\mathbf{k_0}, i\omega_0)$ is the largest value of $\phi(\mathbf{k}, i\omega_0)$ in the Brillouin zone.

7. Renormalize $\phi(\mathbf{k}, i\omega_n)$ by dividing all elements by ρ.

8. Check the convergence of ϕ

The vector $\phi(\mathbf{k}, i\omega_n)$ is not reset to the starting configuration during while in the root finding phase of the T_c algorithm. As the system converges to the the critical temperature, or rather to $\rho = 1$, the eigenvector $\phi(\mathbf{k}, i\omega_n)$ becomes less and less different for successive temperatures and becomes an ideal starting configuration for the next temperature iteration.

A.2 Analytic Continuation via Padé Approximants

Using Padé approximants to analytically continue the imaginary frequency Green's functions to the real axis made for easier numerical calculation since the Eliashberg equations or the response functions could first be determined on the imaginary axis without the hindrance of principal value integrals (Vidberg and Serene 1977). The algorithm for calculating an N-Point Padé approximant to the function $u(z)$, given its values u_i at N complex points z_i, where $i = 1, \ldots, N$, begins from the definition of the continued fraction

$$C_N(z) = \cfrac{a_1}{1 + \cfrac{a_2(z - z_1)}{1 + \cfrac{a_3(z - z_2)}{\cfrac{\ddots}{1 + \cfrac{a_N(z - z_{N-1})}{1}}}}}. \tag{A.26}$$

where the coefficients a_i are determined such that

$$C_N(z_i) = u_i, i = 1, ..., N. \tag{A.27}$$

The coefficients are then given by the recursion relation

$$\begin{aligned} a_i &= g_i(z_i), g_1(z_i) = u_i, i = 1, ..., N, \\ g_p(z) &= \frac{g_{p-1}(z_{p-1}) - g_{p-1}(z)}{(z - z_{p-1})g_{p-1}(z)}, p \geq 2. \end{aligned} \tag{A.28}$$

The recursion formula for continued fractions can then be written

$$C_N(z) = \frac{A_N(z)}{B_N(z)} \tag{A.29}$$

where $A_N(z)$ and $B_N(z)$ are given by the recursion relations

$$\begin{aligned} A_{n+1}(z) &= A_n(z) + (z - z_n)a_n A_{n-1}(z) \\ B_{n+1}(z) &= B_n(z) + (z - z_n)a_n B_{n-1}(z) \\ A_0 &= 0, A_1 = a_1, B_0 = B_1 = 1. \end{aligned} \tag{A.30}$$

Equations (A.29) and (A.30) can then be used to calculate the value of any analytic complex function at the complex point, z. Further improvements to the above algorithm for an $\alpha^2 F(\omega)$ formalism are available (Leavens and Ritchie 1985; Marsiglio, Schossmann, and Carbotte 1988).

A.3 Method of Tetrahedrons

The *Method of Tetrahedrons* is an efficient way of calculating surface integrals on a finite mesh (Lehmann and Taut 1972) when the integral to be solved is in the form

$$I(\epsilon) = \int \frac{dS}{|\nabla\varepsilon(\mathbf{k})|}A(\mathbf{k}) \tag{A.31}$$

where the integration is over the constant energy surface $\delta\varepsilon(\mathbf{k}) = \epsilon$. We shall describe the more general three dimensional case here, however, the reduction to two dimensions is straight forward. The Brillouin zone is divided into tetrahedrons with arbitrary shape, but of the same volume (not a necessary condition, but simplifies the evaluation). The dispersion relation within each tetrahedron is interpolated by a linear function:

$$\varepsilon(\mathbf{k}) = \varepsilon_0 + \mathbf{b} \cdot \mathbf{k}. \tag{A.32}$$

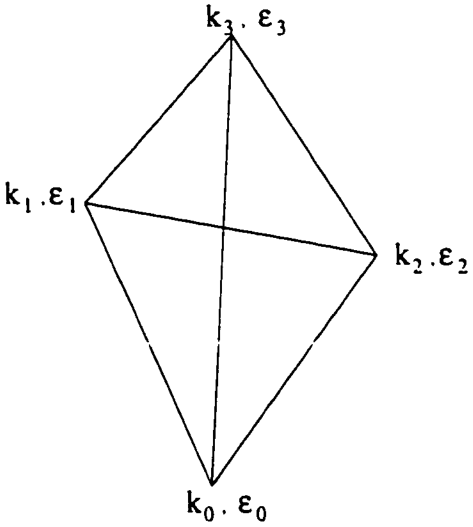

Figure A.1: Tetrahedral element labeled at the nodes by wavevector k_i and energy ε_i, for $i = 0, 1, 2, 3$.

At the corners of an individual element, $\mathbf{k}_i$, the energy values, $\varepsilon(\mathbf{k}_i) = \varepsilon_i$, are known [see figure (A.1)]. The values can then be used to determine the coefficient $\mathbf{b}$. Using the triple $\mathbf{r}_i$ contragradient to $\mathbf{k}_i$

$$\begin{aligned} \mathbf{r}_j\mathbf{k}_i &= \delta_{ij} \\ \mathbf{r}_1 &= \frac{\mathbf{k}_2 \times \mathbf{k}_3}{v} \\ \mathbf{r}_2 &= \frac{\mathbf{k}_3 \times \mathbf{k}_1}{v} \\ \mathbf{r}_3 &= \frac{\mathbf{k}_1 \times \mathbf{k}_2}{v} \end{aligned} \tag{A.33}$$

where $v = \mathbf{k}_1 \cdot \mathbf{k}_2 \times \mathbf{k}_3$. Therefore we can express $\mathbf{b}$ as

$$\mathbf{b} = \sum_{i=1}^{3} (\varepsilon_i - \varepsilon_0)\,\mathbf{r}_i. \tag{A.34}$$

The next step is to approximate the function $A(\mathbf{k})$ as a linear function also inside the each tetrahedral element:

$$a(\mathbf{k}) = a_0 + \mathbf{a} \cdot \mathbf{k}. \tag{A.35}$$

The vector $\mathbf{a}$ is then determined in an analogous fashion to $\mathbf{b}$. Using equation (A.35), the integral over one tetrahedron becomes

$$i(\epsilon) = a_0 i_0(\epsilon) + \mathbf{a} \cdot \mathbf{i}_1(\epsilon) \tag{A.36}$$

where

$$i_0(\epsilon) = \int_{\delta\varepsilon(\mathbf{k})=\epsilon} \frac{dS}{\mid \mathbf{b} \mid} \tag{A.37}$$

and

$$\mathbf{i}_1(\epsilon) = \int_{\delta\varepsilon(\mathbf{k})=\epsilon} \frac{dS}{\mid \mathbf{b} \mid}\mathbf{k}. \tag{A.38}$$

As $|\mathbf{b}|$ is a constant in each element, it can be pulled outside the integral. The integral $i_0(\epsilon)$ is the density of states from one tetrahedron which can be written as

$$i_0(\epsilon) = f(\epsilon) \cdot \mid \mathbf{b} \mid^{-1}, \tag{A.39}$$

where $f(\epsilon)$ is the cross-section of the plane $\delta\varepsilon(\mathbf{k}) = \epsilon$ with the tetrahedron. The value of (ϵ) is then determined by the sum over triangular areas.

Assuming ordered energies at the vertices of the tetrahedra, $\varepsilon_0 < \varepsilon_1 < \varepsilon_2 < \varepsilon_3$, we get

$$f(\epsilon) = \begin{cases} f_0, & \varepsilon \le \epsilon \le \varepsilon_1 \\ f_0 - f_1, & \varepsilon_1 \le \epsilon \le \varepsilon_2 \\ f_3, & \varepsilon_2 \le \epsilon \le \varepsilon_3 \end{cases} \tag{A.40}$$

where

$$\begin{aligned} f_0 \mid \mathbf{b} \mid^{-1} &= \frac{v}{2} \frac{(\epsilon - \varepsilon_0)^2}{(\varepsilon_1 - \varepsilon_0)(\varepsilon_2 - \varepsilon_0)(\varepsilon_3 - \varepsilon_0)} \\ f_1 \mid \mathbf{b} \mid^{-1} &= \frac{v}{2} \frac{(\epsilon - \varepsilon_1)^2}{(\varepsilon_1 - \varepsilon_0)(\varepsilon_2 - \varepsilon_1)(\varepsilon_3 - \varepsilon_1)} \\ f_0 \mid \mathbf{b} \mid^{-1} &= \frac{v}{2} \frac{(\epsilon - \varepsilon_3)^2}{(\varepsilon_3 - \varepsilon_0)(\varepsilon_3 - \varepsilon_1)(\varepsilon_3 - \varepsilon_2)} \end{aligned} \tag{A.41}$$

The evaluation of $\mathbf{i}_1(\epsilon)$ follows in a similar way and gives

$$\mathbf{i}_1(\epsilon) = f(\epsilon) \mid \mathbf{b} \mid^{-1} \mathbf{s}(\epsilon) \tag{A.42}$$

where $\mathbf{s}(\epsilon)$ is the center of gravity of $f(\epsilon)$. It is given by :

$$\mathbf{s}(\epsilon) = \begin{cases} \mathbf{s}_0, & \varepsilon_0 \le \epsilon \le \varepsilon_1 \\ \dfrac{\mathbf{s}_0 f_0 - \mathbf{s}_1 f_1}{f_0 - f_1}, & \varepsilon_1 \le \epsilon \le \varepsilon_2 \\ \mathbf{s}_3, & \varepsilon_2 \le \varepsilon_3 \le \epsilon \end{cases} \tag{A.43}$$

The values of $\mathbf{s}_i$ are determined from the appropriate triangles f_i:

$$\mathbf{s}_i(\epsilon) = \mathbf{k}_i + \frac{(\epsilon - \varepsilon_i)}{3} \sum_{\substack{j=0 \\ (j \neq i)}}^{3} \frac{(\mathbf{k}_j - \mathbf{k}_i)}{(\varepsilon_j - \varepsilon_i)} \tag{A.44}$$

The full integral, equation (A.31), is then determined by summing over the values for all elements.

$$I(\epsilon) = \sum_{e=1}^{N_e} i_e(\epsilon) \tag{A.45}$$

where N_e is the number of elements in the grid.

More details on the method of tetrahedrons can be found in the original paper (Lehmann and Taut 1972).

Appendix B

Coulomb Screening

The vast majority of the literature in theoretical work concerning electronic Raman scattering has focused on tetragonal systems. Since the cuprate superconductors are primarily tetragonal or near-tetragonal this may not matter very much. However, certain systems, such as YBCO, are truly orthorhombic systems. In this appendix, we investigate the effects of orthorhombic distortions on the Raman response function, $\chi_{\gamma\gamma}(\omega)$. Throughout this discussion, we will use the notation for the purely tetragonal system even when the system orthorhombic distortions are introduced. The notation used will follow that of Tinkham(Tinkham 1964)

In the first section, B.1, we derive a general expression for the screened Raman response in Nambu formalism. While we will not worry about vertex renormalizations coming from such things as impurity scattering, and final-state interactions, these corrections are easily included.

In section B.2, we will investigate the effects of the Coulomb screening renormalization on the various Raman scattering channels in both tetragonal (section B.2.1) and orthorhombic (section B.2.2) symmetries.

B.1 Coulomb Screening Equation

The Raman response function in Nambu formalism was introduced in chapter 4. Here we will derive an expression for the renormalized response in the presence of

Coulomb screening. We will follow closely the derivation of Klein and Dierker (Klein and Dierker 1984).

The Coulomb interaction matrix element is given by

$$V_{\mathbf{q}} = \frac{4\pi e^2}{q^2}\langle \mathbf{k}+\mathbf{q}|e^{i\mathbf{q}\cdot\mathbf{r}}|\mathbf{k}\rangle. \tag{B.1}$$

Ultimately, we will take the limit as the momentum transfer goes to zero , therefore we expand the matrix element in the above equation and keep only the lowest order term

$$V_{\mathbf{q}} = \frac{4\pi e^2}{q^2}. \tag{B.2}$$

The general expression for the Raman polarization in the presence of Coulomb screening fields is given by

$$\chi_{\Gamma\gamma}(\mathbf{q}, i\nu_n) = -T\sum_{\mathbf{k},m} Tr\left\{\hat{\Gamma}(\mathbf{q}, i\nu_n; \mathbf{k}, i\omega_m)\hat{G}(\mathbf{k}+\mathbf{q}, i\omega_m + i\nu_n)\gamma_{\mathbf{k}}\hat{\tau}_3\hat{G}(\mathbf{k}, i\omega_m)\right\} \tag{B.3}$$

where the renormalized vertex function is

$$\hat{\Gamma}(\mathbf{q}, i\nu_n; \mathbf{k}, i\omega_m) = \gamma_{\mathbf{k}}\hat{\tau}_3 - V_{\mathbf{q}}\hat{\tau}_3 T\sum_{\mathbf{k}',l} Tr\left\{\hat{\Gamma}(\mathbf{q}, i\nu_n; \mathbf{k}', i\omega_l)\hat{G}(\mathbf{k}'+\mathbf{q}, i\omega_l)\hat{\tau}_3\hat{G}(\mathbf{k}', i\omega_l)\right\}. \tag{B.4}$$

Recognizing that the second term in equation (B.4) is very similar in form to equation (B.3), we can write

$$\hat{\Gamma}(\mathbf{q}, i\nu_n; \mathbf{k}, i\omega_m) = \gamma_{\mathbf{k}}\hat{\tau}_3 + V_{\mathbf{q}}\hat{\tau}_3\chi_{\Gamma 1}(\mathbf{q}, i\nu_n) \tag{B.5}$$

where we have made the definition

$$\chi_{\Gamma 1}(\mathbf{q}, i\nu_n) = -T\sum_{\mathbf{k},m} Tr\left\{\hat{\Gamma}(\mathbf{q}, i\nu_n; \mathbf{k}, i\omega_m)\hat{G}(\mathbf{k}+\mathbf{q}, i\omega_m + i\nu_n)\hat{\tau}_3\hat{G}(\mathbf{k}, i\omega_m)\right\}. \tag{B.6}$$

Now, $\chi_{\Gamma 1}$ can itself be expanded in terms of the renormalized vertex to give

$$\begin{aligned} \chi_{\Gamma 1}(\mathbf{q}, i\nu_n) &= \chi_{\gamma 1}(\mathbf{q}, i\nu_n) + V_{\mathbf{q}}\chi_{\Gamma 1}(\mathbf{q}, i\nu_n)\chi_{11}(\mathbf{q}, i\nu_n) \\ &= \frac{\chi_{\gamma 1}(\mathbf{q}, i\nu_n)}{1 - V_{\mathbf{q}}\chi_{11}(\mathbf{q}, i\nu_n)}. \end{aligned} \tag{B.7}$$

If we now substitute equations (B.5) and (B.7) into (B.3), we get for the screened Coulomb response

$$\chi_{\Gamma\gamma}(\mathbf{q}, i\nu_n) = \chi_{\gamma\gamma}(\mathbf{q}, i\nu_n) - \frac{\chi_{\gamma 1}(\mathbf{q}, i\nu_n)\chi_{1\gamma}(\mathbf{q}, i\nu_n)}{\chi_{11}(\mathbf{q}, i\nu_n) - \frac{q^2}{4\pi e^2}}. \tag{B.8}$$

In the long wavelength limit (i.e. $\lim \mathbf{q} \to 0$), equation (B.8) becomes

$$\chi_{\Gamma\gamma}(i\nu_n) = \chi_{\gamma\gamma}(i\nu_n) - \frac{\chi_{\gamma 1}(i\nu_n)\chi_{1\gamma}(i\nu_n)}{\chi_{11}(i\nu_n)}. \tag{B.9}$$

Throughout the remainder of this appendix, we will investigate the effects of the second term in equation (B.9) on the Raman spectra.

B.2 Raman Symmetries

In general, the Raman vertex for given incident and scattered polarization angles written in terms of the tight-binding Brillouin eigenfunctions is given by (Wenger and Käll 1997)

$$\begin{aligned}
\gamma_{\mathbf{k}} &= \cos(\alpha - \beta)\left[t(\cos(\mathbf{k}_x) + \cos(\mathbf{k}_y)) + 4t'\cos(\mathbf{k}_x)\cos(\mathbf{k}_y)\right] \\
&\quad + \cos(\alpha + \beta)t(\cos(\mathbf{k}_x) - \cos(\mathbf{k}_y)) \\
&\quad - \sin(\alpha + \beta)4t'\sin(\mathbf{k}_x)\sin(\mathbf{k}_y) && \text{(B.10)} \\
&= \cos(\alpha - \beta)\gamma_{A_{1g}}(\mathbf{k}) + \cos(\alpha + \beta)\gamma_{B_{1g}}(\mathbf{k}) + \sin(\alpha + \beta)\gamma_{B_{2g}}(\mathbf{k}) && \text{(B.11)}
\end{aligned}$$

where α and β are the polarization angles of the incident and final photons. Note that $\alpha = \beta = \pi/4$, which corresponds to the configuration $(x + y, x + y)$ defined in chapter 4, measures the $A_{1g} + B_{2g}$ spectra. Using $\alpha = \pi/4$ and $\beta = -\pi/4$, the pure B_{1g} channel can be measured. Pure B_{2g} symmetry can be achieved using the polarizations $\alpha = 0$ and $\beta = \pi/2$.

For now, let us simply write equation (B.11) as

$$\gamma_{\mathbf{k}} = a\,\gamma_{A_{1g}} + b\,\gamma_{B_{1g}} + c\,\gamma_{B_{2g}} \tag{B.12}$$

and remember that a, b and c are functions of the polarization angles of the incident and scattered photons.

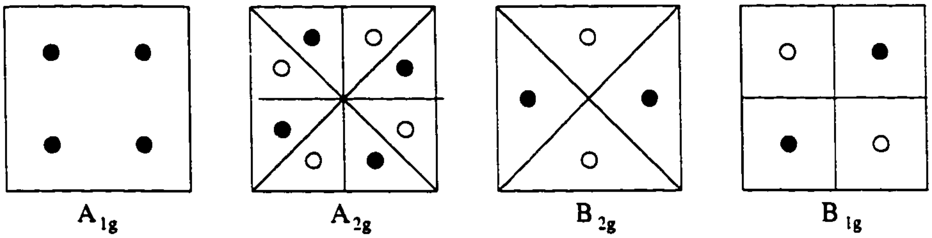

Figure B.1: Mnemonics for the four major irreducible representations

The screened Raman response, $Im\chi^{sc}_{\gamma\gamma}(i\nu_n)$, is given by the imaginary part of equation (B.9) (Klein and Dierker 1984)

$$Im\chi^{sc}_{\gamma\gamma}(i\nu_n) = Im\left(\chi_{\gamma\gamma}(i\nu_n) - \frac{\chi_{\gamma,1}(i\nu_n)\chi_{1,\gamma}(i\nu_n)}{\chi_{1,1}(i\nu_n)}\right). \tag{B.13}$$

The first term on the right hand side of equation (B.13) is the unscreened response. In the second term, both real part and the imaginary part of the various components will be needed. Using equation (B.11) to break the spectra up into the different irreducible representations for the tetragonal system, the second term will vanish for all symmetries other than the A_{1g}. We will motivate this pictorially below instead of using more complex group theoretic arguments to prove it.

In figure (B.1) the A_{1g}, A_{2g}, B_{1g}, and B_{2g} irreducible representations are shown pictorially. The white circles are to interpreted as the "negative" of the black. It is easy to see that the average of any function over the Brillouin zone with A_{1g} symmetry will be finite while for the other symmetries, it will be zero. Below, we list the result of multiplication between a function f_α with pure symmetry α and a second function g_β with symmetry β:

$$\begin{aligned}
f_\alpha\, f_\alpha &= g_{A_{1g}} && \text{(B.14)}\\
f_\alpha\, g_{A_{1g}} &= h_\alpha && \text{(B.15)}\\
f_{B_{1g}}\, g_{A_{2g}} &= h_{B_{2g}} && \text{(B.16)}\\
f_{B_{1g}}\, g_{B_{2g}} &= h_{A_{2g}} && \text{(B.17)}\\
f_{B_{2g}}\, g_{A_{2g}} &= h_{B_{1g}}. && \text{(B.18)}
\end{aligned}$$

We shall use the above relations to analyze equation (B.13) for tetragonal and orthorhombic systems.

In terms of the thermal Green's functions, the Raman susceptibility is

$$\begin{aligned}\chi_{\gamma\gamma}(i\nu_n) &= -T\sum_{\mathbf{k},m}\gamma_{\mathbf{k}}^2 tr\left\{\hat{\tau}_3\hat{G}_{\mathbf{k}}(i\omega_m)\hat{\tau}_3\hat{G}_{\mathbf{k}}(i\omega_{m+n})\right\} \\ &= \sum_{\mathbf{k}}\gamma_{\mathbf{k}}^2\lambda_{\mathbf{k}}(i\nu_n) \qquad \text{(B.19)}\end{aligned}$$

where we have defined the function

$$\lambda_{\mathbf{k}}(i\nu_n) = -T\sum_m tr\left\{\hat{\tau}_3\hat{G}_{\mathbf{k}}(i\omega_m)\hat{\tau}_3\hat{G}_{\mathbf{k}}(i\omega_{m+n})\right\}. \qquad \text{(B.20)}$$

From chapter (4)), we know that equation (B.20) can be written as

$$\lambda_{\mathbf{k}}(i\nu_n) = -T\sum_m \frac{\bar{\varepsilon}_{\mathbf{k}}(i\omega_{m+n})\bar{\varepsilon}_{\mathbf{k}}(i\omega_m) - \phi_{\mathbf{k}}(i\omega_{m+n})\phi_{\mathbf{k}}(i\omega_m) - \tilde{\omega}_{\mathbf{k}}(i\omega_{m+n})\tilde{\omega}_{\mathbf{k}}(i\omega_{m+n})}{D_{\mathbf{k}}(i\omega_m)D_{\mathbf{k}}(i\omega_{m+n})} \qquad \text{(B.21)}$$

where

$$D_{\mathbf{k}}(i\omega_n) = \tilde{\omega}_{\mathbf{k}}(i\omega_n)^2 + \bar{\varepsilon}_{\mathbf{k}}(i\omega_n)^2 + \phi_{bfk}(i\omega_n)^2. \qquad \text{(B.22)}$$

This function has the full symmetry of the crystal. or rather. A_{1g} symmetry. The second term has three further response functions. $\chi_{\gamma 1}$, $\chi_{1\gamma}$ and χ_{11}. Theses can be written as

$$\begin{aligned}\chi_{\gamma,1}(i\nu_n) = \chi_{1,\gamma}(i\nu_n) &= -T\sum_{\mathbf{k},m}\gamma_{\mathbf{k}} tr\left\{\hat{\tau}_3\hat{G}_{\mathbf{k}}(i\omega_m)\hat{\tau}_3\hat{G}_{\mathbf{k}}(i\omega_{m+n})\right\} \\ &= \sum_{\mathbf{k}}\gamma_{\mathbf{k}}\lambda_{\mathbf{k}}(i\nu_n) \qquad \text{(B.23)}\end{aligned}$$

and

$$\begin{aligned}\chi_{1,1}(i\nu_n) &= -T\sum_{\mathbf{k},m} tr\left\{\hat{\tau}_3\hat{G}_{\mathbf{k}}(i\omega_m)\hat{\tau}_3\hat{G}_{\mathbf{k}}(i\omega_{m+n})\right\} \\ &= \sum_{\mathbf{k}}\lambda_{\mathbf{k}}(i\nu_n). \qquad \text{(B.24)}\end{aligned}$$

We can therefore write equation (B.13) as

$$Im\chi_{\gamma\gamma}^{sc}(i\nu_n) = Im\left(\sum_{\mathbf{k}}\gamma_{\mathbf{k}}^2\lambda_{\mathbf{k}}(i\nu_n) - \frac{\left[\sum_{\mathbf{k}}\gamma_{\mathbf{k}}\lambda_{\mathbf{k}}(i\nu_n)\right]\left[\sum_{\mathbf{k}'}\gamma_{\mathbf{k}'}\lambda_{\mathbf{k}'}(i\nu_n)\right]}{\sum_{\mathbf{k}}\lambda_{\mathbf{k}}(i\nu_n)}\right). \qquad \text{(B.25)}$$

In the next two sections we shall concentrate on the term in brackets in equation (B.25). Progress is made by expanding the γ and λ functions in terms of the irreducible representations and arguing which terms vanish due to symmetry. In the next section, B.2.1, we deal with the tetragonal case. Although this case is trivial we proceed anyway in order to compare with the orthorhombic case. Section B.2.2 deals with orthorhombic distortions. We will continue to use the notation of the tetragonal symmetry as this is what is typically done in the literature.

B.2.1 Tetragonal Symmetry

For a system with tetragonal symmetry, $\lambda_{\mathbf{k}}$ has the full symmetry of the crystal, namely A_{1g}, so we can write

$$\lambda_{\mathbf{k}} = \alpha\, \lambda_{A_{1g}}. \tag{B.26}$$

With this, the different terms in the screened response become

$$\begin{aligned}\chi_{\gamma\gamma} &= \sum_{\mathbf{k}} \gamma_{\mathbf{k}}^2\, \lambda_{\mathbf{k}} \\ &= \sum_{\mathbf{k}} \left(a^2\gamma_{A_{1g}}^2 + b^2\gamma_{B_{1g}}^2 + c^2\gamma_{B_{2g}}^2\right) \lambda_{\mathbf{k}}\end{aligned} \tag{B.27}$$

and

$$\begin{aligned}\chi_{1\gamma} = \chi_{\gamma 1} &= \sum_{\mathbf{k}} \gamma_{\mathbf{k}}\, \lambda_{\mathbf{k}} \\ &= \sum_{\mathbf{k}} \left(a\gamma_{A_{1g}} + b\gamma_{B_{1g}} + c\gamma_{B_{2g}}\right) \lambda_{\mathbf{k}} \\ &= \sum_{\mathbf{k}} a\gamma_{A_{1g}}\lambda_{\mathbf{k}}.\end{aligned} \tag{B.28}$$

The cross terms have vanished in the above equations since they average to zero in the sum over the Brillouin zone.

The screened Raman response becomes

$$\chi_{\gamma\gamma}^{sc} = \sum_{\mathbf{k}} \left(a^2\gamma_{A_{1g}}^2 + b^2\gamma_{B_{1g}}^2 + c^2\gamma_{B_{2g}}^2\right) \lambda_{\mathbf{k}} - a^2 \frac{\left(\sum_{\mathbf{k}} \gamma_{A_{1g}} \lambda_{\mathbf{k}}\right)^2}{\sum_{\mathbf{k}} \lambda_{\mathbf{k}}} \tag{B.29}$$

or more appropriately

$$\chi^{sc}_{\gamma\gamma} = \alpha\left(a^2\chi_{A_{1g}} + b^2\chi_{B_{1g}} + c^2\chi_{B_{2g}}\right) \tag{B.30}$$

where

$$\begin{aligned}
\chi_{A_{1g}} &= \sum_{\mathbf{k}} \gamma^2_{A_{1g}}\lambda_{A_{1g}} + \frac{\left(\sum_{\mathbf{k}}\gamma_{A_{1g}}\lambda_{A_{1g}}\right)^2}{\sum_{\mathbf{k}}\lambda_{A_{1g}}} \\
\chi_{B_{1g}} &= \sum_{\mathbf{k}} \gamma^2_{B_{1g}}\lambda_{A_{1g}} \\
\chi_{B_{2g}} &= \sum_{\mathbf{k}} \gamma^2_{B_{2g}}\lambda_{A_{1g}}.
\end{aligned} \tag{B.31}$$

B.2.2 Orthorhombic Symmetry

When the crystal symmetry is distorted such that the symmetry is reduced from D_4 to D_2 (i.e. tetragonal to orthorhombic), the B_{1g} and A_{1g} are no longer distinguishable by group theoretic means; they are members of the same irreducible representation. B_{2g} still remains an irreducible representation.

We can expand $\lambda_{\mathbf{k}}(i\nu_n)$ in the irreducible representations

$$\lambda_{\mathbf{k}}(i\nu_n) = u\lambda^{A_{1g}} + v\lambda^{B_{1g}}. \tag{B.32}$$

Equation (B.27) becomes

$$\begin{aligned}
\chi_{\gamma\gamma} &= \sum_{\mathbf{k}} \gamma^2_{\mathbf{k}}\lambda_{\mathbf{k}} \\
&= \sum_{\mathbf{k}} u\left(a^2\gamma^2_{A_{1g}} + b^2\gamma^2_{B_{1g}} + c^2\gamma^2_{B_{2g}}\right)\lambda_{A_{1g}} \\
&\quad + \sum_{\mathbf{k}} 2vab\gamma_{A_{1g}}\gamma_{B_{1g}}\lambda_{B_{1g}}.
\end{aligned} \tag{B.33}$$

As expected, the orthorhombic distortion has mixed the A_{1g} and B_{1g} symmetries together. Furthermore, one gets for $\chi_{1\gamma}$

$$\begin{aligned}
\chi_{\gamma 1} &= \sum_{\mathbf{k}}\left(a\gamma_{A_{1g}} + b\gamma_{B_{1g}} + c\gamma_{B_{2g}}\right)\lambda_{\mathbf{k}} \\
&= au\sum_{\mathbf{k}}\gamma_{A_{1g}}\lambda_{A_{1g}} + bv\sum_{\mathbf{k}}\gamma_{B_{1g}}\lambda_{B_{1g}}.
\end{aligned} \tag{B.34}$$

The screened Raman response is now much more complicated than in the tetragonal case

$$
\begin{aligned}
\chi^{sc}_{\gamma\gamma} &= u\sum_{\mathbf{k}}\left(a^2\gamma^2_{A_{1g}}+b^2\gamma^2_{B_{1g}}+c^2\gamma^2_{B_{2g}}\right)\lambda_{A_{1g}}+2vab\sum_{bfk}\gamma_{A_{1g}}\gamma_{B_{1g}}\lambda_{B_{1g}} \\
&\quad -\frac{a^2u^2\left(\sum_{\mathbf{k}}\gamma_{A_{1g}}\lambda_{A_{1g}}\right)^2+b^2v^2\left(\sum_{\mathbf{k}}\gamma_{B_{1g}}\lambda_{B_{1g}}\right)^2+2abuv\left(\sum_{\mathbf{k}}\gamma_{A_{1g}}\lambda_{A_{1g}}\right)\left(\sum_{\mathbf{k}}\gamma_{B_{1g}}\lambda_{B_{1g}}\right)}{u\sum_{\mathbf{k}}\lambda_{A_{1g}}} \\
&= u\left(a^2\chi_{A_{1g}}+b^2\chi_{B_{1g}}+c^2\chi_{B_{2g}}\right) \\
&\quad +2abv\left[\sum_{\mathbf{k}}\gamma_{A_{1g}}\gamma_{B_{1g}}\lambda_{B_{1g}}-\frac{\left(\sum_{\mathbf{k}}\gamma_{A_{1g}}\lambda_{A_{1g}}\right)\left(\sum_{\mathbf{k}}\gamma_{B_{1g}}\lambda_{B_{1g}}\right)}{\sum_{\mathbf{k}}\lambda_{A_{1g}}}\right]
\end{aligned}
\tag{B.35}
$$

where

$$
\begin{aligned}
\chi_{A_{1g}} &= \sum_{\mathbf{k}}\gamma^2_{A_{1g}}\,\lambda_{A_{1g}}-\frac{\left(\sum_{\mathbf{k}}\gamma_{A_{1g}}\,\lambda_{A_{1g}}\right)^2}{\sum_{\mathbf{k}}\lambda_{A_{1g}}} \\
\chi_{B_{1g}} &= \sum_{\mathbf{k}}\gamma^2_{B_{1g}}\,\lambda_{A_{1g}}\frac{v^2}{u^2}\frac{\left(\sum_{\mathbf{k}}\gamma_{B_{1g}}\,\lambda_{B_{1g}}\right)^2}{\sum_{\mathbf{k}}\lambda_{A_{1g}}} \\
\chi_{B_{2g}} &= \sum_{\mathbf{k}}\gamma^2_{B_{2g}}\,\lambda_{A_{1g}}.
\end{aligned}
\tag{B.36}
$$

In the case both where both the angles α and β are non-zero, for example in the case with (xx) polarization ($\alpha = \beta = 0°$), not only do we get a sum of the pure A_{1g} and B_{1g} responses, but also a mixing term where v, the amount of B_{1g} admixture to $\lambda_{\mathbf{k}}$, is a multiplicative factor.

It is also clear that even for a pure B_{1g} polarization spectrum the orthorhombic distortions result in Coulomb screening effects. The screening term, not present in the tetragonal case, now makes an appearance for the orthorhombic system.

While one can expect the orthorhombic distortion parameter v to be small in the many cases where the only distortion is in the "buckling" of CuO_2 layers as in the Bismuth compounds, the effects of the chains in YBaCuO are expected to be very large. In this case one would have to consider the mixing terms in equation (B.35).

Bibliography

Abramowitz, M. and I. Stegun (Eds.) (1972). *Handbook of Mathematical Functions*. New York: Dover.

Abrikosov, A. A. and L. A. Fal'kovskii (1961). *Sov. Phys. JETP 13*, 179.

Abrikosov, A. A. and V. M. Genkin (1974). *Sov. Phys. JETP 38*, 417.

Abrikosov, A. A., L. P. Gor'kov, and I. E. Dzyalosinski (1963). *Methods of Quantum Field Theory in Statistical Physics*. Englewood Cliffs: Prentice Hall.

Allen, P. (1971). *Phys. Rev. B 3*, 305.

Allen, P. B. and B. Mitrovic (1982). In F. S. H. Ehrenreich and D. Turnbull (Eds.), *Solid State Physics - Advances in Research and Applications, Vol. 37*, pp. 2. New York: Academic Press.

Anderson, P. W. (1959). *J. Phys. Chem. Solids 11*, 26.

Anderson, P. W. (1987). *Science 235*, 1196.

Anderson, P. W. and W. F. Brinkman (1978). In K. H. Bennemand and J. b. Ketterson (Eds.), *The Physics of Liquid and Solid Helium, Part III*, pp. 177. New York: Wiley.

Annett, J. F., N. Goldenfeld, and A. J. Leggett (1996). In D. M. Ginsberg (Ed.), *Physical Properties of High Temperature Superconductors*, Volume V, pp. 375. Singapore: World Scientific.

Annett, J. F., N. Goldenfeld, and S. R. Renn (1992). In D. M. Ginsberg (Ed.), *Physical Properties of High Temperature Superconductors*, Volume II, pp. 571. Singapore: World Scientific.

Arberg, P. (1995). *Electromagnetic Properties of 2-Dimensional* $d_{x^2-y^2}$ *Symmetry Superconductors*. Ph. D. thesis, McMaster University.

Arberg, P., M. Mansor, and J. P. Carbotte (1993). *J. Phys. Chem. Solids 54*, 1461.

Arfi, B. (1992). *Phys. Rev. B 45*, 2352.

Ashcroft, N. W. and N. D. Mermin (1976). *Solid State Physics*. Philadelphia: Saunders College.

Basov, D. et al. (1996). *Phys. Rev. Lett. 74*, 598.

Bednorz, J. G. and K. A. Muller (1986). *Z. Phys. 64*, 189.

Bickers, N. E. et al. (1990). *Phys. Rev. B 42*, 67.

Birgeneau, R. J. and G. Shirane (1989). In D. M. Ginsberg (Ed.), *Physical Properties of High Temperature Superconductors*, Volume I, pp. 151. Singapore: World Scientific.

Bonn, D. A. et al. (1992). *Phys. Rev. Lett. 68*, 2390.

Bonn, D. A. et al. (1993). *J. Phys. Chem. Solids 54*, 1297.

Branch, D. (1995). Electronic raman scattering in nearly antiferromagnetic fermi liquids. Master's thesis, McMaster University.

Branch, D. and J. P. Carbotte (1995). *Phys. Rev. B 52*, 603.

Branch, D. and J. P. Carbotte (1996). *Phys. Rev. B 54*, 13288.

Campuzano, J. C. et al. (1990). *Phys. Rev. Lett 64*, 2308.

Carbotte, J. P. (1990). *Rev. Mod. Phys. 62*, 1027.

Chakravarty, S. and P. W. Anderson (1994). *Phys. Rev. Lett. 72*, 1196.

Chen, X. et al. (1994). *Phys. Rev. Lett. 73*, 3290.

Chu, C. W. et al. (1993). *Nature 365*, 323.

Cooper, S. L. et al. (1988a). *Phys. Rev. B 37*, 5920.

Cooper, S. L. et al. (1988b). *Phys. Rev. B 38*, 11934.

Devereaux, T. P. (1992). *Phys. Rev. B 45*, 12965.

Devereaux, T. P. (1993). *Phys. Rev. B 47*, 5230.

Devereaux, T. P. (1995). *Phys. Rev. Lett. 47*, 4313.

Devereaux, T. P. and D. Einzel (1995). *Phys. Rev. B 51*, 16336.

Devereaux, T. P., D. Einzel, and B. Stadlober (1994). *Phys. Rev. Lett. 72*, 3291.

Devereaux, T. P. and A. P. Kampf (1997). cond-mat/9702186, to be published in Inter. J. Mod. Phys. B.

Devereaux, T. P., A. Virosztek, and A. Zawadowski (1996). *Phys. Rev. B 54*, 12523.

Dierker, S. B. et al. (1983). *Phys. Rev. Lett. 50*, 853.

Ding, H. et al. (1996). *Phys. Rev. Lett. 78*, 2631.

Ding, H. et al. (1997). *Phys. Rev. Lett. 78*, 2628.

Dolgov, O. V., E. G. Maksimov, and S. V. Shulga (1991). In R. Baquero (Ed.), *Electron-Phonon Interaction in Oxide Superconductors*, pp. 30. Singapore: World Scientific.

Doniach, S. and E. H. Sondheimer (1974). *Green's Functions for Solid State Physicists*. Reading, Mass.: Addison-Wesley.

Donovan, S. et al. (1995). *J. Super. 8*, 417.

Einzel, D. and R. Hackl (1996). *J. Raman Spec. 27*, 307.

Emery, V. G. (1983). *J. Phys. (Paris) Colloq. 44*, C3–977.

Fal'kovskii and Klama (1990). *Physica C 172*, 242.

Farnworth, B. and T. Timusk (1974). *Phys. Rev. B. 10*, 1970.

Fehrenbacher, R. (1996). *Phys. Rev. B 54*, 6632.

Ferrell, R. A. and R. E. Glover (1958). *Phys. Rev. 109*, 1398.

Fetter, A. L. and J. D. Walecka (1971). *Quantum Theory of Many Particle Systems*. New York: McGraw Hill.

Forster, D. (1975). *Hydrodynamic Fluctuations, Broken Symmetry and Correlation Functions*. Reading, Mass.: W.A. Benjamin, Inc.

Foster, C. M. et al. (1990). *Solid State Commun. 76*, 651.

Fraas, L. M., P. F. Williams, and S. P. S. Porto (1970). *Solid State Comm. 8*, 2113.

Fradkin, E. (1991). *Field Theories of Condensed Matter Systems.* Redwood City, CA: Addison-Wesley.

Gasparov, L. V. et al. (1997). *Phys. Rev. B 55*, 1223.

Golub, G. H. and C. F. van Loan (1989). *Matrix Computations, 2nd edition.* Baltimore: Johns Hopkins University Press.

Grimvall, G. (1980). *The Electron-Phonon Interaction in Metals.* Amsterdam: North-Holland.

Gurvich, M. and A. T. Fiory (1987). *Phys. Rev. Lett. 59*, 1337.

Hackl, R. et al. (1988). *Phys. Rev. B 38*, 7133.

Hackl, R., R. Kaiser, and S. Schicktanz (1983). *J. Phys. C 16*, 1729.

Hasegawa, T., H. Ikuta, and K. Kitazawa (1992). In D. M. Ginsberg (Ed.), *Physical Properties of High Temperature Superconductors*, Volume III, pp. 525. Singapore: World Scientific.

Hayden, S. M. et al. (1996). cond-mat/9611179.

Hirsch, J. E. (1985). *Phys. Rev. Lett. 54*, 1317.

Hirschfeld, P., W. Putikka, and D. J. Scalapino (1994). *Phys. Rev. B 50*, 10250.

Hirschfeld, P., D. Volhardt, and P. Wolfe (1986). *Sold State Comm. 59*, 111.

Hirschfeld, P., P. Wolfe, and D. Einzel (1988). *Phys. Rev. B 37*, 83.

Holstein, T. (1954). *Phys. Rev. 96*, 535.

Holstein, T. (1964). *Ann. Phys. 29*, 410.

Hubbard, J. (1963). *Proc. R. Soc. London A276*, 238.

Irwin, C. et al. (1995). *J. Super. 8*, 495.

Iye, Y. (1992). In G. M. Ginsberg (Ed.), *Physical Properties of High Temperature Superconductors*, Volume III. Singapore: World Scientific.

Jiang, C. (1992). Effects of planar anisotropy on eliashberg superconductors.

Jiang, C. et al. (1996). *Phys. Rev. B 54*, 1265.

Jiang, C. and J. P. Carbotte (1996). *Phys. Rev. B 53*, 11868.

Joyce, R. R. and P. L. Richards (1970). *Phys. Rev. Lett. 24*, 1007.

Kampf, A. and J. R. Schrieffer (1990). *Phys. Rev. B 41*, 6399.

Kirtley, J. R. et al. (1987). *Phys. Rev. B 35*, 8846.

Klein, M. V. and S. B. Dierker (1984). *Phys. Rev. B 29*, 4976.

Kostur, V. and B. Mitrović (1995). *Phys. Rev. B 51*, 16388.

Kostur, V. N. (1992). *Z. Phys. B 89*, 149.

Kostur, V. N. and G. M. Eliashberg (1991). *JETP Lett. 53*, 391.

Kosztin, J. and A. Zawadowski (1991). *Solid State Commun. 78*, 1029.

Krantz, M. C. and M. Cardona (1994). *Phys. Rev. Lett. 72*, 3290.

Krantz, M. C. and M. Cardona (1995). *J. Low Temp. Phys. 99*, 205.

Landau, L. D. and E. M. Lifshitz (1960). *Electrodynamics of Continuous Media*. Oxford: Pergamon Press.

Leavens, C. R. and D. S. Ritchie (1985). *Solid State Comm. 53*, 137.

Lee, P. A. (1993). *Phys. Rev. Lett. 71*, 1887.

Lee, P. A. and N. Nagaosa (1992). *Phys. Rev. B 46*, 5621.

Lee, W., D. Rainer, and W. Zimmermann (1989). *Physica C 159*, 535.

Lehmann, G. and M. Taut (1972). *Phys. Stat. Sol.(b) 54*, 469.

Lenck, S., J. P. Carbotte, and R. C. Dynes (1994). *Phys. Rev. B 50*, 10149.

Luttinger, J. M. (1960). *Phys. Rev. 119*, 1153.

Mahan, G. D. (1990). *Many-Particle Physics, 2^{nd} ed.* New York: Plenum Press.

Maki, K. (1969). In R. Parks (Ed.), *Superconductivity*, Volume 1, pp. 1035. New York: Dekker.

Mansor, M. (1994). *Some Properties of s and d-wave 2 Dimensional Superconductors.* Ph. D. thesis, McMaster University.

Marsiglio, F. et al. (1996). *Phys. Rev. B 53*, 9433.

Marsiglio, F. and J. P. Carbotte (1995). *Phys. Rev. B 52*, 16192.

Marsiglio, F. and J. P. Carbotte (1997). unpublished.

Marsiglio, F., M. Schossmann, and J. P. Carbotte (1988). *Phys. Rev. B 37*, 4965.

Mattis, D. C. and J. Bardeen (1958). *Phys. Rev. 111*, 412.

McMillan, W. L. and J. M. Rowell (1965?). *Phys. Rev. Lett. 14*, 108.

McMillan, W. L. and J. M. Rowell (1969). In R. D. Parks (Ed.), *Superconductivity*, Volume 1, pp. 561. New York: Marcel-Dekker.

Migdal, A. B. (1958). *Sov. Phys. JETP 7*, 762.

Millis, A. J. (1992). *Phys. Rev. B 45*, 13047.

Millis, A. J., H. Monien, and D. Pines (1990). *Phys. Rev. B 42*, 167.

Millis, A. J., S. Sachdev, and C. M. Varma (1988). *Phys. Rev. B 37*, 4975.

Mitrović, B. (1981). *Effects of energy dependence in the electronic density of states on some normal and superconducting properties.* Ph. D. thesis, McMaster University.

Mitrović, B. and M. Castle (1996). preprint cond-mat 9608006.

Miyake, K., S. Schmitt-Rink, and C. M. Varma (1986). *Phys. Rev. B 1986*. 6554.

Monien, H. and A. Zawadowski (1990). *Phys. Rev. B 51*, 16336.

Monthoux, P., A. Balatsky, and D. Pines (1991). *Phys. Rev. Lett. 67*, 3448.

Monthoux, P., A. Balatsky, and D. Pines (1992). *Phys. Rev. B 46*, 14803.

Monthoux, P. and D. Pines (1992). *Phys. Rev. Lett. 69*, 961.

Monthoux, P. and D. Pines (1993). *Phys. Rev. B 47*, 6069.

Monthoux, P. and D. J. Scalapino (1994). *Phys. Rev. Lett. 72*, 1874.

Moriya, T., Y. Takahashi, and K. Ueda (1990). *J. Phys. Soc. Jpn 59*, 2905.

Nam, S. B. (1967a). *Phys. Rev. 156*, 470.

Nam, S. B. (1967b). *Phys. Rev. 156*, 487.

Nambu, Y. (1960). *Phys. Rev. 117*, 648.

Nemetalek, R. et al. (1993). *Phys. Rev. B 47*, 5450.

Nicol, E., C. Jiang, and J. P. Carbotte (1993). *Phys. Rev. B 47*, 8131.

Norman, M. R. (1988). *Phys. Rev. B 37*, 4987.

Nuss, M. C. et al. (1991). *Phys. Rev. Lett. 66*, 3305.

Olson, C. G. et al. (1990). *Phys. Rev. B 42*, 381.

Palmer, L. H. and M. Tinkham (1968). *Phys. Rev. 165*, 588.

Pao, C. H. and N. E. Bickers (1994). *Phys. Rev. Lett. 72*, 1870.

Pickett, W. E. (1989). *Rev. Mod. Phys. 61*, 433.

Pines, D. and P. Nozieres (1966). *The Theory of Quantum Liquids.* New York: W. A. Benjamin.

Poole, C. P. and H. A. Farach (1995). *Superconductivity.* San Diego: Academic Press.

Press, W. H., B. P. Flannery, S. A. Teukolsky, and W. T. Vetterling (1993). *Numerical Recipes in C, 2nd ed.* Cambridge: Cambridge University Press.

Puchkov, A. V. et al. (1996). *Phys. Rev. Lett. 77*, 1853.

Puchkov, A. V., D. N. Basov, and T. Timusk (1996). *J. Phys. Condens. Matter 8*, 10049.

Radtke, R. et al. (1992). *Phys. Rev. B 46*, 11957.

Rammer, J. (1987). *Phys. Rev. B 36*, 5665.

Rickayzen, G. (1965). *Theory of Superconductivity.* New York: Wiley–Interscience.

Rickayzen, G. (1980). *Green's Functions and Condensed Matter Physics.* New York: Academic Press.

Rossat-Mignod, J. et al. (1988). *J. Physique Coll. C 8*, 2119.

Rossat-Mignod, J. et al. (1991a). *Physica B 169*, 58.

Rossat-Mignod, J. et al. (1991b). *Physica B 185-189*, 86.

Sacuto, A. et al. (1996). preprint cond-mat 9612052.

Sakurai, J. J. (1967). *Advanced Quantum Mechanics*. New York: Addison-Wesley.

Scalapino, D. J. (1969). In R. Parks (Ed.), *Superconductivity*, Volume 1, pp. 449. New York: Dekker.

Scalapino, D. J., E. Loh, and J. E. Hirsch (1986). *Phys. Rev. B 34*, 8190.

Schachinger, E. and J. P. Carbotte (1997). preprint.

Schneider, T. and M. P. Sorensen (1991). *Z. Phys. B80*, 331.

Schrieffer, J. R. (1964). *Theory of Superconductivity*. New York: Addison-Wesley.

Schrieffer, J. R., D. J. Scalapino, and J. W. Wilkins (1963). *Phys. Rev. Lett 10*, 336.

Schüttler, H. B. and M. R. Norman (1996). *Phys. Rev. B 54*, 13295.

Serene, J. W. and D. W. Hess (1991). *Phys. Rev. B 44*, 3391.

Sharifzadeh, M. H. and P. C. E. Stamp (1996). *Phys. Rev. Lett. 77*, 3017.

Shen, Z. X. et al. (1993). *Phys. Rev. Lett. 70*, 1553.

Shulga, S. et al. (1991). *Physica C 178*, 266.

Sooryakumar, R. and M. V. Klein (1980). *Phys. Rev. Lett. 45*, 660.

Stadlober, B. et al. (1995). *J. Phys. Chem. Solids 56*, 1841.

Startseva, T. et al. (1997). preprint, cond-mat 9706145.

Staufer, T. et al. (1992). *Phys. Rev. Lett. 68*, 1069.

Stojkovic, B. P. and D. Pines (1997a). *Phys. Rev. B 55*, 8576.

Stojkovic, B. P. and D. Pines (1997b). unpublished, cond-mat/9706247.

Strohm, T. and M. Cardona (1997). *Phys. Rev. B 55*, 12725.

Tanner, D. B. and T. Timusk (1992). In D. M. Ginsberg (Ed.), *Physical Properties of High Temperature Superconductors III*, pp. 441. Singapore: World Scientific.

Timusk, T. and D. B. Tanner (1989). In D. M. Ginsberg (Ed.), *Physical Properties of High Temperature Superconductors I*, pp. 339. Singapore: World Scientific.

Tinkham, M. (1964). *Group Theory and Quantum Mechanics*. New York: McGraw-Hill.

Tinkham, M. (1975). *Superconductivity*. New York: McGraw-Hill.

Tinkham, M. and R. A. Ferrell (1959). *Phys. Rev. Lett. 2*, 331.

Varma, C. M. et al. (1989). *Phys. Rev. Lett. 63*, 1996.

Vidberg, H. J. and J. W. Serene (1977). *J. Low Temp. Phys. 29*, 179.

Virosztek, A. and J. Ruvalds (1992). *Phys. Rev. B 45*, 347.

Wenger, F. and M. Käll (1997). *Phys. Rev. B 55*, 97.

Wilkins, J. W. (1980). In M. Springford (Ed.), *Electrons at the Fermi Surface*. pp. 46. Cambridge: Cambridge University Press.

Williams, P. J. (1990). *Spin Fluctuations in Eliashberg Theory*. Ph. D. thesis, McMaster University.

Williams, P. J. and J. P. Carbotte (1991). *Phys. Rev. B 43*, 7960.

Wu, M. K. et al. (1987). *Phys. Rev. Lett. 58*, 908.

Wu, W. C. and J. P. Carbotte (1997). unpublished.

Yamanaka, A. et al. (1992). *Phys. Rev. B 46*, 516.

Zhou, C. and H. J. Schulz (1992). *Phys. Rev. B 45*, 7393.

Ziman, J. M. (1979). *Principles of the Theory of Solids*. Cambridge: Cambridge University Press.